UCLA
UCLA Electronic Theses and Dissertations

Title
Characterizing the Interstellar and Circumgalactic Medium in Distant Star-Forming Galaxies

Permalink
https://escholarship.org/uc/item/6mq1k23r

Author
Du, Xinnan

Publication Date
2018

Peer reviewed|Thesis/dissertation

eScholarship.org Powered by the California Digital Library
University of California

UNIVERSITY OF CALIFORNIA
Los Angeles

Characterizing the Interstellar and Circumgalactic Medium in Distant Star-Forming Galaxies

A dissertation submitted in partial satisfaction
of the requirements for the degree
Doctor of Philosophy in Astronomy

by

Xinnan Du

2018

© Copyright by
Xinnan Du
2018

ABSTRACT OF THE DISSERTATION

Characterizing the Interstellar
and Circumgalactic Medium in
Distant Star-Forming Galaxies

by

Xinnan Du
Doctor of Philosophy in Astronomy
University of California, Los Angeles, 2018
Professor Alice Eve Shapley, Chair

Rest-frame ultraviolet (UV) and optical spectroscopy provides valuable information on the physical properties of the neutral and ionized interstellar medium (ISM) in star-forming galaxies. Such observations probe both the systemic interstellar component originating from H II regions, and the multi-phase outflowing component that is associated with star-formation feedback and can ultimately contribute to the circumgalactic and even intergalactic medium (CGM and IGM, respectively). In this dissertation, I investigate the physical properties of ionized gas in star-forming regions, and the kinematics and evolution of the multi-phase outflowing ISM/CGM in distant star-forming galaxies spanning the redshift range $z \sim 1-4$. This work consists of three studies that examine different aspects of the ISM and CGM, which collectively improve our understanding of the gas content in galaxies and the processes associated with the formation of massive stars near the peak of the star-formation-rate (SFR) density in the universe. I present a comparison of kinematics between the low- and high-ionization absorption features at $z \sim 1$, and demonstrate that the apparent larger blueshift of interstellar C IV relative to the low-ionization features is likely a result from the nature of resonant transitions instead of an evidence of the faster motion of the highly ionized gas. I further investigate the origin of the highly ionized gas by examining the correlations between the spectral properties of C IV and various galaxy properties. Both the blueshift and equivalent width (EW) of C IV are modulated by SFR and specific SFR, suggesting a

direct connection between the highly ionized gas and the formation of massive stars. Nebular emission features provide valuable insights into the physical conditions of the ionized gas in H II regions, as well as the properties of young, massive stars. I show that the nebular C III] emission at $z \sim 1$ is much weaker compared to the detections from galaxies observed during the epoch of reionization ($z > 6$), and explore the factors that modulate the strength of this nebular feature. In combination with the results from photoionization models, I further infer the gas-phase metallicity and abundance pattern in the $z \sim 1$ star-forming galaxies based on the observed rest-frame C III] EW. Studying the lower-redshift analogs of the $z > 6$ C III] emitters is an alternative way to obtain more detailed information on the physical properties of these extreme-emission-line-galaxies (EELGs). By assembling a sample of EELGs at $z \sim 1-2$ and examining C III] and other nebular emission features, I aim to characterize the physical conditions of the $z > 6$ galaxies that are likely responsible for the cosmic reionization. Finally, with carefully constructed samples and uniform measurements, I investigate the evolution of the ISM/CGM at $z \sim 2-4$ as probed by rest-UV spectroscopy. I discover redshift-independent correlations among Lyα emission, low-ionization interstellar absorption lines, and dust extinction. I further show that the covering fraction of neutral gas decreases with increasing redshift at multiple fixed galaxy properties. Gaining a full understanding of galaxy evolution requires further studies of the ISM/CGM in a systemic manner at higher redshifts. With exceptional capabilities in the near-IR and excellent spectroscopic sensitivity, the next generation of large telescopes will enable rest-UV and rest-optical spectroscopic studies of star-forming galaxies out to $z > 10$. Answering key questions regarding the interplay among massive stars, their contribution to the ionizing background, and feedback will deliver a clear picture of the formation and evolution of these distant star-forming galaxies.

The dissertation of Xinnan Du is approved.

Jean L. Turner

James E. Larkin

Matthew A. Malkan

Alice Eve Shapley, Committee Chair

University of California, Los Angeles

2018

To my family

TABLE OF CONTENTS

LIST OF FIGURES

LIST OF TABLES

ACKNOWLEDGMENTS

The five years of life I spent as a graduate student can hardly be summarized in one single dissertation. There are many moments of happiness, excitement, and accomplishment along the journey, accompanied by periods of frustration, disappointment, and struggle. All of these combined have given me a unique experience during one of the most important stages of my life. I am very thrilled to have spent my time in grad school with so many awesome people, without whose support and help I wouldn't have been where I am now.

I wish to express my sincere gratitude to my advisor, Alice Shapley, who has been role model to me the entire time. With exceptional patience, she shows me step by step how to become an astronomer. She always considers what's good for my career, what fits my interests, and I cannot thank her enough for her support for my decision of going into outreach. I feel very lucky to have Alice as my advisor for grad school, and she will always be someone motivating me to go from great to excellent.

I would also like to thank the members of my dissertation committee: Alice Shapley, Matt Malkan, James Larkin, and Jean Turner for their time, support, and guidance during my Advance to Candidacy exam and the review of this document.

It has been such a pleasure to work with so many talented and devoted astronomers, including Alice Shapley, Crystal Martin, Dan Stark, Tucker Jones, Naveen Reddy, Richard Ellis, Chuck Steidel, Dawn Erb, Gwen Rudie, Max Pettini, and Alison Coil, on the work presented in this dissertation. I am truly thankful for all the constructive inputs given by my collaborators. The enlightening discussions with them have significantly contributed to the presentation of my work.

The majority of the data presented in this dissertation were obtained using the Keck I telescope at the W. M. Keck Observatory on Mauna Kea, Hawaii. I wish to extend special thanks to those of Hawaiian ancestry on whose sacred mountain we are privileged to be guests. Without their generous hospitality, most of the observations and work presented

herein would not have been possible. In addition, I want to acknowledge DEEP2, AEGIS, and 3D-HST teams for providing ancillary data for my work on these projects.

I am much obliged to the UCLA Astronomy graduate students, faculty, postdocs, and staff for creating such a inclusive, friendly environment. I fell in love with the department when I did my REU program in 2012 with Matt Malkan, and have been deeply attached to the people here since I started grad school. I would like to express my special appreciation to my friend and cohort Samantha Chappell, with whom I have shared an office as well as moments of ups and downs for the past five years. In addition, I am very appreciative of being in "the Alice group" with Ryan Sanders, Michael Topping, and Tony Pahl, who have been of great help in all aspects of research and life.

Lastly, I want to thank Anowar Jaman Shajib for giving me continuous support and inspiring me to grow into a better person. No words can describe how grateful I am for my family, especially my mom and dad. I feel deeply loved and cared. Although we are separated by 7000 miles and a time difference of 16 hours, they share every detail of my life, and provide extremely valuable suggestions on my career options. It is a regret that my paternal grandparents, who both passed away during my time in grad school, will not be able to read this dissertation and see me getting the PhD degree. But I believe that they, as well as everyone else in the family, are very proud of me.

Chapter 2 is a version of Du et al. (2016, ApJ, 829, 64, DOI:10.3847/0004-637X/829/2/64), and is reproduced with permission from the AAS. I would like to acknowledge my co-authors on this work: Alice Shapley, Alice Shapley, Crystal Martin, and Alison Coil.

Chapter 3 is a version of Du et al. (2017, ApJ, 838, 63, DOI:10.3847/1538-4357/aa64cf), and is reproduced with permission from the AAS. I would like to acknowledge my co-authors on this work: Alice Shapley, Crystal Martin, and Alison Coil.

Chapter 4 is a version of Du et al. (2018, ApJ, 860, 75, DOI:10.3847/1538-4357/aabfcf), which is at the final stage of the production process. I would like to acknowledge my co-authors on this work: Alice Shapley, Naveen Reddy, Tucker Jones, Dan Stark, Chuck Steidel, Allison Strom, Gwen Rudie, Dawn Erb, Richard Ellis, and Max Pettini.

My work on these projects has been supported by the Richard B. Kaplan Endowed Graduate Award in Astrophysics (2013 and 2015) and the David Lucile Packard Foundation. I have presented my dissertation work at other universities and in multiple domestic and international conferences, thanks to support from Richard B. Kaplan, the UCLA Graduate Division Travel Grant, the departmental Richardson Travel Fund, and the AAS Rodger Doxsey Travel Prize.

VITA

2009	Graduated, High School attached to Tsinghua University, China
2013	B.S. (Astronomy), Nanjing University, China
2016	M.S. (Astronomy), University of California, Los Angeles

PUBLICATIONS

Du, X., Shapley, A. E., Martin, C. L., and Coil, A. L. "The Kinematics of C IV in Star-forming Galaxies at $z \sim 1.2$." 2016, ApJ, 829, 64.

Du, X., Shapley, A. E., Martin, C. L., and Coil, A. L. "C III] Emission in Star-forming Galaxies at $z \sim 1$." 2017, ApJ, 838, 63.

Du, X., Shapley, A. E., Reddy, N. A., Jones, T., Stark, D. P., Steidel, C. C., Strom, A. L., Rudie, G. C., Erb, D. K., Ellis, R. S., and Pettini, M. "The redshift evolution of rest-UV spectroscopic properties in Lyman Break Galaxies at $z \sim 2 - 4$." 2018, ApJ, 860, 75.

CHAPTER 1

Introduction

Gas is a crucial component of star-forming galaxies in that it regulates star formation. Giant molecular clouds collapse to form stars. Hot, massive stellar populations ionize their surrounding gas, creating H II regions embedded in the neutral gas and giving rise to collisionally excited lines and the recombination lines. Stellar winds, and especially supernova explosions associated with these massive stars transfer enormous amounts of energy and momentum to the ISM, driving a great volume of both neutral and ionized gas to larger radii with high velocities. These outflows can either escape the galaxy's gravitational potential, removing metals from galaxies and increasing the mass of the circumgalactic medium (CGM), or fall back to the galaxy, recycling into the interstellar medium (ISM).

Three different phases of hydrogen gas are typically found in galaxies: molecular, neutral and ionized phases. The physical properties of the neutral and ionized gas can be characterized by rest-frame ultraviolet (UV) and optical spectroscopy, which spans a rich array of absorption and emission features. Absorption lines are powerful probes of the multi-phase ISM/CGM in galaxies. High-ionization absorption lines arise from the ionized region while the low-ionization absorption features originate mainly from neutral gas. The commonly-observed blueshift of interstellar absorption lines and redshift of Lyα emission provide kinematic evidence for the possibly outflowing neutral and ionized gas (Pettini et al., 2001; Shapley et al., 2003; Steidel et al., 2010). Nebular emission lines (e.g., C III], [O III]) are generated by the warm, ionized gas associated with H II regions, and are therefore typically observed at systemic velocities. Finally, fine-structure emission lines (e.g., Si II*, Fe II*) are important in tracing the structure and the spatial extent of the CGM (e.g., Erb et al., 2012; Jones et al., 2012; Kornei et al., 2013).

1.1 Interstellar features as probes of ISM/CGM properties

With the aid of spectroscopy, detailed constraints regarding kinematics, column density, covering fraction, and spatial extent can be obtained for the absorbing gas based on the interstellar absorption profiles in the rest-frame far-UV (e.g., Si II, O I, C II, Si IV, C IV, Al II, Ni II, Al III) and near-UV (e.g., Fe II, Mg II). At a basic level, the line centroid provides important information on the kinematics of the absorbing gas, enabling us to determine the presence of outflows or inflows. The equivalent width (EW) of the absorption features can be used to constrain the column density, and infer covering fraction of the gas when the lines are saturated.

In addition to the interstellar absorption lines, Lyα can also provide useful information on the physical properties of interstellar gas. Being an emission feature, the observed Lyα strength is not only modulated by radiative transfer through ISM/CGM, but also set by the H II region properties and the dust content in the galaxies. The line profile of Lyα, along with the centroid and EW measurements, imposes valuable constraints on the ionization parameter, H I column density and covering fraction, and dust distribution.

Outflows are commonly observed in star-forming galaxies above a certain threshold in star formation surface density (Heckman et al., 2001), and are ubiquitous among actively star-forming galaxies observed at $z \sim 2$. While extensive studies have been carried out focusing on the spectral properties of the low-ionization features, there is a lack of statistical studies on the high-ionization lines, without which the multi-phase structure of outflows cannot be fully understood. Star-forming galaxies at $z \sim 1$ are useful targets for outflow studies using optical instruments. The coverage of multiple rest-frame far- and near-UV absorption lines ranging in a variety of ionization states enables investigations of different phases of gas. Our work is the first statistical study focusing on the high-ionization kinematics in star-forming galaxies at $z \sim 1$, which provides insights into the different origins of the neutral- and ionized-phases of galactic winds.

$z > 2$ is another focus of star-formation-drive outflow studies given the presence of Lyα and various rest-far-UV interstellar absorption features in the galaxy spectra. Although

multiple statistical samples have been assembled at individual redshifts (Shapley et al., 2003; Kornei et al., 2010; Steidel et al., 2010), evolutionary studies of galactic outflows are limited at this redshift range. Our work presented herein focuses on the evolution of the rest-UV spectroscopic properties in star-forming galaxies with the most systematically controlled samples to date, extending over the widest redshift baseline ($z \sim 2-4$). Rich information on feedback and the mass assembly of the galaxies can be obtained through the investigation of the evolution of ISM/CGM near the peak epoch of cosmic star formation.

1.2 Nebular features and H II region properties

Nebular (e.g., C IV, He II, [O III], C III], [O II]) and recombination transitions (e.g., Lyα, Hα, Hβ) are produced in H II regions. Nebular emission lines are typically collisionally excited, and their strengths are determined by the hardness of the ionizing spectrum, gas-phase metallicity, and abundance pattern (e.g., C/O ratio). Therefore, these nebular lines provide an important window to the physical conditions of the ionized gas in the H II regions. Moreover, the combination of these lines can be further used to infer the gas metallicity, ionization parameter, hydrogen density, electron temperature, and dust extinction.

Of particular interest is the C III]$\lambda\lambda$1907, 1909 emission doublet. As the second strongest emission feature after Lyα in the rest-far-UV, C III] can be detected out to $z \gtrsim 6$, where Lyα is greatly attenuated by the intergalactic medium (IGM; e.g., Treu et al., 2012; Pentericci et al., 2014; Schenker et al., 2014; Konno et al., 2014). More importantly, C III] is a more direct probe of the physical properties of H II regions than Lyα, whose observed profile is affected by resonant scattering through the neutral ISM and CGM.

Studies of strong C III]-emitting galaxies can provide an important window into the physical environment of the young galaxy populations at early cosmic times. Only small samples of C III] emitters (rest-frame C III] EW $\geqslant$ 5Å) have been detected at $z > 2$ and $z \sim 0$ (Shapley et al., 2003; Leitherer et al., 2011; Stark et al., 2014; Steidel et al., 2016), and very few at $z > 6$ (Stark et al., 2015, 2017; Zitrin et al., 2015). Statistical C III] investigations are especially lacking at $z \sim 1$, and searching for C III] emitters at lower redshifts ($z \sim 1-2$

instead of $z > 6$) is extremely important for analyzing the H II regions in these galaxies in greater detail given the current observational capabilities.

In order to characterize the overall physical environment in typical star-forming galaxies, separate studies of both the interstellar and circumgalactic gas components are essential. In addition, the connections among specific emission and absorption features (e.g., nebular emission and Lyα emission, Lyα emission and low-ionization absorption, fine-structure emission and and corresponding interstellar absorption) shed light on the their common origin or related physical processes, enabling the detailed dissection of the gas content in the galaxies.

In this dissertation, I investigate the physical properties of the interstellar and circumgalactic gas in star-forming galaxies spanning the redshift range $z \sim 1 - 4$. Specifically, with the first statistical sample at $z \sim 1$ with rest-frame far- and near-UV spectroscopy, I examine the outflow kinematics of gas in different ionization states, and infer the physical properties of H II regions from nebular emission features. By measuring and analyzing the interstellar absorption and resonant emission features in a uniform manner, I further explore the redshift evolution of the CGM properties in Lyman Break Galaxies (LBGs) spanning $z \sim 2 - 4$, covering the peak epoch of star formation and beyond.

This dissertation is organized as follows. In Chapter 2, I present the first statistical study of the kinematics of interstellar C IV in $z \sim 1$ star-forming galaxies, and infer the multi-phase outflow structure by comparing the C IV kinematics with those of the near-UV Fe II features. I examine the nebular C III] emission in the same $z \sim 1$ sample in Chapter 3. Understanding the nature of this rest-UV nebular feature is crucial for dissecting the bursty galaxy populations at $z > 6$, observed within the first billion years of the universe. Chapter 4 presents the first comprehensive evolutionary study of the rest-UV spectral features at $z \sim 2 - 4$, and discusses possible causes for the CGM evolution based on the observed trends. Finally, I summarize the results of these studies and discuss future directions in Chapter 5.

CHAPTER 2

The Kinematics of C IV in Star-forming Galaxies at $z \sim 1.2$

2.1 Introduction

Outflows play a key role in the evolution of galaxies. Along with inflows, they regulate the amount of gas available for star formation, and remove metals from galaxies, polluting the intergalactic medium (IGM). These galactic-scale outflows have high velocities, typically several hundreds km s^{-1}, and high mass loss rates, commonly ranging from a few tenths up to the same order as the SFR. Galactic winds may either be driven by thermal pressure associated with the supernova explosions, or else radiation pressure on dust grains from absorption and scattering of continuum photons emitted by massive stars (Murray et al., 2005).

Galactic winds appear to be ubiquitous in galaxies with star-formation surface densities above a given threshold (Heckman et al., 2001), ranging from dwarf galaxies (Martin, 1999; Heckman et al., 2001; Schwartz & Martin, 2004) to Ultra Luminous Infrared Galaxies (ULIRGs; Martin, 2005; Martin & Bouché, 2009), and are especially common at high redshift (e.g., Pettini et al., 2002; Shapley et al., 2003; Weiner et al., 2009). Outflows have typically been probed with narrowband imaging (for example, Hα) and spectra of metal absorption lines. Unsaturated lines can be used to infer the ionic column density, which can potentially provides estimates of the mass and metallicity of outflowing material. Saturated lines are still useful for probing outflow kinematics.

Outflows have a complex multi-phase structure, which can be probed using neutral,

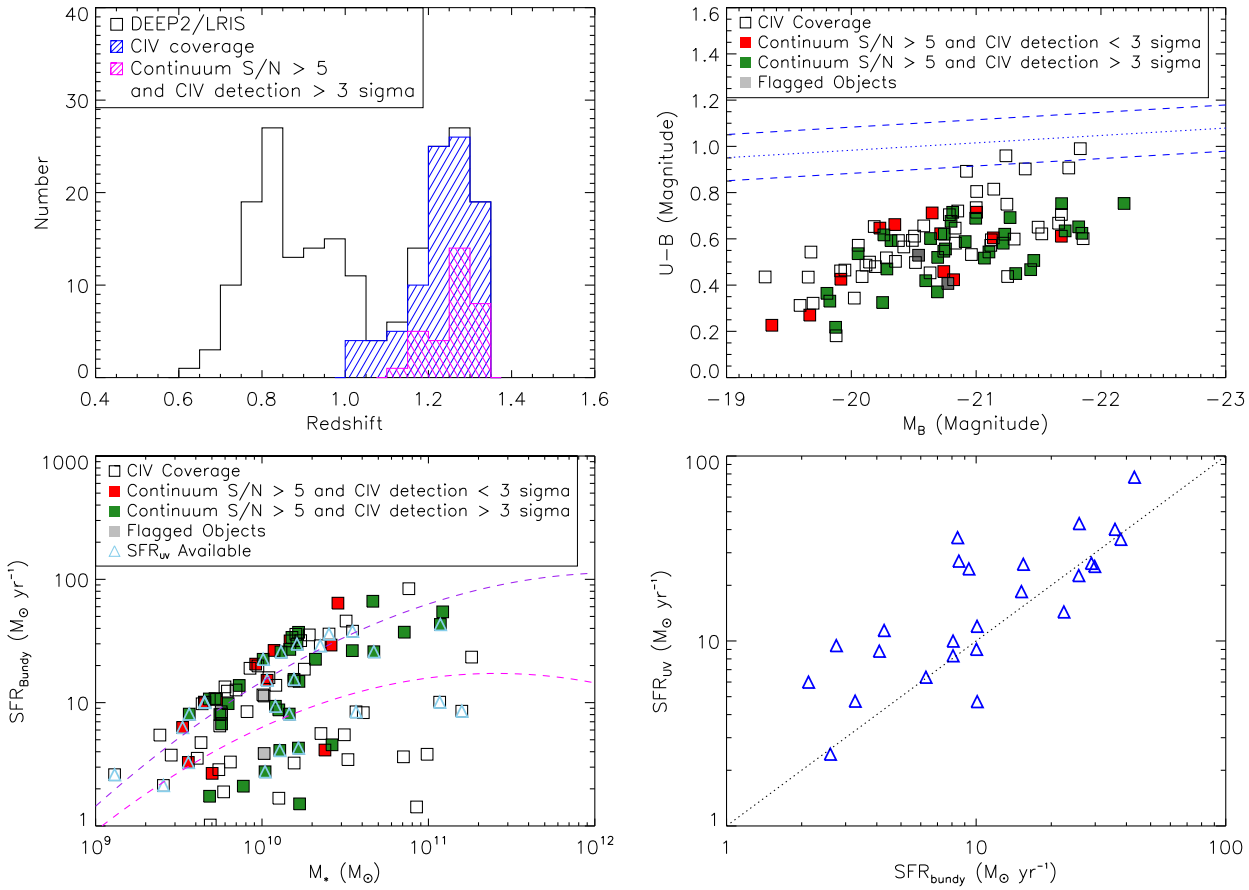

Figure 2.1: Properties of the galaxies in the DEEP2 C IV sample. **Top left:** Redshift distribution. The black open bar represents the parent sample of 208 DEEP2/LRIS galaxies; the dashed blue bar represents 93 galaxies with C IV coverage; The dashed magenta bar represents 32 galaxies meeting the criterion of continuum $S/N > 5$ and C IV detection $> 3\sigma$ ($EW/\delta EW > 3$). **Top right:** $U - B$ vs. M_B color-magnitude diagram. Squares represent 93 objects with C IV coverage; filled squares represent those with continuum $S/N > 5$; green squares denote galaxies with C IV $S/N > 3$ (32 objects) while red squares denote those with C IV $S/N < 3$ (12 objects). Grey squares represent galaxies showing asymmetric absorption on the red end of C IV (2 objects, see Section 2.3.1). The dotted line marks the division between the "red sequence" and the "blue cloud" at $z \sim 1$ in the DEEP2 sample (Willmer et al., 2006). **Bottom left:** Bundy SFR vs. stellar mass. Both stellar mass and Bundy SFR were derived from SED fitting assuming a Chabrier IMF. Color coding of the symbols is the same as in the top right panel. The open triangles show where both Bundy and GALEX SFRs are available. The purple and pink dashed lines denote the SFR - M_* relation for redshift ranges of $0.5 < z < 1.0$ and $1.0 < z < 1.5$, respectively (Whitaker et al., 2014). **Bottom right:** Comparison between Bundy and GALEX SFRs for the subset of 25 objects in the AEGIS field with both types of measurements. The GALEX SFR was measured from the dust-corrected UV luminosity (see the text in Section 4.2 for a full description) and has been converted to a Chabrier IMF. The black dotted line indicates a 1:1 relation.

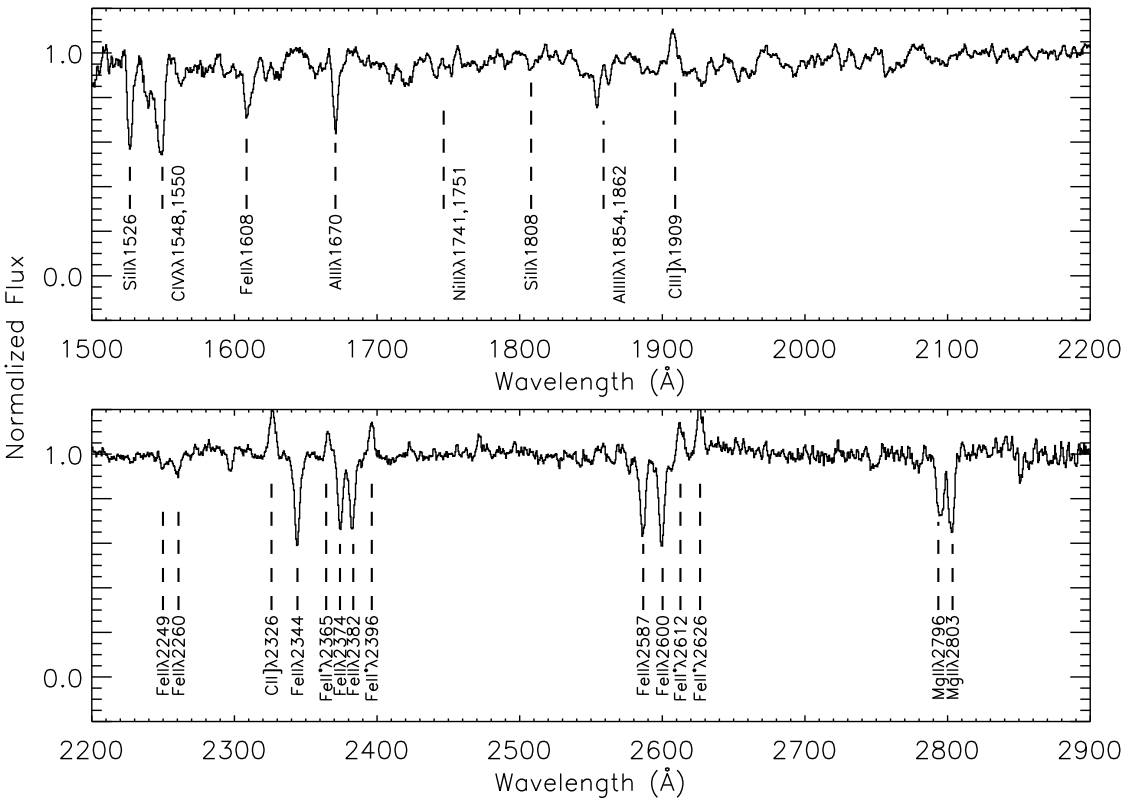

Figure 2.2: Composite continuum-normalized UV spectrum constructed from 93 objects with C IV coverage from the DEEP2/LRIS sample. Both strong and weak absorption features are identified. At the resolution of the LRIS spectra included in this composite, the C IV doublet is blended.

low- and high-ionization absorption features. Most studies of outflows have focused on low-ionization absorption lines, although there are observations of high-ionization lines for a small number of individual galaxies and from specific examples of composite spectra, (e.g., Heckman et al., 2001; Shapley et al., 2003; Schwartz et al., 2006; Grimes et al., 2009). It is not clear how the kinematics of high-ionization features relate in general to those of low-ionization lines. Some results show that the high-ionization absorption lines have a larger blueshift than the low-ionization lines by studying the coronal-phase O VI (e.g. Heckman et al., 2001; Grimes et al., 2009) and C IV (Wolfe & Prochaska, 2000), while others claim that there is no significant difference between the kinematics of high- and low-ionization lines (Pettini et al., 2002; Shapley et al., 2003; Chisholm et al., 2016). In order to gain a robust handle on the overall mass outflow rate in galactic winds, it is important, however, to understand their detailed multi-phase structure, and compare the properties of different phases of the outflow. Despite the challenges associated with using C IV as a tracer of galactic outflows, mainly because of the superposition of stellar and interstellar C IV absorption and emission, this resonant transition potentially provides a very useful probe of the warm and hot phases of outflowing interstellar gas (e.g. Heckman et al., 2001; Shapley et al., 2003; Schwartz et al., 2006; Grimes et al., 2009).

Starburst-driven outflows were first studied in the local universe (e.g., Heckman et al., 1990; Martin, 1999) and at $z > 2$ (Shapley et al., 2003; Pettini et al., 2001; Steidel et al., 2004). Relatively recently, $z \sim 1$ has become a focus of gas outflow studies. Low-ionization lines (e.g., from Mg II and Fe II) are commonly used for probing the cool phase of $z \sim 1$ outflows (e.g. Weiner et al., 2009; Martin et al., 2012; Kornei et al., 2012, 2013; Rubin et al., 2014). Although outflows are much more commonly detected than inflows at this redshift, rare instances of infalling gas have also been discovered (Coil et al., 2011; Martin et al., 2012; Kornei et al., 2012; Rubin et al., 2014). In terms of outflow demographics, the outflow velocity traced by low-ionization lines is correlated with stellar mass, SFR and SFR surface density (Weiner et al., 2009; Kornei et al., 2012), and the strength of these lines increases with stellar mass, B-band luminosity, $U - B$ color and SFR (Martin et al., 2012; Rubin et al., 2014). Finally, in most star-forming galaxies at $z \leqslant 1.5$ outflows are inferred to have

a bipolar geometry, as indicated by the detection fraction of blueshifted gas and extraplanar absorption (e.g. Rupke et al., 2005; Martin et al., 2012; Bordoloi et al., 2014; Rubin et al., 2014) and the fact that face-on galaxies tend to have a slightly faster outflow speed (Kornei et al., 2012).

In this study we focus on the high-ionization C IV$\lambda\lambda$1548,1550 doublet for the first time at $z \sim 1$. We also measure the kinematics of other far-UV low-ionization lines (Si IIλ1526, Fe IIλ1608 and Al IIλ1670) and compare them with motions traced by near-UV Fe II and Mg II lines. Both observations and simulations have shown that C IV appears to trace two distinct types of gas: the hot (T $> 10^5$ K), denser, collisionally ionized gas in the coronal phase also probed by O VI absorption, and the warm (T $< 10^5$ K), less dense, photoionized gas that may be comoving with the gas the low-ionization lines trace (Lehner et al., 2011; Shen et al., 2013). Given the intermediate ionization stage of C IV relative to that of O VI and the low-ionization lines, it is essential to examine how its kinematics differ from those inferred from low-ionization lines. Comparing the properties of different ionization phases will provide us a better understanding of the multi-phase structure of gas flows.

We provide a brief overview of the observations and data reduction, and describe the selection criteria of our C IV sample in Section 4.2. In Section 4.3, we describe the measurements of gas kinematics traced by C IV and by other low-ionization lines. We compare the kinematics of C IV and the far-UV low-ionization lines with those of the near-UV Fe II and Mg II lines in Section 2.4, and present scaling relations between outflows and galaxy properties in Section 3.4.2. Finally, we summarize and discuss our results in Section 4.7.

Throughout this paper, we use a standard Λ-CDM model with $\Omega_m = 0.3$, $\Omega_\Lambda = 0.7$ and H_0 =70 km s^{-1}. All wavelengths are measured in vacuum. Magnitudes and colors are on the Vega system.

2.2 Observations, Data Reduction and Sample

As described in Martin et al. (2012), our sample was drawn from the Deep Extragalatic Evolutionary Probe 2 (DEEP2; Newman et al., 2013) galaxy redshift survey and observed

with the dichroic Low Resolution Imager and Spectrometer (LRIS, Oke et al., 1995; Steidel et al., 2004) on the Keck I telescope. The LRIS observations were conducted over the course of 4 observing runs from 2007 to 2009. Data were collected for 9 multi-object slitmasks using $1.2''$ slits. 208 galaxies were targeted based on apparent magnitude $B < 24.5$ varying in redshift from $z = 0.4 - 1.4$ with $\langle z \rangle = 1.01$. Two sets of masks were developed for the DEEP2/LRIS sample: one set (6 masks) was observed with the 400 lines mm^{-1} grism on the blue side with the average effective resolution of 435 km s^{-1} full width at half-maximum (FWHM), and the 831 lines mm^{-1} grating on the red side with FWHM of 150 km s^{-1} ($R = 700$). The other set (3 masks) was observed with the 600 lines mm^{-1} grism on the blue side with FWHM of 282 km s^{-1}, and the 600 lines mm^{-1} red grating with FWHM of 220 km s^{-1} ($R = 1100$). The integration time for most 400-line masks ranges from 5 to 9 hours. Galaxies at $1.19 \leqslant z \leqslant 1.35$ were prioritized on these masks, as the C IV$\lambda\lambda$1548, 1550 doublet fell in a region of decent sensitivity ($\lambda \geqslant 3400$Å). The 600-line grism masks were mainly designed for less optimal observing conditions in order to obtain the near-UV spectroscopy of brighter galaxies, with typically shorter total exposure time (3-5 hours). For objects observed with the 400-line masks, the blue side of the spectra were designed to contain rest-UV interstellar absorption lines, with the red side covering the [O II] emission doublet. The 600-line spectra were typically designed for continuous wavelength coverage between the blue and red sides.

The data were reduced as described in Martin et al. (2012). In brief, the two-dimensional (2D) spectra were first flat fielded, cleaned of cosmic rays and background-subtracted. Individual 2D exposures were then combined, and extracted into one dimension (1D), and wavelength and flux calibrated. In most cases, the systemic redshift of each galaxy was determined from the [O II] doublet, which typically fell on the red side of the LRIS spectrum. For galaxies with no [O II] coverage in the LRIS spectra, the DEEP2 Keck/DEIMOS redshift was adopted.

Rest-frame B-band luminosities and $U - B$ colors were taken from Willmer et al. (2006), and the stellar mass was derived from SED fitting assuming a Chabrier (2003) initial mass function (IMF). Two types of SFR are shown in Figure 4.6: the one from Bundy et al.

(2006) was estimated from SED fitting with a Chabrier IMF, while SFR_{UV} was derived from *Galaxy Evolution Explorer* (GALEX) measurements and corrected for dust attenuation. GALEX far-UV and near-UV photometry, along with B-band observations were used to determine β, the spectral slope where the continuum flux is in the form $f_\lambda \propto \lambda^\beta$ over the rest-frame wavelength range of 1250 - 2500Å. The β/A_{UV} relationship from Seibert et al. (2005) was then used to estimate the UV attenuation and thus to correct GALEX luminosities. Given the relation from Salim et al. (2007), the dust-corrected UV SFR was then calculated assuming a Salpeter (1955) IMF and converted to a Chabrier IMF by dividing by a factor of 1.8. 25 out of 93 objects in our sample are in the AEGIS field, where both types of SFR measurements are available. Since the SED-based SFR has several limitations and possible biases (e.g., age-dust-metallicity degeneracy, systematic dependence on assumed star-formation history; Papovich et al., 2001), we only adopted the GALEX SFR for the analysis presented here, despite its restricted coverage to our sample.

One unique aspect of the DEEP2/LRIS sample is that we optimized our mask design to cover C IV and the far-UV spectral region at $z \sim 1$. With this approach, we obtained C IV coverage for 93 out of 208 objects. A composite rest-UV spectrum of these 93 objects is shown in Figure 4.3, with the strongest rest-UV interstellar features marked. Of the 93 galaxies with C IV coverage, 46 had continuum signal-to-noise ratio $(S/N) > 5$ in the vicinity of C IV from 1570Å to 1590Å, a region in which the continuum is free of line features. We adopted this S/N threshold to isolate objects with robust C IV absorption-line measurements or limits. These 46 objects comprise the main sample for analysis, and they are representative of the full sample of galaxies with C IV coverage in terms of stellar mass, SFR, B-band luminosity and $U - B$ color, except being slightly bluer than average at the brightest B-band absolute magnitudes (Figure 4.6). In the full sample of 93 objects with C IV coverage, 81 were observed with the 400-line grism, and 12 with the 600-line grism. However, all but one object (ID: 32016683) in the high S/N sample were observed with the 600-line grism.

As illustrated in Figure 4.6, our sample with C IV coverage spans in redshift from 1.01 to 1.35 with a median of 1.25, B-band luminosities $-19.31 > M_B > -22.19$ with a median of

-20.74, stellar mass $9.11 < \log(M_*/M_\odot) < 11.26$ with a median of 10.10, $U - B$ color from 0.18 to 0.99 with a median of 0.58 and SFR_{UV} from 2 to 77 $M_\odot$ yr^{-1} with a median of 14 $M_\odot$ yr^{-1}. These galaxies primarily fall in the "blue cloud" (Faber et al., 2007) of star-forming galaxies at $z \sim 1$.

2.3 Measurements

In this section, we describe the measurements of strong far-UV absorption features at wavelengths 1500Å to 1900Å, including the high-ionization doublet C IV$\lambda\lambda$1548, 1550, and low-ionization Si IIλ1526, Fe IIλ1608 and Al IIλ1670 features. We adopted single-component Gaussian fits as the simplest possible functional form to describe our absorption lines, as the data are not of sufficient resolution and S/N to consider more complicated models (especially for C IV, which already requires both stellar and interstellar model components).

2.3.1 Measurement of C IV

The C IV absorption profile is a complex superposition of stellar and interstellar components that needs to be disentangled in order to characterize the interstellar C IV absorption. The doublet members, C IVλ1548 and C IVλ1550, have a relative oscillator strength of 2:1. Therefore, the doublet ratio ranges from 2:1 in the optically thin case to 1:1 in the optically thick case. In this paper we adopted the saturated doublet ratio of 1:1, based on the typical EW of the C IV feature in our sample (Pettini et al., 2002).

We fit the rest-frame UV continuum in the 1D calibrated LRIS spectra using spectral regions ('windows') that are clean of spectral features as suggested in Rix et al. (2004). These authors modeled the composite UV stellar spectra of star-forming regions at five metallicities ranging from 0.05 to 2 $Z_\odot$ (where $Z_\odot$ indicates solar metallicity) by incorporating the output from the non-LTE atmosphere code WM-Basic (Pauldrach et al., 2001) into Starburst 99 with assumptions of a continuous star-formation history, a Salpeter IMF and a constant SFR. We applied these 'windows' for fitting the continuum for all the spectra with the IRAF *continuum* routine, using a *spline*3 function of order = 8. In cases where the fitted

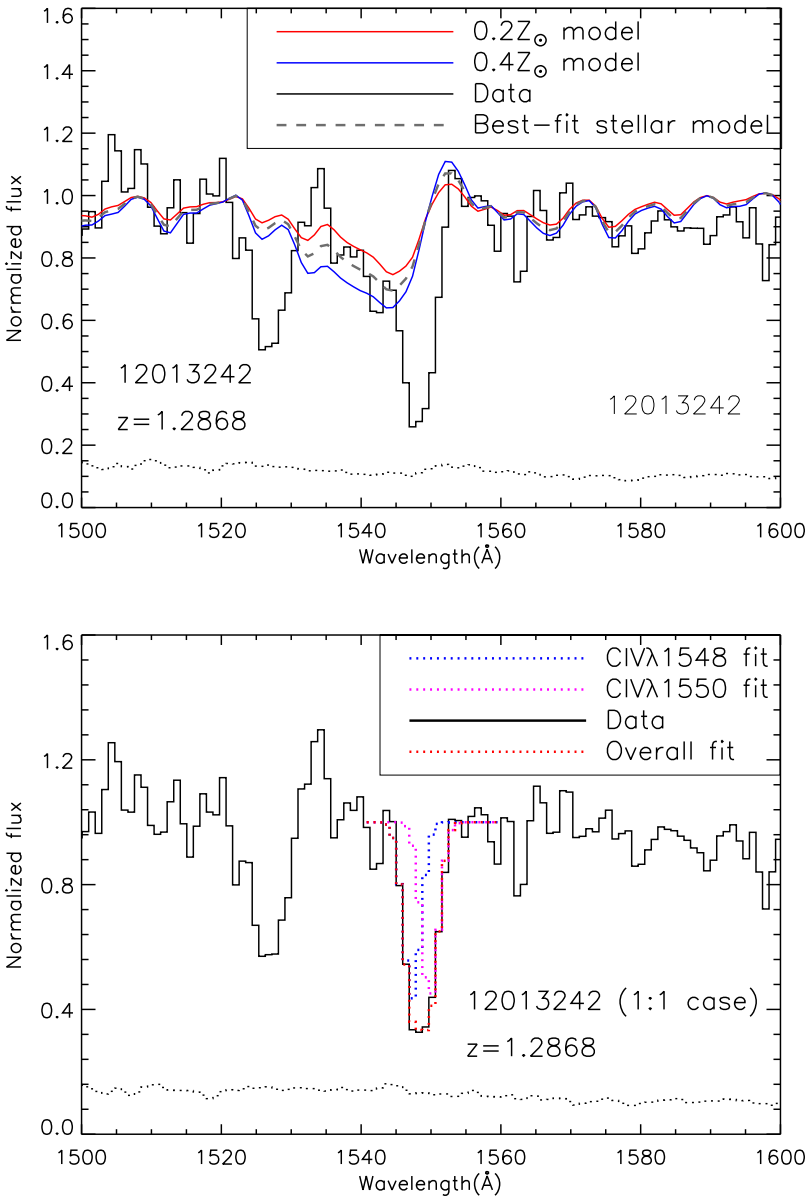

Figure 2.3: **Left:** Determination of the best-fit stellar model of object 12013242 (continuum $S/N = 16.4$). The red and blue lines indicate two stellar models ($0.2Z_{\odot}$ and $0.4Z_{\odot}$, with residuals 0.0624 and -0.0659, respectively) bracketing the P-Cygni absorption feature of C IV. The best-fit stellar model was calculated from a linear combination of these two models based on inverse residual weighting. The black dotted line represents the corresponding error spectrum of this object. **Right:** Deblending the interstellar C IV absorption trough into two Gaussian profiles. The fits for C IVλ1548 and C IVλ1550, respectively, are shown in blue and magenta dotted lines, and the overall fit is marked as the red dotted line. The centroid of the doublet members was fixed at the rest-wavelength ratio, and the EW of each member was assumed equal.

continuum level does not quite follow the observed spectrum due to the limited coverage of windows from Rix et al. (2004), we added additional windows, customized for each object, to keep the fitted continuum reasonable.

The complexity of the observed C IV absorption profile stems from the joint contributions of stellar and interstellar components. The stellar part is the P-Cygni profile mainly produced by O and B stars, where the presence of blue shifted absorption and redshifted emission is the characteristic profile of a fast-moving stellar wind. In order to isolate the interstellar C IV absorption, we must normalize the continuum by the stellar P-Cygni profile. The spectral synthesis code of Leitherer et al. (2010) outputs the rest-frame UV spectra for stellar populations based on the assumption of constant star formation, a Salpeter IMF with mass limits of 1 and 100 $M_{\odot}$, and a range in metallicity including $0.05Z_{\odot}$, $0.2Z_{\odot}$, $0.4Z_{\odot}$, $1.0Z_{\odot}$ and $2.0Z_{\odot}$. These spectra include the predicted stellar P-Cygni profiles based on models for the winds of hot stars from WM-Basic, which ranged in wavelength from 900 to 3000Å at a resolution of 0.4Å. We smoothed all 5 models to the resolution of our LRIS spectra (282 km s^{-1} FWHM or 1.4Å at 1550Å for 600-line masks, and 435 km s^{-1} FWHM or 2.2Å at 1550Å for 400-line masks) and continuum normalized them using the windows from Rix et al. (2004). For each stellar model we calculated the residual to the data based on inverse square weighting over the blue wing of C IV from 1535Å to 1544Å.

As shown in Equation 2.1, the residual, res is defined as:

$$res = \frac{\sum_i \frac{y_{model,i} - y_{data,i}}{y_{err,i}^2}}{\sum \frac{1}{y_{err,i}^2}} \tag{2.1}$$

where $y_{model,i}$, $y_{data,i}$ and $y_{err,i}$ are, respectively, the continuum-normalized stellar model from Leitherer et al. (2010), the science spectrum and the corresponding error spectrum at pixel i.

As presented in the top panel of Figure 2.3, we constructed a best-fit stellar model at each wavelength from the linear combination of the two models (red for $0.2Z_{\odot}$ and blue for $0.4Z_{\odot}$) with P-Cygni absorption depths (i.e., metallicities) that bracketed the observed

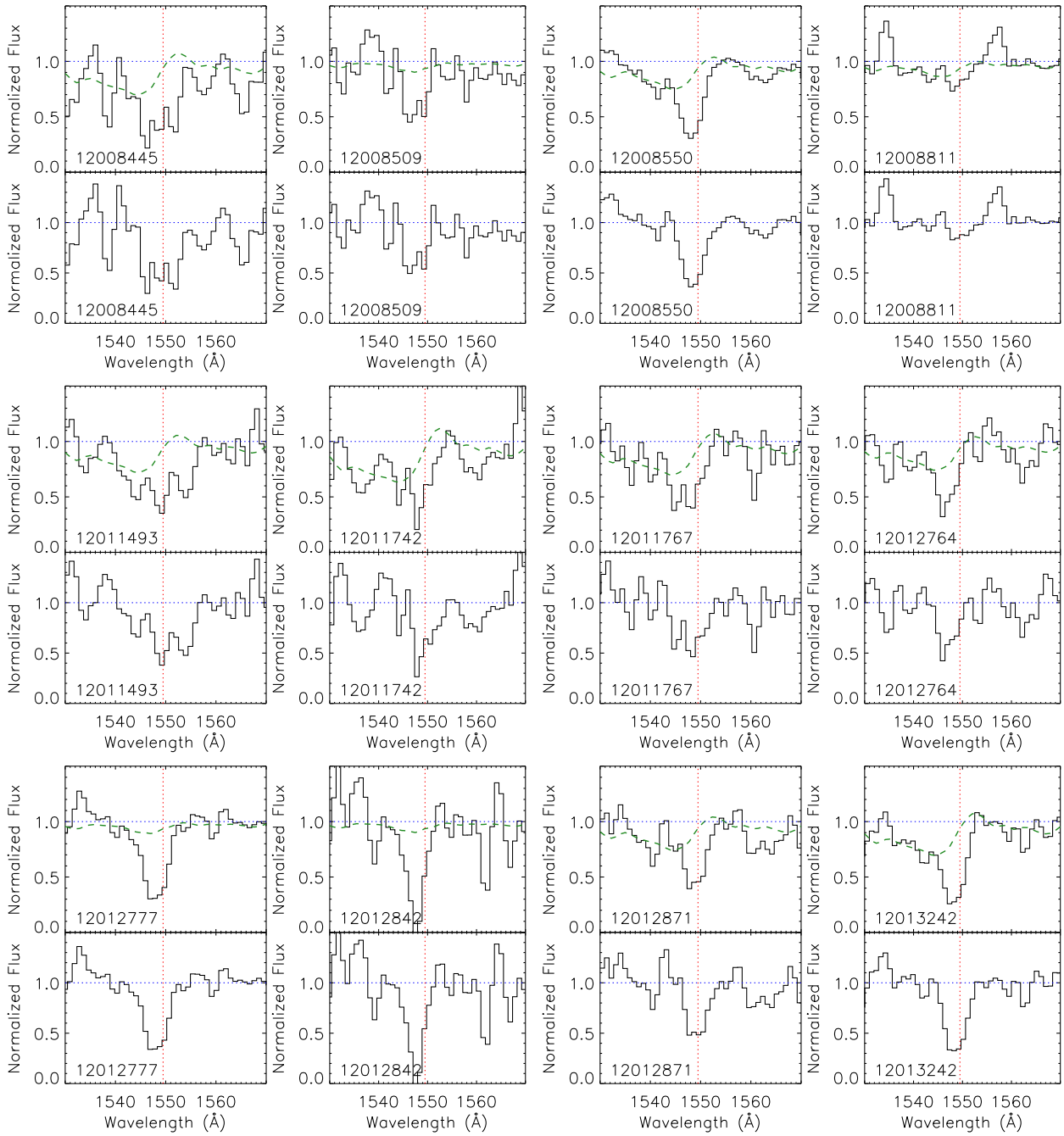

Figure 2.4: Continuum-normalized spectra (top) and spectra normalized by the best-fit stellar model (bottom) for 32 objects with continuum $S/N > 5$ and C IV EW measurements $> 3\sigma$, showing individual detection of C IV absorption. The blue horizontal dotted line indicates the continuum level, the red vertical dotted line suggests the rest-frame wavelength of blended C IV doublet in the 1:1 case (1549.5 Å), and the green dashed line shows the best-fit stellar model for each object.

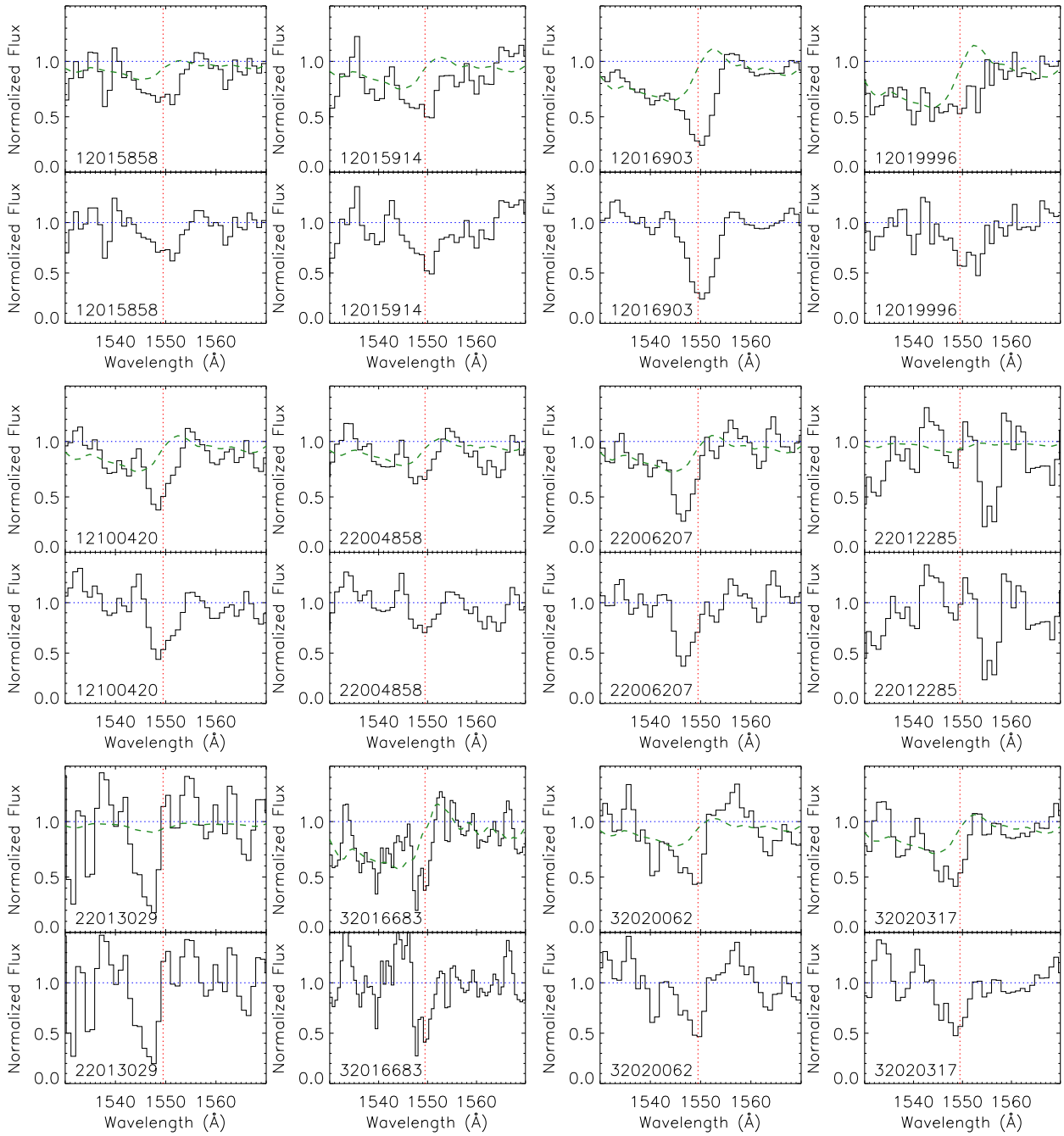

Figure 2.4 (Cont.): Continuum-normalized spectra (top) and spectra normalized by the best-fit stellar model (bottom) for 32 objects with continuum $S/N > 5$ and C IV EW measurements $> 3\sigma$, showing individual detection of C IV absorption. The blue horizontal dotted line indicates the continuum level, the red vertical dotted line suggests the rest-frame wavelength of blended C IV doublet in the 1:1 case (1549.5 Å), and the green dashed line shows the best-fit stellar model for each object.

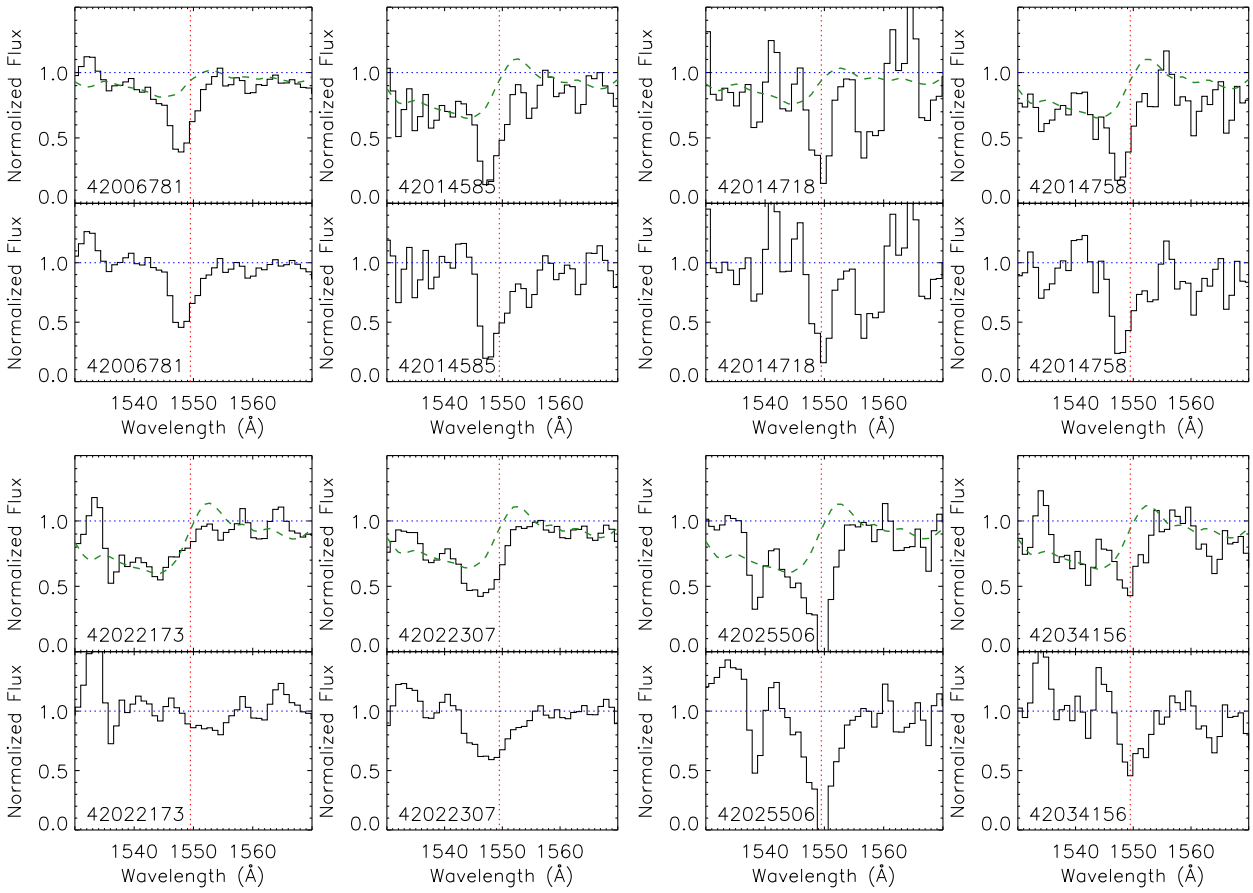

Figure 2.4 (Cont.): Continuum-normalized spectra (top) and spectra normalized by the best-fit stellar model (bottom) for 32 objects with continuum $S/N > 5$ and C IV EW measurements $> 3\sigma$, showing individual detection of C IV absorption. The blue horizontal dotted line indicates the continuum level, the red vertical dotted line suggests the rest-frame wavelength of blended C IV doublet in the 1:1 case (1549.5 Å), and the green dashed line shows the best-fit stellar model for each object.

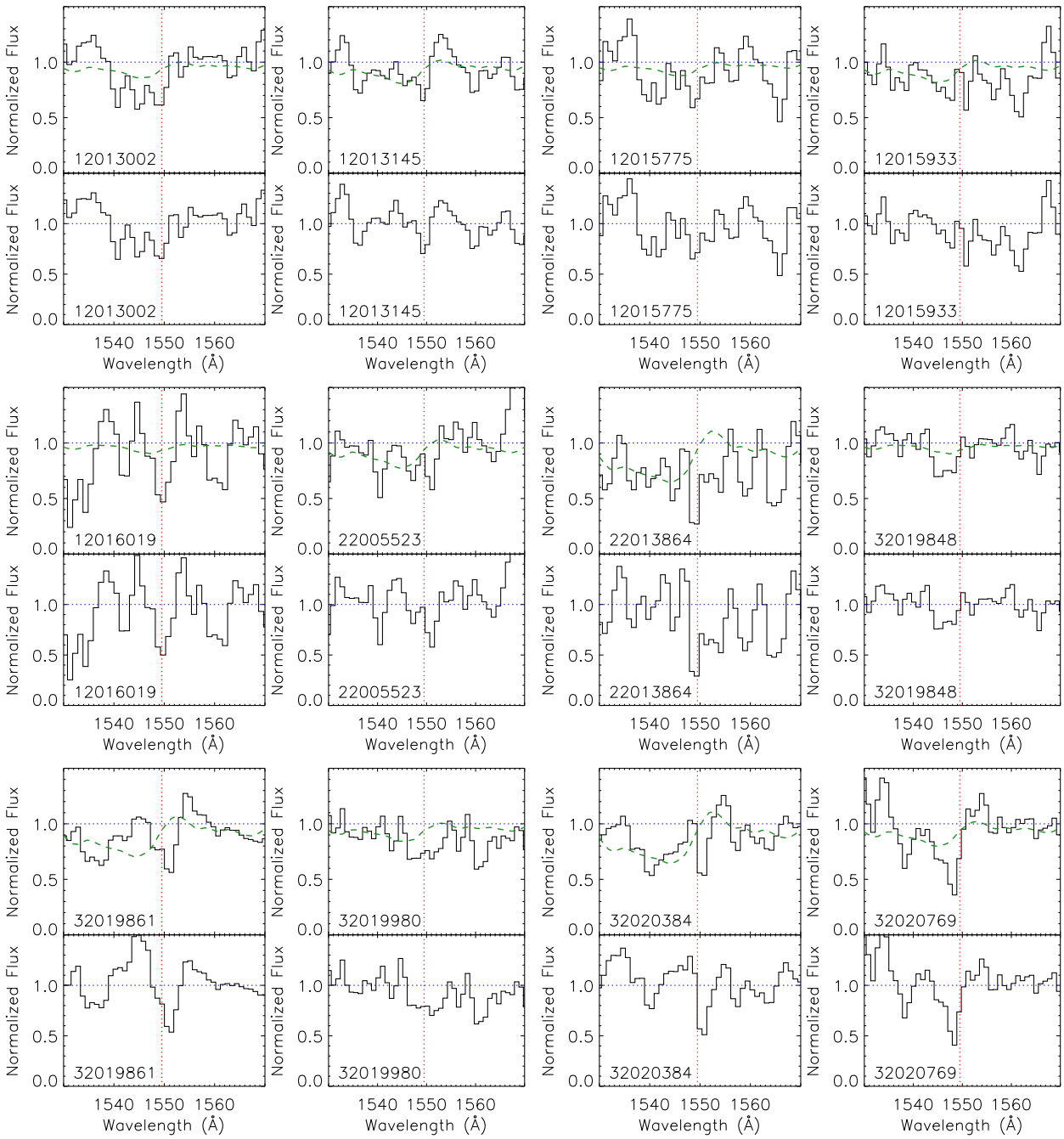

Figure 2.5: Continuum-normalized spectra (top) and spectra normalized by the best-fit stellar model (bottom) for 14 objects with continuum $S/N > 5$ and C IV EW measurements $< 3\sigma$, showing individual C IV absorption profiles. Legends are the same as in Figure 2.4.

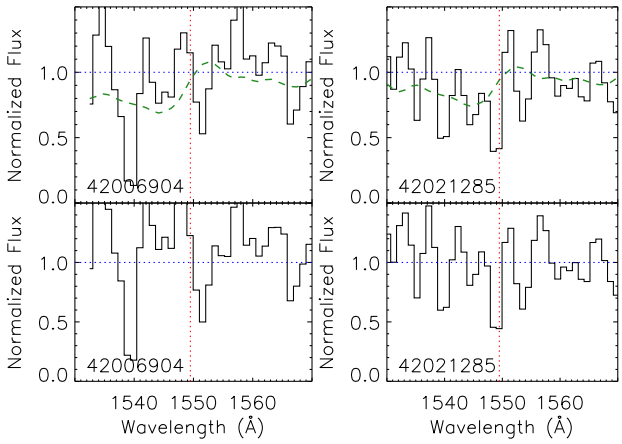

Figure 2.5 (Cont.): Continuum-normalized spectra (top) and spectra normalized by the best-fit stellar model (bottom) for 14 objects with continuum $S/N > 5$ and C IV EW measurements $< 3\sigma$, showing individual C IV absorption profiles. Legends are the same as in Figure 2.4.

profile.

This best-fit model, $Bestfit(\lambda)$, is characterized as:

$$\begin{aligned} Bestfit(\lambda) &= \frac{model_1(\lambda)|\frac{1}{res_1}| + model_2(\lambda)|\frac{1}{res_2}|}{|\frac{1}{res_1}| + |\frac{1}{res_2}|} \\ &= \frac{model_1(\lambda)|res_2| + model_2(\lambda)|res_1|}{|res_1| + |res_2|} \end{aligned} \tag{2.2}$$

where res_1 and res_2 are the residuals for $model_1$ (red), in the top panel of Figure 2.3 and $model_2$ (blue), respectively. As shown in Equation 2.2, the linear combination weights were determined from the inverse residual between model and data. In the top panel of Figure 2.3, the residuals for the $0.2Z_\odot$ and $0.4Z_\odot$ models are 0.0624 and -0.0659, respectively.

While bulk of the sample (93 objects with C IV coverage) is best described by models with $0.05Z_\odot < Z < 2.0Z_\odot$, [1] 22 objects failed to be bracketed with neighboring metallicities, indicating that the C IV wing at 1535Å to 1544Å was either too shallow for the lowest metallicity or too deep for the highest. In such cases, we chose the best-fit to be either $0.05Z_\odot$ (18 objects) or $2.0Z_\odot$ (4 objects) for objects with, respectively, the shallowest and

[1] Although the determination of best-fit stellar models is not robust for objects with continuum $S/N < 5$, the composite resulting from including these low S/N spectra shows no systematic bias in interstellar C IV absorption.

deepest stellar C IV absorption. We then divided both the continuum-normalized spectra and the error spectra by the corresponding best-fit stellar models and, accordingly, isolated the interstellar C IV absorption component.

Since the C IV$\lambda\lambda$1548,1550 doublet was not resolved in these low resolution spectra, we deblended the interstellar C IV profile into two Gaussian profiles for the 46 objects with continuum $S/N > 5$. We used the IDL program MPFIT (Markwardt, 2009) with the initial starting values of continuum flux level, line centroid, EW and Gaussian FWHM for each component estimated from the program *splot* in IRAF. We fixed the doublet wavelengths at the rest-wavelength ratio and forced the FWHM of each doublet member to be identical as well. The bottom panel of Figure 2.3 shows the fitted individual C IV doublet members (blue and magenta dotted lines) and the overall fit to the absorption profile (red dotted line) in the 1:1 case.

We iterated the fitting over a narrower wavelength range: centroid$-4\sigma < \lambda <$centroid$+4\sigma$, where the centroid and σ were, respectively, the returned central wavelength and standard deviation of the best-fit Gaussian profile from the initial MPFIT fit to the C IV doublet over 1540Å to 1560Å. We then determined the significance of the C IV EW in each object and identified 34 out of 46 objects with C IV detection $> 3\sigma$ in the sample for the study of individual velocity shifts.

There were 2 objects, 32019861 and 32020769, showing excessive absorption on the red side of C IV (red asymmetry). In either the 1:1 or 2:1 case, profiles with C IVλ1550 stronger than C IVλ1548 are unphysical. Possible sources of systematic error leading to this situation are associated with continuum fitting, best-fit stellar model determination and sky noise. We flagged and excluded these two objects from further study (grey squares in the top-right and the bottom-left panels in Figure 4.6). The final sample of robust C IV detections includes 32 objects, of which the continuum-normalized spectra, and the spectra normalized by the best-fit stellar model are shown in Figure 2.4. [2] The same sets of spectra are shown in

[2]Dividing out the stellar absorption has the largest effect on the blue side of the C IV profile, tending to make the inferred centroid of interstellar C IV more redshifted compared to that of the overall C IV absorption profile. Normalizing by the stellar model changes the inferred C IV centroid

Figure 2.5 for the 14 objects with continuum $S/N > 5$ and C IV EW $< 3\sigma$.

2.3.2 Measurement of Low-Ionization Lines

Multiple far-UV low-ionization lines fall in the vicinity of C IV, and are covered in our LRIS spectra. These include Si IIλ1526, Fe IIλ1608 and Al IIλ1670. We measure these features and compare the kinematics of different phases of interstellar gas.

We defined our far-UV low-ionization line sample in an analogous manner to that of C IV. We selected objects from the sample of 93 galaxies with C IV coverage and required continuum S/N >5 in the vicinity of each low-ionization feature. Accordingly, there were 46 objects in the Si IIλ1526 sample and 69 in the Fe IIλ1608 and Al IIλ1670 samples. The continuum S/N was calculated from 1570Å to 1590Å for Si II, and from 1690Å to 1750Å for Fe II and Al II. Since all of these features are singlets, we simply fit one Gaussian profile to each line. These profile fits resulted in 22 objects in the Si II sample, 14 in the Fe II sample and 44 in the Al II sample where the absorption lines were significantly detected (EW $> 3\sigma$).

To apply a consistent methodology of simple Gaussian profile fitting for analyzing both near-UV and far-UV features, we also re-measured the near-UV features presented in Martin et al. (2012) for the 93 objects with C IV coverage. These features include Mg II$\lambda\lambda$2796, 2803 and Fe IIλ2344, λ2374, λ2587. To trace the kinematics of low-ionization absorption, Martin et al. (2012) fit the troughs of Fe IIλ2250, 2261, 2344, 2374, 2587 with profiles of the form $I(\lambda) = I_0 e^{-\tau(\lambda)}$, where $\tau(\lambda)$ is a Gaussian parameterized by the central wavelength, λ_0 and the Doppler parameter, b. The central wavelengths of these lines were tied together to define a single-component Doppler shift V_1, and the optical depths were also tied by the ratio of their oscillator strengths. Fe IIλ 2382 and λ2600 may suffer from significant emission filling and were excluded from the fitting (see the text about Fe IIλ1608 in Section 2.4.1).

In our simple Gaussian fits of the near-UV Fe II features, we further excluded the weak transitions Fe IIλ2250, λ2261 (with oscillator strengths 14.2 and 13.3 times lower than that

velocities by a few tens up to ∼150 km s^{-1}, depending on the relative strengths of stellar and interstellar C IV absorption. Division of the best-fit stellar model minimizes the contamination from stellar absorption and thus provides a more robust description of interstellar C IV absorption.

of Fe IIλ2374, respectively) as they provided little constraint on the velocity shift. We fixed the wavelength centroid ratios at their rest-frame values and assumed identical profile widths for all fitted near-UV Fe II lines. The resulting Fe II velocity shifts were consistent with those in Martin et al. (2012). On the other hand, we set the centroids and widths of Mg II to float freely and fit the doublet wherever the χ^2 reaches a minimum, to accommodate the effects of Mg II emission filling. Specifically, the red parts of the Mg IIλ2796 and Mg IIλ2803 absorption profiles may be washed out by different amounts due to Mg II resonant emission. Therefore, the centroids of the doublet members do not necessarily show a fixed wavelength ratio and the widths may also not be the same (Martin et al., 2012). Table 2.1 lists the velocity shift of the measured lines (C IV, Al IIλ1670, Si IIλ1526 and near-UV Fe II) of individual objects derived from Gaussian fitting, as well as the near-UV Fe II velocity shifts from Martin et al. (2012).

2.4 Kinematics

To investigate whether the high-ionization kinematics differ from those of low-ionization lines, we compare the velocity shifts of C IV and near-UV Fe II and Mg II lines in Section 2.4.1. We also compare the low-ionization kinematics traced by both far-UV and near-UV lines, and discuss possible interpretations for the observed discrepancies in Section 2.4.2.

2.4.1 C IV vs. Near-UV lines

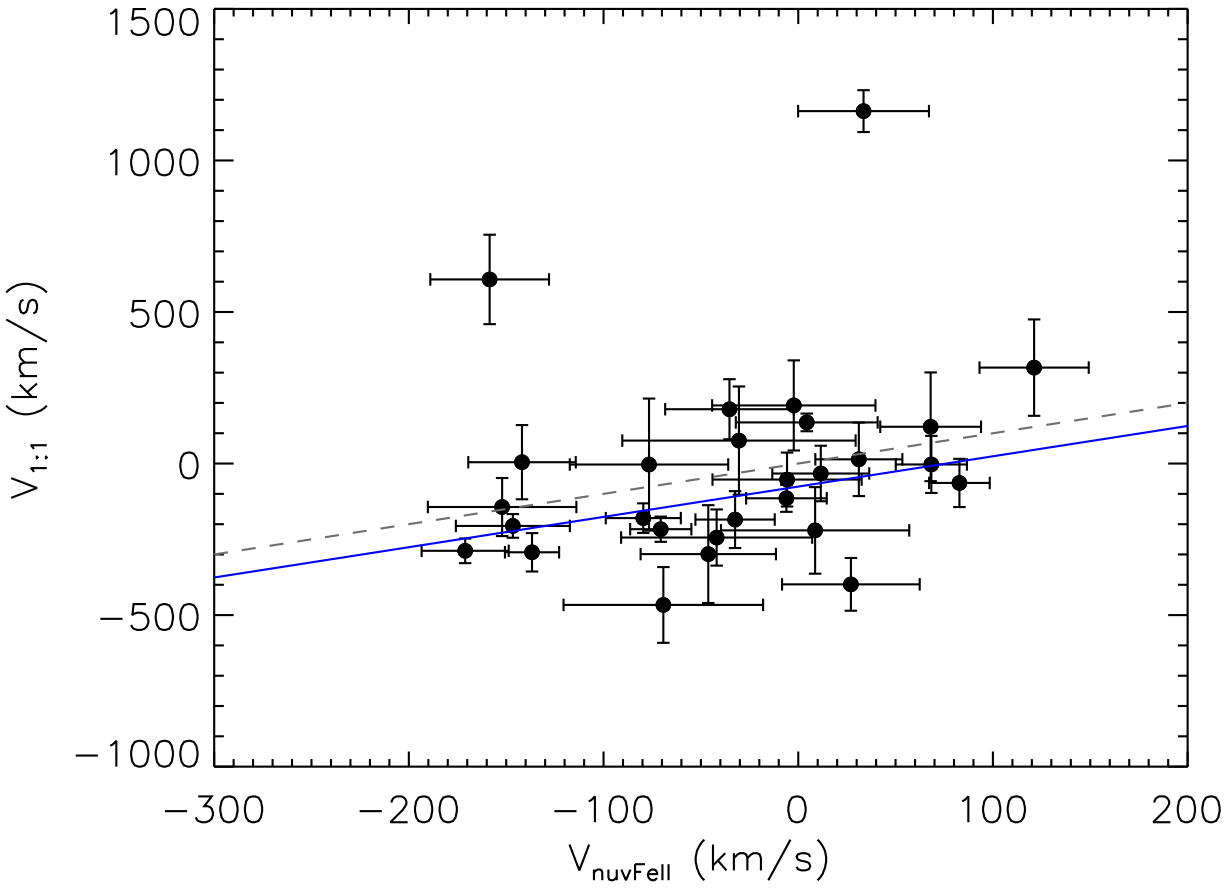

Figure 2.6: Comparison between C IV and near-UV Fe II velocity shifts. There are 28 objects with continuum $S/N > 5$ and EW detections of both C IV and near-UV Fe II $> 3\sigma$. The 1:1 doublet ratio is assumed in modeling the C IV feature. The median velocity shift for C IV and near-UV Fe II (excluding 2 outliers, 22012285 and 42022173) is -64 km s^{-1} and -30 km s^{-1}, respectively. The grey dashed line marks where $V_{1:1}$ and $V_{\rm nuvFe\ II}$ are equal, and the blue solid line presents the best linear fit with the slope fixed at 1. The offset between the grey and blue lines is -76 $\pm$ 26 km s^{-1} ($V_{1:1} - V_{\rm nuvFe\ II}$). The uncertainty on the best-fit intercept were estimated from Monte Carlo methods.

Table 2.1. Galaxy properties and velocity measurements of 93 objects with C IV coverage

ID	Redshift	M_B (mag)	$U-B$ (mag)	$\log(M_*)$ ($M_\odot$)	SFR_{UV} ($M_\odot yr^{-1}$)	$V_{C\ IV,1;1}$ (km s^{-1})	$V_{Al\ II}$ (km s^{-1})	$V_{Si\ II}$ (km s^{-1})	$V_{nuvFe\ II}$ (km s^{-1})	V_1 (km s^{-1})
12008166	1.2854	-19.69	0.32	9.78	···	···	-86± 54	···	-9± 48	31± 62
12008445	1.2774	-20.69	0.52	10.22	···	-3± 217	67± 58	···	73± 95	-193± 79
12008509	1.2158	-19.80	0.36	9.76	···	-362± 120	···	···	113± 53	70± 52
12008550	1.3025	-21.23	0.62	10.08	24	-205± 39	-86± 40	-187± 35	-146± 29	-145± 23
12008811	1.2156	-20.80	0.68	10.16	9	13± 121	119± 32	90± 51	31± 22	33± 20
12011428	1.2841	-19.88	0.18	9.66	9	···	194± 55	···	154± 37	154± 32
12011493	1.2638	-20.74	0.62	10.22	11	191± 148	548± 77	···	-2± 41	-21± 45
12011619	1.0745	-19.31	0.44	9.11	2	···	···	···	···	···
12011742	1.3358	-20.81	0.71	10.23	···	-32± 91	123± 63	···	11± 24	2± 23
12011767	1.2817	-22.19	0.75	11.07	76	-298± 161	···	···	-46± 34	-34± 35
12012764	1.2353	-20.26	0.62	9.80	···	-466± 124	···	···	-69± 51	-62± 47
12012777	1.2743	-21.07	0.52	10.11	22	-287± 40	-270± 26	-156± 45	-171± 22	-217± 13
12012817	1.2158	-20.92	0.89	10.85	···	···	···	···	28± 44	28± 44
12012842	1.3148	-21.68	0.75	11.09	···	-398± 87	-24± 56	170± 78	27± 35	5± 23
12012871	1.3443	-20.75	0.56	10.01	14	-52± 88	-37± 53	-10± 142	-5± 38	-13± 39
12013002	1.2184	-20.23	0.65	9.56	4	···	···	···	1± 49	10± 42
12013145	1.3406	-19.67	0.27	9.52	6	···	···	59± 92	-92± 75	-38± 61
12013242	1.2868	-21.32	0.45	10.19	25	-180± 48	-8± 28	34± 85	-79± 19	-73± 22
12015563	1.2824	-21.30	0.60	10.35	···	···	···	···	-104± 43	-98± 42
12015682	1.2837	-21.53	0.62	11.20	27	···	-186± 60	···	95± 180	-99± 93
12015775	1.2243	-19.36	0.23	9.65	4	···	-218± 177	···	-70± 90	-105± 43
12015792	1.2307	-21.24	0.96	11.07	12	···	···	···	···	-27± 85
12015858	1.2307	-19.87	0.22	9.56	8	75± 178	···	320± 155	-30± 59	-54± 60
12015914	1.1046	-19.83	0.33	10.11	8	121± 179	148± 62	113± 116	68± 25	51± 21
12015933	1.2851	-20.35	0.66	9.70	···	···	···	···	-34± 68	-22± 81
12016019	1.0847	-20.72	0.62	10.03	18	···	69± 108	···	47± 17	48± 14
12016075	1.1174	-19.68	0.54	9.41	5	···	···	···	18± 53	13± 49
12016903	1.1600	-21.46	0.51	10.21	25	135± 29	61± 46	···	4± 36	2± 30
12019542	1.2785	-21.68	0.71	10.40	40	···	···	···	-206± 22	-183± 60
12019996	1.2813	-21.71	0.63	10.67	43	316± 159	52± 68	···	121± 28	117± 24
12020064	1.3148	-21.12	0.60	10.35	26	···	-136± 58	···	-46± 29	-62± 56
12024014	1.2977	-20.51	0.50	9.91	···	···	···	···	-89± 17	···
12024133	1.1241	-21.14	0.81	10.56	36	···	···	···	-45± 24	-57± 43
12024181	1.0869	-21.00	0.80	10.54	35	···	···	···	-2± 54	-57± 32
12100420	1.1995	-20.63	0.60	10.02	9	-2± 94	127± 69	114± 59	68± 18	71± 18
22004858	1.2687	-21.85	0.62	10.54	···	-64± 79	199± 29	112± 42	82± 15	61± 11
22005523	1.2188	-21.68	0.61	10.41	···	···	94± 69	···	-26± 26	-31± 20
22005715	1.2345	-20.28	0.52	9.75	···	···	···	···	-73± 36	-70± 36
22006207	1.2709	-20.60	0.42	9.89	···	-472± 60	-285± 46	···	···	-199± 39
22012180	1.2894	-19.91	0.46	9.63	···	···	···	···	···	-159± 66
22012285	1.1700	-20.05	0.54	9.75	···	1162± 68	143± 111	···	33± 33	33± 32
22012322	1.1941	-20.42	0.57	9.84	···	···	214± 114	···	-144± 55	-121± 41
22012678	1.1959	-21.86	0.60	10.93	···	···	82± 109	···	148± 57	154± 56
22013029	1.2710	-21.00	0.69	10.32	···	-658± 92	···	···	59± 52	26± 44
22013827	1.2378	-21.25	0.75	10.52	···	···	···	···	4± 57	74± 45
22013864	1.2283	-21.00	0.72	10.38	···	···	-115± 94	···	-99± 28	-77± 38
22020736	1.1236	-21.83	0.99	10.99	···	···	···	···	-41± 88	-133± 49
22036666	1.3468	-20.96	0.53	10.23	···	···	···	···	···	-101± 37
22036984	1.0804	-20.79	0.70	10.19	···	···	···	···	-39± 23	-55± 19
22044809	1.1869	-19.59	0.31	9.39	···	···	···	···	-50± 27	-48± 51
22100920	1.2735	-21.12	0.57	10.25	···	···	-18± 29	···	-32± 17	-41± 25
32016683	1.3006	-21.22	0.58	10.42	···	-114± 44	22± 28	14± 69	-6± 20	11± 32
32017188	1.2526	-20.83	0.58	9.98	···	···	···	···	···	···
32019848	1.3433	-21.14	0.60	10.46	···	···	···	···	···	···
32019861	1.3077	-20.54	0.53	10.01	···	···	···	···	-1± 64	···
32019900	1.2478	-20.83	0.65	9.75	···	···	···	···	···	···
32019980	1.3487	-19.92	0.43	9.73	···	···	···	127± 54	···	···
32020062	1.2808	-20.32	0.59	9.86	···	-244± 92	···	···	-41± 49	-70± 47

Table 2.1 (Cont.).

ID	Redshift	M_B (mag)	$U-B$ (mag)	$\log(M_*)$ ($M_\odot$)	SFR_{UV} ($M_\odot yr^{-1}$)	$V_{C\ IV,1:1}$ (km s^{-1})	$V_{Al\ II}$ (km s^{-1})	$V_{Si\ II}$ (km s^{-1})	$V_{nuvFe\ II}$ (km s^{-1})	V_1 (km s^{-1})
32020258	1.2461	-20.58	0.66	10.10	···	···	···	···	···	···
32020274	1.2589	-20.85	0.72	10.19	···	···	···	···	-78± 69	-73± 66
32020317	1.1871	-20.28	0.47	9.72	···	-220± 142	284± 178	···	8± 48	-43± 64
32020384	1.2493	-20.82	0.42	9.96	···	···	51± 51	157± 102	-33± 29	-32± 32
32020441	1.0451	-20.51	0.61	10.04	···	···	254± 100	···	-42± 35	-18± 28
32020468	1.2355	-21.00	0.73	10.28	···	···	···	···	113± 46	123± 39
32020670	1.2330	-21.39	0.90	10.49	···	···	···	···	-22± 58	···
32020728	1.0446	-19.95	0.47	9.76	···	···	···	···	-27± 39	-52± 30
32020769	1.3144	-20.77	0.41	10.01	···	···	-11± 104	1± 75	15± 42	-33± 37
32020873	1.2491	-20.49	0.59	9.77	···	···	···	···	-112± 40	···
42006781	1.2860	-20.74	0.55	9.69	···	-216± 41	-153± 22	-175± 29	-70± 15	-70± 13
42006799	1.2021	-21.74	0.91	11.26	···	···	···	···	-7± 30	-17± 41
42006898	1.2410	-20.06	0.57	10.01	···	···	-300± 168	···	38± 38	38± 42
42006904	1.0228	-20.74	0.46	10.07	···	···	···	···	-78± 46	-18± 26
42014585	1.2706	-20.91	0.59	10.18	···	-143± 95	-76± 49	30± 97	-152± 38	-177± 30
42014618	1.0131	-20.38	0.59	9.81	···	···	-150± 84	···	-71± 15	-76± 13
42014718	1.1904	-21.27	0.69	10.86	···	4± 122	-119± 194	···	-141± 27	-156± 19
42014758	1.2702	-21.82	0.65	10.67	···	-184± 93	-98± 49	-126± 62	-32± 20	-43± 18
42018218	1.2253	-20.15	0.50	9.79	···	···	···	···	142± 58	144± 55
42021285	1.1082	-20.65	0.71	10.17	···	···	···	···	-35± 28	-40± 19
42022173	1.3112	-20.25	0.32	9.68	···	607± 147	-338± 58	176± 133	-158± 30	-134± 27
42022307	1.2595	-21.44	0.47	10.22	···	-292± 63	-78± 28	-32± 36	-136± 13	-146± 10
42025506	1.3358	-21.10	0.54	10.17	···	-10± 84	-32± 77	1± 66	-113± 30	-116± 39
42025525	1.2946	-20.12	0.49	9.61	···	···	···	···	···	···
42025744	1.2024	-20.18	0.65	9.69	···	···	···	···	···	···
42025804	1.2435	-20.35	0.50	9.93	···	···	···	···	85± 45	···
42026237	1.3385	-21.50	0.65	10.61	···	···	···	···	···	···
42026243	1.3457	-21.66	0.67	10.88	···	···	-193± 102	···	-309± 52	-302± 38
42026308	1.1700	-20.19	0.48	10.08	···	···	···	···	···	···
42026327	1.3461	-20.63	0.45	10.20	···	···	···	···	178± 46	···
42026601	1.2272	-20.02	0.34	9.64	···	···	···	···	···	···
42033338	1.2237	-19.65	0.43	9.74	···	···	···	···	-103± 59	···
42034098	1.3465	-21.25	0.44	10.51	···	···	0± 72	···	0± 55	-28± 47
42034156	1.3464	-20.69	0.37	10.10	···	179± 99	···	91± 120	-35± 33	-38± 36
42034223	1.2000	-20.09	0.44	9.45	···	···	-57± 91	···	8± 35	10± 35

Note. — Redshifts are from the DEEP2 catalog. The B-band luminosity and $U-B$ color are values taken from Willmer et al. (2006). SFR_{UV} is the dust-corrected UV luminosity from GALEX measurements (full description in Section 4.2). Column 7-10 are velocity shifts measured from objects with continuum $S/N > 5$ and a line detection greater than 3σ (in terms of EW) using simple Gaussian fits. V_1 is the single-component Doppler shift presented in Martin et al. (2012). The listed line S/N was calculated by combining the doublet members for C IV, and Fe IIλ2344, λ2374 and λ2587 for the near-UV Fe II.

In order to compare the kinematics of C IV with those of the low-ionization lines, we calculated the velocity shifts for C IV in the 1:1 case and the near-UV Fe II lines. We define these velocity shifts, respectively, as $V_{1:1}$ and $V_{\text{nuvFe II}}$. [3] In Figure 2.6, the black circles (28 objects) represent objects with robust measurements for both C IV and near-UV Fe II features (continuum $S/N > 5$ and EW $\geqslant 3\sigma$). Two objects stand out as having significantly redshifted C IV centroid velocities. One object, 22012285, is extremely redshifted with a velocity of +1162 km s^{-1}. We interpret the C IV redshift of this object with caution, as the absorption (while formally significant), may be caused by systematic oversubtraction of the sky spectrum. Another object, 42022173 has a C IV velocity of +607 km s^{-1} which could be due to systematics in the normalization of the stellar wind component. The best-fit stellar model for this object (bracketed by models with $0.4Z_{\odot}$ and $1.0Z_{\odot}$), while based on the blueshifted stellar absorption profile, overproduces C IV emission at $\sim$ 1552Å. Therefore, after division by the best-fit model, some apparent interstellar absorption remains on the red side of the C IV profile. It is not clear whether this absorption is real or an artifact of the mismatch between model and data. Given the potentially large uncertainties associated with these two objects, we removed them from the sample when deriving the statistical properties.

After eliminating these 2 outliers, we find that the rest of the sample (26 objects) show that C IV (median velocity shift -64 km s^{-1}) is more blueshifted than the near-UV Fe II lines (median velocity shift -30 km s^{-1}), with a median velocity difference, $V_{1:1} - V_{\text{nuvFe II}}$, of -65 km s^{-1}. Furthermore, the best-fit linear model (measurement errors considered) gives an intercept of -76 $\pm$ 26 km s^{-1} with a fixed slope at 1, which confirms the larger blueshift of C IV at the $\sim$ 3-sigma level. The error bar on the best-fit intercept was estimated using Monte Carlo methods. Specifically, we bootstrap resampled the velocity shifts, $V_{1:1}$ and $V_{\text{nuvFe II}}$, of these 26 objects and performed a inverse-squared weighted linear regression to the bootstrap sample. The process was repeated 100 times and the standard deviation of

[3] Assuming the doublet ratio of 2:1 results in a velocity shift $\sim$ 84 km s^{-1} less blueshifted than in the 1:1 case, although the optically-thin 2:1 ratio is unlikely to apply given the type of systems we probe.

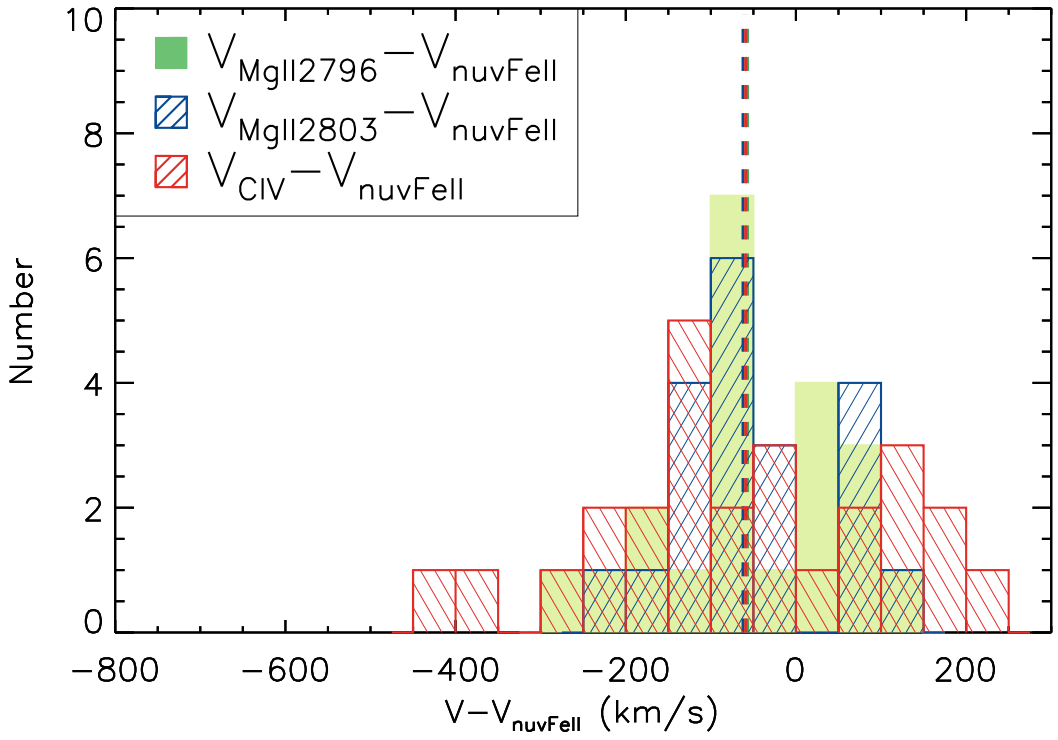

Figure 2.7: Histogram of C IV, Mg II, and Fe II velocity differences. Velocity differences are only plotted for objects with continuum $S/N > 5$ and EW$> 3\sigma$ detection for C IV and near-UV Fe II lines (red histogram, 26 objects, excluding 22012285 and 42022173), and Mg II and near-UV Fe II lines (green and blue histograms, 21 and 20 objects, respectively). The vertical colored dashed lines show the median velocity difference of corresponding pairs, which are -65 km s^{-1}, -57 km s^{-1} and -63 km s^{-1} for C IV, Mg IIλ2796 and Mg IIλ2803 with respect to near-UV Fe II, respectively.

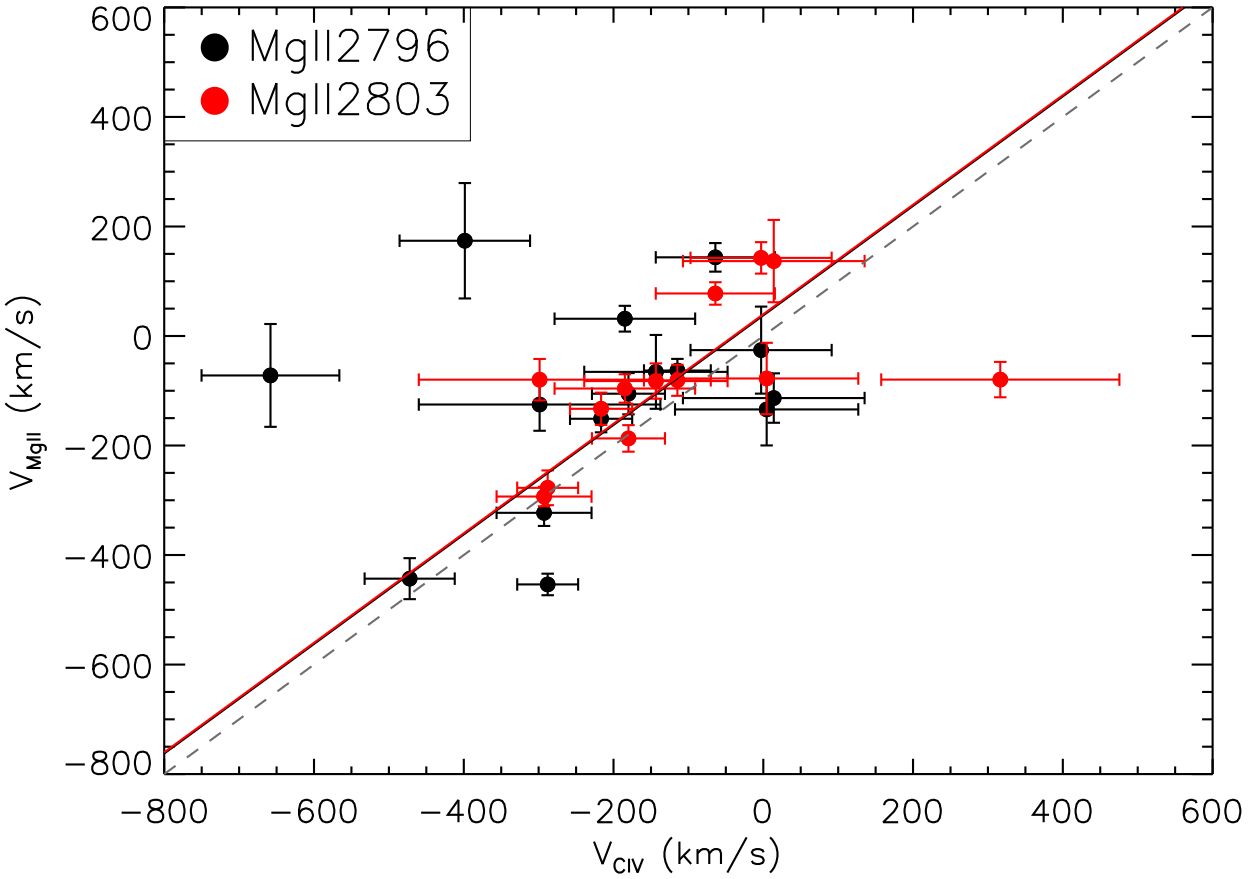

Figure 2.8: Comparison of C IV and Mg II velocity shifts. Red circles represent Mg IIλ2796 (15 objects) and black circles represent Mg IIλ2803 (13 objects). All objects shown here have continuum $S/N > 5$ and line EWs $> 3\sigma$ for both C IV and the corresponding Mg II doublet member. The red and black solid lines are the best-fit linear models for Mg IIλ2796 and Mg IIλ2803, respectively. The intercept for the doublet members are $+38 \pm 43$ km s^{-1} and $+40 \pm 18$ km s^{-1}. The grey dashed line marks the 1:1 relation.

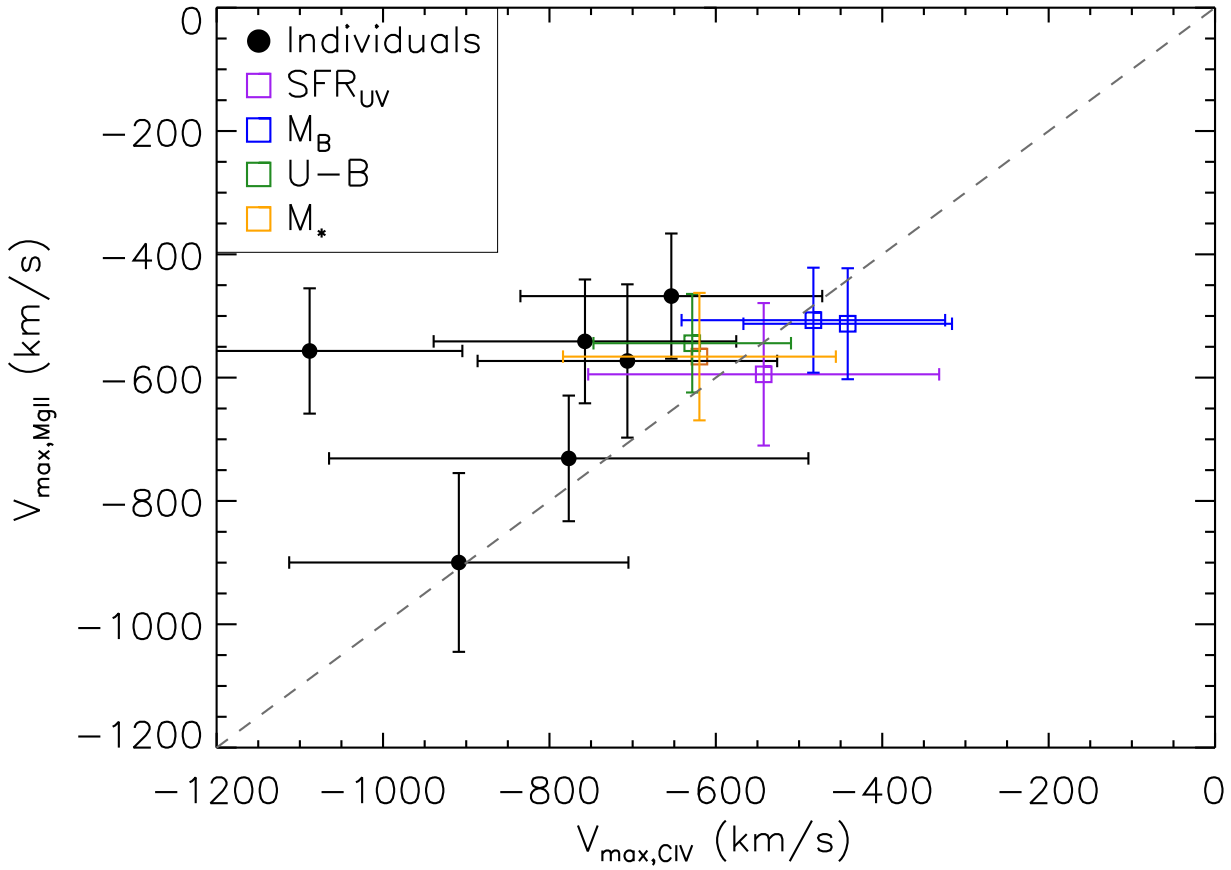

Figure 2.9: Comparison between C IV and Mg II V_{max} for resolved blue wings. The black dots represent individual objects with the highest continuum S/N (> 10.0), and the colored open squares are from the composite spectra (purple, blue, green, yellow for SFR, M_B, $U-B$ and M_*, respectively) described in Section 3.4.2. The grey dashed line indicates where the two velocities are equal, and all objects fall close to the 1:1 line but the outlier 42022307.

the intercept distribution was taken as the corresponding uncertainty. Finally, at least as large a fraction of C IV absorption profiles shows a blueshift with respect to the systemic velocity (69 % for $V_{1:1} < 0$ km s^{-1}), compared with 65 % of the near-UV Fe II profiles. [4]

Although the larger blueshift of C IV may suggest that the highly-ionized gas is in fact traveling at a slightly higher speed, a close investigation of the kinematics of Mg II absorption reveals another possibility. Figure 2.7 shows histograms of the velocity differences between C IV and near-UV Fe II ($V_{1:1} - V_{\rm nuvFe\ II}$, red, 26 objects, excluding 22012285 and 42022173) and individual Mg II doublet members and near-UV Fe II ($V_{\rm Mg\ II\lambda2796} - V_{\rm nuvFe\ II}$, green, 21 objects and $V_{\rm Mg\ II\lambda2803} - V_{\rm nuvFe\ II}$, blue, 20 objects), where all the lines have a continuum $S/N > 5$ and $\geqslant 3\sigma$ absorption detection. We note that the sample here comparing C IV and near-UV Fe II is the same as that used in Figure 2.6. The dashed lines of corresponding colors indicate the median velocity shift between C IV and Fe II, between Mg IIλ2796 and Fe II and between Mg IIλ2803 and Fe II, respectively. The median values of these three distributions are very close to each other, suggesting that the velocity shift of C IV is nearly identical to that of Mg II.

Moreover, when directly comparing the velocity shifts derived from C IV and Mg II (Figure 2.8), we find that the data points scatter around the 1:1 line despite a few outliers. We note that while the best-fit intercepts give $\sim +40$ km s^{-1} for both Mg II doublet members, this result does not necessarily suggest that C IV is more blueshifted than Mg II, given the small size of the sample. In fact, we find that the blueshift (derived from centroid velocities) of C IV is on average similar to that of Mg II when combining both Figure 2.7 and 2.8. As the Mg II profile is significantly affected by interstellar emission filling, a natural conclusion is that C IV, another resonant line showing a similar velocity shift, may be similarly affected.

For a better understanding of the blueshift of C IV, we further studied the blue wing of the absorption trough. We focused on the extent to which measurable absorption extends blueward of the line centroid by calculating the maximum velocity, V_{max}. V_{max} is defined with respect to the blue side of the absorption profile where the measured flux meets with

[4] 65% of the near-UV Fe II absorption lines are blueshifted with respect to the systemic velocity in Martin et al. (2012).

the spectral continuum at the 1σ level (Martin et al., 2012), and represents the largest velocity at which there is measurable absorption, regardless of the shape of the absorption trough. To obtain V_{max} and the associated error bars, we perturbed the spectrum at each wavelength with a Gaussian random variable determined by the corresponding error spectrum, measured V_{max} in the perturbed spectrum, and then repeated the process 500 times for each object. We then calculated the average V_{max} and assigned the error bars as the larger of the standard deviation of the V_{max} distribution or half the pixel width (Martin et al., 2012). We determined V_{max} for C IV and Mg II in both the composite spectra (in different bins of galaxy properties, see Section 3.4.2) as well as 10 individual objects with the highest continuum S/N, as plotted in Figure 2.9. Note that we only included V_{max} for the resolved line wings which required V_{max} to be more significantly blueshifted than -282 km s^{-1} for the 600-line spectra, or -435 km s^{-1} for the 400-line spectra. Nearly all the points lie on the 1:1 line, indicating that the V_{max} for C IV and for Mg II are statistically the same. The only outlier is 42022307, which has a $V_{max,\mathrm{C\ IV}} <$ -1000 km s^{-1}. We flagged this object since the C IV absorption is unusually broad, and the Mg II measurement is also not robust due to a sky line residing just bluewards of Mg IIλ2796.

In summary, the small but significant blueshift of C IV relative to near-UV Fe II suggests either the highly-ionized gas is faster-moving, or else the kinematics of low and high ions are in general consistent while the red side of the interstellar absorption trough is filled up from the C IV resonant emission. Although we favor the latter case as C IV shows a similar blueshift to that of Mg II, further studies at both higher resolution and S/N are needed to break the degeneracy.

2.4.2 Far-UV vs. Near-UV lines

In order to establish a velocity frame traced by far-UV absorption lines, we also plotted Si IIλ1526, Fe IIλ1608 and Al IIλ1670 against the near-UV Fe II lines. From Figure 2.10, we find that Al IIλ1670 scatters around the 1:1 line (median velocity shift -15 km s^{-1}) while Si IIλ1526 displays a systematic redshift relative to the near-UV Fe II (median velocity shift

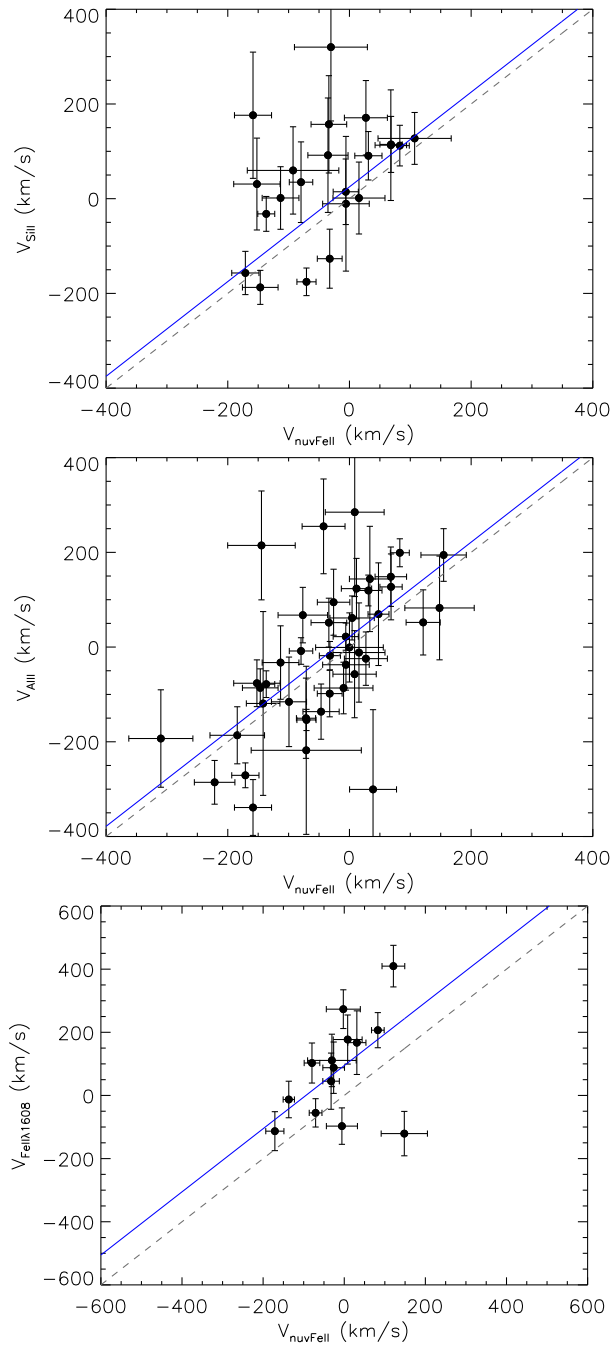

Figure 2.10: Si IIλ1526 (top), Al IIλ1670 (middle), and Fe IIλ1608 (bottom) velocity shifts compared with those from near-UV Fe II lines. Legends are the same as in Figure 2.6. The median velocity for Si IIλ1526, Al IIλ1670 and Fe IIλ1608 is +47 km s^{-1}, -15 km s^{-1} and +95 km s^{-1}, respectively. The intercept for the best linear fits with slope fixed at 1 for those lines are +25 ± 25 km s^{-1}, +22 ± 19 km s^{-1} and +94 ± 37 km s^{-1}, respectively.

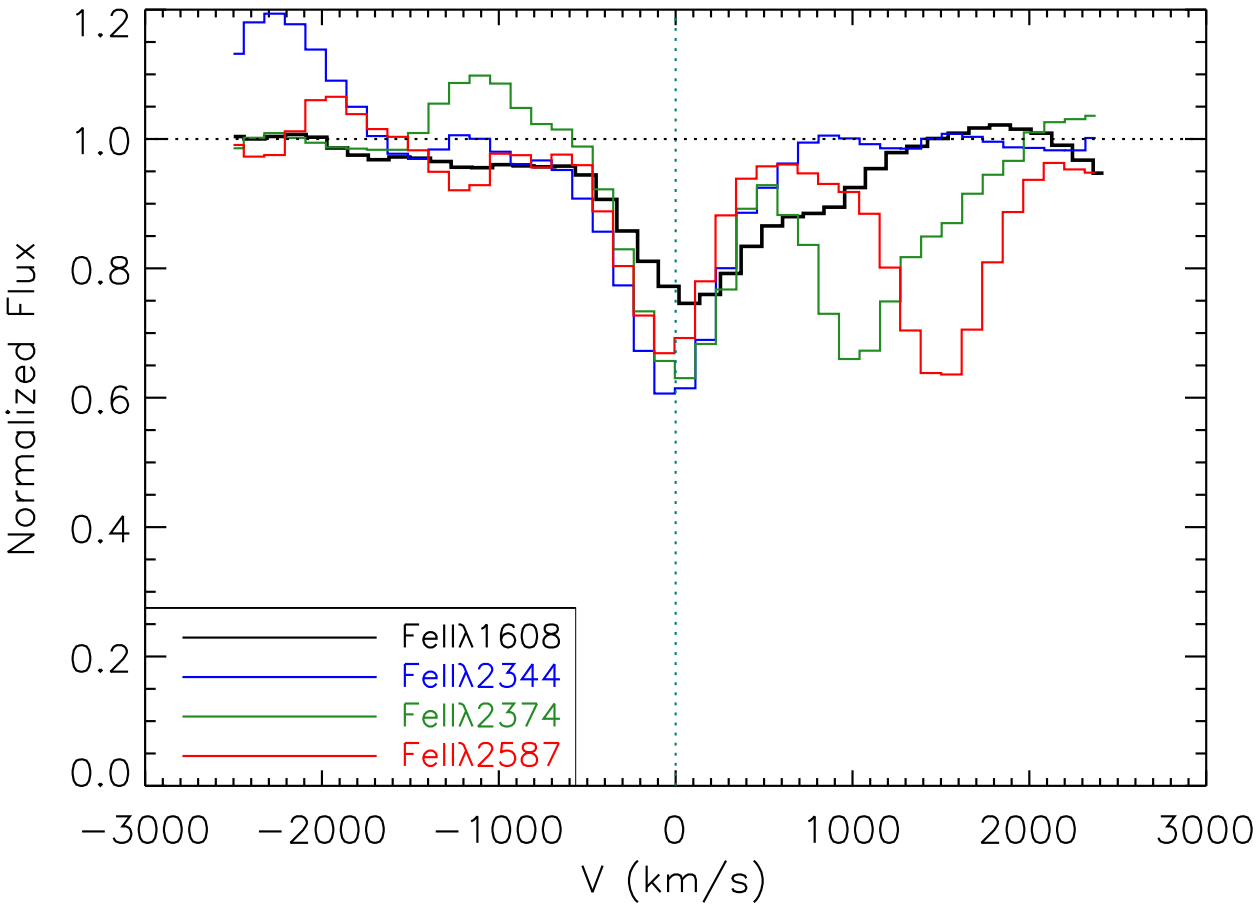

Figure 2.11: The stacked velocity profile of Fe IIλ1608 and Fe IIλ2344, 2374, 2587 for objects observed in the 400-line masks with continuum $S/N > 5$ (65 objects). The black line shows the absorption profile of Fe IIλ1608, and those of Fe IIλ2344, Fe IIλ2374 and Fe IIλ2587 are shown in blue, green and red, respectively. The dotted horizontal line marks the expected continuum level, and the dotted vertical line indicates the systemic velocity.

+47 km s^{-1}). This offset is caused by the larger error bars associated with the objects at the top left corner of the top panel of Figure 2.10. In fact, the intercepts for the best-fit models with slope fixed at 1.0 for Si IIλ1526 and Al IIλ1670 are, respectively, +25 km ± 25 km s^{-1} and +22 ± 19 km s^{-1}, which suggests that both Si II and Al II have velocities that are roughly consistent on average with those of the near-UV Fe II lines. Therefore, we claim that the velocity shifts traced by far-UV Si II and Al II in general agree with that traced by near-UV Fe II lines despite larger uncertainties associated with the velocity measurements of Si IIλ1526.

It is worth noting that Fe IIλ1608, on an individual basis, appears to be significantly more redshifted relative to C IV (median $V_{\text{Fe II}\lambda1608} - V_{1:1} = +161$ km s^{-1}), and near-UV Fe II lines (median $V_{\text{Fe II}\lambda1608} - V_{\text{nuvFe II}} = +124$ km s^{-1} median). To investigate the reason for the relative redshift of Fe IIλ1608, we constructed a composite spectrum and compared the absorption profiles of both Fe IIλ1608 and the near-UV Fe II lines. We selected a subset of 65 galaxies, which were observed with 400-line masks (to ensure the same resolution), with continuum $S/N > 5$ in the vicinity of the near-UV Fe II features from 2400 Å to 2550 Å. We then stacked individual continuum-normalized spectra, and extracted the median value at each wavelength to create a composite spectrum. In Figure 2.11, Fe IIλ1608, 2344, 2374 and 2587 are plotted with respect to their rest wavelengths using black, blue, green and red lines, respectively. While there is an agreement among the velocity profiles of Fe IIλ2344, 2374, 2587, Fe IIλ1608 shows an extended wing on the red side at ∼+800km s^{-1}, making the fitted centroid redshifted compared to the other Fe II lines.

One plausible interpretation of this profile is that Fe IIλ1608 suffers less emission filling than the other near-UV Fe II lines. The continuum photons emitted by galaxies can be absorbed by the interstellar medium (ISM) and re-emitted in random directions. The electrons, after getting excited to a higher energy level from the ground state, can either decay back to the ground state (resonant emission) or to an excited ground state (fluorescent emission). The resonant emission cannot cancel out the resonant absorption exactly because of different Doppler velocities of the emitting and absorbing gas, thus we have to consider the extent to which the resonant emission, usually expected in galaxy spectra, fills

the absorption trough and results in a more blueshifted absorption profile than it would otherwise (Prochaska et al., 2011; Martin et al., 2012). Based on the Einstein A coefficients of the resonant and fluorescent emission, following the absorption in the Fe IIλ1608 resonant transition, only 26% of the photons are redirected into into fluorescent emission lines at FeII$^*\lambda$1618.47 (22%) and FeII$^*\lambda$1625.91 (4%). In comparison, Fe IIλ2382 absorption results in no fluorescent emissions (i.e., all photons return to the ground state exclusively through resonant emission), and the fractions of fluorescent emission of the Fe IIλ2344, 2374, 2587 and 2600 resonant transitions are 35%, 86%, 67%, 13%, respectively. Thus emission filling is apparently more significant for the Fe IIλ1608 profile than for the near-UV Fe II lines used in Martin et al. (2012), and is only slightly less of an issue than for the lines excluded (i.e., Fe IIλ2382 and Fe IIλ2600). Since emission filling should affect Fe IIλ1608 more than the other lines plotted, and, if anything, should result in a larger blueshift due to more emission filling on the red side of the absorption profile (in contract to what is observed), this process clearly does not provide an explanation for the discrepant kinematics between Fe IIλ1608 and the near-UV Fe II features.

Another possible explanation is additional absorption by a nearby resonant transition, i.e., Fe IIλ1611, at the red edge of Fe IIλ1608. Fe IIλ1611 has an oscillator strength $\sim 2.5\%$ that of Fe IIλ1608 and gives additional absorption at $\sim$+500km s^{-1} when blended with the Fe IIλ1608 line. Meanwhile, inspection of the Leitherer et al. (2010) far-UV spectra indicates that stellar photospheric Fe IV absorption at $\sim$ 1610Å may also contribute to the redshifted profile of Fe IIλ1608 (Dean & Bruhweiler, 1985; Leitherer et al., 2010, private communication). Due to the potential contamination from Fe IIλ1611 (more than 2.5% if the Fe II lines are not optically thin), Fe IV and possibly additional unidentified absorption lines, we do not use Fe IIλ1608 for determining low-ionization absorption kinematics.

2.5 Galaxy Properties

While the study of individual velocity shifts can only be performed on objects with high S/N and significant line detections, composite spectra enable us to utilize the full sample

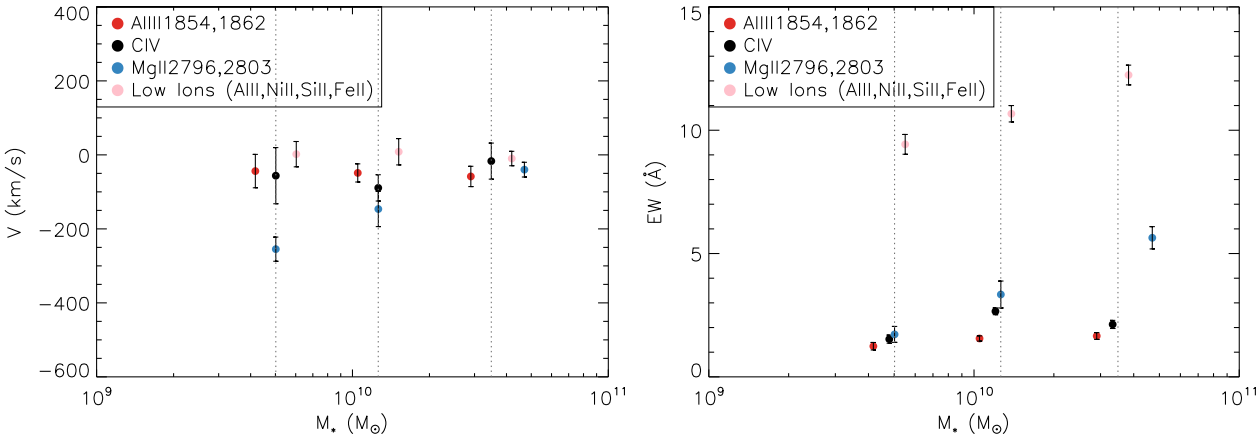

Figure 2.12: Interstellar absorption velocity shift and EW vs. stellar mass in the composite spectra. The median stellar mass of each bin is indicated with the vertical grey dashed lines, and the data points are offset horizontally for display purposes. The black points represent C IV measurements, while the red points indicate the Al III doublet. The light pink points indicate a set of low-ionization lines (Si IIλ1526, Al IIλ1670, Si II$\lambda\lambda$1741,1751, Si IIλ1808 and near-UV Fe II), representing the average velocity shift of the total EW. Finally, the Mg II doublet, as isolated from the other low-ionization lines, is shown by blue points.

and study the overall correlations between spectral and galaxy properties. Moreover, using composite spectra potentially enables the measurement of weak absorption lines by increasing continuum S/N (continuum S/N increased by a fact of $\sqrt{N}$, where N is the number of objects that go into each composite spectrum).

Within the coverage of the DEEP2/LRIS spectra, there reside multiple weak far-UV transition lines, including Ni II$\lambda\lambda$1741, 1751, Si IIλ1808 and Al III$\lambda\lambda$1854, 1862, which we were not able to measure robustly in individual spectra. Composite spectra enabled the measurement of these weak lines in addition to the strong UV absorption lines we described before (Si IIλ1526, C IV$\lambda\lambda$1548, 1550, Al IIλ1670, Fe IIλ2344, λ2374, λ2587 and Mg II$\lambda\lambda$2796, 2803). In light of the fact that outflows have a multi-phase structure, we included Al III measurements here to explore the kinematics of an intermediate-ionization phase in the composite spectra.

To investigate the correlation between the kinematics and strength of both high- and low-ionization lines and galaxy properties, we divided all 93 objects with C IV coverage into three bins in stellar mass, $U-B$ color and B-band luminosity, and two bins in SFR, SFR surface density and sSFR, given that only 25 objects in the AEGIS field have GALEX

SFR measurements. Each bin contained nearly the same number of galaxies. To create the composite spectra, we used individual continuum-normalized spectra for measurements of the low-ionization lines and spectra normalized by the Leitherer et al. (2010) stellar models for measurements of C IV and Al III. Al III, like C IV, has a complex profile including both the absorption from stellar winds and the ISM. However, since the stellar wind component contributing to the Al III profile is several times weaker than that of C IV (Leitherer et al., 2010), we simply used the blue wing of the C IV feature to determine the stellar absorption affecting both C IV and Al III. For each object, we divided the continuum-normalized spectrum by the best-fit stellar model determined from C IV (described in Section 2.3.1). All the normalized spectra (both continuum-normalized ones and those normalized by the best-fit stellar models) were then interpolated on a grid with wavelength spacings of 1Å from 1400Å to 3000Å. The median value at each wavelength of the normalized spectra in each bin was then extracted to create a normalized composite spectrum. To create the corresponding error spectrum for each composite spectrum, we bootstrap resampled each bin and perturbed each spectrum in the bootstrap sample according to its own error spectrum. The perturbed spectra in the bootstrap sample were then combined to create a new composite spectrum. The process was repeated 100 times and the standard deviation of these 100 fake composites at each wavelength was taken to create a composite error spectrum for each bin. With this approach, we accounted for both sample variance and measurement uncertainty.

Both centroid velocity and V_{max} can be used to probe the kinematics of interstellar gas. Although V_{max} is not subject to potential emission filling, it is not resolved in all the bins of the stacked spectra, especially for C IV. On the other hand, the centroid velocity is well measured for features in all stacked spectra. Accordingly, we used centroid velocity inferred from the absorption features for the kinematic analysis in this section.

We fit the C IV, Si IIλ1526, λ1808, Al II, Ni II, Al III, near-UV Fe II and Mg II features in the stacked spectra with Gaussian profiles using MPFIT to measure their centroids and EWs. We required all centroids of the doublet members and the near-UV Fe II lines to be fixed with the exception of Mg II, for the reason stated in Section 2.3.2. We also forced the FWHM of each C IV and near-UV Fe II member to be the same. We allowed the width of

doublet members to float freely for Ni II and Al III, since the profile of these weak features is significantly affected by noise, and thus may deviate from 1:1 width ratio. [5]

Since we found no significant correlations between the spectral properties (blueshift and strength) of any lines listed above and $U - B$ color or B-band luminosity in the composite spectra, we only discuss stellar mass, SFR and sSFR in this section where systematic trends have been observed.

2.5.1 Stellar Mass

The plot of measured velocity shift and EW versus stellar mass is shown in Figure 2.12. The median stellar mass of each bin is plotted as a grey dashed line, and the data points are offset horizontally for display purposes. We show the summed EW and average velocity shift for all low-ionization lines (Si IIλ1526, Al IIλ1670, Ni II$\lambda\lambda$1741,1751, Si IIλ1808 and near-UV Fe II) with the exception of Mg II. Mg II is plotted separately, as the trends it follows may be more significant due to emission filling.

In Figure 2.12, all lines except Mg II reside near the systemic velocity, and none but Mg II exhibits a trend between the velocity shift and stellar mass. It indicates that the blueshift of C IV, Al III and the low-ionization lines, Mg II excluded, is not sensitive to stellar mass. Mg II displays a smaller blueshift and a larger EW in galaxies with higher stellar masses. Given that $V_{max,\mathrm{Mg\ II}}$ for all three stellar mass bins are similar (-519 km s^{-1}, -566 km s^{-1} and -538 km s^{-1} for the high-, medium- and low-M_* bins, respectively), this trend suggests that outflow velocity does not depend strongly on stellar mass (See also Martin et al., 2012). Rather, it results from the fact that resonant Mg II emission fills more of the absorption trough in less massive galaxies, making the observed profile more blueshifted while having a smaller EW. The strength of the low-ionization lines shows a positive correlation with stellar mass. Since massive galaxies tend to have more interstellar gas, larger covering fractions for the cold gas content in ISM lead to a deeper absorption trough for the low-ionization lines

[5]The results do not change significantly if the FWHMs of the doublet members are fixed at 1:1 for the weak transitions.

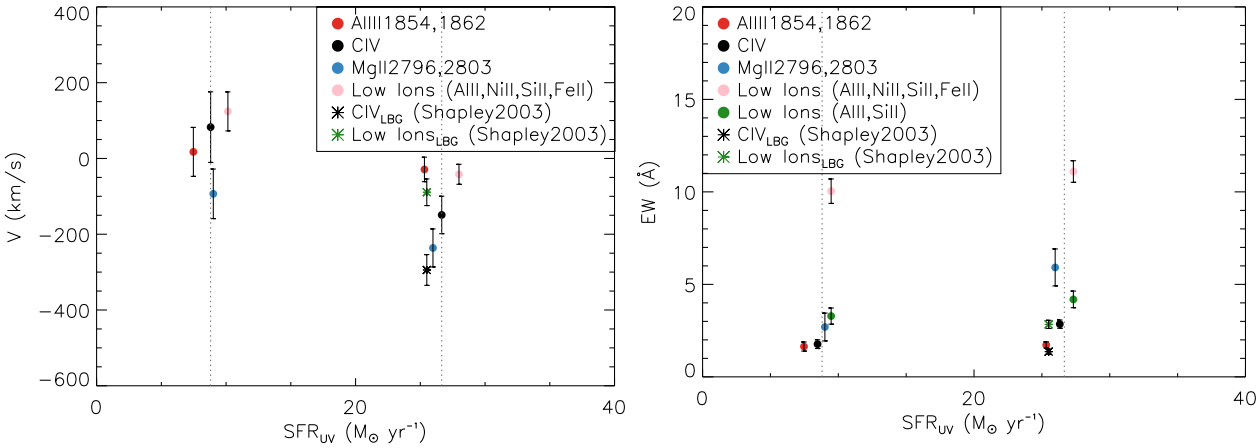

Figure 2.13: Interstellar absorption velocity shift and EW vs. SFR in the composite spectra. Legends are the same as in Figure 2.12. The green and black stars are measurements from the LBG composite in Shapley et al. (2003), where only Si IIλ1526 and Al IIλ1670 are available for the low-ionization line measurements. The errors for the LBG sample was estimated from fitting 500 fake composites, perturbing the returned parameters (centroids, EW) with associated error for each fake composite, and taking the standard deviation from the final distribution of the 500 perturbed centroids or EWs. The green circle in the right panel represents the total EW of Si IIλ1526 and Al IIλ1670 in the DEEP2 sample, in order to make reasonable comparison with the measurements from Shapley et al. (2003).

(Erb et al., 2006a). C IV and Al III, on the other hand, show no significant correlations in EW, suggesting that the strength of intermediate- and high-ionization absorption lines is independent of stellar mass.

2.5.2 SFR

Figure 2.13 shows how the measured velocity shift and EW vary with SFR for absorption transitions tracing different ionization states. In the right panel, the green circles represent the total EW of only Si IIλ1526 and Al IIλ1670 for the comparison with the measurements from Lyman break galaxies (LBGs) from Shapley et al. (2003) (see Section 2.6.1).

We find that both the blueshift and EW of C IV increase with an increasing SFR. The same trends of both blueshift and EW with SFR also hold for the low-ionization lines, Mg II included. In addition, it is interesting that the centroids of C IV and the low-ionization lines (excluding Mg II) are *redshifted* in the low-SFR bin, and the low-ionization lines are barely blueshifted in the high-SFR bin. Figure 2.13 shows that the C IV properties are

exclusively related to SFR, suggesting that massive star formation and associated processes drive the properties of the highly-ionized gas traced by C IV, while for low-ionization lines, the properties correlate with both SFR and stellar mass. Many studies have revealed a relationship between SFR and stellar mass in star-forming galaxies (often referred as the 'main sequence'; Elbaz et al., 2007; Noeske et al., 2007; Kashino et al., 2013). Hence, the observed correlation between low-ionization absorption line properties and SFR may simply be a byproduct of the relationship with stellar mass. The intermediate-ionization doublet, Al III, appears to have a nearly zero velocity shift (at systemic velocity) in both bins and displays no significant correlation with SFR.

It is worth mentioning that C IV shows a larger blueshift relative to the low ions in the high-SFR bin than in the low-SFR bin. This larger differential blueshift may result from a larger contribution of shocked, collisionally ionized gas to the C IV absorption in the high-SFR bin. Alternatively, C IV may simply be more affected by emission filling at higher SFRs.

The larger blueshift of Mg II relative to that of C IV in the low-SFR bin at first seems to be inconsistent with our results stated in Section 2.4.1 that these two transitions display similar velocity shifts on average. However, we find that the objects that contribute to the low-SFR composite are not representative of the parent sample (93 objects with C IV coverage) in terms of C IV kinematics, and those with detected C IV tend to have less blueshifted and even significantly redshifted absorption profiles (measured velocity shifts ranged from -52 km s^{-1} to +191 km s^{-1}, with a median of +44 km s^{-1}). [6] We are not certain at this point whether this discrepancy is due to the selection effect of a small sample (13 objects

[6]In order to reduce the potential bias introduced by small sample size, we did the same analysis using the Bundy SFR. Although we believe the GALEX SFR measurements are more reliable, they only cover 25 out of 93 objects in our sample. Bundy SFRs, on the other hand, are available for all 93 objects. Given these two SFR measurements are correlated (Figure 2.1), the composite spectra created using the Bundy SFR should qualitatively reproduce the results derived from GALEX-SFR-generated composites. Therefore, we produced three composite spectra (low-, median- and high-SFR bins) according to Bundy SFR and each bin contained 31 objects. Again, C IV is less blueshifted than Mg II in the low-SFR_{Bundy} bin (measured C IV velocity shifts ranged from -472 km s^{-1} to +191 km s^{-1}, with a median of -32 km s^{-1}). Note that the median blueshift of C IV in this case is still not as large compared to that in the sample with robust C IV measurements (-64 km s^{-1}). Hence, a larger sample cannot fully account for the discrepancy we observe.

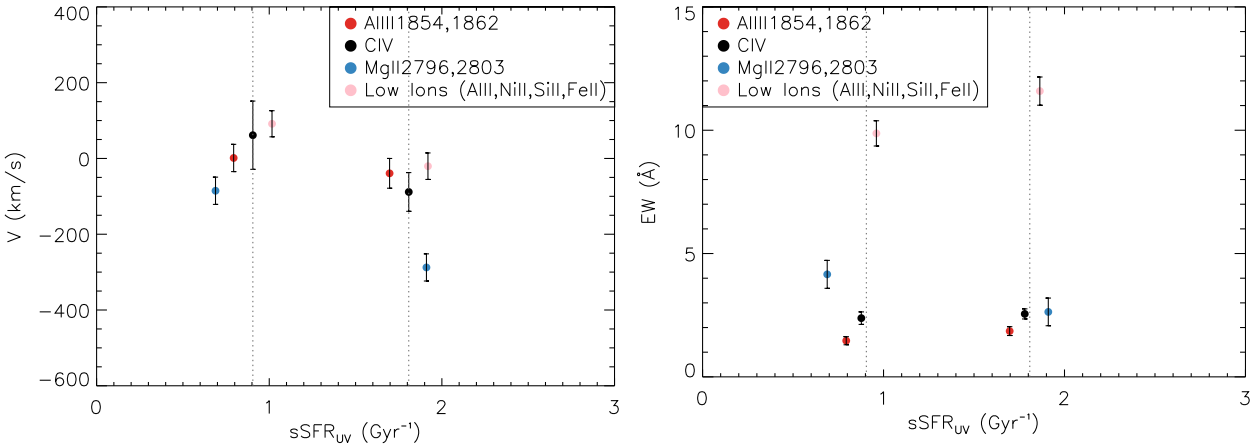

Figure 2.14: Interstellar absorption velocity shift and EW vs. sSFR in the composite spectra. The legends are the same as in Figure 2.12.

in the low-SFR bin), or whether galaxies with low SFRs are intrinsically associated with high-ionization inflows. A larger sample is required to address this question.

2.5.3 Specific SFR

Figure 2.14 shows the relation between kinematics of low-, intermediate- and high-ionization lines and sSFR. While becoming more blueshifted and stronger at higher sSFR, both C IV and the low-ionization lines (excluding Mg II) are redshifted in the low-sSFR bin and have marginally blueshifted centroids in the high-sSFR bin. Although Mg II also shows a larger blueshift at higher sSFR due to the increased effects of emission filling, its strength actually decreases at higher sSFR. The contrasting behavior of the EWs of Mg II and the other low-ionization lines can be explained in terms of the interplay between SFR and stellar mass. All low-ionization lines, Mg II included, increase in strength with both increasing SFR and stellar mass. The observed trends with sSFR (i.e., SFR/M_*) are therefore weak, and reflect a stronger dependence of Mg II emission filling on stellar mass than on SFR. The intermediate-ionization phase Al III, is not sensitive to sSFR and shows no strong correlations.

2.6 Summary and Discussion

In this paper, we have analyzed the far-UV LRIS spectra of a sample of 93 DEEP2 galaxies at $z \sim$1 with coverage of C IV$\lambda\lambda$1548,1550. We focused on 46 objects with continuum $S/N > 5$ and investigated the kinematics of highly-ionized gas in 32 objects with significant C IV detections. We have also measured low-ionization far-UV lines as well as near-UV Mg II and Fe II. We found that the typical blueshift of C IV absorption was slightly greater than that of near-UV Fe II resonant absorption lines at the $\sim$ 3-sigma level (intercept of the best-fit linear regression -76 $\pm$ 26 km s^{-1}), with a similar detection fraction of blueshifted C IV absorption. We further compared the C IV absorption profile with that of Mg II. Given that both the centroid velocity shifts and the maximum velocities of C IV and Mg II are nearly identical, we concluded that the larger blueshift of C IV absorption with respect to the near-UV Fe II may be caused by either faster motion of the highly-ionized gas, or else filling in on the red side from resonant C IV emission in analogy to what has been observed in Mg II and Fe II (Martin et al., 2012; Kornei et al., 2012).

We also investigated the scaling relations between C IV kinematics and galaxy properties by making composite spectra of galaxies binned according to stellar mass, SFR, sSFR, SFR surface density, $U - B$ color and B-band luminosity. We found that both the blueshift and EW of C IV increase as SFR and sSFR increase, suggesting that outflowing high-ionization gas is associated with processes related to star formation, such as energy and momentum input from massive stars and their supernovae. The strength of the low-ionization lines, on the other hand, is more correlated with the stellar mass, which can be explained by larger covering fractions and velocity dispersions of the cold phase of the ISM in more massive galaxies, due, respectively, to the greater amount of interstellar gas and overall dynamical mass. The properties of Al III are not sensitive to any of the galaxy properties we studied.

2.6.1 Redshift Evolution

To investigate the possible evolution of the C IV kinematics, we compared our results with the $z \sim 3$ Lyman Break Galaxy (LBG) composite from Shapley et al. (2003). The com-

posite was constructed from 811 individual LBG spectra, and spans from 900Å to 2000Å in wavelength. Since no near-UV spectral features were available, and all the absorption lines beyond 1800Å were poorly detected in the LBG composite, we only measured C IV, Si IIλ1526 and Al IIλ1670. Due to the lack of the corresponding composite error spectrum, we estimated the uncertainties using a method consistent with that of Shapley et al. (2003): we measured the noise from a relatively featureless range of the continuum (1700 Å to 1825 Å) and assigned this value as a constant error across the full spectrum to account for pixel variance. To account for sample variation, we fit the far-UV absorption lines in 500 fake composite spectra, which were constructed from bootstrap resampling from the original sample used for the real composite. For each fake composite, the parameters returned by MPFIT were then perturbed by the associated errors. The final error on the parameters for the real composite was derived from the standard deviation of the parameter distributions over the fake composites. SFRs for LBGs were estimated from dust-corrected rest-frame UV luminosities, combining apparent R magnitudes, and extinction based on observed $G - R$ colors. The median SFR from the LBG sample is 26 $M_\odot$ yr^{-1} (assuming a Chabrier IMF and $H_0 = 70$ km s^{-1}), which is close to that of the high SFR bin in the DEEP2/LRIS sample. Stellar mass and sSFR are not available for the LBGs, thus SFR is the only galaxy property we study here.

As shown in Figure 2.13, both C IV and far-UV low-ionization lines in LBGs have a higher blueshift yet a lower EW compared to our sample with similar SFRs. This difference may be caused by a different proportion between outflowing and interstellar gas in galaxies. Absorption from the systemic and outflowing portions of the ISM jointly contribute to the observed absorption profile. If instead, we model each absorption line (individual doublet member in the C IV case) with a two-component fit: a dominant systemic component with no Doppler shift representing the absorption from ISM, and a Doppler component characterizing the contribution from outflows (Steidel et al., 2010; Coil et al., 2011; Martin et al., 2012), the change in either component may alter the shape of the absorption trough. Lack of ISM absorption around systemic velocity results in a more blueshifted centroid as well as a smaller EW, as the LBG sample suggests.

However, this difference can also result from emission filling, especially for resonant lines like C IV. In order to investigate the real cause, we further compared the maximum velocity of C IV, $V_{max,\mathrm{C\ IV}}$, in both the LBG composite and the DEEP2/LRIS sample. The measurement of $V_{max,\mathrm{C\ IV}}$ in LBGs was performed in an analogous way to that described in Section 2.4.2. For a rough estimate of uncertainties in the LBG composite, we increased the constant error, which was derived from the continuum noise over the wavelength range of 1700 Å - 1825 Å, by a factor of two. We then measured $V_{max,\mathrm{C\ IV}}$ of the LBGs in 500 fake composite spectra (the same set as described previously in this section) and derived an average value of -649 km s^{-1}. In comparison, $V_{max,\mathrm{C\ IV}}$ of the high-SFR bin in the DEEP2/LRIS sample is -542 km s^{-1} with a similar SFR (30 $M_{\odot}$ yr^{-1}). The larger V_{max}, along with a bluer centroid, suggests that the entire absorption profile of C IV in LBGs is shifted bluewards with less absorption, rather than only having emission filling on the red side of the absorption trough. This observed trend may arise as a consequence of a patchier systemic ISM component and a more significant Doppler component in the LBGs compared to that in the DEEP2/LRIS galaxies.

2.6.2 C IV vs. O VI

Our results demonstrate that low- and high-ionization interstellar absorption lines only have small differences in terms of kinematics, in the spectra of star-forming galaxies at z $\sim$ 1. Objects with robust measurements of both C IV and near-UV Fe II show a median velocity difference of $V_{1:1} - V_{\mathrm{nuvFe\ II}}$ = -65 km s^{-1}, and the best-fit linear regression of $V_{1:1}$ on $V_{\mathrm{nuvFe\ II}}$ of this sample is charaterized by an intercept of -76 $\pm$ 26 km s^{-1}, assuming a slope of unity. Moreover, given that the velocity shifts of C IV measured from both line centroids and blue wings agree with those of Mg II, we conclude that C IV, being a resonant transition like Mg II, is affected by emission filling to the same extent. Therefore, the small apparent velocity discrepancy between C IV and near-UV Fe II can be explained by filling in on the red side of the C IV absorption trough by resonant emission, instead of evidence for highly-ionized gas outflowing at a larger speed than that of gas traced by low-ionization lines.

Similar results on the relative velocity shifts between low and high ions have been reported for $z \sim 3$ LBGs and low-redshift star-forming galaxies. In the composite spectrum from Shapley et al. (2003), the high-ionization Si IV feature displays a similar mean blueshift and velocity FWHM to those of low-ionization lines, including Si II, O I, C II, Fe II, and Al II. In addition, Pettini et al. (2002) studied the kinematics of different phases in ISM using the gravitationally lensed LBG, MS 1512-cB58, with much higher spectral resolution (58 km s^{-1} FWHM). The spectrum of cB58 suggests that all the observed ion stages span the same overall range in velocity, and that the gas with the highest optical depth is blueshifted by roughly the same amount for both low (e.g., Si II, C II,) and high ions (e.g., Si IV, C IV). At low redshift, recent work by Chisholm et al. (2016) yields similar results. These authors study 37 nearby star-forming galaxies using tracers at different ionization stages (O I, Si II, Si III, and Si IV), and show that absorption lines with similar strength, regardless of ionization state, have comparable outflow velocities. These findings suggest that gas clouds traced by low- and high-ionization lines may actually be co-moving.

In apparent contrast, Heckman et al. (2001) find that high-ionization lines in general have larger outflow velocities compared to the low ions by studying the rest-far-UV spectrum of the dwarf starburst galaxy NGC 1705. One distinction highlighted by Heckman et al. (2001) is that O VI, which traces the coronal-phase gas, has broader and more blueshifted absorption profile than the low ions. Grimes et al. (2009) extended the sample to 16 local starbursts, finding similar results. Specifically, Grimes et al. (2009) detect a more significant blueshift in O VI than in the low-ionization C II, N II features, and the intermediate-ionization stage C III line, suggesting that highly-ionized gas in general has larger outflow velocities.

These seemingly contradictory conclusions are in fact due to different tracers used as 'high-ionization lines.' In fact, although both C IV and O VI can be produced both from cooler ($T < 10^5$ K), photoionized gas, and hotter ($T > 10^5$ K), collisionally ionized gas, observations and simulations suggest that the hot, collisionally ionized phase makes a more significant contribution to circumgalactic O VI. Most observations of circumgalactic C IV (e.g., Lehner et al., 2011; Liang & Chen, 2014) find that this transition arises in photoionized gas (but see Borthakur et al., 2013). In simulations of galaxies including feedback (e.g., Shen

et al., 2013; Liang et al., 2016), the gas traced by O VI absorption is hotter on average, and more diffuse and spatially extended, while the gas giving rise to C IV absorption is clumpier, and traces gas at smaller galactocentric radii. In terms of line strength, although the covering fraction of both C IV and O VI decreases less rapidly in the radial direction than that of the low ions (Steidel et al., 2010; Shen et al., 2013; Liang & Chen, 2014), C IV displays a sharper drop in the radial profile of column density compared to that of O VI (Liang et al., 2016). In short, both observations and simulations show that C IV and O VI probe different distributions of circumgalactic gas, and, therefore, may trace distinct outflow kinematics.

Given similar velocity shifts observed in C IV and the low ions in our sample, it is possible that the cool and warm gas, traced by the low-ionization lines and C IV, respectively, are largely co-spatial and moving at similar velocities. At the same time, these gas phases are cooler, with lower characteristic outflow velocity compared to the gas typically probed by O VI. One possible explanation is that O VI, which is a characteristic feature of starburst galaxies, is produced when hot, X-ray emitting gas interacts with cold, dense clouds in its path (Grimes et al., 2009). Meanwhile, C IV may arise from the interface layer between the low-ionization clouds and the hot, radiative cooling gas flow where O VI is seen.

2.6.3 Future Outlook

Investigations comparing the properties of different phases of the outflowing gas are crucial for mapping detailed multi-phase structure and estimating the overall mass loss rate through galactic winds. In this paper, we do not observe large difference in the velocity shifts between the high-ionization C IV and the low-ionization near-UV Fe II features. This result suggests that the gas traced by C IV and low ions may be co-moving, and, even co-spatial. In addition, we find that the strength of C IV scales mainly with SFR, while that of the low-ionization lines is more sensitive to stellar mass. These results indicate that the gas probed by C IV is more associated with outflows, while the low-ionization lines additionally trace the systemic ISM component in the galaxies. Considering the different cases discussed in Section 2.4, we propose two scenarios to explain the origin of the small blueshift interstellar C IV shows

relative to near-UV Fe II lines.

If the more highly-ionized gas is indeed traveling faster, our findings suggest that although C IV and the low ions both have absorption profiles consisting of a Doppler (outflow) component and a systemic ISM component, the ISM component is dominant in the low ions while the outflow component contributes more to the CIV absorption profile. If the outflowing gas traced by C IV and by the low ions are co-moving, one would expect their outflow components to have roughly the same blueshifts. Therefore, the stronger outflow component relative to that of the low-ionization lines makes C IV show a slightly more blueshifted overall absorption profile than the low ions, as suggested by our data. Alternatively, if the larger blueshift of C IV is caused by emission filling, our results indicate that in high-SFR galaxies more C IV absorption is produced in the ISM due to various reasons (e.g., stellar wind from massive stars, supernova explosions, shocks). In this case, the highly-ionized gas is not necessarily associated with outflows, and the apparent larger blueshift of C IV is only a result of stronger emission filling due to higher C IV column density. Future simulations studying the relation between feedback and the circumgalactic medium should be able to reproduce these results.

At the same time, it is essential to have access to spectroscopic data with higher S/N and spectral resolution in order to resolve the C IV doublet members. Such data would enable us to perform the two-component fit to individual C IV doublet members, modeling the outflow and ISM components separately. In this way, one would be able to draw more robust conclusions about the low- and high-ionization kinematics. A larger sample is also crucial to investigate the relative blueshifts shown by C IV, Mg II and near-UV Fe II. Such improvements will enable us to fully comprehend the links and distinctions among the kinematics of different gas phases in star-forming galaxies.

CHAPTER 3

C III] Emission in Star-forming Galaxies at $z \sim 1$

3.1 Introduction

Rest-frame UV spectroscopy contains rich information regarding the physical properties of the interstellar medium (ISM) in star-forming galaxies. The abundant nebular emission features in the far-UV, including C III]$\lambda\lambda$1907, 1909, C IV$\lambda\lambda$1548, 1550, He IIλ1640, O III]$\lambda\lambda$1661, 1666 and Si III]$\lambda\lambda$1882, 1892, are especially important in probing the ionized gas in H II regions. These lines can be combined to infer various physical parameters, such as metallicity, abundance pattern, and ionization parameter, and provide valuable constraints on the ionizing stellar populations.

One of the strongest far-UV emission lines is typically the C III]$\lambda\lambda$1907, 1909 doublet. Given its prominence and detectability in bright, star-forming galaxies at $z \sim 6-7$, C III] has been suggested as an alternative to Lyα emission for estimating redshifts during the reionization epoch (Stark et al., 2014, 2015). Indeed, spectroscopic confirmation is crucial yet challenging for $z > 6$ galaxy candidates, in which Lyα is significantly attenuated by the neutral intergalactic medium (IGM) (e.g., Vanzella et al., 2011; Treu et al., 2012, 2013; Schenker et al., 2014; Pentericci et al., 2014; Tilvi et al., 2014; Caruana et al., 2014). In contrast, nebular C III] photons are negligibly affected by IGM absorption.

Nebular C III] emission has been studied both in the local universe (Giavalisco et al., 1996; Leitherer et al., 2011; Berg et al., 2016, Pena-Guerrero et al. 2015) and at redshift > 2 (Shapley et al., 2003; Erb et al., 2010; Bayliss et al., 2014; Stark et al., 2014, 2015; Rigby et al., 2015; Zitrin et al., 2015; Stark et al., 2017; de Barros et al., 2016; Vanzella et al., 2016; Steidel et al., 2016). Large rest-frame EWs (> 5Å) of C III] have been detected at all

these redshifts, and appear common at $z \gtrsim 6-7$ ($\gtrsim 10$Å; Stark et al., 2015, 2017). It has been suggested that galaxies showing strong C III] emission are in general blue, faint and low-mass, with high specific star-formation rates (sSFRs; Stark et al., 2014). Furthermore, results from photoionization models indicate that C III] emission is enhanced at lower gas-phase metallicity, higher ionization parameters and harder radiation fields (e.g., Erb et al., 2010; Stark et al., 2015, 2017; Berg et al., 2016; Jaskot & Ravindranath, 2016). Many studies have also shown that the strength of C III] correlates with that of other emission features, such as Lyα (Shapley et al., 2003; Stark et al., 2014, 2015; Rigby et al., 2015; Jaskot & Ravindranath, 2016) and [O III]λ5007 (Jaskot & Ravindranath, 2016), in the sense that large C III] EW tends to appear in galaxies with strong Lyα and [O III] emission.

In principle, strong C III] emitters at $z > 6$ are ideal sources to study how C III] emission relates in general to the properties of host galaxies and other emission lines. However, due to the poor data quality and small current sample of these extreme C III] emitters, it is exceptionally challenging to conduct studies in a statistical manner. Another way of dissecting the $z > 6$ C III] emitters is by studying lower-redshift analogs. It is more straightforward at lower redshift to assemble multi-wavelength data over a wide rest-frame wavelength range and collect rest-UV spectra with higher signal-to-noise. Therefore, targeting lower-redshift systems enables us to study in detail the factors that modulate the strength of C III].

Here we analyze the nebular C III] emission transition for the first time at $z \sim 1$. One of our goals is to investigate whether the correlations between C III] and a variety of galaxy properties, seen both at lower and higher redshifts, are redshift-independent (i.e., that they also remain true at $z \sim 1$). Our $z \sim 1$ sample can potentially connect the local and $z > 2$ universe in redshift space and provide a complete understanding of the factors affecting the production of nebular C III] emission. More importantly, we aim to infer the physical conditions in typical star-forming galaxies at $z \sim 1$ from the characteristic strength of C III], based on both observational constraints and photoionization models.

We provide a brief overview of the observations and data reduction, and discuss the properties of the C III] sample in Section 4.2. In Section 4.3, we describe the measurement of the C III] emission profile in our data. We present the C III] EW distribution in Section 3.4,

along with the correlations of the C III] strength with multiple galaxy properties (i.e., M_B, $U-B$, M_*, SFR, sSFR), the strength of the near-UV Fe II* and Mg II emission features, and gas-phase metallicity. Finally, we discuss and summarize our results in Sections 4.6 and 4.7, respectively.

Throughout this paper, we adopt a standard ΛCDM model with $\Omega_m = 0.3$, $\Omega_\Lambda = 0.7$ and H_0 =70 km s^{-1}. All wavelengths are measured in vacuum. Magnitudes and colors are on the AB system.

3.2 Observations, Data Reduction and Sample

A full description of our $z \sim 1$ dataset has been presented in Martin et al. (2012). We summarize the relevant details in this section. Objects presented in this paper were drawn from the Deep Extragalatic Evolutionary Probe 2 (DEEP2; Newman et al., 2013) galaxy redshift survey and observed with the Low Resolution Imager and Spectrometer (LRIS, Oke et al., 1995; Steidel et al., 2004) on the Keck I telescope. The LRIS data were collected during 4 observing runs from 2007 to 2009 using 9 multi-object slitmasks with 1.2″ slits. A total of 208 $B < 24.5$ galaxies were observed in the redshift range $z = 0.4 - 1.4$ with $\langle z \rangle = 1.01$, based on apparent magnitude $B < 24.5$. We used two configurations for the LRIS observations: the primary set-up (6 masks) featured the 400 lines mm^{-1} grism on the blue side with an average effective resolution of 435 km s^{-1} full width at half-maximum (FWHM), the d680 dichroic, and the 831 lines mm^{-1} grating on the red side with FWHM of 150 km s^{-1} ($R = 700$). The secondary configuration (3 masks), which was mainly designed to obtain near-UV spectroscopy of brighter galaxies under less optimal observing conditions, had the 600 lines mm^{-1} grism on the blue side with FWHM of 282 km s^{-1}, the d560 dichroic, and the 600 lines mm^{-1} red grating with FWHM of 220 km s^{-1} ($R = 1100$). The primary set-up enabled the coverage of the rest-UV spectra of our targets on the blue side, and the [O II] nebular emission doublet (a systemic redshift diagnostic) on the red side. For 600-line masks, we aimed for continuous wavelength coverage between blue and red side spectra, across the dichroic. The integration time ranged from 5 to 9 hours for most 400-line masks

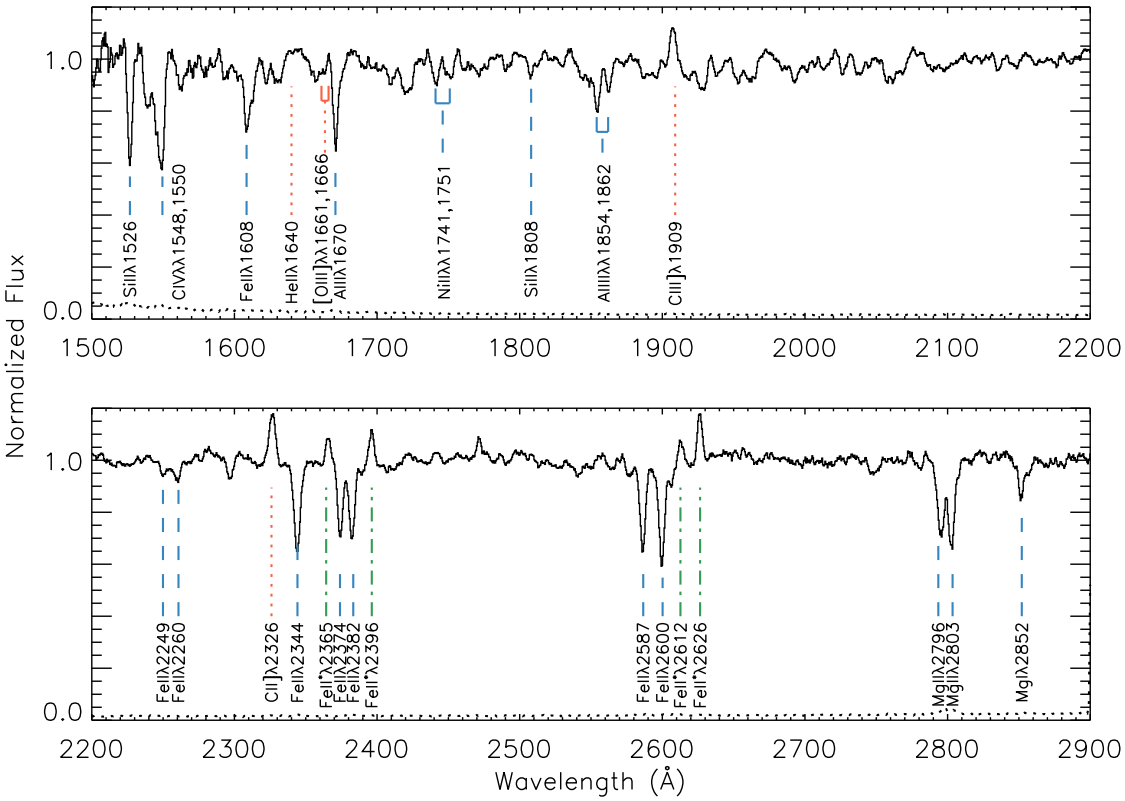

Figure 3.1: Composite continuum-normalized UV spectrum (black solid line) constructed from 184 objects with C III] coverage in the DEEP2/LRIS sample. The composite spectrum was created using median stacking, with the noise level (black dotted line) estimated from Monte Carlo methods, as described in Section 3.4.2. Characteristic emission and absorption features are identified, with the following labels: interstellar absorption transitions (blue dashed lines), fine structure transitions (green dash-dot lines) and nebular emission transitions (red dotted lines). At the resolution of the LRIS spectra included in this composite (i.e., 400-line spectra, and 600-line spectra smoothed to match the 400-line resolution), the C III] doublet is blended.

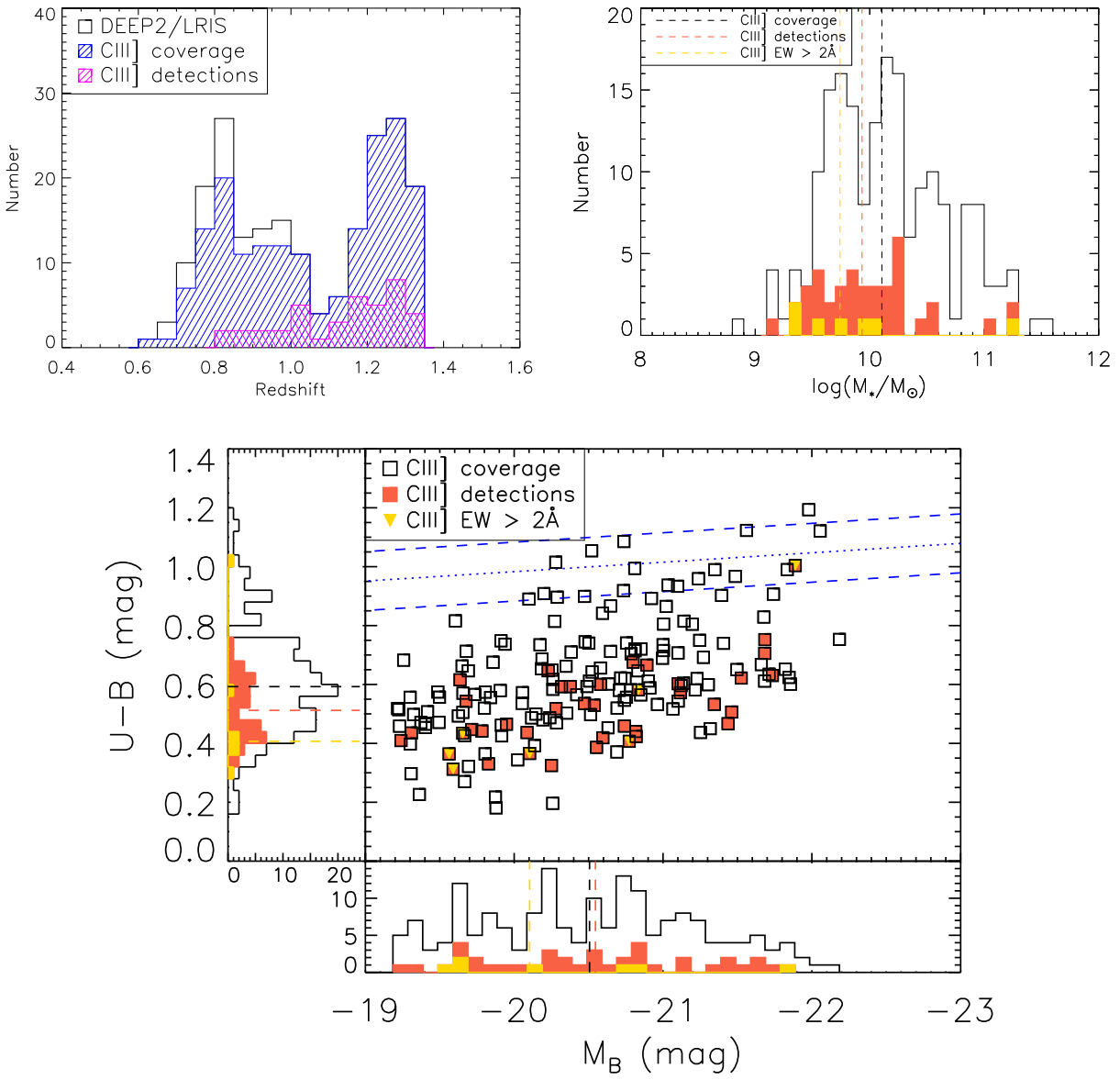

Figure 3.2: Properties of the galaxies in the DEEP2 C III] sample. **Top left:** Redshift distribution. The black open bar represents the parent sample of 208 DEEP2/LRIS galaxies; the dashed blue bar represents 184 star-forming galaxies with C III] coverage; the dashed magenta bar represents 40 galaxies meeting the criterion of $> 3\sigma$ C III] EW detection in the rest frame. **Top right:** Stellar mass distribution. The black histogram shows the full sample with C III] coverage (184 objects); the red and yellow filled histograms show, respectively, objects with significant C III] detections (40 objects) and rest-frame EW > 2Å (7 objects). The median values of these different samples are shown with dashed vertical lines in corresponding colors. **Bottom:** $U-B$ vs. M_B color-magnitude diagram with histograms in $U-B$ color and $B-$ band absolute magnitude. Squares represent 184 objects with C IV coverage; red filled squares represent those with C III] $S/N > 3$ (40 objects); yellow triangles represent 7 objects with C III] rest-frame EW measurements > 2Å. The dotted line marks the division between the "red sequence" and the "blue cloud" at $z \sim 1$ in the DEEP2 sample (Willmer et al., 2006). Legends for $U-B$ and M_B histograms are the same as in the top right panel.

and was typically shorter (3-5 hours) for the 600-line masks.

All two-dimensional spectra were flat fielded, cleaned of cosmic rays, background-subtracted, extracted into one dimension (1D), wavelength and flux calibrated, and transformed to the rest frame. We utilized rest-frame B-band luminosities and $U-B$ colors measured from Willmer et al. (2006), and stellar masses derived SED fitting with $BRIK$ photometry, assuming a Chabrier (2003) IMF and Bruzual & Charlot (2003a) spectral templates (see Bundy et al. (2006) for a full description). We also adopted SFR_{UV}, the dust-corrected SFR derived from *Galaxy Evolution Explorer* (GALEX) UV measurements in our work. The spectral slope β, which characterizes the continuum flux ($f_\lambda \propto \lambda^\beta$) over the rest-frame wavelength range of $1250-2500$Å, was used to determine the dust extinction in the UV based on the relationship from from Seibert et al. (2005). The SFR_{UV} values presented in this paper have been converted to a Chabrier IMF. 42 out of 184 objects in our sample fall in the AEGIS field, where the SFR_{UV} measurements are available. For a detailed discussion of the DEEP2/LRIS galaxy properties, we refer the reader to Martin et al. (2012) and Kornei et al. (2012).

The DEEP2/LRIS data are unique in that the masks were designed to have the coverage of the far-UV spectral region at $z \sim 1$. As shown in the composite spectra (Figure 4.3), multiple far-UV nebular emission features were covered in the LRIS data. These include C IV$\lambda\lambda$1548, 1550, He IIλ1640, O III]$\lambda\lambda$1661, 1666 and C III]$\lambda\lambda$1907, 1909, which can be potentially modeled to provide a rich window into the physical properties of the galaxies in our sample. Among these far-UV features, C III] is the strongest emission transition, and the one detected in the largest number of individual spectra. Therefore, we focus the bulk of our analysis on nebular C III] emission. We identified 186 out of 208 galaxies with coverage of C III]. Of these, we removed 2 objects (12015320 and 22028607) with obvious spectroscopic evidence of activity from an active galactic nucleus (AGN), in the form of [Ne V]λ3425 emission. The remaining 184 objects comprise the first statistical sample of C III] at $z \sim 1$. Among these 184 objects, 144 were observed on 400-line masks, and 40 on 600-line masks. Figure 4.3 shows a composite rest-UV spectrum created by stacking the continuum-normalized spectra of the sample of 184 galaxies with C III] coverage. Spectra

were normalized as described in Du et al. (2016). The strongest interstellar emission and absorption features are labeled.

We plot the galaxy properties (i.e., redshift, stellar mass, $U-B$ color and B-band absolute magnitude) of the sample of 184 galaxies with C III] coverage in Figure 4.6. These objects range in redshift from 0.64 to 1.35 with a median of 1.08, B-band absolute magnitude (M_B) from -18.31 to -22.19 with a median of -20.51, stellar mass ($\log(M_*/M_\odot)$) from 8.88 to 11.58 with a median of 10.10, $U-B$ color from 0.18 to 1.19 with a median of 0.59 and SFR_{UV} from 2 to 97 $M_\odot$ yr^{-1} with a median of 13 $M_\odot$ yr^{-1}. Galaxies in our sample are predominantly star-forming galaxies in the "blue cloud" (Faber et al., 2007) at $z \sim 1$.

3.3 Measurements

In this section, we describe the measurement of the strong far-UV nebular emission doublet, C III]$\lambda\lambda 1907, 1909$. The C III] doublet is a collisionally excited forbidden/semi-forbidden transition, which is typically observed in H II regions in star-forming galaxies. The C III] doublet ratio is determined by the electron density. In the low-density regime, which we believe is the case for galaxies in our sample, [C III]λ1907 is stronger than C III]λ1909, and $I_{\text{[C III]}\lambda 1907}/I_{\text{C III]}\lambda 1909}$ asymptotes to a value of 1.55 in the low-density limit (Osterbrock & Ferland, 2006).

We continuum normalized the rest-frame UV calibrated 1D LRIS spectra using multiple discrete wavelength ranges ('windows') that are clean of spectral features, as defined by Rix et al. (2004). Based on these windows, we modeled the continuum for all 184 spectra with C III] coverage using the IRAF *continuum* routine, with a *spline*3 function of order = 8. In cases where the fitted continuum level did not provide a good description of the observed spectrum due to the limited coverage of windows from Rix et al. (2004), additional windows customized for each object were added to keep the fitted continuum reasonable and make sure that it scattered around unity. Monte Carlo simulations indicate that the systematic uncertainty at each wavelength associated with continuum fitting is less than the corresponding 1σ error spectrum, and therefore does not dominate the uncertainties in our

EW measurements.

Given the different resolutions in the primary and secondary masks, the C III] doublet is blended in the 400-line spectra at the rest-frame wavelength while in principle resolved in the 600-line spectra. Accordingly, we fit the C III] emission with a single Gaussian profile for the 400-line spectra, and deblended the feature into two Gaussians for those observed with the 600-line masks.

We used the IDL program MPFIT (Markwardt, 2009) with the initial values of continuum flux level, line centroid, EW and Gaussian FWHM (for the overall blended profile in the 400-line spectra and/or for each deblended component in the 600-line spectra) estimated from the program *splot* in IRAF. For the 600-line spectra, we fixed the doublet wavelengths at the rest-wavelength ratio, $\lambda_{1907}/\lambda_{1909} = 1906.683/1908.734$**,** and constrained the doublet EW ratio to vary between 1.0 to 1.55, as expected in the low-density regime.[1] The best fit was then determined where the χ^2 of the fit reached a minimum.

We iterated the fitting over a narrower wavelength range for both 400-line and 600-line spectra: centroid$-4\sigma < \lambda <$centroid$+4\sigma$, where the centroid and σ are, respectively, the returned central wavelength and standard deviation of the best-fit Gaussian profile from the initial MPFIT fit to the C III] doublet over 1898Å to 1918Å. We then determined the significance of the C III] EW in each object and identified 40 out of 184 objects with a $> 3\sigma$ C III] detection. Although we did not apply an explicit continuum S/N threshold when determining the sample with significant C III] detections, all 40 galaxies have continuum $S/N > 4$. We list the rest-frame C III] EW measurements for these 40 objects in Table 3.1, along with other basic galaxy properties.

3.4 Results

In order to examine the factors that modulate the C III] emission profile and understand the physical nature of the gas probed by C III], we compare the distribution of C III] EWs in the

[1]Given that the doublet members are adjacent in wavelength, the doublet ratio in terms of intensity should be almost identical to that in terms of rest-frame EW.

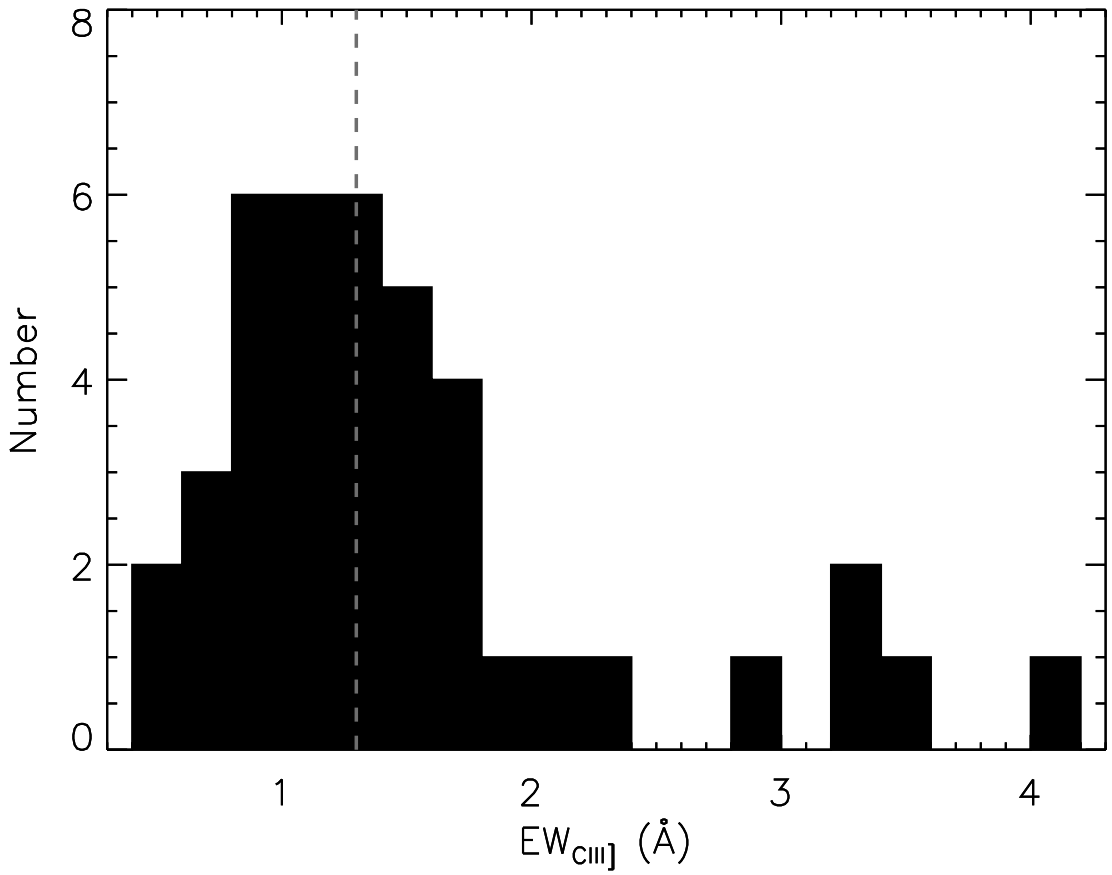

Figure 3.3: C III] rest-frame EW distribution for the DEEP2/LRIS sample. Objects shown in the histogram have $\geqslant 3\sigma$ C III] EW detections. The gray dashed line marks the median EW, 1.30Å.

DEEP2/LRIS sample with those in studies at other redshifts in Section 3.4.1. In addition, we investigate how C III] strength correlates with galaxy properties in both individual and composite spectra in Section 3.4.2, and whether the strength of C III] displays any connections with those of other near-UV emission features in Section 3.4.3. Finally, we explore the relation between C III] and metallicity in Section 3.4.4.

3.4.1 C III] EW distribution

As described in Section 4.3, we found 40 objects with C III] EW $> 3\sigma$. Figure 3.3 shows the rest-frame EW distribution of significant C III] detections in the DEEP2/LRIS sample. The C III] EW in this sample ranges from 0.5Å to 4.1Å, with a median of 1.3Å. In comparison with the C III] measurements in the low-mass, low-metallicity systems at high redshift ($z > 6$;

Table 3.1: Galaxy properties and C III] EW measurements

ID	Redshift	R.A. (J2000)	Dec. (J2000)	M_B (Magnitude)	$U-B$ (Magnitude)	$\log(M_*)$ ($M_\odot$)	SFR_{UV} ($M_\odot yr^{-1}$)	$EW_{C\ III]}$ (Å)
12008811	1.2156	14:16:55.33	52:30:24.91	-20.80	0.68	10.16	17.98	1.3 ± 0.2
12011619	1.0745	14:18:24.69	52:32:48.67	-19.31	0.44	9.11	4.40	1.6 ± 0.5
12012842	1.3148	14:16:56.46	52:33:13.77	-21.68	0.75	11.09	···	1.0 ± 0.3
12013002	1.2184	14:16:50.04	52:33:46.59	-20.23	0.65	9.56	8.51	1.1 ± 0.3
12015682	1.2837	14:18:49.05	52:36:29.66	-21.53	0.62	11.20	48.63	0.9 ± 0.3
12015914	1.1046	14:18:22.11	52:35:27.05	-19.83	0.33	10.11	15.85	0.9 ± 0.2
12016050	0.9797	14:18:08.67	52:35:13.82	-19.71	0.45	9.53	28.58	1.7 ± 0.5
12016075	1.1174	14:18:05.99	52:34:08.43	-19.68	0.54	9.41	10.78	1.5 ± 0.4
12016903	1.1600	14:17:12.79	52:34:28.41	-21.46	0.51	10.21	45.53	1.0 ± 0.2
12019542	1.2785	14:18:49.95	52:40:22.16	-21.68	0.71	10.40	72.25	0.8 ± 0.2
22005715	1.2345	16:51:20.54	34:44:32.09	-20.28	0.52	9.75	···	1.3 ± 0.4
22006207	1.2709	16:51:19.82	34:46:18.62	-20.60	0.42	9.89	···	1.1 ± 0.2
22013182	0.8298	16:51:36.11	34:48:00.57	-19.56	0.36	9.36	···	2.3 ± 0.5
22028986	1.1680	16:51:13.91	34:56:19.81	-20.58	0.60	10.16	···	1.0 ± 0.2
22036194	1.1665	16:51:23.95	34:59:51.49	-21.73	0.63	10.26	···	0.5 ± 0.1
22036688	1.1675	16:51:19.59	34:57:36.24	-20.47	0.54	9.90	···	1.7 ± 0.3
22036975	0.9367	16:51:16.36	34:58:36.68	-21.89	1.00	11.27	···	4.1 ± 1.1
22044809	1.1869	16:51:03.76	35:01:13.24	-19.59	0.31	9.39	···	3.6 ± 0.2
22100920	1.2735	16:51:17.13	35:00:52.83	-21.12	0.57	10.25	···	0.7 ± 0.1
22100930	1.2808	16:51:16.94	35:00:11.55	-21.34	0.53	10.29	···	1.3 ± 0.1
32016857	0.9392	23:29:24.95	00:07:05.85	-20.82	0.44	9.82	···	1.7 ± 0.2
32017018	1.1458	23:29:15.66	00:06:25.34	-19.78	0.44	9.50	···	1.0 ± 0.3
32017112	1.0085	23:29:16.29	00:08:04.48	-20.89	0.67	10.24	···	0.9 ± 0.3
32017188	1.2526	23:29:17.68	00:08:30.29	-20.83	0.58	9.98	···	3.2 ± 0.3
32017272	1.0190	23:29:07.87	00:06:18.04	-20.10	0.37	9.53	···	2.8 ± 0.3
32019861	1.3077	23:30:34.70	00:11:38.54	-20.54	0.53	10.01	···	1.5 ± 0.5
32020062	1.2808	23:30:27.03	00:11:14.80	-20.32	0.59	9.86	···	1.3 ± 0.4
32020384	1.2493	23:30:19.50	00:11:06.88	-20.82	0.42	9.96	···	1.1 ± 0.3
32020728	1.0446	23:30:08.53	00:10:09.60	-19.95	0.47	9.76	···	1.8 ± 0.3
32020769	1.3144	23:30:10.40	00:11:25.69	-20.77	0.41	10.01	···	2.2 ± 0.3
42006875	0.8697	02:30:33.47	00:26:21.15	-21.10	0.60	10.50	···	1.4 ± 0.3
42006904	1.0228	02:30:35.65	00:25:00.98	-20.74	0.46	10.07	···	0.6 ± 0.1
42006915	0.8945	02:30:37.04	00:24:36.58	-20.55	0.39	10.50	···	1.0 ± 0.2
42014618	1.0131	02:30:23.06	00:30:02.69	-20.38	0.59	9.81	···	0.5 ± 0.2
42014653	0.8376	02:30:22.78	00:28:58.83	-19.24	0.41	9.60	···	1.6 ± 0.4
42021266	0.9766	02:30:34.80	00:30:58.34	-19.64	0.62	9.50	···	1.3 ± 0.2
42022173	1.3112	02:30:22.97	00:30:13.48	-20.25	0.32	9.68	···	1.5 ± 0.2
42022307	1.2595	02:30:21.45	00:30:09.51	-21.44	0.47	10.22	···	0.8 ± 0.1
42033338	1.2237	02:29:03.37	00:33:34.35	-19.65	0.43	9.74	···	3.4 ± 0.8
42034223	1.2000	02:28:41.70	00:33:46.33	-20.09	0.44	9.45	···	1.3 ± 0.4

* The B-band luminosity and $U-B$ color are taken from Willmer et al. (2006). Stellar mass was estimated from SED fitting with $BRIK$ photometry, as presented in Bundy et al. (2006). SFR_{UV} is the dust-corrected UV SFR from GALEX measurements (full description in Section 4.2). The typical uncertainty is 3×10^{-4} in redshift, 0.1 - 0.2 dex in stellar mass, ∼0.05 mag in $U-B$ color, and < 0.1 mag in M_B. Rest-frame C III] EWs were measured using Gaussian fits.

Erb et al., 2010; Stark et al., 2014, 2015; Zitrin et al., 2015; Stark et al., 2017; Vanzella et al., 2016; de Barros et al., 2016, see Figure 3.7), which have a median of $\gtrsim$ 10Å, the EW of C III] at $z \sim 1$ is noticeably smaller. We discuss the causes of the weak C III] emission and inferred physical environment in $z \sim 1$ star-forming galaxies in Section 4.6.

3.4.2 C III] vs. galaxy properties

Studies of $z > 2$ galaxies show that strong C III] emission tends to be observed in blue, faint, low-mass galaxies with large sSFRs (Stark et al., 2014). In order to examine if these correlations also apply to $z \sim 1$, we investigate how galaxy properties relate to the C III] strength. For this analysis, we utilize the subsample of individual C III] detections and the composite spectra constructed from our full sample with C III] coverage (both individual detections and non-detections). We observe no apparent relations ($\lesssim 1.0\sigma$) between C III] and either SFR_{UV} or sSFR_{UV} (middle right and bottom panels of Figure 3.4). Therefore, we only highlight results regarding $B-$band absolute magnitude, $U-B$ color and stellar mass in this section.

We mark galaxies with individual C III] detections as red squares in the upper right and bottom panels of Figure 4.6. These objects segregate from the full sample of C III] coverage in that they have bluer $U-B$ color and lower stellar mass. The median color and stellar mass of objects with significant C III] detections are $U-B = 0.51$ (0.08 magnitude bluer than that of the full sample) and $\log(\mathrm{M}_*/\mathrm{M}_\odot) = 9.93$ (0.18 dex smaller than that of the full sample), respectively. Moreover, objects with large C III] EW (> 2Å) (7 objects, yellow triangles in Figure 4.6), mainly occupy the lower-left corner in the color-magnitude diagram. These objects have a median $U-B$ color of 0.41 and a median stellar mass of $\log(\mathrm{M}_*/\mathrm{M}_\odot) = 9.74$, indicating that strong C III] emission is associated with blue and low-mass systems with little dust extinction. The only outlier in the color-magnitude diagram is the galaxy 22036975, which has the highest C III] EW (4.09Å) in the sample of detections and stands out in having an unusual red color ($U-B = 1.00$ mag) compared to other objects with C III] detections. In fact, this object falls in the "green valley" between the blue cloud and red sequence (Figure

4.6, bottom). One possible explanation of strong C III] emission accompanied by a red color is the presence of an AGN. Indeed, both of the AGNs identified spectroscopically in our sample (see Section 4.2) show green-valley colors and significant C III] emission. However, we find no evidence of an AGN in 22036975 based on the non-detection of the [Ne V]λ3425 line. The 3σ upper limit on the [Ne V] rest-frame EW is 0.72 Å in 22036975, which is much lower than the typical EW observed in the optically-selected narrow-line AGNs (Zakamska et al., 2003). Therefore, although we are not certain about the physical explanation of the redder color shown by this object relative to other C III] detections, we still treat it as a star-forming galaxy and retain it in our sample.

While the connections between C III] emission and $U - B$ color and stellar mass are suggestive in the sample of individual detections, we cannot ignore the fact that these 40 objects only comprise $\sim 20\%$ of the full sample with C III] coverage. In order to investigate the correlations between spectral and galaxy properties displayed by the entire sample with C III] coverage, we constructed composite spectra in bins of specific galaxy properties. Additionally, using composite spectra potentially enables the measurement of weak transitions that are difficult to detect on an individual basis due to the low continuum S/N in a single spectrum.

We divided the set of 184 objects with C III] coverage into four bins in stellar mass, $U - B$ color and B-band absolute magnitude, and two bins in SFR_{UV} and sSFR_{UV}, given that the SFR_{UV} measurements are only available for 42 objects observed in the AEGIS field. Each bin in stellar mass, $U - B$, and M_B contained nearly the same number of galaxies (i.e., ~ 46). We combined individual continuum-normalized spectra to create composite spectra, smoothing the 600-line spectra to the resolution of the 400-line spectra. We then used the IRAF routine *scombine* to extract the median value of the normalized spectra at each wavelength to create a normalized composite spectrum for each bin in galaxy properties. To create the corresponding composite error spectra that account for both sample variance and measurement uncertainty, we bootstrap-resampled each bin and perturbed each spectrum in the bootstrap sample according to its own error spectrum. The perturbed spectra in the bootstrap sample were then combined to create a new composite spectrum. The process

was repeated 100 times and the standard deviation of these 100 fake composites at each wavelength was adopted as the value of the composite error spectrum for each bin.

We fit the C III] feature in the stacked spectra with a single Gaussian profile using MPFIT to measure the EW (i.e., the method described in Section 4.3). Figure 3.4 shows the behavior of C III] EW in the stacked spectra in terms of $B-$band absolute magnitude, stellar mass, $U-B$ color, SFR_{UV}, and sSFR_{UV}. We find a monotonic trend between C III] EW and M_B such that C III] EW increases at fainter values of M_B and is significantly stronger (3.82σ) in the faintest M_B bin.[2] A similar connection between C III] EW and luminosity has been observed in previous studies at $z \sim 2$ (Stark et al., 2014).

The scaling relation of C III] strength with stellar mass is shown in the upper right panel of Figure 3.4. Despite the C III] emission showing less dependence on stellar mass than on $B-$band absolute magnitude, the two bins with lower stellar masses display significantly larger (3.29σ) C III] EWs on average than the higher stellar mass bins. This trend could also be interpreted as a secondary correlation with the $B-$band absolute magnitude, if we assume a constant mass-to-light ratio for the galaxies in our sample.

As for $U-B$ color, although the correlation is not as evident as with the $B-$band absolute magnitude, the C III] EW is significantly higher (4.54σ) in the bluest bin. This finding agrees with the results from individual spectra, that significant C III] detections are found in bluer galaxies (Figure 4.6, bottom). The reddest bin does not show the smallest C III] EW, contrary to the expectation based on the trend discovered in individual C III] detections. However, the increase in C III] strength in the reddest bin with respect to the middle two bins is not significant, especially given the comparatively large error bar on the corresponding C III] EW measurement. It is worth noting that none of the objects going into this bin have a significant individual C III] detections except 22036975 (Figure 4.6).[3]

[2]The significance levels indicated in parentheses were determined by grouping data points into two sets according to C III] EW (relatively large or small), calculating their respective means and errors in C III] EW, and dividing the difference in their mean values by the square root of the sum in quadrature of the overall errors of the two sets of data.

[3]The C III] EW remains almost unchanged (rest-frame EW decreases by 0.06Å, which is less than half of the associated 1σ error bar) if 22036975 is removed from the reddest bin. We note that

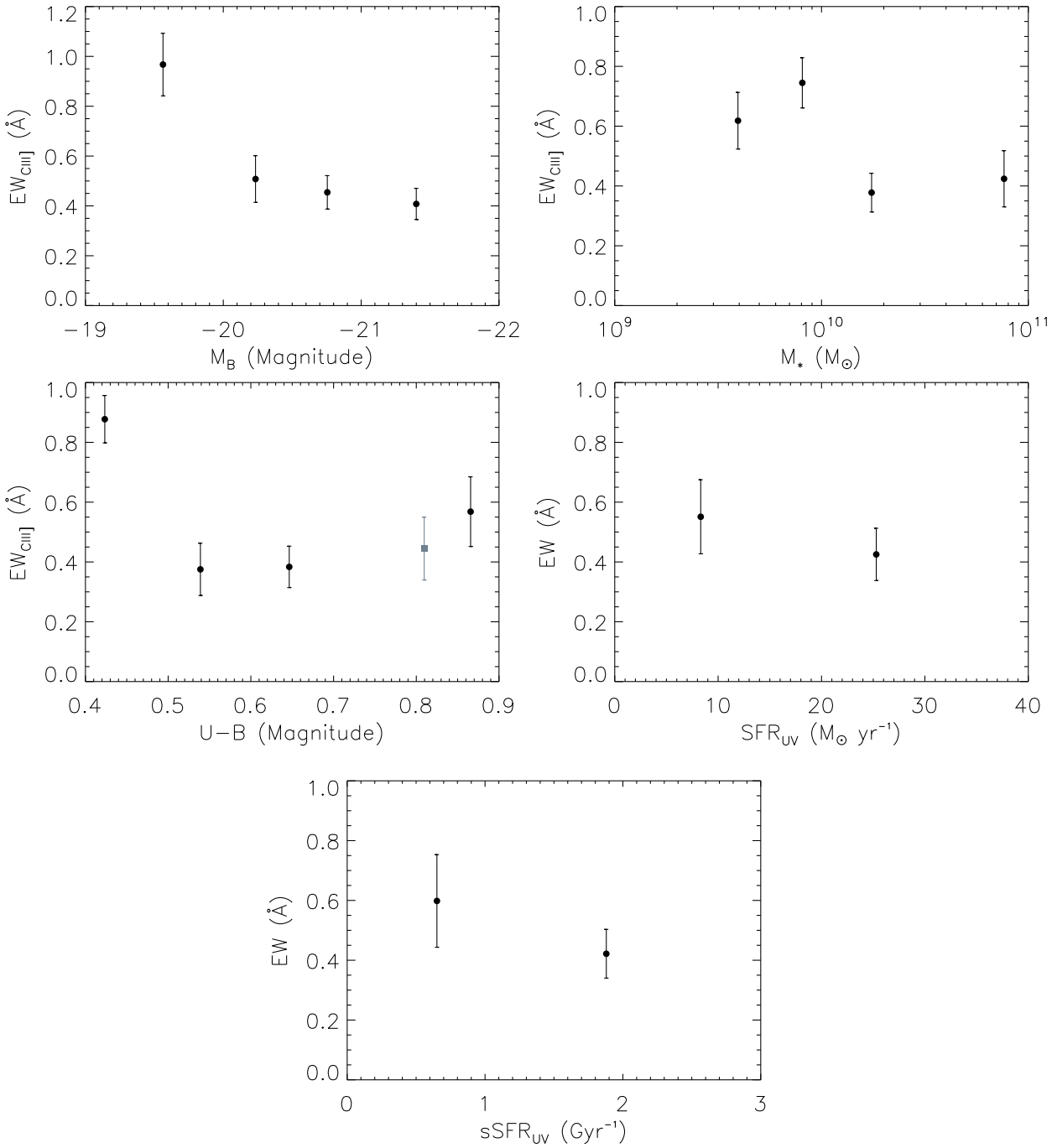

Figure 3.4: **Top to bottom, left to right:** C III] EW vs. $B-$band absolute magnitude, stellar mass, $U-B$ color, SFR_{UV}, and sSFR_{UV} in the composite spectra. The gray square in the middle left panel represents the C III] EW measurement from the reddest $U-B$ composite spectrum made out of a more controlled sample, where 32 objects with [Ne V] coverage and insignificant ($\leqslant 3\sigma$) [Ne V] detections are included.

Furthermore, the spectra used to create the reddest $U-B$ composite were in general noisier than those in the bluer bins, especially for spectra in which C III] fell on the blue side. Therefore, it is the relatively poor data quality in the far-UV that is responsible for the large uncertainty associated with the reddest $U-B$ composite.

One possible origin of the enhanced C III] emission observed in the reddest $U-B$ bin is potential AGN contribution. [Ne V]λ3425, a high-ionization transition in the near-UV, is one of the common signatures of AGN activity. While the LRIS spectra have [Ne V] coverage for many objects in our sample, there are cases where this feature falls in the gap between the blue and red spectral coverage and is therefore not available. As a result, we utilized the DEEP2 spectra observed with the Deep Imaging Multi-Object Spectrograph (DEIMOS; Faber et al., 2003) on the Keck II telescope as a complementary dataset for objects without [Ne V] coverage in the LRIS spectra. The DEEP2/DEIMOS spectra have a high spectral resolution (maximum $R \sim 6000$) and spectral coverage of $\sim 6500-9300$Å, which corresponds to the near-UV and blue optical band at the DEEP2 redshift ($z \sim 1$) and thus enables us to inspect multiple rest-optical emission features. Out of 46 objects in the reddest $U-B$ bin, 32 have [Ne V]λ3425 coverage (3 in the LRIS spectra and 29 in the DEIMOS spectra) and none of them shows a $\geqslant 3\sigma$ [Ne V] line detection. Restricting the stack to these 32 objects with both [Ne V] coverage and no significant [Ne V] detection reduces the possibility of any AGN contribution to the C III] emission. The strength of C III] emission measured from this more controlled composite spectrum is shown as the gray square in the bottom panel of Figure 3.4. In this stack, the C III] EW is smaller than in the original composite with all objects included, and similar to the C III] EW measured in the two middle $U-B$ bins. Accordingly, we conclude that there is no strong evidence for an increase in C III] at the reddest U-B colors.

In order to evaluate the extent to which AGN contamination affects our sample in general, we examined the DEIMOS and LRIS spectra for 164 objects with [Ne V] coverage. None of these objects shows a $\geqslant 3\sigma$ [Ne V] line detection. We then constructed corresponding

this result is a natural outcome of our approach of performing median stackings.

composite spectra by dividing these 164 objects into 4 bins according to M_B, M_*, and $U-B$, with each bin containing 41 objects. The rest-frame EWs of C III] measured from these more restricted stacks remain almost unchanged with respect to those measured from the original composite spectra, except that the C III] emission becomes weaker in the "cleaned" reddest $U-B$ bin. In fact, the C III] EW in the "cleaned" reddest $U-B$ bin is very similar to that in the stack made out of a set of 32 objects with [Ne V] coverage and insignificant [Ne V] line detections from the original reddest $U-B$ bin. Therefore, we believe that AGN contamination is a negligible effect for the majority of objects in our sample.

In summary, we observe consistent trends of C III] EW increasing with fainter values of $B-$band absolute magnitude, bluer $U-B$ color and smaller stellar mass in both individual and composite spectra. These results imply that strong C III] emitters are more likely to be faint, blue and low-mass galaxies.

3.4.3 C III] vs. near-UV lines

Our LRIS spectra typically cover a set of several near- and far-UV emission features, in addition to C III]$\lambda\lambda$1907, 1909. These include C IV$\lambda\lambda$1548, 1550, He IIλ1640, O III]$\lambda\lambda$1661, 1666 and Si III]$\lambda\lambda$1882, 1892, the near-UV Fe II*λ2365, 2396, 2612, 2626 fluorescent transitions, and the Mg II $\lambda\lambda$2796, 2803 emission doublets. Although we only observe weak C IV$\lambda\lambda$1548, 1550, He IIλ1640, O III]$\lambda\lambda$1661, 1666 in the overall composite spectrum, strong near-UV Fe II* and Mg II transitions are well-detected in the stacked spectra described in Section 3.4.2 and numerous individual spectra.

It has been illustrated that galaxies with strong Fe II* and Mg II emission typically have higher sSFRs, lower stellar masses and bluer UV slopes (Erb et al., 2012; Kornei et al., 2013). In light of the fact that C III] emission displays similar correlations with stellar mass and color, it is possible that the strength of C III] is related to that of the Fe II* and Mg II emission. In order to investigate the relationship between C III] and the near-UV transitions and potentially study the possible underlying physical connection between the gas components these lines trace, we measured both the C III] and the near-UV Fe II* and

Mg II lines in the stacked spectra. For this analysis, we used the M_B, $U-B$, SFR_{UV}, and $sSFR_{UV}$ stacks described in Section 3.4.2, where the M_B and $U-B$ stacks were based on the full sample of objects with C III] coverage, and the SFR_{UV} and $sSFR_{UV}$ stacks only included 42 objects with SFR_{UV} measurements .

To obtain a characteristic Fe II* line strength, we fit Fe II*λ2365, 2396, 2612 and 2626 individually with single Gaussian profiles using MPFIT and combined the EWs of those 4 lines. The case for Mg II is more complicated. It is difficult to obtain a robust estimate of the separate contribution of Mg II emission, as the Mg II emission and absorption components are significantly blended. The presence of emission is indirectly inferred from the apparent Mg II absorption profile, which has a more blueshifted centroid (due to the filling in from Mg II emission on the red side), and a greater variation in strength than the near-UV Fe II absorption lines (Martin et al., 2012; Kornei et al., 2013). Therefore, we used the variation of the Mg II$\lambda\lambda$2796, 2803 absorption doublet as a proxy for the associated Mg II emission, and examined the correlation between apparent Mg II absorption EW and C III] emission. Figure 3.5 shows the correlations between the strength of C III] and that of Fe II* emission (top) and Mg II absorption (bottom).

We find that the Fe II* strength does not change significantly (2.89σ) with C III] EW, while C III] emission is noticeably stronger (16.6σ) in the two composite spectra with the weakest Mg II absorption. Furthermore, the decline in the absorption strength is much more pronounced in Mg II than in the near-UV Fe II in those two composites. As the Fe II absorption profiles are less affected by resonance emission filling (Erb et al., 2012), they can be used as a proxy for the intrinsic, unaffected profiles of Mg II absorption. Given the greater EW decrease in Mg II absorption than Fe II absorption (i.e., where the Fe II variation indicates the change in underlying absorption), we interpret the observed trend between C III] and Mg II as a joint effect of Mg II absorption becoming weaker and Mg II emission becoming stronger with increasing C III] emission EW (Martin et al., 2012; Kornei et al., 2013). The distinct behavior between Mg II and Fe II* is likely a result of the difference in the underlying source function. Although both Mg II and Fe II* photons are scattered by circumgalactic gas (Rubin et al., 2011; Martin et al., 2013), the source function for Mg II includes an emission

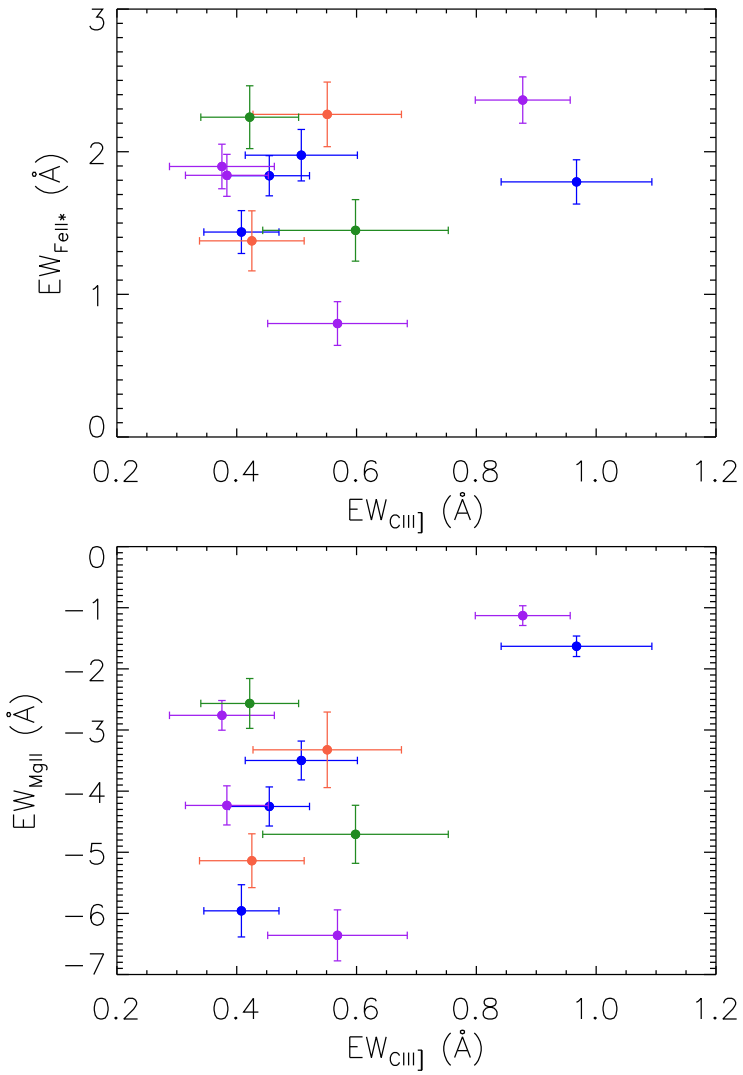

Figure 3.5: **Top:** C III] EW vs. near-UV Fe II* EW in the composite spectra described in Section 3.4.2. The combined EW of Fe II*λ2365, 2396, 2612, 2626 is shown. Blue, purple, red and green circles correspond to measurements from stacked spectra of M_B, $U-B$ color, SFR_{UV} and $sSFR_{UV}$, respectively. **Bottom:** C III] EW vs. Mg II $\lambda\lambda$2796, 2803 absorption EW in the composite spectra.

line (i.e., nebular emission from the H II regions), which becomes stronger in lower-mass galaxies. The source function for Fe II*, however, is a flat continuum (Erb et al., 2012), which is absorbed and re-emitted in the possibly outflowing circumgalactic gas (Erb et al., 2012; Kornei et al., 2013), resulting in Fe II absorption and Fe II* emission transitions, respectively.

3.4.4 C III] vs. Metallicities

Photoionization models and observations at different redshifts have revealed that low gas metallicity leads to enhanced nebular C III] emission due to the hard ionizing SED of the associated metal-poor stars exciting the gas, and the elevated electron temperature resulting from reduced metal cooling (e.g., Erb et al., 2010; Stark et al., 2014; Rigby et al., 2015; Jaskot & Ravindranath, 2016, see Section 3.5.2.2 for a detailed discussion). In order to examine if the correspondence between C III] emission and metallicity found in high-redshift studies also holds for $z \sim 1$, we estimated metallicities using optical emission features.

Ideally, we would like to use the combination of [O II]λ3727, [O III]λ5007 and Hβ to obtain estimates of both metallicity and ionization parameter (e.g., $R_{23} \equiv ([\text{O II}] + [\text{O III}])/\text{H}\beta$ and $O_{32} \equiv [\text{O III}]/[\text{O II}]$). Since [O III] and H$\beta$ are not typically covered in the LRIS spectra, we inspected the DEIMOS spectra for 26 objects in the DEEP2/LRIS sample with redshift lower than ~ 0.9, where these optical diagnostic features fall within the DEIMOS spectral coverage. However, the lack of robust flux calibration and nebular dust extinction estimate for the DEIMOS spectra led us to focus instead on the simple combination of [O III] and Hβ, which are relatively close in wavelength. The measured [O III]/Hβ flux ratio should not be significantly affected by dust extinction, and, due to the proximity of the lines, this flux ratio can be estimated even if the spectrum does not have a precise flux calibration.

[O III]/Hβ shows a dependence on the gas metallicity, $12 + \log(\text{O/H})$, such that at very low metallicities [O III]/Hβ increases with increasing $12 + \log(\text{O/H})$, as a result of increasing oxygen abundance. [O III]/Hβ reaches a maximum value at $12 + \log(\text{O/H}) \sim 8.0$, and then declines with increasing metallicity due to lower electron temperature and lower ionization

state (Maiolino et al., 2008; Jones et al., 2015). Given the form of this relationship, the translation between [O III]/Hβ is double valued over a wide range in [O III]/Hβ. However, it is possible to use external information to determine on which branch of the [O III]/Hβ vs. metallicity relation a given galaxy falls. For example, given the mass-metallicity relationship (MZR) observed among star-forming galaxies over a wide range of redshifts (Tremonti et al., 2004; Erb et al., 2006a; Maiolino et al., 2008), and the stellar mass range of the 26 objects in our sample with $z < 0.9$ ($\log(M_*/M_\odot) = 8.88 - 11.21$), we infer that these objects fall within the high stellar-mass, high-metallicity branch, despite the uncertainties associated with the MZR (0.1 dex, Tremonti et al., 2004) and the [O III]/Hβ vs. metallicity relation (~ 0.1 dex, Maiolino et al., 2008). In this regime, [O III]/Hβ monotonically decreases with increasing metallicity.

We fit the [O III] and Hβ emission profiles with single Gaussians using MPFIT, the same procedure as described in Section 4.3. As we do not detect individual C III] emission in any of these 26 objects, we performed binary stacks according to the [O III]/Hβ ratio, with the low and high bins containing nearly equal numbers of objects. Although the C III] feature in both stacked spectra is not significant, we find that Mg II absorption becomes weaker (or equivalently, Mg II emission becomes stronger) with higher [O III]/Hβ. Based on the correlation in strength between C III] and Mg II emission (Section 3.4.3), this result suggests indirectly that stronger C III] may be found within lower-metallicity galaxies in our sample. Our inferred correlation between C III] and metallicity is not only consistent with both models and observations of C III] at other redshifts (Stark et al., 2014; Rigby et al., 2015; Jaskot & Ravindranath, 2016), but is also supported by the result that C III] emission is significantly stronger in the lower-mass half of our sample, given the well-measured correlation between metallicity and stellar mass (e.g., Tremonti et al., 2004; Zahid et al., 2013).

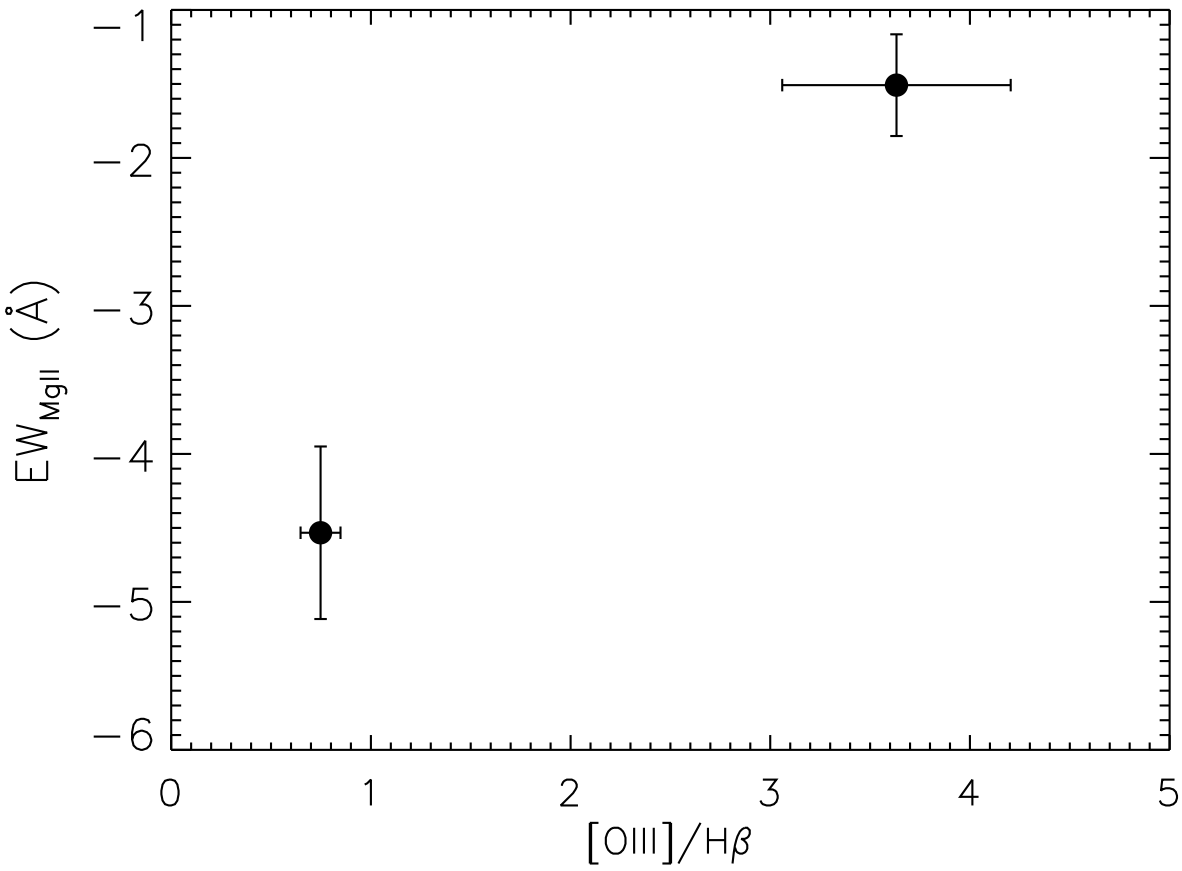

Figure 3.6: EW of Mg II $\lambda\lambda$2796, 2803 absorption doublet vs. [O III]/Hβ in the composite spectra. There are 26 objects at $z < 0.9$ in the DEEP2/LRIS sample with [O III] and Hβ coverage in their DEIMOS spectra. These objects were used to generate the composite spectra.

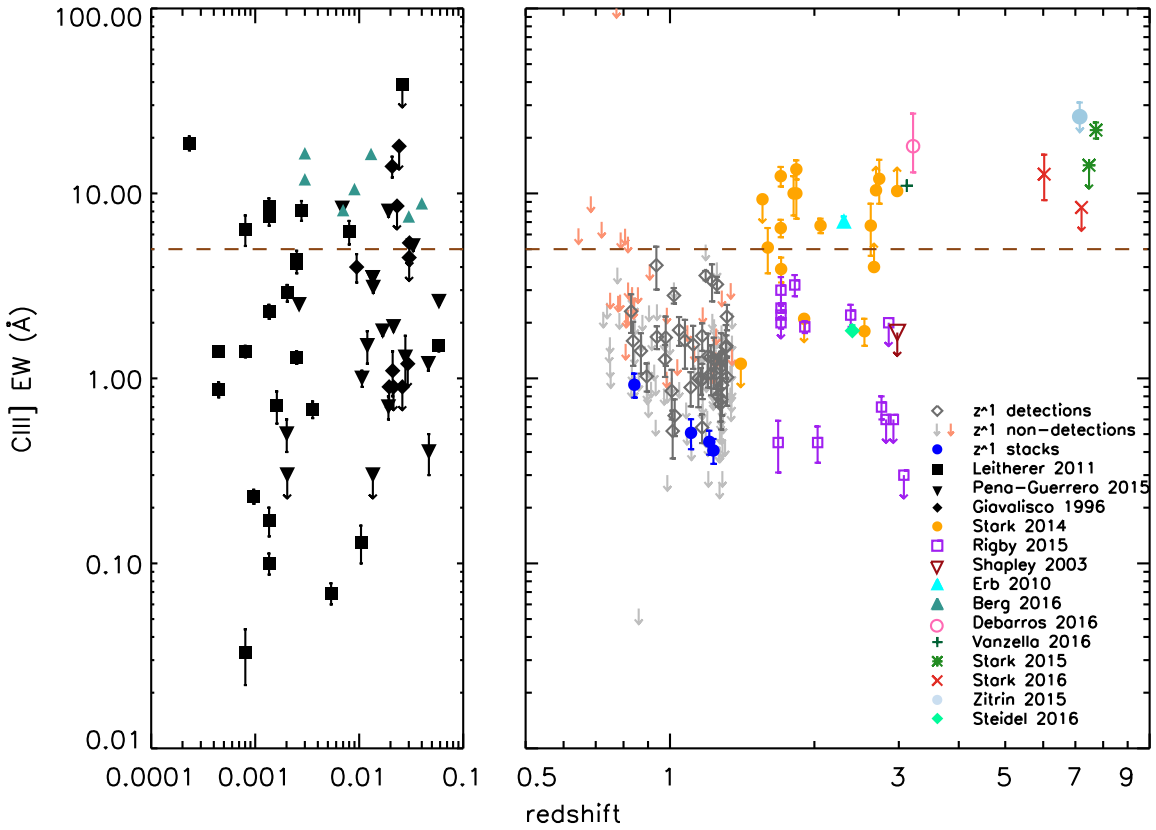

Figure 3.7: C III] EW at different redshifts, with measurements drawn from the literature. The error bars represent 1σ uncertainties for significant detections, while the downward-pointing arrows indicate 3σ upper limits for EW measurements that are not significant. Measurements from the individual C III] detections and composite spectra in 4 M_B bins from the DEEP2/LRIS sample are shown, respectively, in gray open diamonds and dark blue circles. The gray and pink arrows indicate the $z \sim 1$ non-detections with continuum $S/N > 5$ and $S/N < 5$, respectively. The local samples include measurements from Giavalisco et al. (1996, black diamonds), Leitherer et al. (2011, black circles), Pena-Guerrero et al. (in prep.) (black triangles) and Berg et al. (2016, dark cyan triangles). The high-redshift samples include measurements from Stark et al. (2014, orange circles), Rigby et al. (2015, purple squares), Steidel et al. (2016, light green diamond), Shapley et al. (2003, dark red triangle), Erb et al. (2010, cyan triangle), Vanzella et al. (2016, green plus sign), de Barros et al. (2016, pink circle), Stark et al. (2017, red crosses), Stark et al. (2015, green stars), and Zitrin et al. (2015, light blue circles). The brown dashed line marks where EW= 5Å.

3.5 Discussion

3.5.1 C III] EW at other redshifts

As a promising alternative redshift diagnostic, C III] has been investigated in various types of galaxies in multiple high-redshift ($2 \lesssim z \lesssim 7$) studies of UV emission lines. Large C III] EWs ($\geqslant 5$Å, as defined in Rigby et al. 2015) have been identified in galaxies at high redshift ($z \geqslant 2$) and in the local universe. Several studies have measured C III] EWs $\gtrsim 10$Å in galaxies formed prior to and during the epoch of reionization ($z > 6$). Stark et al. (2015) studied two star-forming galaxies at $z \simeq 6$ with Lyα detections, where the EWs of the C III] doublet were measured to be 12.7 ± 3.5 and 7.8 ± 2.8Å, respectively. In addition, Zitrin et al. (2015) presented a sample of 14 lensed galaxies at $z_{phot} \simeq 7 - 8$. Although these authors did not have individual convincing detections of C III] in their sample, an upper limit on the C III] doublet rest-frame EW was estimated to be 26 ± 5Å with 95% confidence. More recently, Stark et al. (2017) observed 3 galaxies at $z \sim 7$ with extreme rest-optical emission line ([O III]+Hβ) fluxes. These authors measured a C III] EW of 22 ± 2Å for EGS-zs8-1 and a 3σ upper limit of 14Å for EGS-zs8-2. We note that all three galaxies at $z > 6$ with significant C III] detections also have strong Lyα emission (rest-frame EW$> 20\AA$).

Besides observations at the high-redshift frontier, various studies have been conducted to examine the properties of galaxies at $z \sim 2.5$, near the peak of the SFR density in the universe ($z \sim 2.5$; Madau & Dickinson, 2014). Stark et al. (2014) examined 17 $z \sim 2$ low-mass, low-luminosity lensed galaxies, among which 16 have detections of C III]. The measured C III] EW has a mean of 7.1Å and a maximum of 13.5Å. C III] has also been detected in multiple individual galaxies at similar redshifts. These include a C III] EW measurement of 7.1 ± 0.4Å from a low-mass, low-metallicity, unreddened system, Q2343-BX418 at $z = 2.3$ (Erb et al., 2010); strong C III] emission (11Å) in a low-mass, compact, star-forming galaxy at $z = 3.12$ (Vanzella et al., 2016); and an 18^{+9}_{-5}Å C III] detection in a low-metallicity, Lyman continuum emitter at $z = 3.2$ (de Barros et al., 2016).

Observations of local galaxies have shown that strong C III] emission is not exclusive to the high-redshift universe. Rigby et al. (2015) presented a compilation of 46 C III] measurements

from nearby starburst galaxies, which were analyzed in Giavalisco et al. (1996), Leitherer et al. (2011), and Pena-Guerrero et al. (in prep.). The local samples show a large scatter in C III] EW, and 22% of them show strong (> 5Å) C III] emission. Most of these local strong C III] emitters are low-metallicity galaxies, with a typical oxygen abundance $12+\log(\mathrm{O/H}) \lesssim 8.0$. Moreover, Berg et al. (2016) recently reported 7 significant C III] detections from a sample of 12 nearby, low-metallicity ($12 + \log(\mathrm{O/H}) = 7.3 - 8.2$) dwarf galaxies with typical stellar masses $\log(\mathrm{M_*/M_\odot}) \sim 6-7$. These C III] measurements yield a larger EW on average compared to the other local samples, with a median of 10.6Å.

While galaxies with large (> 5Å) C III] EW have been identified at both low and high redshift, at least at $z \leqslant 3$, these systems are not common given the typical ranges in stellar mass and metallicity probed for "main sequence" (Noeske et al., 2007) galaxies. The strong C III] emitters tend to have low mass, luminosity (in some cases accessible due to the effects of strong gravitational lensing), and metallicity. In contrast to what is observed in these extreme systems, studies focusing on the general star-forming populations find a characteristic C III] EW of only $\sim 1 - 2$Å. Shapley et al. (2003) analyzed a composite spectrum created out of 811 individual Lyman Break Galaxy (LBG) spectra at $z \sim 3$, and reported a weak C III] emission feature of 1.67 ± 0.59Å (i.e., $\sim 2.8\sigma$). Rigby et al. (2015) measured C III] in 11 lensed star-forming galaxies at $z \sim 1.6 - 3$, finding the median EW in their sample to be 2.0Å. More recently, Steidel et al. (2016) observed a sample 30 star-forming galaxies at $z \sim 2.4$, and the estimated C III] EW from the composite spectrum was 1.81 ± 0.13Å (C. Steidel, private communication). [4]

In Figure 3.7 we compare our $z \sim 1$ DEEP2/LRIS sample with studies discussed above in terms of C III] EW. As shown by the dividing line at $\mathrm{EW_{C\ III]}} = 5$Å, none of the individual or composite spectra in our sample displays the large EW (> 5Å) observed in the extreme

[4]In Steidel et al. (2016), these authors only presented the flux measurement of C III] from the composite spectrum. The quoted value of the rest-frame C III] EW resulted from our measurement from the continuum-normalized Steidel et al. (2016) composite, following the method described in Section 4.3. Due to the lack of the corresponding composite error spectrum, we estimated the continuum noise from a relatively featureless range ($2000 - 2200$Å) and assigned that value as a constant error across the full spectrum. We note that in this manner, the uncertainty on the EW is underestimated, as the sample variance has not been accounted for.

systems (i.e., $z > 6$ galaxies, lensed $z \sim 2$ galaxies, some local starbursts). Specifically, the typical EW observed in our $z \sim 1$ DEEP2/LRIS sample with C III] detections is ~ 1Å, which is very similar to those measured in the global galaxy studies at $z \sim 2-3$ (e.g., Shapley et al., 2003; Steidel et al., 2016). This result suggests that typical star-forming galaxies at $z \sim 1-3$ (with stellar masses of $\log(M_*/M_\odot) \sim 9-11.5$) are quite distinct in rest-UV emission properties from the galaxies studied thus far at $z > 6$.

3.5.2 Physical Conditions at $z \sim 1$

As discussed in Section 3.5.1, we observe a small typical C III] EW (~ 1Å) at $z \sim 1$ and detect no strong C III] emitters (> 5Å) like those discovered at both higher and lower redshift. In order to gain a comprehensive understanding of the physical conditions in H II regions in star-forming galaxies at $z \sim 1$, we present estimates of the gas-phase metallicity and C/O abundance for a small subset of objects in our sample, and compare our results with the predictions from photoionization models.

3.5.2.1 Gas Metallicity and C/O Ratio

In Section 3.4.4, we have used [O III]λ5007/Hβ as an indicator of gas metallicity for a subset of 26 galaxies in our $z \sim 1$ sample. The median [O III]/Hβ measured in the 26 DEIMOS spectra is 2.50, which corresponds to a gas metallicity of $12+\log(O/H) \sim 8.4$ (i.e., $\sim 0.5 Z_\odot$; Maiolino et al., 2008; Jones et al., 2015). Our metallicity measurement is $\sim$0.5 dex lower at $10^{10} M_\odot$ (close to the median stellar mass of our sample) than that in Zahid et al. (2013) estimated from $z \sim 0.8$ DEEP2 galaxies. For this comparison, we use the same metallicity indicator ([O III]/Hβ), and calibration (Maiolino et al., 2008) for both samples. This discrepancy in metallicity primarily comes from sample selection. Galaxies in our DEEP2/LRIS sample are predominantly "blue cloud" star-forming galaxies and are bluer in $U-B$ color on average than the full DEEP2 sample (Martin et al., 2012). Based on the assumption that $U-B$ color tracks sSFR, and that the fundamental metallicity relationship (e.g., Mannucci et al., 2010) holds at $z \sim 1$, the O/H ([O III]/Hβ) in our sample should be systematically lower

(higher) than in the full DEEP2 sample from Zahid et al. (2013). We also note that given the small number of objects (26 galaxies) with [O III]/Hβ measurements, the quoted median [O III]/Hβ value may not be representative of the full DEEP2/LRIS sample.

The C/O ratio has been found to correlate with oxygen abundance, which is due to either the weaker stellar winds in metal-poor stars, or the delay in carbon enrichment in the ISM from low-mass stars (e.g., Henry et al., 2000; Akerman et al., 2004; Erb et al., 2010). Carbon is on average more abundant in high-metallicity environments (e.g., Erb et al., 2010; Berg et al., 2016). However, the softer radiation field and lower electron temperature (due to enhanced metal cooling) associated with higher oxygen abundance result in reduced C III] strength, with the net effect being weaker C III] emission at higher C/O ratio.

Given the spectral coverage of the LRIS spectra, we were able to additionally constrain the C/O ratio, which can be measured from the observed flux ratio of [O III]$\lambda\lambda$1661, 1666 and C III]λ1909. We created a composite spectrum out of 128 objects with both [O III] and C III] coverage in the LRIS data. In order to scale these spectra to the same flux level, we took the median flux value of individual 1-D, flux-calibrated spectra over the wavelength range of $2110 - 2200$Å as the characteristic value for corresponding objects. We then scaled the spectra accordingly to the median of those 128 "characteristic values." The 600-line spectra were smoothed to the resolution of the 400-line spectra, and the median value at each pixel was extracted to generate the composite spectrum. Due to noise and the intrinsic weak nature of the [O III]λ1661 transition, we did not have a robust detection of that feature. Instead, we adopted the doublet ratio (i.e., $I_{[O\ III]\lambda1666}/I_{[O\ III]\lambda1661}$) of 2.48 for the doublet members, and inferred the strength of [O III]λ1661 from the stronger doublet member, [O III]λ1666. We then fit [O III]λ1666 and C III]λ1909 separately with local continuum using MPFIT.

The best-fit parameters yield a C III]/[O III] flux ratio of 2.58±0.57, which corresponds to a C^{++}/O^{++} abundance ratio of 0.13±0.03 following Equation 3 in Erb et al. (2010), assuming a typical temperature of 10^4 K for H II regions in our sample galaxies, and neglecting the effect of dust extinction. We approximated this value as the C/O abundance ratio with the assumption of a unity ionization correction factor (ICF), which results in $\log(C/O) = -0.89^{+0.09}_{-0.11}$ (i.e., $\sim 0.3(\mathrm{C/O})_{\odot}$). Compared with the C/O vs. metallicity relation observed in

local galaxies and H II regions (Garnett et al., 1995; Erb et al., 2010; Berg et al., 2016), the C/O ratio we measured is ~ 0.4 dex lower at a metallicity of $12+\log(\mathrm{O/H}) \sim 8.4$ ($\sim 0.5\mathrm{Z}_{\odot}$). This low C/O value could possibly result from the assumption of ICF$=1$, which implies that C^{++} and O^{++} characterize the overall carbon and oxygen abundances. However, if the ICF in our $z \sim 1$ galaxies is larger than unity due to, for example, larger ionization parameters ($\log \mathrm{U} \geqslant -2$; Erb et al., 2010; Gutkin et al., 2016), the inferred C/O ratio would increase and become consistent with other local measurements. Furthermore, we note that the formal error bar on the C/O flux ratio estimated from MPFIT does not include the systematic uncertainty in the placement of the continuum level, which could potentially affect the flux measurement of weak features such as O III]$\lambda\lambda$1661, 1666.

3.5.2.2 Photoionization Models

The correlations between C III] strength and galaxy properties have been investigated not only from the observational side, but also from a theoretical perspective. Multiple studies have used photoionization models to examine the factors that regulate the emission profile of C III]. Stark et al. (2014) combined a stellar population synthesis model with a photoionization code to describe the ensemble of H II regions and the diffuse gas ionized by young stars. These authors concluded that metal-poor gas ($\lesssim 0.2-0.4\mathrm{Z}_{\odot}$) and stars, young stellar populations ($6-50$ Myr), subsolar C/O ratios and large ionization parameters were responsible for large C III] EWs. More recently, Jaskot & Ravindranath (2016) analyzed the C III] EW and various emission line ratios as a function of multiple properties (e.g., starburst age, metallicity and ionization parameter) in star-forming galaxies using Cloudy(Ferland et al., 1998) photoionization models. In these models, Jaskot & Ravindranath (2016) incorporated a range of C/O abundance, dust content, gas density, optical depth, and different nebular geometries. These authors find that low metallicities and high ionization parameters enhance C III] emission, and the highest C III] EWs are observed in models including binary interactions among the massive stars whose radiation ionizes the H II regions (e.g., Stanway et al., 2016). Furthermore, C III] emission peaks at young galaxy ages ($\lesssim 3$ Myr after an instantaneous burst or $\lesssim 10$ Myr of continuous star formation), lower dust content, and higher

nebular densities. Shell-like geometries and shocks are also claimed as possible secondary effects to boost C III] emission.

These simulations lead to a physical picture in which strong C III] emission is a consequence of various factors. Young, metal-poor stellar populations generate a hard radiation field, ionizing the interstellar medium and elevating the electron temperature in the H II regions (Stark et al., 2014). With large sSFRs, more ionizing photons are produced per unit mass, increasing the density of free electrons and giving rise to large EWs in collisionally excited emission lines (Stark et al., 2014). The presence of high-energy, ionizing photons also results in a high ionization state of carbon (i.e., being in the state of C^{++} instead of C^{+}). At the same time, the low gas metallicity prevents efficient metal cooling, further maintaining the electron temperature and securing a stable production of the nebular C III] emission (Rigby et al., 2015).

The absence of strong C III] emitters in our sample indicates that the conditions in the $z \sim 1$ star-forming galaxies are significantly different from what we just described. Jaskot & Ravindranath (2016) predicted a weaker C III] emission of only a few Å at high metallicities and older ages in all stellar population models they explored (Padova, Geneva and BPASS) with either instantaneous or continuous star-formation regardless of the ionization parameter ($\log \mathrm{U}$ from -1 to -4) and hydrogen density ($\log \mathrm{n}_H$ from 1 to 4). Specifically, the C III] EW declines to $\lesssim$ 1Å, the typical value we observe in our $z \sim 1$ sample, in several cases with continuous star formation[5]: all models with $\mathrm{Z} \geqslant 0.008$ ($0.57\ \mathrm{Z}_{\odot}$) at ages > 20 Myr with hydrogen density $\log \mathrm{n}_H \leqslant 3$, and models with lower metallicities ($\mathrm{Z} \leqslant 0.004$ or $0.29\ \mathrm{Z}_{\odot}$) at ages > 20 Myr with moderate to low ionization parameter and hydrogen density ($\log \mathrm{U} = -3$ - -4), $\log \mathrm{n}_H = 1 - 3$.[6] Combining the outputs of photoionization models and our estimates of metallicity and C/O ratio, we infer that the typical $z \sim 1$ star-forming galaxies in the

[5]We consider the continuous star-formation model as a better description of the star-forming history than the instantaneous burst model for majority of the galaxies in our sample. Therefore, although low C III] EW ($\lesssim$ 1Å) has also been predicted in a few instantaneous burst models, we do not include those results in our discussion here.

[6]The BPASS models, which take into account the binary interactions and rotation, produce higher C III] EW than the Padova and Geneva models with the same input parameters.

stellar mass range probed here have high gas-phase metallicities ($\gtrsim 0.5Z_{\odot}$), subsolar C/O ratios, and stellar population ages > 50 Myr.[7]

Spectra with high S/N and spectral resolution are required for the detection of weak far-UV emission lines (i.e., C III]$\lambda\lambda$1907, 1909, C IV$\lambda\lambda$1548, 1550, [O III]$\lambda\lambda$1661, 1666). Such data will enable robust measurements of multiple physical parameters, such as ionization parameter and C/O abundance for individual objects, and provide a comprehensive picture of the physical environment in typical star-forming galaxies at $z \sim 1$.

3.6 Summary

C III] has been proven to be a key emission feature in the far-UV, not only because it can potentially be used as an alternative redshift indicator to Lyα for galaxies at $z > 6$, but also because of the useful information it provides regarding the physical conditions of star-forming regions. In this paper, we have analyzed the far-UV C III]$\lambda\lambda$1907, 1909 emission doublet in the LRIS spectra of a sample of 184 $z \sim$1 star-forming galaxies with C III] coverage, and list our key results below:

1. We have found that only $\sim 20\%$ of the galaxies in the full sample (40 out of 184) have $> 3\sigma$ C III] detections, with a median EW of 1.3Å, which is significantly weaker than the typical values observed so far at $z > 6$.

2. We have further investigated the correlations between the C III] strength and galaxy properties. By studying both individual C III] detections and composite spectra binned according to B-band absolute magnitude, $U - B$ color, stellar mass, SFR and sSFR, we have discovered that larger C III] EW appears in fainter, bluer and lower-mass systems, in which the gas metallicity and dust extinction are likely to be lower as well.

3. We have also explored the connections between C III] and near-UV emission transitions, specifically Fe II* and Mg II, using composite spectra created according to galaxy properties. While we observed no significant dependence of C III] on Fe II* in terms of strength, C III]

[7]In fact, we estimated the typical ages of our sample galaxies to be several hundreds of Myr based on their stellar masses and specific SFRs (Martin et al., 2012).

EW increases with increasing inferred Mg II emission. The behavior of C III], Fe II*, and Mg II can be explained by different source functions for these features: there are net sources of nebular C III] and Mg II photons in H II regions, whereas Fe II* emission originates in circumgalactic, perhaps outflowing gas at larger radii, representing the redistribution of the stellar continuum (i.e., no underlying emission feature).

4. Finally, we examined the effect metallicity has on the strength of C III] by adopting [O III]/Hβ as a crude metallicity diagnostic. From the composite spectra created out of 26 $z < 0.9$ objects with [O III] and Hβ coverage in the DEEP2 DEIMOS spectra, we indirectly inferred stronger C III] emission at lower metallicity, based on the variation of Mg II absorption with [O III]/Hβ. This observational result is consistent with models showing that the harder ionizing spectrum and higher nebular gas temperature at lower oxygen abundance lead to enhanced C III] emission by producing more ionizing photons and suppressing metal cooling (Jaskot & Ravindranath, 2016).

5. We concluded that higher metallicity and older stellar population ages are probably the major causes of the lower typical C III] EW in our $z \sim 1$ sample, compared with C III] detections at $z > 6$.

Extreme C III] emitters at $z > 6$ (with an average C III] EW > 10Å) are important for our understanding of the physical conditions in galaxies at early times. However, due to the low S/N and the generally poor detection of metal lines, searching for such galaxies is exceptionally challenging. An alternative way to learn about these high-redshift C III] emitters is by using low-redshift analogs. With low-redshift observations, we can potentially obtain detailed information, with higher S/N, on the physical properties (e.g., metallicity, ionization parameter, dust extinction) from rest-UV and optical spectroscopy, and infer the stellar populations from SED fits using multi-wavelength photometry.

Despite the lensed sample from Stark et al. (2014), the abundance of galaxies with strong rest-UV emission is especially low at $z \sim 1 - 3$. Therefore, our main aim for future observations is to find the "missing" C III] emitters within this redshift range. We will prioritize objects for rest-UV spectroscopy that show blue color (see discussion in Section 3.4.2) and

large [O III] EW, as the strength of C III] has found to be positively correlated with that of [O III] (Stark et al., 2014; Berg et al., 2016; Jaskot & Ravindranath, 2016). In addition, full coverage of rest-optical features (e.g., [O II], [O III] and Hβ) is essential for confirming the correlation of C III] EW and metallicity at this redshift. By studying the analogs of high-redshift extreme C III] emitters, we will gain a better understanding of the physical conditions that give rise to this nebular feature and the nature of the sources that contribute to reionization within the first billion years of cosmic time.

CHAPTER 4

The redshift evolution of rest-UV spectroscopic properties in Lyman Break Galaxies at $z \sim 2 - 4$

4.1 Introduction

The rest-frame ultraviolet (UV) spectra of star-forming galaxies provide rich insights into the physical properties of not only their massive stars, but also their gas. This gas includes the multi-phase interstellar medium (ISM) and circumgalactic medium (CGM), which extends to the virial radius (Tumlinson et al., 2017). Both low- and high-ionization interstellar (LIS and HIS, respectively) absorption lines are probes of the ISM and CGM, which typically reflect the kinematic signatures of galaxy-wide outflows in star-forming galaxies at these redshifts (e.g., Shapley et al., 2003; Steidel et al., 2010; Jones et al., 2012). LIS features primarily trace the neutral phase of outflows while HIS lines mainly trace the ionized phase. Fine-structure emission lines (e.g., Si II*, Fe II*) arise from the emission of a photon corresponding to a drop down to the excited ground state following resonant absorption. These fine structure features are typically coupled with corresponding resonant LIS absorption, and are thus effective tracers of the structure and the spatial extent of the CGM (e.g., Erb et al., 2012; Jones et al., 2012; Kornei et al., 2013). The H I Lyα feature, on the other hand, has a more complex nature. Lyα photons are produced by recombination in H II regions, and then propagate through the ISM, interacting with both neutral hydrogen and dust grains. As such, Lyα photons potentially offer insights into the properties of both their HII regions of origin, and the more extended ISM and CGM through which they propagate. Nebular emission lines, such as C III]$\lambda\lambda$1907,1909 and [O III]$\lambda\lambda$1661, 1666, are produced in H II regions, and serve as useful probes of the ionized ISM and radiation field produced by

massive stellar populations (e.g., Erb et al., 2010; Berg et al., 2016; Stark et al., 2017; Du et al., 2017; Senchyna et al., 2017). When measured over a wide range of redshifts, the properties of rest-UV absorption and emission features provide a window into the evolution of ISM/CGM properties. Properties of particular interest include the evolving gas covering fraction, which modulates the emergent Lyα properties and escape of ionizing radiation; and the characteristics of galaxy outflows, which play a crucial role in the formation and evolution of galaxies.

As Lyα photons are produced in H II regions and scattered and absorbed in the dusty ISM, Lyα is a key probe of the physical conditions of interstellar gas (e.g., metallicity, ionization parameter, H I column density and covering fraction, and dust distribution) given its unique detectability especially at high redshift. Numerous studies have been carried out to understand the factors modulating the strength of Lyα emission at $z \sim 2-6$. Observationally, larger Lyα equivalent width (EW) is typically found in galaxies with bluer UV color, lower metalliticity, lower stellar mass, lower UV luminosity, and lower SFR (e.g., Shapley et al., 2003; Reddy et al., 2006; Kornei et al., 2010; Pentericci et al., 2010; Stark et al., 2010; Berry et al., 2012; Jones et al., 2012; Trainor et al., 2016; Erb et al., 2016; Hathi et al., 2016). Furthermore, understanding the mechanisms underlying the existence of strong Lyα emitters (LAEs; rest-frame Lyα EW > 20Å) is critical for our interpretation of the galaxy populations during the reionization epoch, where, thus far, the majority of data are only photometric.

The connections between Lyα and other spectral features, including LIS and HIS absorption lines and nebular emission lines, have been extensively studied in star-forming galaxies. Stronger Lyα appears to be associated with weaker LIS absorption lines (Shapley et al., 2003; Jones et al., 2012; Berry et al., 2012) and stronger nebular emission lines (Shapley et al., 2003; Stark et al., 2014, 2015; Rigby et al., 2015; Jaskot & Ravindranath, 2016; Erb et al., 2016; Trainor et al., 2016). In contrast, Lyα EW does not show significant correlation with the strength of HIS absorption lines (Shapley et al., 2003; Berry et al., 2012). The shape of the Lyα profile (e.g., peak location, number of peaks, asymmetry) can also be used as a probe of the kinematics and density distribution of outflowing neutral gas (e.g., Verhamme

et al., 2006; Steidel et al., 2010; Kulas et al., 2012).

While much of the work on Lyα emission and other rest-UV spectroscopic properties of star-forming galaxies at high redshift has been focused on characterizing samples at individual redshifts (e.g., Shapley et al., 2003; Pentericci et al., 2007, 2009; Kornei et al., 2010; Steidel et al., 2010), there have been limited studies on the evolution of these spectroscopic properties at $z \gtrsim 2$. LAEs are found to be more prevalent at higher redshifts up to $z \sim 6$ (Reddy et al., 2008; Stark et al., 2010; Schenker et al., 2014), and stronger Lyα and weaker LIS absorption are observed with increasing redshift at fixed UV luminosity (Stark et al., 2010; Jones et al., 2012). Specifically, by comparing a sample of $z \sim 4$ LBG spectra to the $z \sim 3$ LBG composites from Shapley et al. (2003), Jones et al. (2012) found no evidence for evolution of the correlation between Lyα and LIS absorption EWs. However, these authors discovered smaller characteristic radii of fine-structure emission and overall weaker LIS absorption at higher redshifts. While Jones et al. (2012) created a subsample of $z \sim 4$ galaxies to match the $z \sim 3$ galaxies in UV absolute magnitude for a fair comparison, the study was limited in that the SED-derived galaxy properties (e.g., stellar mass) were unavailable at that time for the majority of the galaxies in the $z \sim 3$ comparison sample from Shapley et al. (2003). Furthermore, the $z \sim 3$ spectroscopic measurements (e.g., Lyα and LIS absorption EWs) were taken from Shapley et al. (2003) and not necessarily performed in a manner consistent with that of Jones et al. (2012). When conducting evolutionary studies on the connection between rest-UV spectroscopic and galaxy properties, both the spectroscopic measurements and the modeling of galaxy photometry must be performed in a uniform, controlled fashion.

The redshift range $z \sim 2 - 4$ spans nearly 2 billion years of cosmic time and covers the peak epoch of star formation and beyond (Madau & Dickinson, 2014). The active star formation and mass assembly over this period must have been shaped by various processes (e.g., feedback, mergers, gas accretion), that will also be reflected in the physical characteristics of the ISM/CGM. Accordingly, it is of key interest to trace the evolving ISM/CGM with galaxy spectra.

Here we present the first comprehensive study of the evolution of the ISM and CGM

as probed by rest-UV spectra in star-forming galaxies at $z \sim 2-4$. In order to perform meaningful comparisons between galaxy samples at different redshifts, we carefully construct these samples with galaxies spanning the same range in UV absolute magnitude and stellar mass. Furthermore, we model the stellar populations and measure the spectral features in all redshift samples in a uniform manner to avoid potential systematic biases. By comparing the rest-UV spectroscopic properties in the controlled samples at different redshifts, we aim to investigate the evolution of covering fractions of gas and dust, structure and kinematics of the multi-phase ISM/CGM, and the intrinsic Lyα production, which, in combination, provide rich insights into galaxy evolution.

We provide a brief overview of the observations and data in Section 4.2, along with a description of galaxy SED modeling and the construction of controlled samples in UV luminosity and stellar mass. In Section 4.3, we describe methods for creating composite spectra, and measuring Lyα emission and interstellar absorption profiles. We present multiple $z \sim 2-4$ evolutionary trends in Section 4.4, including the connections among key spectroscopic features (Lyα, and LIS and HIS absorption features), between Lyα and galaxy stellar populations, and fine-structure emission properties. We also investigate the correlation between Lyα and C III] emission. In Section 4.5, we examine the evolution of outflow kinematics as probed by both Lyα and LIS absorption features over the same redshift range. In Section 4.6, we connect our results to the evolution of outflow kinematics over $z \sim 0-2$, and present a physical picture for the evolving distribution of Lyα emission and interstellar absorption measurements at $z \sim 2-4$. Finally, we summarize our results in Section 4.7. In Appendix 4.A.2, we consider the rest-UV spectroscopic properties of galaxies with mid-IR SED excesses, another topic of interest that can be explored with our data.

Throughout this paper, we adopt a standard ΛCDM cosmology with $\Omega_m = 0.3$, $\Omega_\Lambda = 0.7$ and H_0 =70 km s^{-1}. All wavelengths are measured in the vacuum frame. Magnitudes are on the AB system.

4.2 Observations, Data Reduction and Samples

In this section, we describe the $z \sim 2-4$ LBG data used in this study, along with the derivation of stellar population parameters from spectral energy distributions (SEDs), and the sample properties. We refer readers to the original papers in which these data were presented for a more in-depth discussion of sample selection, data reduction, and photometric measurements of the samples presented here.

4.2.1 Samples

4.2.1.1 LRIS Sample

The $z \sim 2-3$ sample was drawn from the UV-selected galaxy surveys described in Steidel et al. (2003, 2004) and Reddy et al. (2008). These galaxies were preselected photometrically according to the U_nGR color cuts to an apparent magnitude limit of $R_{AB} = 25.5$, and spanned 15 fields covering a total area of ~ 1900 arcmin^2. The candidates were then followed up spectroscopically with the Low Resolution Imager and Spectrometer (LRIS; Oke et al., 1995; Steidel et al., 2004) on the Keck I telescope. We note that galaxies selected in this manner at $z \sim 2$ are not technically LBGs, as their actual Lyman break falls bluewards of the U_n band. However, as described in Steidel et al. (2004), the $z \sim 2$ U_nGR-selected galaxies have very similar properties to those of the $z \sim 3$ LBGs. Therefore, we also refer to the $z \sim 2$ U_nGR-selected galaxies as LBGs hereafter for simplicity.

The data were collected during multiple observing runs from 1997 to 2009 using 1."2 slits for the multislit masks. The majority of the objects in the LRIS sample were observed with the 400-line mm^{-1} ($\sim 57\%$) and 600-line mm^{-1} ($\sim 33\%$) grisms. A small fraction of the data was obtained using the 300-line mm^{-1} grism ($\sim 3\%$), and the 300-line mm^{-1} grating ($\sim 4\%$), the latter taken before the LRIS-B upgrade in 2000 (Steidel et al., 2004). Twenty-one spectra ($\sim 2\%$) were combined from multiple observations with a mixture of the 400- and 600-line mm^{-1} grisms. The effective spectral resolutions of the 400-, 600-, 300-line mm^{-1} grisms, and the 300-line mm^{-1} grating are $R \sim 800$, 1330, 530, and 670, respectively. The typical

integration time for each slit mask is 1.5 hours, and is significantly longer ($5-8$ hours) for a small subset of the slitmasks observed as part of specialized investigations (e.g., searches for Lyman continuum radiation Reddy et al., 2016, Steidel in prep.). All two-dimensional spectra were flat fielded, cleaned of cosmic rays, background subtracted, extracted, wavelength and flux calibrated.

Ideally, the systemic redshift can be robustly measured from strong rest-frame optical nebular emission lines (e.g., [O II]λ3727, H$\beta\lambda$4861, [O III]$\lambda\lambda$4959, 5007, and H$\alpha\lambda$6563). However, nebular lines were not measured for the vast majority of the $z \sim 2-3$ objects in our sample, so the systemic redshift of these objects was estimated instead based on the redshift of Lyα emission and/or low-ionization interstellar (LIS) absorption lines. Due to the presence of outflowing neutral gas in the galaxies, Lyα emission and the LIS absorption features are typically observed to be redshifted and blueshifted, respectively, relative to each other, and therefore do not trace the galaxy systemic velocity. Instead, the systemic redshift was determined following the procedure described in Rudie et al. (2012) assuming that Lyα is redshifted by $+300$ km s^{-1}from the systemic velocity, and the LIS absorption lines are blueshifted by -160 km s^{-1}. The Lyα velocity correction was applied to all spectra with measurable Lyα, and the LIS correction was applied to those with LIS redshift measurements only. In this manner, we obtained the systemic redshift for all the $z \sim 2-3$ LBGs observed with LRIS, and the typical uncertainty on the systemic redshift is ~ 125 km s^{-1}. The systemic redshift, as estimated above, was used to transform each spectrum to the rest frame.

The resulting LRIS sample includes 1297 LBGs spanning the redshift range $1.7 \lesssim z \lesssim 3.65$. These galaxies have secure redshift measurements, spectral coverage of Lyα, and detections in the K- band and/or IRAC channel 1 or 2, enabling reliable stellar population modeling.

4.2.1.2 DEIMOS/FORS2 Sample

To probe $z \sim 4$ LBGs, we primarily use the spectra presented in Jones et al. (2012). This sample includes 70 objects (81 spectra accounting for duplicate observations) with $3.5 < z < 4.5$ and apparent magnitude of $z'_{AB} < 26.0$. These galaxies were selected as B-band dropouts in the two GOODS fields (Giavalisco et al., 2004) and have a spectroscopic completeness of $\sim 100\%$ at $z'_{AB} < 24.75$ (Stark et al. in prep.). Detailed descriptions of sample selection and photometric measurements can be found in Stark et al. (2009, 2010) and Jones et al. (2012). In the $z \sim 4$ sample, 42 out of 70 objects (53 out of 81 spectra) were observed with the Deep Imaging Multi-Object Spectrograph (DEIMOS; Faber et al., 2003) on the Keck II telescope. The DEIMOS spectra have a constant resolution of $\simeq 3.5$Å across the spectral range of $4100 - 9300$Å. The typical integration time for the DEIMOS spectra is $5 - 7$ hours per mask. The other 28 objects (28 spectra) were obtained from the archival spectroscopic database of the FOcal Reducer and low dispersion Spectrograph 2 (FORS2; Vanzella et al., 2005, 2006, 2008, 2009). The FORS2 data have a spectral resolution of $R \sim 660$ over $6000 - 10000$Å, corresponding to ~ 9.0 Å near the observed wavelength of Lyα. The FORS2 spectra typically have $4 - 6$ hr integrations for each mask. Similar to the $z \sim 2 - 3$ LRIS data, standard data reduction procedures (flat fielding, cosmic ray rejection, background subtraction, extraction, wavelength and flux calibration, and transformation to the vacuum wavelength frame) were performed on the DEIMOS and FORS2 data to obtain calibrated one-dimensional spectra.

The systemic redshift of the $z \sim 4$ galaxies was also estimated based on Lyα emission and LIS absorption features, using a procedure analogous to the one described in Section 4.2.1.1. To correct Lyα and LIS absorption redshifts to the systemic value, Jones et al. (2012) assumed a velocity offset of $+330$ km s^{-1}for Lyα and -190 km s^{-1}for the LIS features. The systemic redshift of individual galaxies was determined from the Lyα redshift when available, given its robustness compared to that of the LIS features, and from the LIS absorption redshift when the Lyα redshift was not measurable.

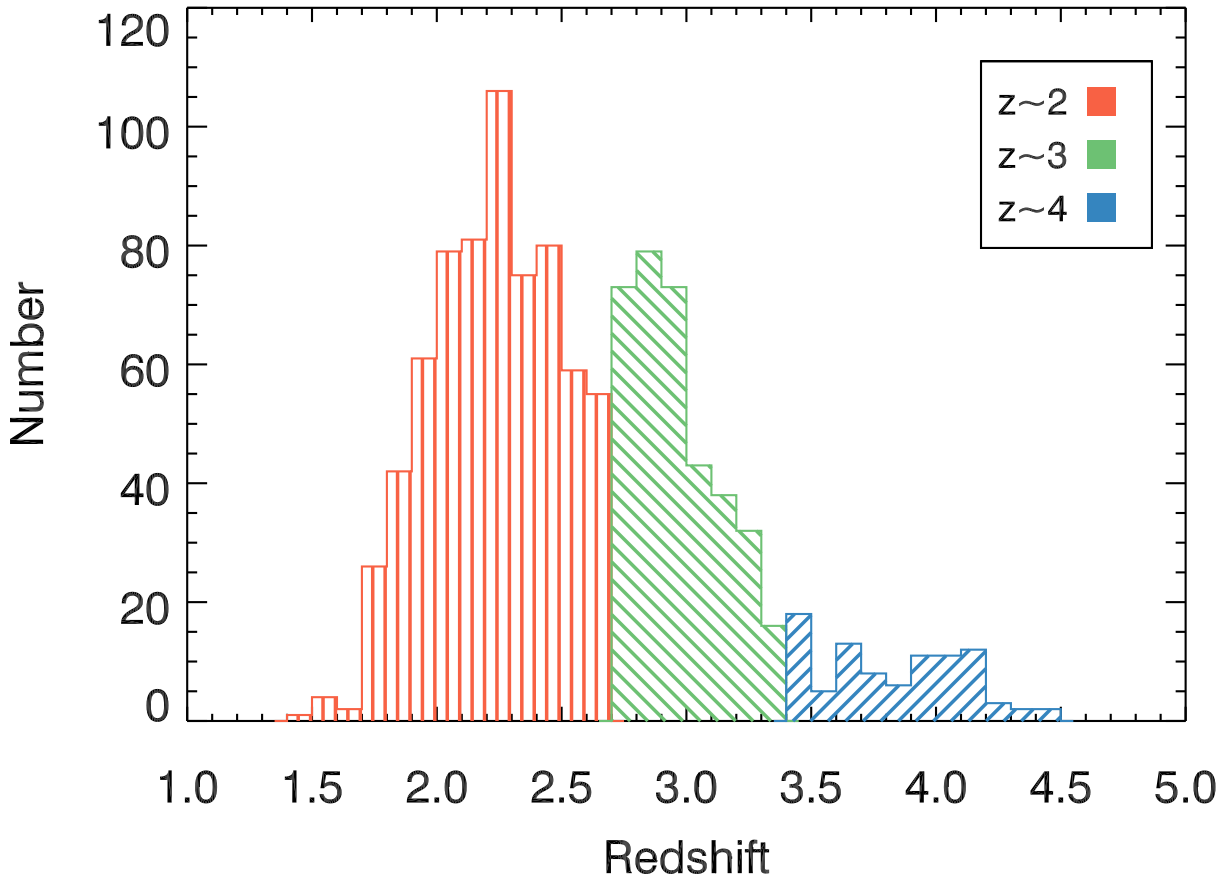

Figure 4.1: Redshift distribution of our sample, divided according to boundaries at $z = 2.7$ and $z = 3.4$. The $z \sim 2$ sample (671 objects) is indicated in red, the $z \sim 3$ sample (352 objects) in green, and the $z \sim 4$ sample (80 objects, 91 spectra) in blue. UV absolute magnitude and mass cut offs have not been applied here.

4.2.1.3 Redshift Samples

We applied fixed redshift cuts to the LRIS, DEIMOS, and FORS2 datasets to define the $z \sim 2, 3$, and 4 samples. We considered galaxies with $z < 2.7$ to be in the $z \sim 2$ sample, galaxies with $2.7 \leqslant z < 3.4$ to be in the $z \sim 3$ sample, and those with $z \geqslant 3.4$ to be in the $z \sim 4$ sample. The application of the redshift cuts results in 671, 352, and 80 objects (91 spectra) in the $z \sim 2$, $z \sim 3$, and $z \sim 4$ samples, respectively. Figure 4.1 shows the redshift histograms of the $z \sim 2, 3$ and 4 samples defined by fixed redshift cuts, with median redshifts of 2.25, 2.93, and 3.86, respectively. In practice, the $z \sim 2$ and $z \sim 3$ samples are all probed with LRIS data, while the $z \sim 4$ sample is mainly covered by DEIMOS and FORS2 spectra, with a small addition of objects observed with LRIS.

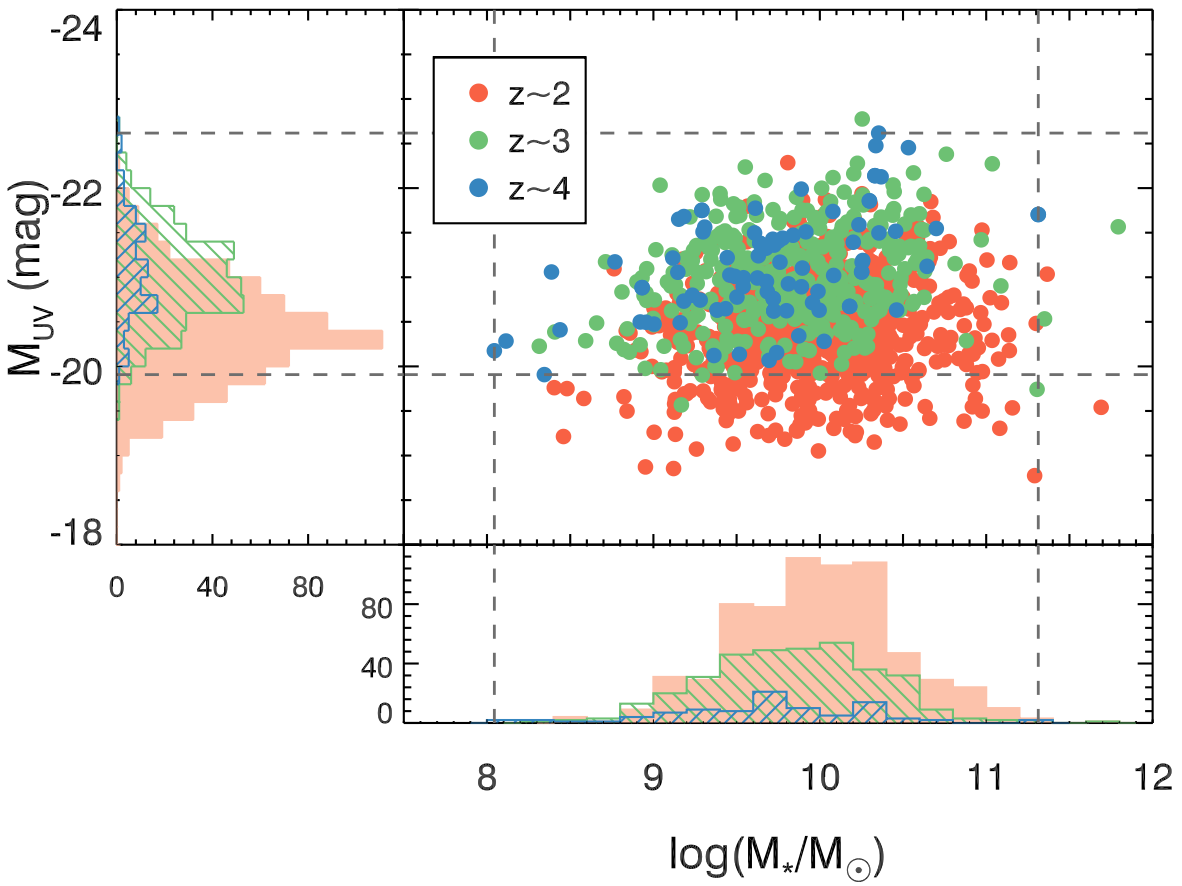

Figure 4.2: UV absolute magnitude vs. stellar mass for the $z \sim 2$ (red), $z \sim 3$ (green), and $z \sim 4$ (blue) samples. Histograms in M_* and M_{UV} are indicated, respectively, along the x- and y-axes. The vertical and horizontal gray dashed lines indicate the cuts in stellar mass and UV absolute magnitude, respectively, imposed onto the $z \sim 2$ and $z \sim 3$ samples, determined by the dynamic range of these properties in the $z \sim 4$ sample.

4.2.2 SED Fitting

In order to make fair comparisons among LBGs at different redshifts, one important aspect of our study is the measurement of the spectral and galaxy properties in a systematic, uniform manner. In this subsection, we describe the SED fitting procedure adopted for fitting all the galaxies in our samples from $z \sim 2 - 4$.

We collected the most up-to-date photometry for all objects in the redshift samples, and the photometric bands available for SED modeling are listed in Table 4.1. For objects observed in the GOODS fields (145 objects in the $z \sim 2$ sample, 59 objects in the $z \sim 3$ sample, and 69 objects in the $z \sim 4$ sample), we acquired the publicly available photometric

Table 4.1: Photometric Bands Used in SED Modeling

Fields	Photometric bands
GOODS-N[1]	U, $F435W$, B, G, V, $F606W$, R, R_s, i, $F775W$, z, $F850LP$, $F125W$, $F140W$, J, H, $F160W$, Ks, $IRAC1$, $IRAC2$, $IRAC3$, $IRAC4$
GOODS-S[1]	U_{38}, U, $F435W$, B, V, $F606W_{candels}$, $F606W$, R, Rc, $F775W$, i, $F814W_{candels}$, $F850LP$, $F850LP_{candels}$, $F125W$, J, J_{tenis}, $F140W$, H, $F160W$, K_{tenis}, Ks, $IRAC1$, $IRAC2$, $IRAC3$, $IRAC4$
Q0100, Q0142, Q0449, Q1009, Q1217, Q1549, Q2343	U_n[2], G[2], R_s[2], $J1$[3], $J2$[3], $J3$[3], J[4], $F140W$, H_s[3], H[3], $F160W$, H_l[3], K[4], $IRAC1$, $IRAC2$, $IRAC3$, $IRAC4$
Q0933, Q1307, Q1422, Q1623, Q1700, Q2206, Q2346	U_n[2], G[2], R_s[2], i[5], J[6], H[7], K[6], $F160W$, $IRAC1$, $IRAC2$, $IRAC3$, $IRAC4$

* While some objects in our samples miss photometric data from a subset of the bands listed here, we ensured that every object in our final, controlled samples has detections in the K- band and/or one of the IRAC channels.

[1] Photometric bands as described in the 3D-HST catalog (Skelton et al., 2014; Brammer et al., 2012).

[2] Observed with LRIS.

[3] Observed with the Four Star IR camera on the Magellan Baade Telescope.

[4] Observed with Multi-Object Spectrometer For Infra-Red Exploration (MOSFIRE) at the Keck I telescope.

[5] Observed with the Kitt Peak 4m Mayall telescope.

[6] Observed with the Palomar 5.08m telescope.

[7] Observed with the Wide-field InfraRed Camera (WIRCam) at the Palomar 200-in Hale telescope.

catalog from the 3D-HST survey (Skelton et al., 2014) and matched the objects in our samples with the targets observed in the GOODS-N and GOODS-S fields. The objects were matched according to their RA, Dec, and redshift. We excluded objects from the samples if there was no unique, unambiguous match in the 3D-HST $F606W$ science image. In this way, we removed 7 objects from the $z \sim 2$ sample, 1 object from the $z \sim 3$ sample, and 3 objects from the $z \sim 4$ sample because we were unable to identify them in the 3D-HST photometric catalog. For galaxies in the $z \sim 2-3$ samples in fields other than GOODS-N and GOODS-S, we utilized the updated photometric measurements from Steidel et al. (2003, 2004, private communication), Reddy et al. (2012), and Strom et al. (2017).

Based on the photometric measurements of the objects in our samples, we aimed to derive key galaxy properties (e.g., stellar mass, dust extinction, age, and SFR) by fitting the SEDs of individual galaxies. In order to ensure the robustness of the stellar population modeling, we required at least one photometric measurement redward of the Balmer break. 12 objects in the $z \sim 2$ sample and 28 objects in the $z \sim 3$ sample were removed due to a lack of near- and mid-IR photometry.

We fit the galaxy SEDs with stellar population templates from Bruzual & Charlot (2003b) assuming a Chabrier (2003) initial mass function (IMF). We note that Bruzual & Charlot (2003b) models do not account for emission lines or nebular continuum emission. Strong emission lines (e.g., Hα, [O III]$\lambda\lambda 4959, 5007$) could bias the shape of the SED redward of the Balmer break, resulting in an older best-fit galaxy age than the value derived from the stellar continuum alone. In the case of our $z \sim 2-4$ galaxies, [O III] and Hα fall in the H and K bands, respectively, for the $z \sim 2$ sample, [O III] falls in the K band for the $z \sim 3$ sample, and Hα falls within IRAC channel 1 for galaxies with $z \geqslant 3.8$ (38 out of 70 objects) in the $z \sim 4$ sample. As discussed in Section 4.4.2, the contamination from [O III] has a significant impact on the age estimate for the $z \sim 3$ galaxies, but nebular emission does not appear to significantly bias results from the $z \sim 2$ and $z \sim 4$ samples (bottom panel of Figure 4.6). Hence, we excluded K-band photometry from the SED fits for the $z \sim 3$ sample [1], but did

[1]Excluding K-band photometry resulted in another 41 objects being removed from the $z \sim 3$ sample, as K-band was the reddest photometric bands available for those objects.

not reject any photometric data in the H and K bands (IRAC channel 1) for the $z \sim 2$ ($z \sim 4$) sample.

Following Reddy et al. (2018), we adopted two combinations of metallicity and extinction curves for the SED modeling. These include 1.4 solar metallicity ($Z_{\odot} = 0.014$) with the Calzetti et al. (2000) attenuation curve (hereafter "1.4 $Z_{\odot}$+Calzetti"), and 0.28 $Z_{\odot}$ with the SMC extinction curve (hereafter "0.28 $Z_{\odot}$+SMC"). The grid of each model includes different star-formation histories (exponentially declining, constant and rising), age ranging from 10 Myr to 5 Gyr, and $E(B-V)$ ranging from $E(B-V) = 0.00$ to 0.60.

Although our SED-fitting grid enables numerous combinations of stellar parameters, we applied several constraints on the best-fit stellar population model based on our current knowledge of the galaxies in our samples. For all the redshift samples, we considered the constant SFR model as a satisfactory description of the star-formation history for the typical star-forming galaxies at $z \sim 2-4$ (Reddy et al., 2012; Steidel et al., 2014; Strom et al., 2017). Furthermore, we required the age of the $z \sim 2$ and $z \sim 3$ galaxies to be no younger than 50 Myr based on the typical dynamical timescales of these galaxies (Reddy et al., 2012). With these constraints, we calculated a set of best-fit stellar parameters for individual galaxies in our samples for both the 1.4 $Z_{\odot}$+Calzetti and the 0.28 $Z_{\odot}$+SMC models. While the former model has been traditionally used to describe the SEDs of the L^* galaxies at $z \gtrsim 2$, recent work suggests that sub-solar metallicity models with an SMC curve provide a better description of the IRX-β relation for these objects (e.g., Reddy et al., 2018), especially at higher redshifts ($z \gtrsim 4$; Oesch et al., 2013; Bouwens et al., 2016). Therefore, we adopted the best-fit stellar parameters of the 0.28 $Z_{\odot}$+SMC model as the final best-fit parameters for the $z \sim 4$ galaxies, given that these objects are in general younger and likely less enriched on average, compared with the samples at lower redshift. For the $z \sim 2$ and $z \sim 3$ objects, we found that the 1.4 $Z_{\odot}$+Calzetti model gave a systemically better fit to the observed SEDs than the 0.28 $Z_{\odot}$+SMC model above a given stellar mass threshold, which is consistent with the presence of the mass-metallicity relation (Sanders et al., 2015; Steidel et al., 2014; Onodera et al., 2016). As a result, we adopted the best-fit stellar parameters yielded by the 1.4 $Z_{\odot}$+Calzetti model above $\log(\mathrm{M}_{*,0.28Z_{\odot}+SMC}/\mathrm{M}_{\odot}) = 10.45$ (10.65) for the $z \sim 2$ ($z \sim 3$)

sample, and used those from the 0.28 $Z_{\odot}$+SMC model for galaxies below the corresponding stellar mass thresholds.

4.2.2.1 Controlled Samples

In order to conduct a well-controlled comparison, we need to ensure that we are comparing galaxies at different redshifts with similar galaxy properties. Two key properties that can be used to constrain the galaxy populations are luminosity and stellar mass. To determine the UV absolute magnitude for individual objects in our samples, we selected the corresponding photometric bands that cover the rest-frame wavelength $\lambda_{rest} = 1500$Å. $\lambda_{rest} = 1500$Å falls in the U-, G-, V- bands and $F435W$ for the $z \sim 2$ sample depending on the exact galaxy redshift, in the R_s band for the $z \sim 3$ sample, and in $F775W$ for the $z \sim 4$ sample. The observed magnitude in the corresponding band was then converted into UV absolute magnitude by accounting for the monochromatic luminosity distance (since AB magnitudes correspond to flux density). The UV absolute magnitude estimated from photometry agrees well with that calculated from the best-fit galaxy SED at $\lambda_{rest} = 1500$Å, and using SED-based M_{UV} instead of M_{UV} estimated from the photometry has negligible effect on the sample selection as well as the Lyα trends discussed in Section 4.4.2.

The $z \sim 4$ sample spans a narrower range in UV absolute magnitude and stellar mass than the $z \sim 2$ and $z \sim 3$ samples. Therefore, we selected a subsample of galaxies from each of the $z \sim 2$ and $z \sim 3$ samples that span the same range in UV absolute magnitude ($-22.62 < M_{UV} < -19.91$) and stellar mass ($8.04 < \log(M_*/M_{\odot}) < 11.31$) as the full $z \sim 4$ sample. In Figure 4.2, we plot the M_{UV} vs. M_* diagram for the $z \sim 2$, 3, and 4 samples defined according to the fixed redshift boundaries (the same sets of objects as in Figure 4.1), along with the cuts in UV absolute magnitude and stellar mass we applied to construct the final, controlled samples. In the following sections, we present results based on the analyses of the controlled samples restricted in UV absolute magnitude and stellar mass. The resulting sample sizes for the $z \sim 2, 3$, and 4 samples after being matched in UV absolute magnitude and stellar mass are 539, 309, and 91, respectively.

Table 4.2: Median Galaxy Properties in Controlled $z \sim 2-4$ Samples

Sample	Redshift	M_{UV} (Magnitude)	$\log(M_*/M_\odot)$	$E(B-V)$	Age (Myr)	SFR ($M_\odot yr^{-1}$)	Sample Size
$z \sim 2$	2.267	-20.51	10.00	0.09	806	13	539
$z \sim 3$	2.925	-21.00	9.87	0.08	404	16	309
$z \sim 4$	3.856	-21.06	9.72	0.04	321	13	91

We list the median galaxy properties of the controlled $z \sim 2-4$ samples in Table 4.2. Although the final redshift samples are constrained within a range in UV luminosity and stellar mass, the median values of these properties and other stellar parameters differ slightly among the samples. The $z \sim 2$ sample median is ~ 0.5 magnitude fainter than in the $z \sim 3$ and $z \sim 4$ samples, and the median stellar masses agree to within a factor of two, with $z \sim 2$ ($z \sim 4$) having the highest (lowest) mass. We note that objects falling onto the faint tail of UV luminosity in the $z \sim 2$ sample will not affect the evolutionary trends we explore here. Specifically, we have verified that the results presented in Sections 4.4 and 4.5 do not change significantly if the $z \sim 2$ sample is further restricted to have a similar median UV luminosity and stellar mass to those of the $z \sim 3$ and $z \sim 4$ samples (i.e., by removing the high-mass, faint wedge in the $z \sim 2$ sample that doesn't overlap with the $z \sim 3$ and $z \sim 4$ samples in Figure 4.2). As shown in the top right panel of Figure 4.6, the strength of Lyα barely changes with M_{UV}, indicating that having a slightly larger portion of fainter objects will not affect the collective neutral ISM/CGM properties noticeably at $z \sim 2$. Similarly, given that Lyα EW has little variation with stellar mass on the higher-mass end (middle left panel of Figure 4.6), we do not consider the $z \sim 2$ sample having a relatively larger median stellar mass as a potential bias against the results presented in Sections 4.4 and 4.5. As for other galaxy properties, the lower redshift samples on average have a higher level of dust extinction and older age. The median SFRs of the samples are comparable, with that of the $z \sim 3$ sample being slightly higher than the SFRs of $z \sim 2$ and $z \sim 4$ samples.

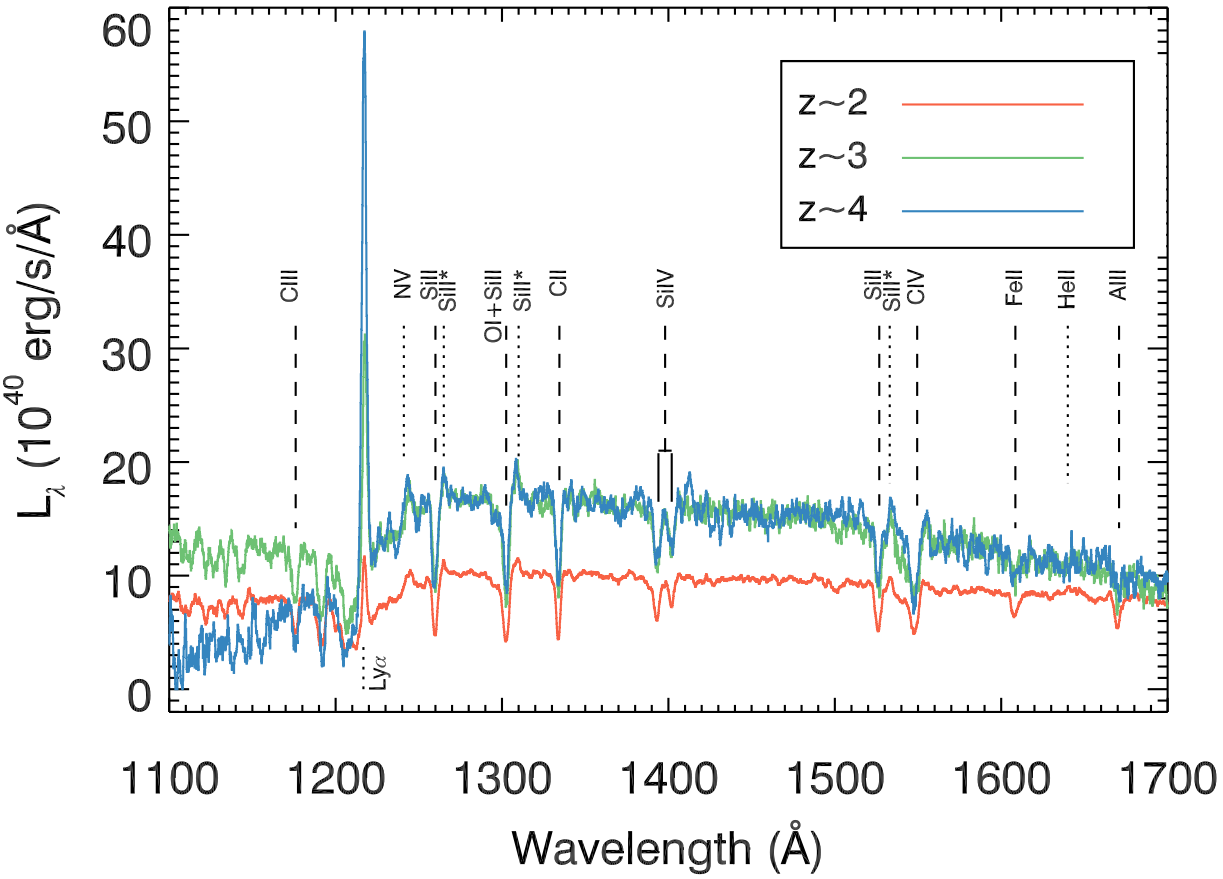

Figure 4.3: Composite UV spectra of the LBGs in the $z \sim 2$ (red), $z \sim 3$ (green), and $z \sim 4$ (blue) samples with UV luminosity and stellar mass constrained. Emission (dotted lines) and absorption (dashed lines) lines analyzed in this study are identified. At the resolution of the LRIS spectra ($z \sim 2$ and 3 objects) and FORS2 spectra ($z \sim 4$ objects), O Iλ1302 and Si IIλ1304 are blended, as is the C IV$\lambda\lambda$1548, 1550 doublet.

4.3 Measurements

The rest-UV spectral range covered by the $z \sim 2-3$ LRIS spectra and the $z \sim 4$ DEIMOS and FORS2 spectra includes multiple interstellar absorption lines and fine-structure emission features in addition to Lyα. These include the low-ionization absorption lines Si IIλ1260, O Iλ1302+Si IIλ1304, C IIλ1334, and Si IIλ1527, the high-ionization features Si IV$\lambda\lambda$1393, 1402, and C IV$\lambda\lambda$1548, 1550, and the Si II*λ1265,1309,1533 fine-structure emission lines. While Lyα and the strong absorption features are detected individually in many but not all cases, composite spectra enable us to study the universal correlations between the spectral and galaxy properties by utilizing all objects in the samples. Moreover, composite spectra provide significantly higher continuum S/N than individual detections, which potentially allows the measurement of weak emission and absorption lines that are not typically detected on an individual basis. In light of these advantages, we investigate the correlations among spectral and galaxy properties by studying the spectral features in the composite spectra at different redshifts. In this section, we describe our methods of creating composite spectra, and measuring the rest-frame EW of both the Lyα feature and interstellar absorption lines.

4.3.1 Composite Spectra

To examine how Lyα correlates with other spectral lines and galaxy properties, we divided each redshift sample into 4 bins in Lyα EW, UV luminosity, stellar mass, $E(B-V)$, age, and SFR, with each bin containing nearly the same number of galaxies. Given the fact that galaxies in the same bin have different rest-frame spectral coverage, resulting from the difference in their redshifts and observed-frame coverage, we further required that, in every composite spectrum, the same set of objects contribute to all the wavelengths. For the measurements of Lyα, Si IIλ1260, Si II*λ1265, O Iλ1302+Si IIλ1304, and C IIλ1334 in the composite spectra, we required individual contributing objects to have spectral coverage from Lyα to at least 1340Å. Similarly, we set the minimum reddest wavelength of individual contributing spectra to be 1410Å for measuring Si IV$\lambda\lambda$1393, 1402, and 1560Å for measuring Si IIλ1527, Si II*λ1533 and C IV$\lambda\lambda$1448, 1550 from the composites. In general, the extra

requirement on spectral coverage has an insignificant impact on the sample size for the measurement near Lyα (up to C IIλ1334; 0%, 6%, and 8% reduction for the $z \sim 2$, 3, and 4 samples, respectively). Objects included in the composites made for the measurement of Si IV are of 99%, 60%, and 96% of the full $z \sim 2$, 3, and 4 samples, respectively, and 97%, 53%, and 81% for the spectral line measurements near C IV.

We constructed the composite spectra according to the following steps. First, we converted the individual spectra from F_ν space to L_λ space, in order to capture the contribution of their *intrinsic* luminosity to the overall composite. The 600-line spectra were smoothed to the resolution of the 400-line spectra for the $z \sim 2$ and $z \sim 3$ samples,[2] and the DEIMOS and LRIS spectra were smoothed to match the resolution of the FORS2 spectra in the $z \sim 4$ sample. Next, all the individual spectra were interpolated onto a grid with 0.15Å increments in wavelength, and scaled to have the same median value over the wavelength range $1270 - 1290$Å, which itself represents the median of the median values estimated over $1270 - 1290$Å of all individual contributing spectra. After the scaling, the median of all input spectra was estimated at each wavelength increment to create a composite spectrum. Figure 4.3 shows the overall composite spectra of the $z \sim 2$, 3, and 4 samples created from the luminosity- and stellar mass-constrained galaxies, with strong emission and absorption features marked. We describe our method of estimating individual and composite error spectra in Appendix 4.A.1.

We note that adopting a different stacking method (e.g., sigma-clipped mean) has a negligible effect ($\lesssim 5\%$ difference) on the EW and centroid measurements of the interstellar absorption and fine-structure and nebular emission features, as the measurements were performed on the continuum-normalized spectra. As for the Lyα measurements, median stacking yields a systemically lower rest-frame Lyα EW, and a more redshifted Lyα centroid. However, given that our main results about Lyα are presented in a relative sense among the redshift samples, and that the spectra were analyzed in a consistent manner,

[2]Given the negligible fraction of the 300-line spectra we have in our samples, and the similarity of the spectral resolution of the 400- and the 300-line spectra, we did not further smooth the spectra down to the resolution of the 300-line spectra.

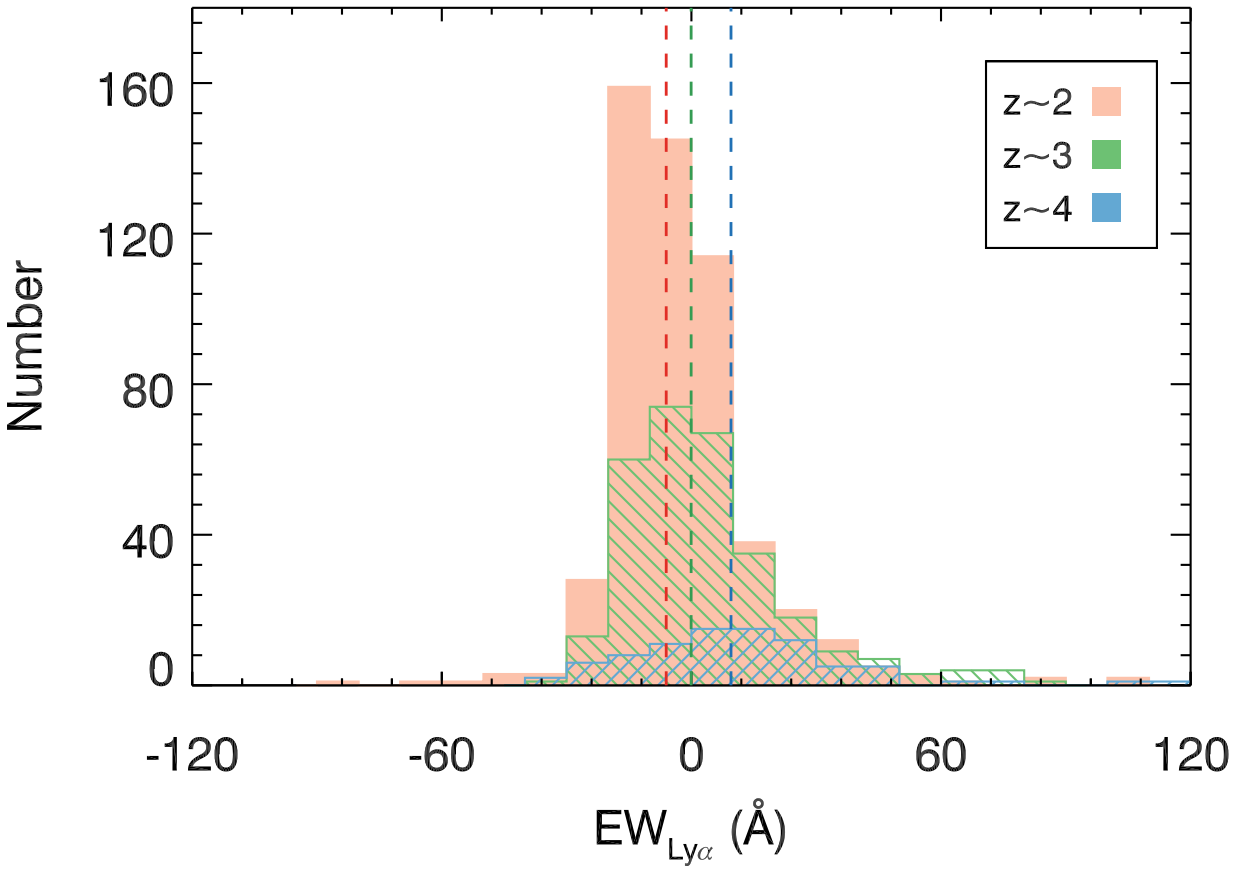

Figure 4.4: Lyα rest-frame EW distribution for the $z \sim 2$ (red), $z \sim 3$ (green), and $z \sim 4$ (blue) samples constrained in UV luminosity and stellar mass. The color dashed lines mark the median Lyα EW in corresponding samples: -6.07Å, -0.08Å, and 9.51Å at $z \sim 2$, $z \sim 3$, and $z \sim 4$, respectively.

they are robust regardless of the manner in which the composite spectra are produced.

Although the establishment of systemic redshift was not verified for individual galaxy spectra in our samples, the rest-frame composite spectra at all three redshifts indicate a close alignment with the systemic velocity. The centroid velocities of C IIIλ1176, a stellar absorption feature that typically indicates the galaxy systemic velocity (i.e., $v = 0$), are measured to be -22 ± 20 km s^{-1}, -24 ± 27 km s^{-1}, and 18 ± 123 km s^{-1}, respectively, at $z \sim 2$, $z \sim 3$, and $z \sim 4$ in the overall composites controlled in UV luminosity and stellar mass (Figure 4.3).

4.3.2 Lyα Measurement

To measure the Lyα rest-frame EW in both the individual and composite spectra (the former being a property for binning), we adopted the procedure described in Kornei et al. (2010). In brief, the morphology of Lyα in individual galaxy spectra is classified into 4 categories through visual inspection: "emission," "absorption," "combination," and "noise." The blue and red side continuum levels were measured over the wavelength range of $1225-1255$Å and $1120-1180$Å, respectively. The integrated Lyα flux was calculated between the blue and red wavelength "boundaries," λ_{blue} and λ_{red}, which are defined as where the flux density level first meets the blue and red side continuum, respectively, on either side of the Lyα feature. However, without additional constraints imposed on λ_{blue}, the measured Lyα EWs appear to have a bi-modal distribution, with an apparent deficit near $\mathrm{EW}_{Ly\alpha} \simeq 0$. A solution to this issue is fixing λ_{blue} at 1208Å for the "emission" objects, and requiring λ_{blue} to be no bluer than 1208Å for the "combination" objects. The Lyα rest-frame EW was then estimated by dividing the enclosed Lyα flux by the red side continuum level.

While the method described above worked well for measuring the Lyα EW in individual galaxy spectra at $z \sim 2$ and $z \sim 3$, it failed to handle the $z \sim 4$ spectra due to the limited spectral coverage blueward of Lyα. Five out of 91 spectra do not have Lyα coverage, and an additional 19 spectra do not have a full spectral coverage of $1120-1180$Å, the default window used to determine the blue side continuum in Kornei et al. (2010). Out of these 19 spectra, 16 have their bluest wavelength greater than 1160Å, such that the spectral region available for estimating the blue-side continuum level is less than 20Å, and therefore insufficient for obtaining a robust value. In order to estimate the Lyα EW for these objects, we measured the relative level of the blue and red side continua from objects with sufficient spectral coverage on both sides within the $z \sim 4$ sample. The median blue-to-red continuum ratio is 0.434, the value we adopted to obtain a rough estimate of the blue side continuum for the objects without sufficient blue-side spectral coverage. The same method as described above was then applied to calculate the Lyα EW for these 16 objects. Figure 4.4 shows the rest-frame EW distribution of Lyα in the controlled redshift samples. While spanning

the same range in UV absolute magnitude and stellar mass, objects at higher redshift in general have a higher Lyα EW than the lower-redshift counterparts. The median Lyα EWs in the three redshift samples are consistent with the Lyα EWs measured from the overall composites (Figure 4.3), which are -4.27 ± 0.09Å, -0.12 ± 0.12Å, and 8.02 ± 1.15Å for the $z \sim 2$, $z \sim 3$, and $z \sim 4$ samples, respectively.

The Lyα EW of composite spectra was measured in the same manner as in the individual spectra at $z \sim 2-3$, except that the composite spectra have much higher S/N and accordingly never fall in the "noise" category. In order to obtain the uncertainty associated with the Lyα measurement in the composites, we perturbed in the composite science spectra 100 times with the corresponding composite error spectra. The Lyα profiles in the 100 fake composite spectra were measured, and we adopted the average and standard deviation of the measurements as the composite Lyα EW and the 1σ error bar, respectively.

4.3.3 Absorption Line Measurement

Many interstellar absorption lines are covered within the $z \sim 2-4$ rest-frame UV spectra described here. These include the low-ionization features of Si IIλ1260, O Iλ1302+Si IIλ1304, C IIλ1334, and Si IIλ1527. As for the high-ionization lines, Si IV$\lambda\lambda$1393, 1402 and C IV$\lambda\lambda$1548, 1550 are covered in a majority of the spectra. Interstellar absorption lines were only measured in composite spectra, which have a fairly low spectral resolution. Hence, we adopted single-component Gaussian fits as the simplest possible functional form to describe the interstellar absorption lines in the composites. The key best-fit parameters from such fits are the line centroid and EW.

We continuum normalized the rest-frame composite spectra using spectral regions ('windows') that are clean of spectral features defined by Rix et al. (2004). Based on these windows, we modeled the continuum for all composite spectra with the IRAF *continuum* routine, using a *spline*3 function of order = 16 in order to provide a reasonable fit near Lyα, where the continuum is fairly curved. In cases where the fitted continuum level did not provide a proper description of the observed spectrum due to the limited coverage of

windows from Rix et al. (2004), additional windows customized for each object were added to provide reasonable constraints on the fit.

The absorption line profile fitting was performed on the continuum-normalized composite spectra. In general, we used the IDL program MPFIT (Markwardt, 2009) with the initial values of continuum flux level, line centroid, EW and Gaussian FWHM estimated from the program *splot* in IRAF. The best-fit was then determined where the χ^2 of the fit reached a minimum. We iterated the fitting over a narrower wavelength range for all the interstellar absorption lines: centroid$-4\sigma < \lambda <$centroid$+4\sigma$, where the centroid and σ are, respectively, the returned central wavelength and standard deviation of the best-fit Gaussian profile from the initial MPFIT fit to respective lines over $\lambda_{rest} - 10$Å to $\lambda_{rest} - 10$Å.

Some extra care was required for the high-ionization lines, Si IV$\lambda\lambda$1393, 1402 and the blended C IV$\lambda\lambda$1548, 1550 feature. As Si IV is a spectrally resolved doublet, each doublet member was individually fit with a single-component Gaussian profile, and the centroids of the doublet members were fixed at the rest-wavelength ratio in both the initial and iterated fits. As for C IV, the overall absorption profile includes a P-Cygni profile originating from the stellar wind common in the most massive stars. Without proper treatment, the presence of stellar absorption may bias the measurement of interstellar C IV. Accordingly, we removed the stellar component following the method presented in Du et al. (2016), and the remaining interstellar absorption trough was then fit with a single-Gaussian profile for the EW measurement.[3]

4.4 Line Strength

A key goal of our study is to examine the redshift evolution of the neutral and ionized ISM/CGM using luminosity- and mass-controlled samples. In particular, in this section we investigate the relations in line strength among multiple rest-far-UV spectral features in an

[3]We did not try to model the individual C IV doublet members as done in Du et al. (2016), as in the present study we did not infer any kinematic information from the interstellar C IV profile. The single-component Gaussian profile is sufficient in characterizing the line profile for the purpose of EW measurement.

evolutionary context. These include the relations between Lyα and (1) both LIS and HIS absorption features (Section 4.4.1); (2) multiple galaxy properties (Section 4.4.2); and (3) nebular C III] emission (Section 4.4.5). We also investigate the mutual relationships among Lyα, LIS absorption lines and dust extinction (Section 4.4.3) and fine-structure emission properties at $z \sim 2-4$ (Section 4.4.4).

4.4.1 Lyα vs. Interstellar Absorption Lines

Previous studies have shown that the strength of Lyα is tightly correlated with that of LIS absorption lines in LBGs at $z \sim 3-4$, such that stronger Lyα emission corresponds to weaker LIS absorption (e.g., Shapley et al., 2003; Quider et al., 2009; Vanzella et al., 2009; Jones et al., 2012). In contrast, no significant correlation has been found between Lyα and HIS absorption lines (e.g., Shapley et al., 2003). These observations can be explained by a physical model in which clumpy neutral clouds are embedded in a more smoothly distributed halo of ionized gas (Shapley et al., 2003). Both the EWs of LIS absorption features, which are typically saturated in the galaxy spectra in our samples, and Lyα emission are modulated by the covering fraction of neutral gas: the higher covering fraction of the neutral ISM/CGM, the higher the fraction of Lyα photons that are resonantly scattered out of the line of sight, resulting in a weaker Lyα emission profile (e.g., Reddy et al., 2016). At the same time, an increasing covering fraction of neutral gas leads to stronger LIS absorption lines as these neutral and singly-ionized metal species primarily arise in neutral gas. The lack of direct link between HIS absorption and Lyα emission strengths is consistent with a picture in which the HIS absorption primarily arises in different gas from the phase responsible for the radiative transfer of Lyα. Furthermore, recent work suggests that while the LIS absorption occurs spatially closer to the galaxy, HIS gas is seen with high covering fraction out past the virial radius (Rudie in prep.). Thus, the different spatial distribution of the LIS and HIS absorbers is likely to be another factor responsible for the different behaviors of LIS and HIS with Lyα in EW.

Motivated by this physical picture, we investigated whether the correlations between Lyα

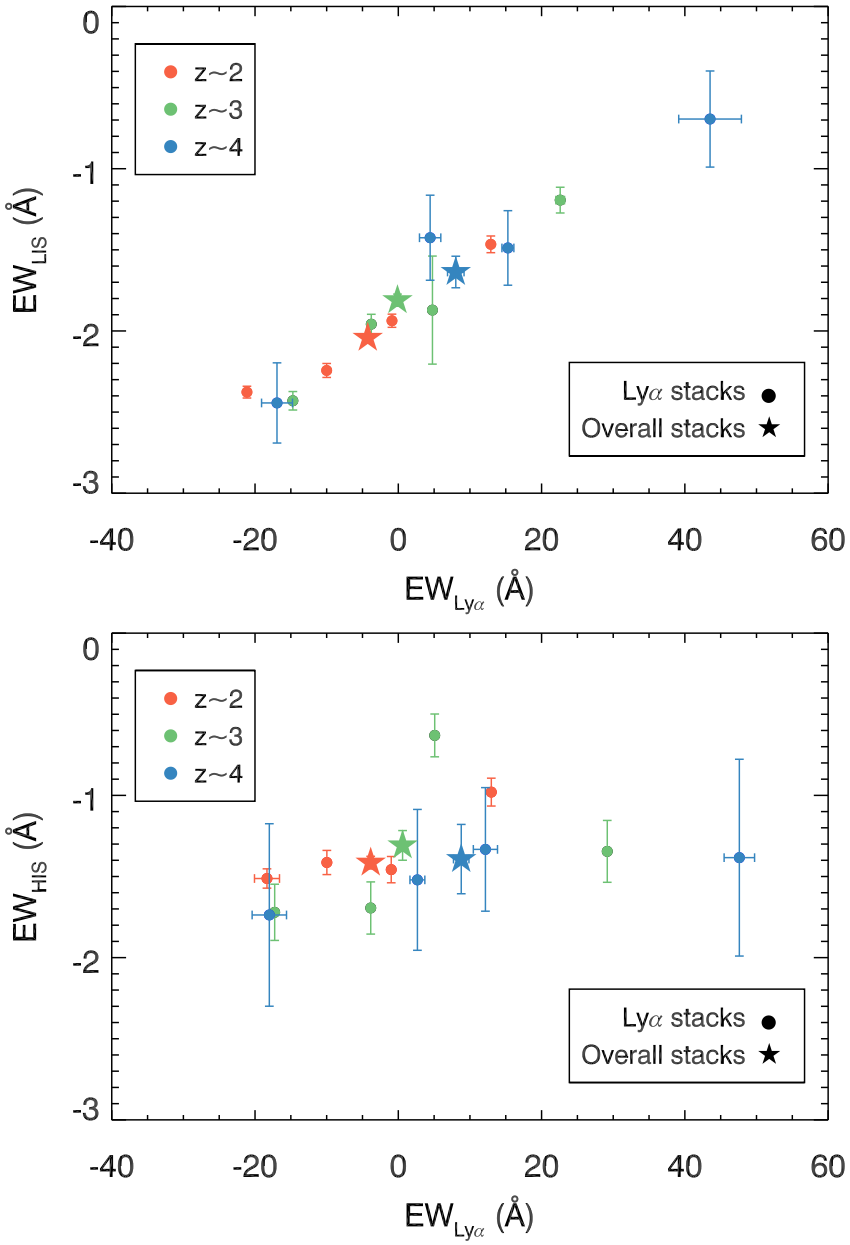

Figure 4.5: **Top:** EW$_{LIS}$ vs. EW$_{Ly\alpha}$ in the composite spectra binned according to EW$_{Ly\alpha}$ (circles) and in the overall composite spectra (stars, as measured from the spectra shown in Figure 4.3). The plotted EW for LIS absorption features was calculated by averaging the EW of Si IIλ1260, O Iλ1302+Si IIλ1304, C IIλ1334, and Si IIλ1527. **Bottom:** EW$_{HIS}$ vs. EW$_{Ly\alpha}$ in the same set of composites. Color coding of the symbols is the same as in the top panel. The combined EW of Si IV$\lambda\lambda$1393, 1402 and C IV$\lambda\lambda$1548, 1550 is shown.

and the absorption features from different ionization states evolve with time from $z \sim 4$ down to $z \sim 2$, using carefully controlled comparison samples and uniformly measured spectra. Figure 4.5 shows the relation between rest-frame Lyα EW ($\mathrm{EW}_{Ly\alpha}$) and the rest-frame LIS (top) and HIS (bottom) absorption line EWs (EW_{LIS} and EW_{HIS}, respectively) at $z \sim 2-4$ from the composite spectra binned according to $\mathrm{EW}_{Ly\alpha}$. We also show the stacks of the full samples at each redshift. EW_{LIS} was calculated by averaging the EW of Si IIλ1260, O Iλ1302+Si IIλ1304, C IIλ1334, and Si IIλ1527, and EW_{HIS} was estimated by averaging the EW of Si IV$\lambda\lambda$1393, 1402 and interstellar C IV$\lambda\lambda$1548, 1550.

From the EW_{LIS} vs. $\mathrm{EW}_{Ly\alpha}$ relation, we find that the $z \sim 4$ sample spans a wider dynamic range in $\mathrm{EW}_{Ly\alpha}$ extending towards larger emission EW than the $z \sim 2$ and $z \sim 3$ samples. In addition, the $z \sim 4$ galaxies on average show stronger Lyα emission and weaker LIS absorption in the overall stacks than the lower-redshift samples, as suggested by the measurements from the overall stacks. This result is in agreement with what Jones et al. (2012) found when comparing the strengths of Lyα and the LIS lines in the $z \sim 4$ and $z \sim 3$ LBG composites. In terms of redshift evolution, it is important to notice that there is no apparent evolutionary trend associated with the EW_{LIS} vs. $\mathrm{EW}_{Ly\alpha}$ correlation (Figure 4.5). The absence of evolution in the trend itself suggests that Lyα and the LIS absorption features are fundamentally related, indicating that the gas giving rise to LIS absorption modulates the radiative transfer of Lyα photons. While not fixing the galaxies in UV luminosity and stellar mass would introduce a slightly larger scatter into the EW_{LIS} vs. $\mathrm{EW}_{Ly\alpha}$ relation, this trend remains qualitatively the same in terms of the absence of redshift evolution, offering additional support to the picture of this relationship being fundamental.

As for the HIS absorption lines, we notice that they appear to be decoupled from Lyα, in that little variation in the HIS absorption strength is observed with increasing $\mathrm{EW}_{Ly\alpha}$. This result is consistent with previous findings (e.g., Shapley et al., 2003) and provides further evidence that the HIS absorption features are produced in a different phase of gas from that controlling the radiative transfer of Lyα. In addition, we discover that the "flat" trend of HIS absorption with $\mathrm{EW}_{Ly\alpha}$ does not seem to evolve with redshift either. Instead, the measured EW_{HIS} at all redshifts seems to scatter around a constant value of ~ -1.5Å. We note that

in contrast to the LIS absorption lines, Si IV appears to be at least partially optically thin, based on the observed $EW_{Si\ IV\lambda1393}/EW_{Si\ IV\lambda1402}$ doublet ratios that are greater than unity at all redshifts we study here. In the optically-thin regime, the rest-frame EW of Si IV, $EW_{Si\ IV}$, does not depend on only the ionized gas covering fraction and velocity range, but is also determined by the column density. In the overall composite spectra, the Si IV doublet ratio decreases from 2.13 ± 0.13Å at $z \sim 2$, to 1.67 ± 0.18Å and 1.70 ± 0.55Å at $z \sim 3$ and $z \sim 4$, respectively. The decreasing doublet ratio suggests that a larger fraction of gas is optically thick at $z \sim 3 - 4$ than at $z \sim 2$, and that the column density of Si IV increases with increasing redshifts. In the meantime, the total $EW_{Si\ IV}$ and the FWHM of individual doublet members remain almost constant, suggesting that the covering fraction of the Si IV gas may decrease at higher redshifts. We will expand the discussion of the covering fraction of the ionized gas and relate it to a physical picture for the evolving ISM/CGM in Section 4.6.2.

4.4.2 Lyα vs. Galaxy Properties

Extensive studies have been carried out to examine the connection between Lyα emission and galaxy properties, in an effort to understand the factors modulating the escape fraction of Lyα photons. Among all the relations, the one for which there is the most consensus is between Lyα and rest-frame UV color (alternatively dust reddening, i.e., $E(B-V)$), according to which galaxies with stronger Lyα emission have bluer UV continuua (e.g., Shapley et al., 2003; Vanzella et al., 2009; Kornei et al., 2010; Pentericci et al., 2010; Berry et al., 2012; Jones et al., 2012; Erb et al., 2016). In contrast, controversies remain as to how $EW_{Ly\alpha}$ relates to galaxy ages. While some studies claim that stronger Lyα is typically found in older galaxies (e.g., Shapley et al., 2001; Kornei et al., 2010), others found no apparent relation between $EW_{Ly\alpha}$ and age (e.g., Pentericci et al., 2009), or that galaxies with stronger Lyα emission are much younger on average (e.g., Pentericci et al., 2007). In terms of the trends with UV luminosity, stellar mass, and SFR, studies have shown that stronger Lyα emission is typically associated with fainter (e.g., Vanzella et al., 2009; Stark et al., 2010; Jones et al., 2012), lower-mass galaxies (e.g., Erb et al., 2006c; Pentericci et al., 2007, 2009;

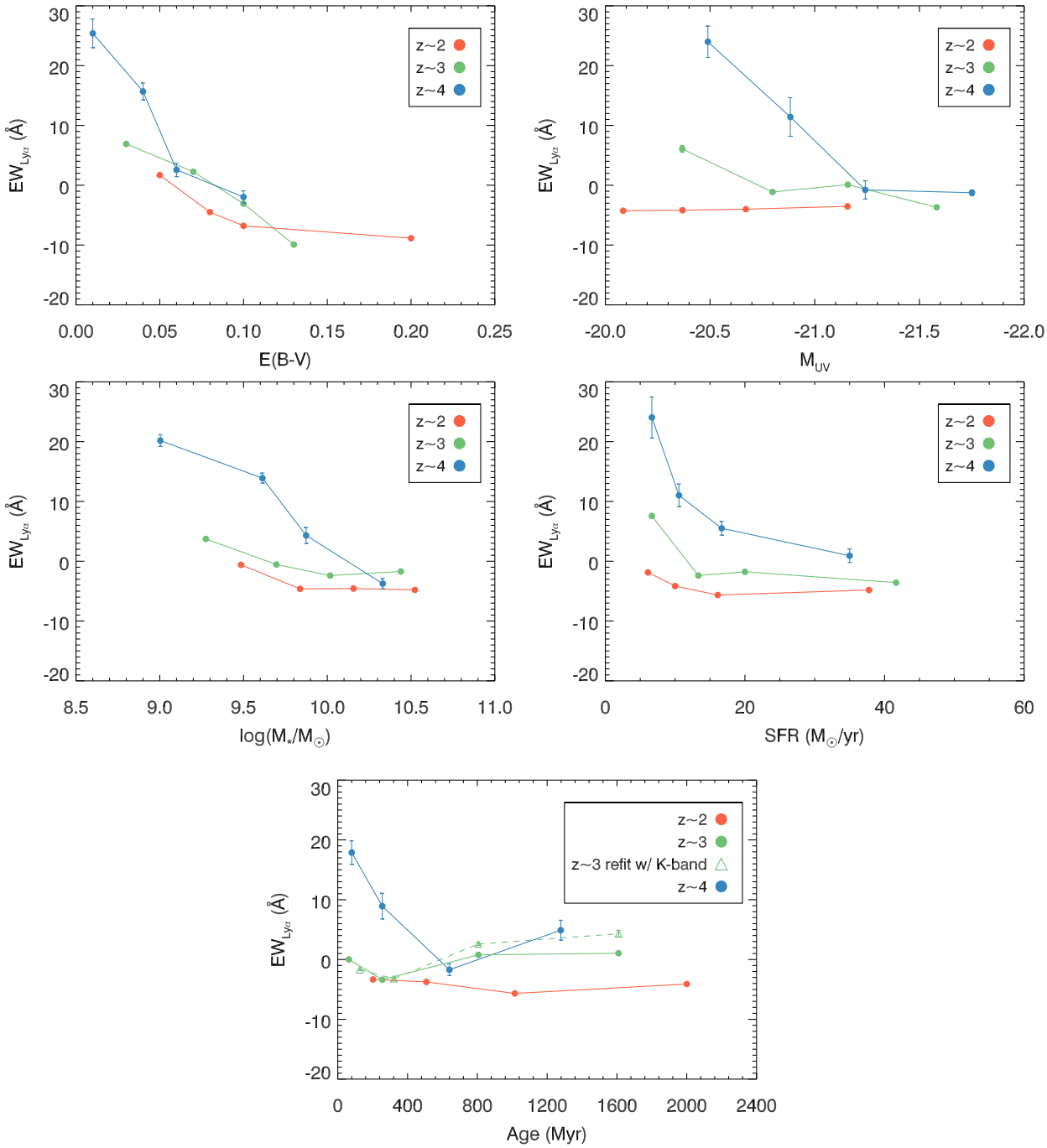

Figure 4.6: **Top to bottom, left to right:** EW$_{Ly\alpha}$ vs. UV absolute magnitude, stellar mass, dust extinction, star-formation rate, and galaxy age in the composite spectra. The triangles and dashed lines in the bottom panel represent the measurements from fitting the $z \sim 3$ galaxy SED with the K-band photometry included.

Jones et al., 2012) with lower SFRs (e.g., Shapley et al., 2003; Kornei et al., 2010; Hathi et al., 2016).

In most cases, the relations described above have been investigated at individual redshifts. Now we examine whether these relations ($EW_{Ly\alpha}$ vs UV luminosity, stellar mass, dust extinction, SFR, and galaxy age) exhibit any evolutionary trends between $z \sim 2-4$. We plot the relations between $EW_{Ly\alpha}$ and $E(B-V)$, M_{UV}, M_*, SFR, and age in Figure 4.6. The composite spectra were created by binning individual spectra according to respective galaxy properties, and the median galaxy property in each bin is plotted. The choice of SED models is not the dominant factor for the relations between $EW_{Ly\alpha}$ and galaxy properties at $z \sim 2-4$ (i.e., the results will remain qualitatively the same with properties derived from the 1.4 $Z_\odot$+Calzetti model for all redshift samples) except for the $EW_{Ly\alpha}$ vs. age relation at $z \sim 3$, as discussed below.

Among all the Lyα relations with galaxy properties, the most striking one is between Lyα and $E(B-V)$. In addition to the previously observed negative correlation between $EW_{Ly\alpha}$ and dust extinction at individual redshifts, we find that the $EW_{Ly\alpha}$ vs. $E(B-V)$ relation lacks significant evolution from $z \sim 4$ to $z \sim 2$. This result implies that dust affects the Lyα photons in the same manner in galaxies at all redshifts studied here, and that the connection between Lyα emission and dust extinction is more direct than those observed between Lyα emission and the other galaxy properties described in this subsection. Shapley et al. (2003) proposed that the patchy neutral gas lying within the more extended ionized gas halo could also be dusty, and the Lyα photons would be absorbed if they encounter the dust grains. We revisit this physical picture in Section 4.6.2.2.

For the relation between Lyα and UV absolute magnitude, we note that only the $z \sim 4$ galaxies display noticeably stronger Lyα in fainter galaxies. The same relation at $z \sim 3$ is not as strong, and at $z \sim 2$ the UV absolute magnitude has a flat correlation with $EW_{Ly\alpha}$. Furthermore, the strength of Lyα increases with increasing redshift at fixed UV luminosity, likely as a result of lower covering fraction of both neutral gas and dust in the galaxies at fixed UV luminosity. This interpretation is consistent with the manner in which $E(B-V)$ evolves from $z \sim 2$ to $z \sim 4$.

Similar evolutionary trends can also be observed from the relations of Lyα with stellar mass and SFR: in general, galaxies with lower stellar mass and lower SFR have stronger Lyα emission, but these relations become weaker as redshift decreases. Higher $\mathrm{EW}_{Ly\alpha}$ is also generally found in higher-redshift samples at fixed stellar mass and/or SFR. We note that the correlation among Lyα and UV luminosity, stellar mass, and SFR are not independent, since galaxies with larger stellar masses are likely to have higher UV luminosities and higher SFRs.

The relation between Lyα and galaxy age has also been explored previously. Without excluding the K-band photometry (where both Hβ and [O III] fall for the $z \sim 3$ LBGs) from the SED fits, Shapley et al. (2001) and Kornei et al. (2010) found that Lyα is stronger in older galaxies. These authors interpreted the results as an evolution in time towards higher $\mathrm{EW}_{Ly\alpha}$ as the neutral gas and dust are blown out by supernovae and massive stellar winds, resulting in a reduced covering fraction of both at older galaxy ages. We revisited this correlation for our three redshift samples, and found that, after excluding the photometric bands potentially contaminated by strong emission lines (Hβ, [O III], and Hα), the $z \sim 2$ and $z \sim 3$ galaxies do not exhibit a significant positive trend between $\mathrm{EW}_{Ly\alpha}$ and galaxy age. As for the $z \sim 4$ galaxies, Lyα emission is more prominent in younger galaxies than in the older ones, an opposite trend from what was found by Shapley et al. (2001) and Kornei et al. (2010).

We further explored the connection between $\mathrm{EW}_{Ly\alpha}$ and age at $z \sim 3$. The positive correlation of Lyα and age can be reproduced if we do not discard the contaminated K-band from SED fitting at $z \sim 3$ (triangles in the bottom panel of Figure 4.6). It is worth noting, though, that when using the 1.4 $Z_{\odot}$+Calzetti model, which was adopted both in Shapley et al. (2001) and Kornei et al. (2010), the derived galaxy age $z \sim 3$ does reveal a positive correlation with $\mathrm{EW}_{Ly\alpha}$. The exclusion of the K-band, while making the relation flatter, cannot completely remove the positive trend. On the other hand, the $\mathrm{EW}_{Ly\alpha}$ vs. age relation at $z \sim 2$ and $z \sim 4$ is not sensitive to the choice of SED models. Although it is unclear why the adoption of the 1.4 $Z_{\odot}$+Calzetti model only affects the $\mathrm{EW}_{Ly\alpha}$ relation with age specifically at $z \sim 3$, galaxy age is undoubtedly the least well-determined property among

those we explore here. Therefore, we conclude with caution that, with the most reasonable assumptions of our $z \sim 3$ sample (0.28 $Z_{\odot}$+SMC for the majority and 1.4 $Z_{\odot}$+Calzetti for very high-mass galaxies), there is no evidence for a positive correlation between $\mathrm{EW}_{Ly\alpha}$ and age at $z \sim 3$. The previously reported positive $\mathrm{EW}_{Ly\alpha}$ trend with age at $z \sim 3$ is best explained as a combination of the choice of SED models and the contamination in the K band from strong nebular [O III] emission.

As described in Section 4.2.2, excluding the H- and K- bands for the $z \sim 2$ sample and IRAC channel 1 for the $z \sim 4$ sample has little impact on the age estimates. However, there are plausible factors to explain the fact that strong emission lines affect the SED fits at $z \sim 3$. For the $z \sim 4$ sample, only objects with $z \geqslant 3.8$ (38 out of 70 objects) have SEDs that are potentially affected by emission-line contamination (i.e., Hα) in IRAC channel 1 while the remainder will not suffer from significant emission-line contribution to the SED. As for the $z \sim 2$ sample, the best-fit SED models are less sensitive to the emission lines because (1) 75 objects (14% of the sample) already had the H- and K- bands corrected for strong nebular emission, and (2) a larger fraction of objects in the $z \sim 2$ sample (474 out of 539 galaxies) than in the $z \sim 3$ sample (273 out of 349 galaxies) have IRAC coverage to constrain the overall shape of the SEDs. Therefore, the relative importance of the H and K bands in determining the best-fit stellar population parameters is lower in the $z \sim 2$ sample than at $z \sim 3$.

In summary, we do not observe an apparent correlation between $\mathrm{EW}_{Ly\alpha}$ and galaxy age within the $z \sim 2$ and $z \sim 3$ samples, and there is no strong evidence for a physical picture in which gas and dust are systematically cleared away in galaxies as a function of time (e.g., as described in Kornei et al., 2010). It is suggestive, though, that at $z \sim 4$ Lyα is stronger in younger galaxies. At fixed galaxy age, the $z \sim 4$ galaxies have stronger Lyα emission than galaxies at $z \sim 2-3$. Furthermore, there appears to be a tendency towards smaller $\mathrm{EW}_{Ly\alpha}$ (and thus increased dust content and H I covering fraction) at older ages within the $z \sim 4$ sample. In contrast to the physical picture proposed by Shapley et al. (2001) and Kornei et al. (2010), the trend we observe at $z \sim 4$ suggests that galaxies at the youngest ages in our sample (< 200 Myr) have a less substantial neutral ISM/CGM and are possibly

experiencing the first generations of star formation. At the same time, comparably young $z \sim 2-3$ galaxies may be more chemically enriched than at $z \sim 4$, and the relatively higher neutral gas and dust covering fractions have reduced the observed $\mathrm{EW}_{Ly\alpha}$.

In this section, we found that galaxies with stronger Lyα emission tend to be fainter, younger, lower-mass galaxies with lower SFRs. The correlations between Lyα and these galaxy properties are the strongest at $z \sim 4$, and become much weaker at $z \sim 2-3$. The evolutionary change of Lyα dependence on galaxy properties has also been reported in previous studies (e.g., Pentericci et al., 2010). However, before making any physical interpretation of the observed evolution, one needs to consider the larger spectroscopic incompleteness of the $z \sim 4$ sample relative to that of the $z \sim 2$ and $z \sim 3$ samples especially at the faint, low-mass end (i.e., the $z \sim 4$ galaxies have to show a stronger Lyα in order to be detected and included in the sample at faint luminosities).

To investigate how the sample incompleteness impacts our results, we conducted two tests. First, we constructed composites from a "complete" subsample at each redshift. We selected galaxies with $z^{'} \leq 24.75$ at $z \sim 4$, where the spectroscopic completeness is nearly 100%, to be in the "complete" subsample. Galaxies in this subsample have UV absolute magnitudes extending down to $\mathrm{M}_{UV} = -20.78$. We then constructed subsamples at $z \sim 2$ and $z \sim 3$ with galaxies brighter than $\mathrm{M}_{UV} \leq -20.78$, which are also spectroscopically complete (Shapley et al., 2003; Steidel et al., 2003). The progressive evolution of $\mathrm{EW}_{Ly\alpha}$ being stronger at higher redshifts still exists in the "complete" composites, with $\mathrm{EW}_{Ly\alpha} = -4.0$Å, -2.2Å, and 6.5Å at $z \sim 2$, $z \sim 3$, and $z \sim 4$, respectively. In our second test we limited the $z \sim 2$ and $z \sim 3$ samples in each galaxy property bin such that they had the same fraction of galaxies with only Lyα redshift as the $z \sim 4$ sample, and examined how the trends in Figure 4.6 would be affected. We note that intentionally selecting objects with "$z_{Ly\alpha}$ only" in the lower-redshift samples would bias the samples to objects with stronger Lyα. As expected, the resulting $\mathrm{EW}_{Ly\alpha}$ in the censored $z \sim 2$ and $z \sim 3$ composites is systemically larger, but the trends at $z \sim 4$ are still steeper than those at lower redshifts across the same dynamic range in galaxy properties. Additionally, we measure larger $\mathrm{EW}_{Ly\alpha}$ at $z \sim 4$ in the overall composite than in the censored $z \sim 2$ and $z \sim 3$ stacks. Therefore, we

conclude that while the difference in sample incompleteness needs to be seriously taken into account when studying galaxies at different redshifts, our key results are robust regarding the redshift evolution of Lyα emission and LIS absorption strengths, and $E(B-V)$.

The steeper Lyα trends with galaxy properties at $z \sim 4$ can be attributed to a relatively larger range in H I and dust covering fractions, which results in a larger dynamic range in $\mathrm{EW}_{Ly\alpha}$ (see Figure 4.5) especially towards the stronger-Lyα end where galaxies have very little dust. In contrast, the $z \sim 2-3$ galaxies have higher $E(B-V)$ than the $z \sim 4$ galaxies even in the faintest, youngest, lowest-mass, and lowest-SFR bin. The higher minimum $E(B-V)$ limits the highest $\mathrm{EW}_{Ly\alpha}$ we could possibly observe at $z \sim 2-3$, resulting in a much smaller range in the measured $\mathrm{EW}_{Ly\alpha}$ in composites binned according to galaxy properties.

4.4.3 Lyα, LIS absorption features, and dust

In Sections 4.4.1 and 4.4.2, we presented our result of the seemingly invariant relations between $\mathrm{EW}_{Ly\alpha}$ and EW_{LIS} (Figure 4.5) and between $\mathrm{EW}_{Ly\alpha}$ and dust extinction (Figure 4.6). These non-evolving correlations indicate an interdependence among Lyα emission, LIS absorption, and dust extinction independent of redshift. If these three properties are inherently inter-related, we would expect strong correlations among any two of them regardless of galaxy properties. As a result, we utilize the composite spectra binned according to different galaxy properties (no longer restricted to the Lyα stacks as shown in Section 4.4.1) and further examine the relations among Lyα, the LIS lines, and the dust content. Figure 4.7 shows the measurements of the strength of Lyα emission, LIS absorption, and $E(B-V)$ plotted against each other in composites divided according to M_{UV}, M_*, $E(B-V)$, SFR, age, and $\mathrm{EW}_{Ly\alpha}$. While the measurements from these composite spectra are not entirely independent in the way that measurements from individual galaxies would be, the relation between the most fundamentally correlated parameters should show the least scatter in the composites binned in galaxy properties. With high S/N and the inclusion of the entire samples, composite spectra provide a comprehensive view of the relative tightness and the

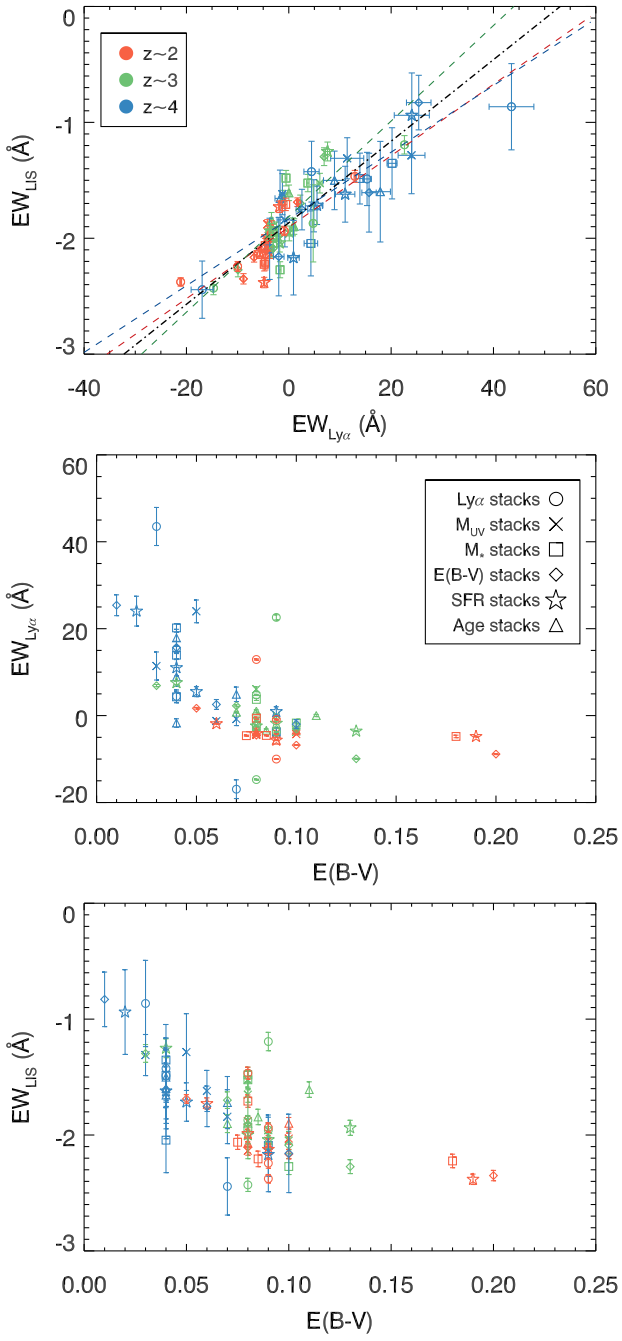

Figure 4.7: **Top to bottom:** EW$_{Ly\alpha}$ vs. EW$_{LIS}$, EW$_{Ly\alpha}$ vs. $E(B-V)$, and EW$_{LIS}$ vs. $E(B-V)$ in composite spectra divided according to EW$_{Ly\alpha}$ (circles), UV absolute magnitude (crosses), stellar mass (squares), dust extinction (diamonds), star-formation rate (stars), and galaxy age (triangles). The median $E(B-V)$ in each bin is plotted. Color coding of the symbols is the same as in Figure 4.5. In the top panel, the colored dashed lines denote the best-fit linear model for the $z \sim 2$ (red), $z \sim 3$ (green), and $z \sim 4$ (blue) samples, and the black dash-dotted line represents the overall best-fit linear model for the EW$_{Ly\alpha}$ vs. EW$_{LIS}$ relation accounting for all three redshift samples.

redshift dependence, if any, of the correlations among $\mathrm{EW}_{Ly\alpha}$, EW_{LIS}, and $E(B-V)$. Therefore, although we recognize that the correlation significances associated with these composite scatter plots do not hold the same meaning as for independent data points, we still use the Spearman correlation coefficient and significance as gauges of the relative tightness of these correlations.

To quantify the EW_{LIS} vs. $\mathrm{EW}_{Ly\alpha}$ relation, we performed an inverse-squared weighted linear regression to the data points for each redshift sample. The best-fit linear models are parameterized as $\mathrm{EW}_{LIS} = -1.90 + 0.031 \times \mathrm{EW}_{Ly\alpha}$, $\mathrm{EW}_{LIS} = -1.81 + 0.041 \times \mathrm{EW}_{Ly\alpha}$, and $\mathrm{EW}_{LIS} = -1.83 + 0.029 \times \mathrm{EW}_{Ly\alpha}$ at $z \sim 2$, 3, and 4, respectively. As shown in the top panel of Figure 4.7, the best-fit linear model for each redshift sample predicts very similar values over the ranges of $\mathrm{EW}_{Ly\alpha}$ and EW_{LIS} probed in our study, and shows no progressive, evolutionary trend at $z \sim 2-4$. The overall fit to all the $z \sim 2-4$ data points yields $\mathrm{EW}_{LIS} = -1.87 + 0.035 \times \mathrm{EW}_{Ly\alpha}$, with a Spearman correlation coefficient $\rho = 0.87$ (7.4σ away from the null hypothesis).

Similar to Figure 4.6, the middle panel of Figure 4.7 shows that $\mathrm{EW}_{Ly\alpha}$ decreases with increasing $E(B-V)$ in all composites binned according to galaxy properties. This correlation is less tight than the $\mathrm{EW}_{Ly\alpha}$ vs. EW_{LIS} relation, and has a Spearman correlation coefficient $\rho = -0.71$ (5.9σ away from the null hypothesis). Given the common dependence of $\mathrm{EW}_{Ly\alpha}$ on both EW_{LIS} and dust extinction, a correlation between EW_{LIS} and $E(B-V)$ is also expected. The tightness of the EW_{LIS} vs. $E(B-V)$ relation is comparable to that of the $\mathrm{EW}_{Ly\alpha}$ vs. $E(B-V)$ relation, with a Spearman $\rho = -0.70$ (5.9σ away from the null hypothesis). A comparison of correlation coefficients and significances suggests that the dependence between Lyα and the LIS absorption lines is the strongest, whereas their correlation with $E(B-V)$ may be secondary.

While the grid of discrete $E(B-V)$ values in the stellar population templates may potentially introduce larger scatter to the relations with $E(B-V)$, we argue that this discretization has a negligible impact on the resulting correlation coefficient and significance. To mimic the discrete $E(B-V)$ values and match the number of $E(B-V)$ bins, we discretized $\mathrm{EW}_{Ly\alpha}$ into 21 values from -20Å to 40Å with a 3Å increment. Each $\mathrm{EW}_{Ly\alpha}$ was assigned

to the closest fixed value of the grid. Discretizing $\mathrm{EW}_{Ly\alpha}$ results in a Spearman $\rho = 0.86$ (7.2σ away from the null hypothesis), which is almost unchanged relative to the original correlation strength. We therefore conclude, as in Shapley et al. (2003), that the correlation between Lyα and the LIS lines is likely the primary one among the three. We note, however, that the larger scatter in the EW_{LIS} and $E(B-V)$ and $\mathrm{EW}_{Ly\alpha}$ vs. $E(B-V)$ relation may partially result from the uncertainty in $E(B-V)$ due to photometric errors and systematic uncertainty from the assumption of stellar population models and attenuation curves, and may not reflect the intrinsic scatter with $\mathrm{EW}_{Ly\alpha}$ and EW_{LIS}. Individual measurements of $\mathrm{EW}_{Ly\alpha}$, EW_{LIS}, and $E(B-V)$ from deep spectra will provide additional confirmation on which relationship is most fundamental.

These relations, which appear to be roughly independent of redshift and other galaxy properties, have significant implications for understanding galaxy evolution. For example, the strength of both Lyα emission and LIS absorption can be predicted based on the measurement of the other, and the evolutionary trends shown in the $\mathrm{EW}_{Ly\alpha}$ vs. galaxy property relations (Figure 4.6) can be directly linked to the evolution of the range of LIS absorption and thus the neutral gas covering fraction at different redshifts.

4.4.4 Fine-structure Emission

Aside from Lyα and LIS absorption lines, multiple fine-structure emission features, Si II*λ1265, 1309, 1533, are also detected in the LBG composite spectra at $z \sim 2-4$. Fine-structure emission comes from the re-emission of photons when the electrons return to the excited ground state following the absorption of continuum photons, as traced by the resonant interstellar absorption lines. Accordingly, the optically thin fine-structure emission lines are considered to originate from the outflowing ISM/CGM (e.g., Erb et al., 2012; Kornei et al., 2013), and offer rich information on the spatial extent and geometry of galactic-scale outflows (e.g., Prochaska et al., 2011; Finley et al., 2017). In the absence of dust, the total strength of the fine-structure emission is expected to be equal to that of the associated interstellar absorption for optically thick gas probed by the saturated LIS lines, as the resonant photons cannot

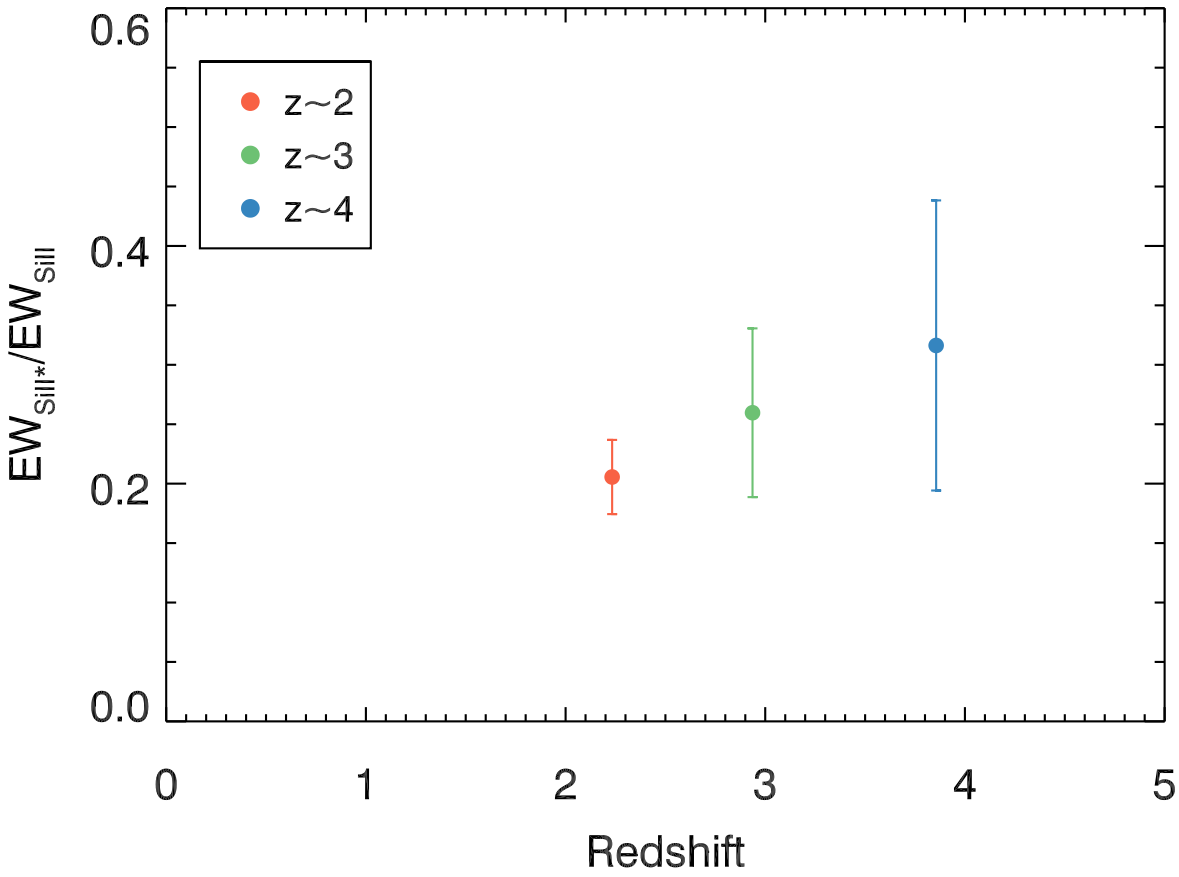

Figure 4.8: The fine-structure-to-LIS-absorption ratio vs. redshift in the composite spectra with fixed median $E(B-V) = 0.05$. The ratio is calculated by dividing the total EW of Si II*λ1265+Si II*λ1533 by that of Si IIλ1260+Si IIλ1527.

escape until they emerge as fine-structure photons. However, observations have shown that the fine-structure emission always appears to be weaker than the LIS absorption for Si II (Shapley et al., 2003; Jones et al., 2012) and Fe II transitions (Erb et al., 2012). Several factors may contribute to this discrepancy: the presence of dust, the geometry of the outflows, and spectroscopic slit loss (Prochaska et al., 2011; Erb et al., 2012). By comparing the EW ratio of the Si II* fine-structure emission and Si II absorption (i.e., $R_{FS} = \mathrm{EW_{Si\ II*}}/\mathrm{EW_{Si\ II}}$) in the overall LBG composites at $z \sim 3$ and $z \sim 4$, Jones et al. (2012) found that this ratio is higher for the $z \sim 4$ galaxies than for those at $z \sim 3$. These authors interpreted such results as evidence of a smaller characteristic size for the fine-structure emitting regions in $z \sim 4$ LBGs, such that a larger fraction of emission gets captured in the slit at $z \sim 4$ than at $z \sim 3$.

In order to investigate the effect of slit loss alone and whether the size of the fine-structure emission region evolves with redshift, we utilized the full $z \sim 4$ sample and constructed composites at $z \sim 2$ and $z \sim 3$ with a fixed median $E(B-V) = 0.05$ matched with that of the $z \sim 4$ sample. We only sampled galaxies on the blue tail of the $E(B-V)$ distribution of the $z \sim 2$ and $z \sim 3$ samples, selecting objects from smaller to larger $E(B-V)$ until the median $E(B-V)$ is matched. This approach results in 179, 129, and 84 spectra in the $E(B-V)$-controlled subsamples at $z \sim 2$, 3, and 4, respectively. We measured R_{FS} using Si II*λ1265,1533 and Si IIλ1260,1527. The pair of Si II*λ1309 and Si IIλ1304 was excluded from the measurement because the latter is blended with O Iλ1302 in the composite spectra. We define $R_{FS} = -(\mathrm{EW_{1265}} + \mathrm{EW_{1533}})/(\mathrm{EW_{1260}} + \mathrm{EW_{1527}})$, as in Jones et al. (2012). We measure a ratio of 0.21 ± 0.03, 0.26 ± 0.07, 0.32 ± 0.12 for the $z \sim 2$, $z \sim 3$, and $z \sim 4$ composites, respectively. Figure 4.8 shows R_{FS} plotted against redshift, and does not indicate a significant evolutionary trend. Given that the composites are fixed in $E(B-V)$, our result suggests that there may not be a redshift evolution in the size of the fine-structure emission region in galaxies with similar dust extinction. In fact, if the median $E(B-V)$ is not fixed, R_{FS} is measured to be 0.16 ± 0.02 and 0.18 ± 0.04 for the $z \sim 2$ and $z \sim 3$ samples, respectively (R_{FS} at $z \sim 4$ remains the same), from the overall composites. This trend is consistent with that reported by Jones et al. (2012), that galaxies at higher redshifts on average have stronger

fine-structure emission at given resonant absorption strength. However, our results suggest that the larger R_{FS} in the $z \sim 4$ galaxies measured by Jones et al. (2012) reflects the lower dust content in higher-redshift galaxies on average (Table 4.2 and Figure 4.6).

We note that while we reported $R_{FS} = 0.32 \pm 0.12$ for the $z \sim 4$ composite, Jones et al. (2012) measured a higher value, $R_{FS} = 0.53 \pm 0.17$, using the $z \sim 4$ LBG spectra from the same set of Si II and Si II* lines. Several factors may contribute to this discrepancy. First, the composites were constructed from different samples. By adding 14 objects with $z > 3.4$ from the LRIS sample, removing one galaxy from the DEIMOS/FORS2 sample with $z < 3.4$, and excluding 3 galaxies without an unique match in photometry, our $z \sim 4$ sample includes 81 objects (91 spectra) [4] while that in Jones et al. (2012) includes 70 objects (81 spectra). Second, the individual galaxy spectra were combined in different ways. In Jones et al. (2012), all the individual spectra were normalized to $F_\nu = 1$ over $1250-1500$Å, and the mean value at each wavelength was taken with 1σ clipping. In comparison, we constructed the composites accounting for the *intrinsic* shape of the galaxy spectra in the L_λ space. We scaled all galaxy spectra in the same bin such that they have the same median L_λ over $1270-1290$Å, a spectral window that all individual spectra have coverage for, and performed median stacking to create the composite spectra. Additionally, we required that the same set of objects contribute to all wavelengths in a single composite. For example, to measure the features of Si IIλ1527 and Si II*λ1533, we only included objects with spectral coverage at least up to 1540Å when creating the composite. While the requirement on wavelength coverage reduced the $z \sim 2$, 3, and 4 sample sizes to 173, 71, and 74, respectively, the composites represent the average of the same set of objects at all wavelengths, and the S/N of the composite does not vary significantly across the spectrum due to the different numbers of objects contributing at each wavelength.

In conclusion, we created the $z \sim 4$ composite using a different method with a slightly different sample from the one in Jones et al. (2012), and a different R_{FS} value is therefore

[4] As we discuss below, the constraint on wavelength coverage results in 66 objects (74 spectra) contributing to the $z \sim 4$ composite from which we measured R_{FS}. Among these individual spectra, 60 are in the DEIMOS/FORS2 sample Jones et al. (2012) used to measure R_{FS}, and the remaining 14 spectra are from LRIS.

not unexpected. In fact, the R_{FS} value quoted in Jones et al. (2012) can be reproduced if we use the same sample to create the composite following the same stacking approach described in Jones et al. (2012). Since we have performed uniform stacking schemes and spectral feature measurements across the redshift samples, the results presented earlier in this subsection are free from any systematic bias and reflect the true (lack of) redshift evolution of the size of the fine-structure emitting region with fixed dust extinction. We note, however, that although the redshift rules used to determine the systemic redshift (Section 4.2.1) yield a well-established rest frame for the composite spectra, as evidenced by the lack of significant velocity offset for stellar features, the average velocity shift may not be accurate in determining the redshift of each individual galaxy. As a result, redshift errors for individual objects can potentially broaden the fine-structure emission profiles in the composites, as these features were not included in determining the redshift rules. Some fine-structure emission flux can therefore be lost during our measurements of these features due to the fixed wavelength range we used for fitting the profiles, leading to smaller measured fine-structure emission EWs than the intrinsic values. Individual spectra with high S/N, spectral resolution, and precise redshift measurements will provide key information on the intrinsic R_{FS} of star-forming galaxies at $z \sim 2-4$.

4.4.5 Lyα vs. C III] at $z \sim 2$

As typically the second strongest emission feature in the rest-frame far-UV (after Lyα), the nebular C III]$\lambda\lambda$1907, 1909 emission doublet has received great attention as a potential redshift probe at $z > 6$ (Stark et al., 2014, 2015), where Lyα is significantly attenuated by the neutral intergalactic medium (IGM; e.g., Treu et al., 2012; Pentericci et al., 2014; Schenker et al., 2014; Konno et al., 2014). More importantly, C III] is a useful probe of the physical conditions of the H II regions in star-forming galaxies when combined with other nebular lines from [O III] and C IV. Photoionization models predict that large rest-frame C III] EWs, $\mathrm{EW_{C\ III]}}$, result from lower gas-phase metallicity, higher ionization parameters, and harder radiation fields (e.g., Erb et al., 2010; Steidel et al., 2016; Berg et al., 2016; Senchyna et al., 2017). The common dependence of C III] and other emission line properties

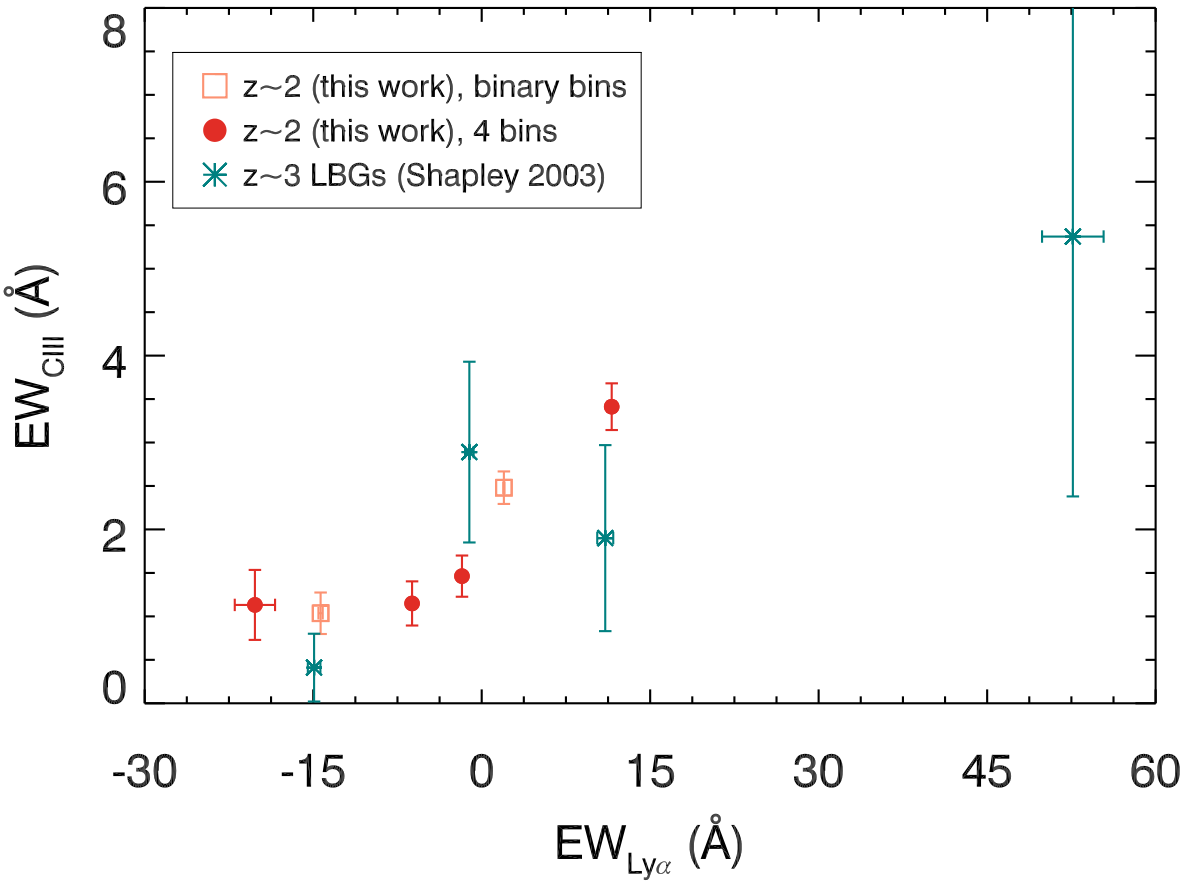

Figure 4.9: Rest-frame $\mathrm{EW_{C\ III]}}$ vs. $\mathrm{EW}_{Ly\alpha}$ in the $z \sim 2$ composite spectra with C III] coverage divided in 2 bins (light red squares) and 4 bins (dark red circles). The C III] emission is not significant in any of the $z \sim 3$ and $z \sim 4$ composites, and is therefore not shown in the figure.

(both nebular and recombination features) on the hardness of the ionizing spectrum leads to positive predicted correlations of $\mathrm{EW_{C\ III]}}$ with $\mathrm{EW}_{Ly\alpha}$ (Jaskot & Ravindranath, 2016), [O III] (Stark et al., 2014; Jaskot & Ravindranath, 2016; Senchyna et al., 2017; Maseda et al., 2017), and the escape fraction of Lyman continuum (LyC) photons (Vanzella et al., 2016; Jaskot & Ravindranath, 2016; de Barros et al., 2016). Previous work has suggested a connection between $\mathrm{EW}_{Ly\alpha}$ and $\mathrm{EW_{C\ III]}}$ (e.g., Shapley et al., 2003; Stark et al., 2014, 2015; Rigby et al., 2015; Guaita et al., 2017). The evidence for a positive correlation between Lyα and C III] emission EWs suggests that the observed $\mathrm{EW}_{Ly\alpha}$, aside from being modulated by the covering fraction of neutral gas and dust, may also show differences in *intrinsic* Lyα production. For example, the $z \sim 4$ composite made of galaxies in the quartile with the strongest Lyα emission (the rightmost blue circle in the top panel of Figure 4.7) falls off the mean EW_{LIS} vs. $\mathrm{EW}_{Ly\alpha}$ relation, showing stronger Lyα emission at fixed LIS absorption strength than all other composites. This result suggests variations in the properties of H II regions and massive stars even among galaxies in our samples. Since C III] is covered in some of the individual $z \sim 2-4$ LBG spectra, it is of great interest to examine how the strength of C III] in general relates to that of Lyα, and whether such correlation evolves with time using the large datasets at hand.

We selected a subset of objects with C III] coverage from each redshift sample controlled in UV luminosity and stellar mass. The selection results in 291, 37, and 34 objects in the $z \sim 2$, $z \sim 3$, and $z \sim 4$ samples, respectively. Given the small number of objects with C III] coverage at $z \sim 3$ and $z \sim 4$, we performed binary stacks at each redshift according to $\mathrm{EW}_{Ly\alpha}$, with the low and high bins containing nearly equal numbers of objects. We measured the C III] emission profile on the continuum-normalized spectra, in the same manner as described in Section 4.3.3.

Unfortunately, the C III] feature is not significantly detected in any of the $z \sim 3$ and $z \sim 4$ composites due to relatively low S/N, making it impossible to study the redshift evolution of the relation between $\mathrm{EW}_{Ly\alpha}$ and $\mathrm{EW_{C\ III]}}$. The $z \sim 2$ composites, on the other hand, have much higher S/N thanks to the significantly larger sample size, and therefore enable the first measurement of C III] from a statistical sample at this redshift.

As shown in Figure 4.9, the $z \sim 2$ binary stacks (squares) follow a clear trend of increasing $\mathrm{EW_{C\ III]}}$ at higher $\mathrm{EW}_{Ly\alpha}$. In order to achieve a larger dynamic range in both C III] and $\mathrm{EW}_{Ly\alpha}$, we further divided each $z \sim 2$ Lyα bin into two (four bins in total), and investigated if any underlying trends are obscured by simple binary. From the 4-bin composites (circles in Figure 4.9), we observe a fairly flat behavior between $\mathrm{EW_{C\ III]}}$ and $\mathrm{EW}_{Ly\alpha}$, with the exception of the strongest Lyα bin. The strongest Lyα bin has a measured $\mathrm{EW_{C\ III]}} = 3.41 \pm 0.27$Å while that in the rest of the Lyα stacks is ~ 1.25Å. This trend is consistent with what has been found in previous studies (e.g., Shapley et al., 2003; Stark et al., 2014, 2015; Rigby et al., 2015; Jaskot & Ravindranath, 2016), suggesting *intrinsic* difference in the Lyα photon production between galaxies showing strong and weak Lyα emission. Although we were unable to detect the C III] feature at $z \sim 3-4$, measurements were made using the $z \sim 3$ LBG composites by Shapley et al. (2003).[5] These authors show a suggestive positive correlation between $\mathrm{EW}_{Ly\alpha}$ and $\mathrm{EW_{C\ III]}}$, which is consistent with our much cleaner trend at $z \sim 2$.

The positive correlation between C III] and Lyα strengths suggest that environments favorable for C III] production are also conducive to higher Lyα production and large Lyα escape fractions. As C III] is a collisionally excited transition, the emission is enhanced in H II regions with strong radiation fields and low metallicities (Jaskot & Ravindranath, 2016; Senchyna et al., 2017). In the meantime, the harder ionizing spectrum given by young, metal-poor stars leads to higher $\mathrm{EW}_{Ly\alpha}$ by (1) boosting the intrinsic production rate of Lyα photons, and (2) reducing the neutral covering fraction due to the higher ionization state of the ISM (Trainor et al., 2015), allowing more Lyα photons to escape the galaxy. Therefore, the hard ionizing spectrum and the low gas-phase metallicity modulate both the C III] and Lyα emission in the same direction, resulting in the positive correlation we observe between these two transitions. Similarly, $\mathrm{EW}_{Ly\alpha}$ has also been demonstrated to correlate with the rest-optical nebular emission properties, such as [O III]λ5008/Hβ and [N II]λ6585/Hα (Erb

[5]The $z \sim 3$ LRIS spectra presented in Shapley et al. (2003) were mainly collected before the LRIS-B upgrade, and typically have significantly redder wavelength coverage than the LRIS blue-side dichroic spectra presented here. As such the sample of $z \sim 3$ spectra with C III] coverage is significantly larger in Shapley et al. (2003).

et al., 2016; Trainor et al., 2016), which, like C III], can be used to probe the physical conditions of H II regions (e.g., gas-phase metallicity, electron temperature and density, and ionization parameter).

4.5 Kinematics

The measurement of the Lyα and LIS absorption profiles in the composite spectra enables us to study not only their line strengths, but also kinematics. The line centroids measured from LIS absorption features offer at least a crude measure of the bulk velocities of outflowing ISM, and the observed Lyα centroid may further constrain the kinematics of the neutral outflows (e.g., velocity distribution). In this Section, we focus on the evolution of Lyα (Section 4.5.1) and LIS (Section 4.5.2) kinematics across $z \sim 2-4$.

4.5.1 Lyα Kinematics

As described in Section 4.2, the centroids of Lyα emission (or absorption) and LIS absorption lines typically do not trace the galaxy systemic velocity because of the presence of galactic-scale outflows. Furthermore, it has been shown empirically how ISM kinematics affect the emergent Lyα profile. By studying a composite spectrum of $z \sim 3$ LBGs, Shapley et al. (2003) discovered that weaker Lyα emission corresponds to a larger velocity offset between Lyα and the LIS absorption lines, Δv_{em-abs}. A similar trend has been measured in the $z \sim 4$ LBGs by Jones et al. (2012), and these authors found no redshift evolution of the $\mathrm{EW}_{Ly\alpha}$ vs. Δv_{em-abs} relation from $z \sim 4$ to $z \sim 3$. Motivated by these previous studies, we revisit the correlation between Lyα kinematics and strength, and investigate if the covering fraction of the neutral ISM modulates the observed Lyα profile differently at different redshifts.

We characterized the kinematics of Lyα by measuring the centroid of the Lyα emission feature in the composite spectra binned according to $\mathrm{EW}_{Ly\alpha}$. Even in the composite with the weakest Lyα where the line profile is classified as "absorption," a small Lyα emission peak is still discernible and therefore its peak wavelength can be evaluated. We used MPFIT to fit the Lyα emission profile in a similar manner to the measurement of the LIS absorption

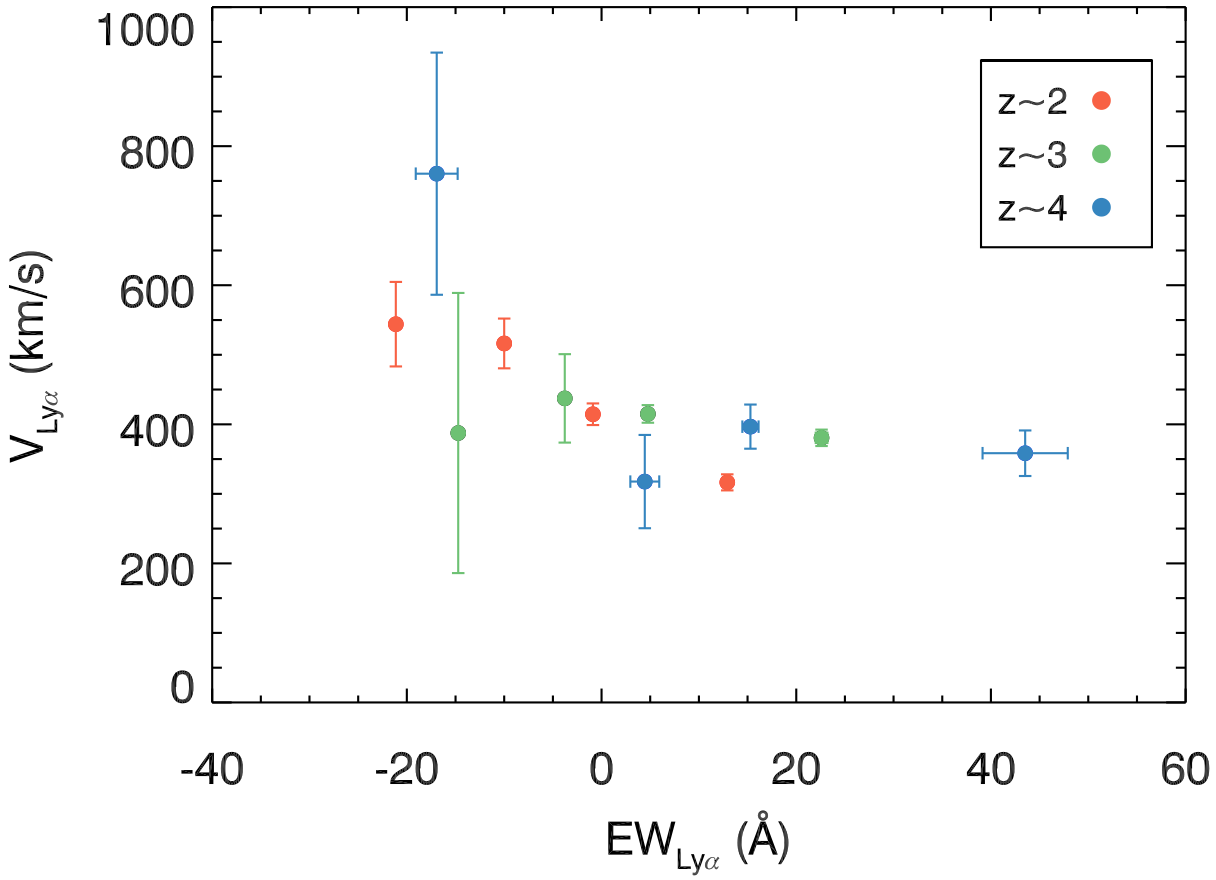

Figure 4.10: Centroid velocity of Lyα emission and Lyα rest-frame EW in the composite spectra binned according to $EW_{Ly\alpha}$.

lines, except that the fitting was performed on composites in L_λ space (i.e., not continuum normalized). The initial estimate of line parameters (centroid, EW, and Gaussian FWHM) were obtained from the IRAF routine *splot* by fitting the Lyα profile from the blue-side base to the red-side base of the line. We did not iterate the wavelength range for the Lyα emission profile in all Lyα morphological categories, given that the wavelength range bracketed by the blue- to red-bases of the Lyα profile already well defines the feature, and that iterations would not work for the "absorption" composites as a result of the extremely weak emission line.

We plot the centroid velocity of Lyα emission and the rest-frame $\mathrm{EW}_{Ly\alpha}$ in Figure 4.10. The three redshift samples span different dynamic ranges in $\mathrm{EW}_{Ly\alpha}$, with the $z \sim 2$ galaxies having on average the weakest Lyα and the $z \sim 4$ showing the strongest. The $z \sim 2$ and $z \sim 4$ measurements show a clear trend of less redshifted Lyα centroid with stronger emission, similar to what has been found for LAEs in both individual and composite spectra at $z \sim 2-4$ (Erb et al., 2014; Guaita et al., 2017), while for the $z \sim 3$ sample there does not appear to be a dependence between these two parameters. Although the correlation between Lyα kinematics and strength is not conclusive at $z \sim 3$ based *only* on our measurements, given previous kinematics studies of Lyα at this redshift (e.g., Shapley et al., 2003), we believe that this relation holds at $z \sim 3$ as well. Generally speaking, the data points from different redshift samples seem to follow the same curve, and we do not see any evolutionary trend of the peak velocity vs. EW relation for Lyα from $z \sim 4$ to $z \sim 2$.

In explaining the trend of more redshifted Lyα with weaker Lyα emission across $z \sim 2-4$, we consider two physical scenarios. The first possibility is that the larger (positive) offset of Lyα to the systemic velocity results from the faster-moving outflows on the far side of the galaxies, which at the same time have a larger covering fraction, leading to weaker Lyα emission. In light of the fact that the outflow kinematics can be characterized by the centroid velocity of LIS absorption features, we can test this hypothesis by examining whether the composites with more redshifted (and therefore weaker) Lyα also show more blueshifted LIS lines. In fact, the measured LIS centroid velocities are fairly similar between composites with the strongest and weakest Lyα, counter to what the "faster outflowing gas" hypothesis

predicts.

Alternative models are therefore needed to explain the observed correlation between $EW_{Ly\alpha}$ and its peak velocity. Several studies have attempted to generate the emergent Lyα profile with assumed neutral gas kinematics (e.g., Verhamme et al., 2006, 2008; Steidel et al., 2010). Specifically in Steidel et al. (2010), where the observed profiles of Lyα and the LIS absorption lines are simultaneously recovered by a kinematic model considering the velocity distribution of the neutral gas, these authors found that the apparent velocity shift of Lyα primarily results from the absorption of Lyα photons by neutral gas near the systemic velocity. As the covering fraction of neutral gas increases around $v = 0$, more Lyα photons get resonantly scattered out of the line of sight, pushing the observed Lyα centroid to a redder wavelength, resulting in a weaker Lyα emission at the same time. The model from Steidel et al. (2010) successfully explains our results, and thus the largest $EW_{Ly\alpha}$ seen at $z \sim 4$ is likely caused by the smallest covering fraction near the systemic velocity. Furthermore, the redshift independence of the Lyα velocity vs. EW relation suggests a direct impact of the covering fraction and kinematics of the neutral ISM on the observed Lyα emission profile across $z \sim 2 - 4$. Due to the low resolution of the spectra, we were unable to study the detailed structure of the Lyα profile (e.g., the presence and properties of multiple emission peaks). Future spectroscopic data with high spectral resolution will provide further information on the kinematics and covering fraction of the H I gas.

4.5.2 LIS Absorption Kinematics

While the centroid velocity of Lyα can provide valuable information on neutral gas kinematics, LIS absorption features are typically used to probe the bulk velocities of the neutral phase of ISM/CGM. Ideally, we would like to decompose the interstellar absorption profiles into a systemic and an outflow component, with the latter representing the absorption truly occurring in the outflowing gas. Unfortunately, the relatively low resolution of our data prevents us from obtaining robust measurements from a two-component fit. Therefore, we fit the absorption profiles with a single Gaussian, and used the centroid velocity of the best-fit

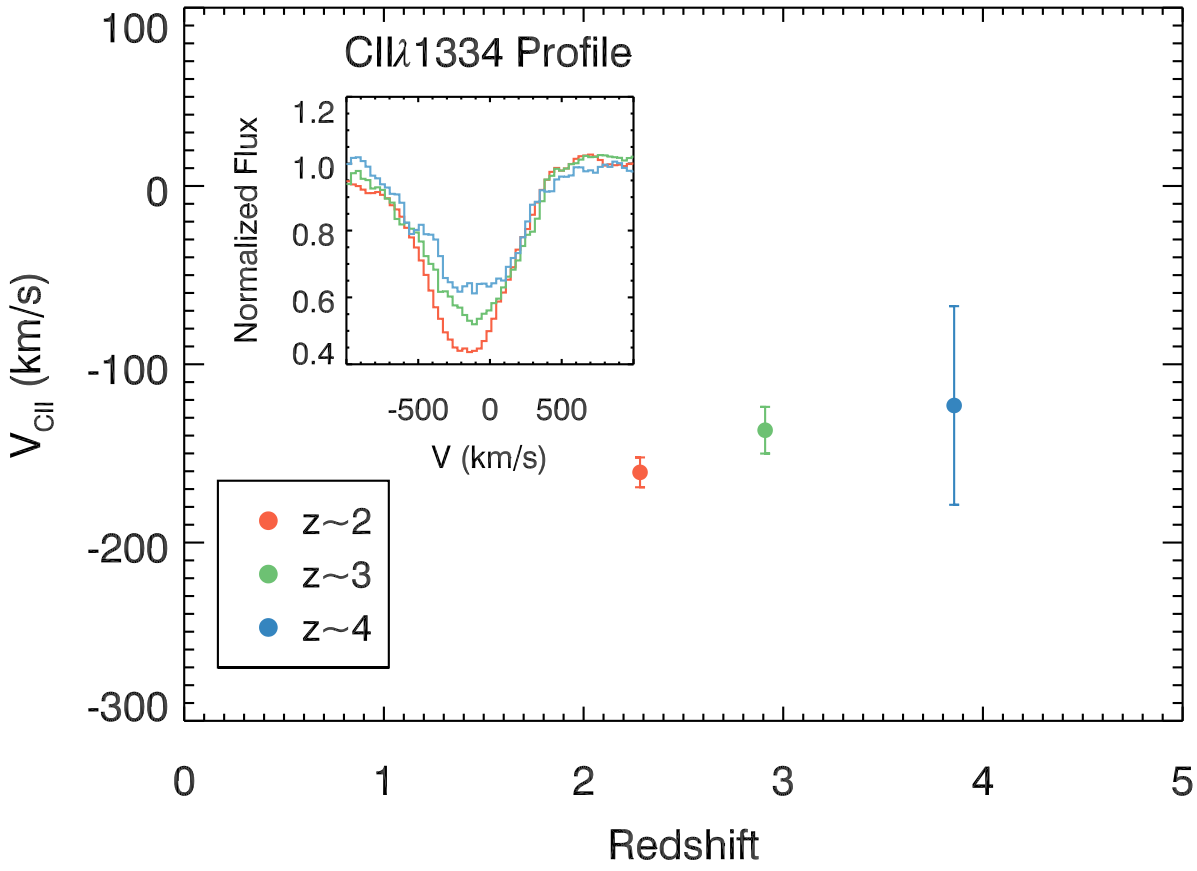

Figure 4.11: Centroid velocity of the C IIλ1334 absorption feature vs. redshift in the composite spectra with fixed median stellar mass, $\log(M_*/M_\odot) = 9.98$. The 1σ error bar on the centroid velocity was estimated based on the composite error spectra, and does not include the uncertainty on the systemic velocity. The C IIλ1334 line profiles in the $z \sim 2$, 3, and 4 fixed-mass composites are shown in the inset panel.

Gaussian model as a crude estimator of the bulk kinematic properties.

In addition, it is most ideal to compare galaxies at different redshifts not only spanning the same UV luminosity and stellar mass ranges, but also having the same median values of these properties. However, due to the different distributions of the redshift samples in the $M_{UV} - M_*$ plane (Figure 4.2), it is difficult to construct such subsamples at each redshift with the same median M_{UV} and stellar mass at the same time. Considering that these two properties are correlated, we chose stellar mass as the "control" and created composite spectra for the $z \sim 2$, $z \sim 3$ samples such that they have the same median stellar mass, $\log(M_*/M_\odot) = 9.98$ as the full $z \sim 4$ sample. Specifically, we constructed the matching-M_* subsamples by including objects starting from the lower-mass end of the $z \sim 2$ and $z \sim 3$ samples, until the median values of these subsamples become the closest to that of the $z \sim 4$ sample. The resulting subsamples include 290, 235, and 84 spectra at $z \sim 2$, 3, and 4, respectively. The higher-redshift subsamples have slightly brighter UV luminosities, with the median M_{UV} for the $z \sim 2$, $z \sim 3$, and $z \sim 4$ samples being -20.48, -20.96, and -21.06, respectively.

In principle, Si IIλ1260, C IIλ1334, and Si IIλ1527 are all good tracers of the ISM kinematics. However, we chose C IIλ1334 as the probe of the low-ion kinematics, mainly to ensure a fair comparison to the evolutionary study at $z \sim 0 - 2$ by Sugahara et al. (2017) (Section 4.6.1), in which the authors used C IIλ1334 to trace neutral gas kinematics. Using the averaged centroid velocity of Si IIλ1260, C IIλ1334, and Si IIλ1527 yields qualitatively the same answer regarding the evolution of interstellar kinematics at $z \sim 2 - 4$ as using C IIλ1334 alone.

Figure 4.11 shows the averaged centroid velocity plotted against redshift. The centroid velocities of C II are -161 ± 8 km s^{-1}, -137 ± 13 km s^{-1}, and -123 ± 56 km s^{-1}, for the $z \sim 2$, $z \sim 3$, and $z \sim 4$ samples, respectively. We note that the error bars quoted here on the velocity measurements do not include the formal uncertainty on the systemic velocity of the composites, Δv_{sys}, which is ~ 25 km s^{-1}for $z \sim 2-3$ galaxies and ~ 120 km s^{-1}for $z \sim 4$

galaxies as estimated from MPFIT.[6] Taking into account Δv_{sys} of all redshift samples, we do not observe a noticeable evolutionary trend of the neutral gas kinematics from $z \sim 2$ to $z \sim 4$ for galaxies at fixed stellar mass. These results, as derived from the centroid velocities, suggest that the kinematics of the neutral ISM/CGM are mostly indistinguishable in galaxies with similar UV luminosity and stellar mass in spite of being at different redshifts. Spectroscopic data with higher S/N and spectral resolution will be of great help for examining the evolution of neutral gas kinematics in greater detail by enabling precise measurements of the outflow component from two-component profile fits. Additionally, high-quality imaging data will provide unique insights into the evolution of outflows through the study of the factors that modulate the strength of the outflows (e.g., size, SFR surface density).

4.6 Discussion

Although we have primarily investigated how the physical properties of the cool ISM/CGM evolve with redshift, the wide spectral coverage in the rest-UV and the unprecedentedly large size of our galaxy samples at $z \gtrsim 2$ enable various analyses that may potentially shed light on multiple key questions in the study of galaxy evolution. Here we extend our results from Sections 4.4 and 4.5, examining the redshift evolution of outflow velocities all the way from $z \sim 0-4$ (Section 4.6.1), and present a physical picture that accounts for the observed spectroscopic trends (Section 4.6.2).

4.6.1 Outflow Velocity at $z \sim 0-4$

In this paper, we have explored how the kinematics of neutral gas evolve from $z \sim 2$ to $z \sim 4$, as probed by the centroid velocity of LIS absorption features. While we did not find noticeable evolution of the outflow velocities of the neutral gas within the $z \sim 2-4$ redshift interval, Sugahara et al. (2017) report evidence of increased outflow velocity from

[6]As described in Section 4.3.1, these formal error bars were estimated by measuring the stellar feature C IIIλ1176 in the overall composites, and therefore do not reflect the systematic uncertainty associated with the redshift rules.

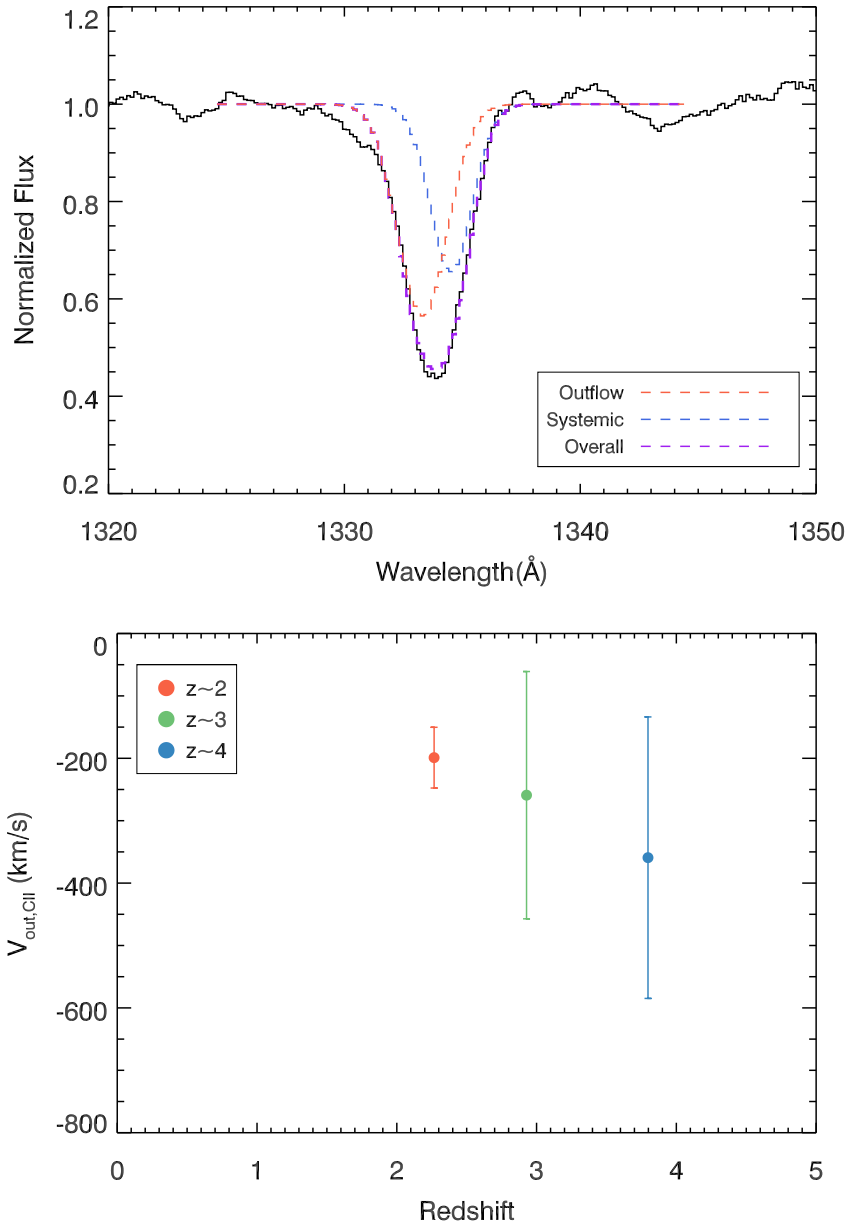

Figure 4.12: **Top:** Best-fit outflow (orange), systemic (blue), and overall (purple) absorption profiles in the two-component fit to the $z \sim 2$ overall composite. **Bottom:** Outflow velocity (determined by the centroid velocity of the outflow component) measured from the $z \sim 2$, $z \sim 3$, and $z \sim 4$ composite spectra including all objects within the UV luminosity and stellar mass constraints.

$z \sim 0$ to $z \sim 2$ based on the measurement of LIS absorption features. These authors studied galaxy spectra at $z \sim 0$, $z \sim 1$, and $z \sim 2$, drawn, respectively, from the Sloan Digital Sky Survey (SDSS; York et al., 2000), DEEP2, and Erb et al. (2006c,b), with the last comprising a subset of the $z \sim 2-3$ LRIS sample presented in this paper. Considering the different rest-frame spectral coverage of the three datasets, Sugahara et al. (2017) used ions with similar ionization energy for the comparison at different redshifts: Na I D$\lambda\lambda$5891, 5897 and Mg Iλ2853 from $z \sim 0$ to $z \sim 1$, and Mg II$\lambda\lambda$2796, 2803 and C IIλ1334 from $z \sim 1$ to $z \sim 2$. Given that we also cover the C II feature in our $z \sim 2-4$ spectra, it is possible to extend the $z \sim 0-2$ evolutionary study of neutral gas kinematics by Sugahara et al. (2017) up to $z \sim 4$, connecting the lower- and higher-redshift universe.

Sugahara et al. (2017) constructed the $z \sim 0-2$ samples such that they have similar normalized stellar mass distributions. The $z \sim 0$ and $z \sim 1$ composites were binned according to SFRs, while the $z \sim 2$ stacks included all objects in the $z \sim 2$ sample. To characterize the interstellar absorption profiles in the composite spectra, Sugahara et al. (2017) adopted a two-component model, which includes an outflow component and a systemic component. The profile of each component in the model is described by $I(\lambda) = 1 - C_f + C_f e^{-\tau(\lambda)}$ and $\tau(\lambda) = \tau_0 e^{-(\lambda-\lambda_0)^2/(\lambda_0 b_D/c)^2}$, where C_f is the covering fraction, τ is the optical depth as a function of wavelength, τ_0 is the optical depth at the rest wavelength λ_0, and b_D is the Doppler parameter. Since the absorption lines were fit with a single Gaussian profile in our study, we cannot directly compare our results with those presented in Sugahara et al. (2017). Instead, we conducted a crude two-component Gaussian fit to the C IIλ1334 absorption line profile in the continuum-normalized, overall composites at $z \sim 2$, 3, and 4. According to Sugahara et al. (2017), the observed flux of the interstellar absorption in the continuum-normalized spectra is $I_{obs}(\lambda) = I_{out}(\lambda) I_{sys}(\lambda)$, where $I_{out}(\lambda)$ and $I_{sys}(\lambda)$ are the outflow and systemic components with the continuum normalized to unity, respectively. Accordingly, we fit the C II profile using MPFIT to simultaneously model the systemic component at the rest wavelength (1334.5Å), and the blueshifted outflow component. The functional form of the model we adopted is

Table 4.3: Best-fit Parameters of 2-Component Models for $z \sim 2-4$ Composites

Sample	λ_{sys} (Å)	$FWHM_{sys}$ (Å)	$Area_{sys}$ (Å)	λ_{out} (Å)	$FWHM_{out}$ (Å)	$Area_{out}$ (Å)
$z \sim 2$	1334.532	0.79 ± 0.29	0.31 ± 0.41	1333.647 ± 0.216	1.25 ± 0.09	1.61 ± 0.32
$z \sim 3$	1334.532	0.96 ± 0.26	0.70 ± 0.73	1333.379 ± 0.881	1.37 ± 0.36	1.06 ± 0.76
$z \sim 4$	1334.532	1.04 ± 0.31	0.87 ± 0.33	1332.934 ± 1.003	1.03 ± 0.77	0.53 ± 0.43

* Column $2-4$ and $5-7$ represent the line centroid, Gaussian FWHM, and enclosed area for the systemic and outflow components in the continuum-normalized composites, respectively. The systemic component was fixed at the rest-wavelength of C II, 1334.532Å.

$$I_{obs} = (1.0 - P_{sys}) \times (1.0 - P_{out}) \tag{4.1}$$

where P_{sys} and P_{out} are the Gaussian profiles parameterized by line centroid, Gaussian FWHM, and enclosed area for the systemic and outflow components in the continuum-normalized composites, respectively. We list the best-fit parameters of the two-component models for the $z \sim 2$, 3, and 4 overall composites in Table 4.3. In contrast to Sugahara et al. (2017), we did not apply additional constraints on the covering fraction, optical depth, and the impact parameter.

We show an example of the two-component best-fit we obtained with the $z \sim 2$ composite in the top panel of Figure 4.12. The outflow velocity, V_{out}, can therefore be derived from the shift in centroid of the outflow component. Best-fit values of $V_{out,\mathrm{C\ II}}$ over $z \sim 2-4$ are plotted in the bottom panel of Figure 4.12. We measure an outflow velocity of -199 ± 49 $\mathrm{km\,s^{-1}}$, -259 ± 198 $\mathrm{km\,s^{-1}}$, and -359 ± 226 $\mathrm{km\,s^{-1}}$for the $z \sim 2$, $z \sim 3$, and $z \sim 4$ samples, respectively. Within the error bars, [7] no clear evolution is shown for the C II kinematics. Specifically, our measurement of $V_{out,\mathrm{C\ II}}$ at $z \sim 2$ is in good agreement with the value quoted in Sugahara et al. (2017), -208 ± 30 $\mathrm{km\,s^{-1}}$, assuming $C_{f,sys} = 0.1$ without any additional constraints. We also note that this result is consistent with what we found in Section 4.5.2,

[7]We note that the uncertainty on the outflow velocities is fairly large, which is likely due to the lack of constraints on both the outflow and systemic components, leading to numerous possible combinations near the minimum χ^2.

that the neutral gas kinematics do not appear to evolve significantly when being probed by the Gaussian centroid velocity of multiple LIS absorption features. While the lack of redshift evolution of the outflow velocity may not be definitive based *only* on Figure 4.12, we can conclude that we do not see an apparent evolution of the neutral gas kinematics from $z \sim 2-4$ when combining our result here with that in Section 4.5.2.

If we consider the overall evolution of the neutral gas kinematics from $z \sim 0$ to $z \sim 4$, combining both our results and those from Sugahara et al. (2017), the outflow velocity seems to stop increasing significantly beyond $z \sim 2$. A couple of factors may contribute to this "turning point." First, given the positive relation between outflow velocities and the SFR surface density observed in star-forming galaxies (Heckman et al., 2000; Chen et al., 2010; Kornei et al., 2012), the flattening of the outflow velocity at higher redshifts may result from a smaller change in SFR surface density at fixed mass by a factor of ~ 2.5 at $z \sim 2$ to $z \sim 4$ relative to that at $z \sim 0$ to $z \sim 2$ (e.g., Shibuya et al., 2015). Secondly, galaxies at $z \leqslant 1.5$ tend to show a bipolar outflow geometry (e.g., Rupke et al., 2005; Martin et al., 2012; Rubin et al., 2014), as inferred by the outflow detection rate among galaxies with similar star-forming properties as well as the detection of extraplanar gas perpendicular to the plane (e.g., Bordoloi et al., 2011). Galactic-scale outflows at $z \gtrsim 2$, on the other hand, are much more ubiquitous (e.g., Pettini et al., 2002; Shapley et al., 2003; Steidel et al., 2010), suggesting a more spherical geometry. Therefore, the smaller detection fraction of blueshifted interstellar absorption lines may make those line profiles less blueshifted in the composites at $z \sim 0-2$ than at $z \sim 2-4$, resulting in an apparent plateau in outflow speed at $z \sim 2$ and higher. Since both factors can collectively affect the observed interstellar absorption profiles in the composites, individual spectra with significant outflow detections or composite spectra constructed by *only* stacking those with individual detections of outflows would help determine if the SFR surface density or the outflow geometry plays a more important role in this "turning point" at $z \sim 2$.

4.6.2 A physical picture

We now interpret our results in a physical picture for the evolution of Lyα emission, and the properties of the absorbing ISM. We also consider the implications of our results for estimates of the Lyman-continuum escape fraction during the epoch of reionization.

4.6.2.1 Lyα Emission

Lyα emission is commonly the strongest feature in the UV spectra of distant star-forming galaxies and has been used to confirm the spectroscopic redshifts of galaxies out to $z > 8$ (Zitrin et al., 2015). Furthermore, large samples of LAEs have been assembled at $z \sim 6 - 7$ in order to probe the neutral fraction of the IGM (e.g., Konno et al., 2018). Given the prevalence of Lyα measurements, it is important to describe how $\mathrm{EW}_{Ly\alpha}$ relates to other galaxy properties, and, more fundamentally, to understand the factors controlling the observed strength of Lyα emission. This knowledge will enable us to relate LAEs to the star-forming galaxy population in general over a wide range of redshifts, and to use the measurement of Lyα as a probe of other key galaxy properties that cannot be directly measured (e.g., escaping Lyman-continuum radiation during the epoch of reionization).

There are three key factors to highlight when attempting to explain the observed Lyα emission properties of high-redshift star-forming galaxies: (1) the intrinsic production of Lyα photons through nebular recombination emission; (2) the radiative transfer of Lyα photons through the ISM and CGM; (3) the radiative transfer of Lyα photons through the increasingly neutral IGM at higher redshifts. Here we consider the importance of these factors, as suggested by our results.

We have established the constancy of the relations among Lyα emission, LIS absorption, and dust extinction (as parametrized by $E(B-V)$), extending over the widest redshift baseline ($z \sim 2 - 4$), and using the most systematically controlled samples to date. In fact, a similar relationship between $\mathrm{EW}_{Ly\alpha}$, and EW_{LIS} has even been observed in $z \sim 0$ star-forming galaxies (e.g., Henry et al., 2015; Chisholm et al., 2017). The direct and non-evolving connection between $\mathrm{EW}_{Ly\alpha}$, EW_{LIS}, and $E(B-V)$ suggests that the evolving

relations between Lyα and other galaxy properties (e.g., M_{UV}, age, M_*, SFR) arise as the LIS-absorption gas and dust reddening (at fixed galaxy properties) evolve with redshift. Furthermore, according to one simple interpretation of the trends among $\mathrm{EW}_{Ly\alpha}$, EW_{LIS}, and $E(B-V)$, galaxies in our samples all have similar *intrinsic* Lyα EWs, as determined by the ionizing photon production efficiency for a given mass of stars formed, and a relatively constant (and small) escape fraction of Lyman-continuum photons. Together these two factors determine the ratio of Lyα recombination luminosity to UV continuum luminosity density (i.e., the rest-frame Lyα EW Reddy et al., 2016). Accordingly, in this simple picture, the observed range of $\mathrm{EW}_{Ly\alpha}$ at $z \sim 2-4$ is entirely determined by the range of LIS-absorbing gas covering factors and dust reddenings – i.e., the radiative transfer of Lyα through the ISM and CGM.

However, our results on the correlation between Lyα and C III] emission suggest that, at the highest Lyα EWs, the H II region properties and the massive stars that ionize them, are intrinsically different. Specifically, in our $z \sim 2$ sample, galaxies in the quartile with the strongest Lyα emission (median $\mathrm{EW}_{Ly\alpha} \sim 10$Å) also have significantly stronger C III] emission than in the remainder of the sample. As shown in theoretical and observational work (e.g., Rigby et al., 2015; Jaskot & Ravindranath, 2016; Senchyna et al., 2017) stronger C III] EWs are typically produced in lower metallicity (i.e., significantly sub-solar) H II regions where the electron temperature is higher and the stellar ionizing radiation is stronger. Accordingly, this result indicates a connection between Lyα emission strength and nebular metallicity. This result is consistent with the work of Trainor et al. (2016), who show that $\mathrm{EW}_{Ly\alpha}$ is strongly correlated with nebular metallicity at $z \sim 2$, as probed by rest-optical emission line ratios indicating the degree of excitation and ionization. Therefore, the strength of Lyα emission, at least at the highest values of $\mathrm{EW}_{Ly\alpha}$, reflects not only the transfer Lyα photons through the ISM but also the ionizing spectra, ionization parameters, and nebular metallicities of the H II regions where Lyα photons are originally produced.

The increasing neutral hydrogen opacity in the IGM is evident in the $z \sim 2$, 3, and 4 composite spectra shown in Figure 4.3. Specifically, the ratio of continuum flux density bluewards of Lyα relative to that redwards of Lyα decreases significantly from $z \sim 2$ to

$z \sim 4$. Simulations (e.g., Laursen et al., 2011) suggest that increasing IGM opacity will lead to a measurably reduced Lyα EW, by $\sim$25% at $z = 3.5$, and by $\sim$ 75% at $z = 5.8$. Jones et al. (2012) in fact find evidence for this effect when comparing the Lyα and LIS properties of composite spectra constructed from LBG subsamples at $\langle z \rangle = 3.8$ and $\langle z \rangle = 4.7$. For roughly the same EW$_{Ly\alpha}$, the $\langle z \rangle = 4.7$ sample has a significantly weaker EW$_{LIS}$ ($\sim$ 1Å at $\langle z \rangle = 4.7$ vs. $\sim$ 1.7Å at $\langle z \rangle = 3.8$). This difference can be explained if the $\langle z \rangle = 3.8$ and $\langle z \rangle = 4.7$ galaxies follow the same intrinsic relationship between EW$_{Ly\alpha}$ and EW$_{LIS}$, but the average EW$_{Ly\alpha}$ in the subset of LBGs at $\langle z \rangle = 4.7$ is suppressed by roughly a factor of two by IGM absorption – consistent with the predictions by Laursen et al. (2011). In our work, we find no significant difference among the EW$_{LIS}$ vs. EW$_{Ly\alpha}$ relations from $z \sim 2$ to $z \sim 4$. This result suggests that, even in our $z \sim 4$ sample, the IGM absorption of Lyα photons produced in LBGs is not significant, or that we are not measuring the part of the Lyα profile that is affected by IGM absorption. Alternatively, $z \sim 4$ galaxies may follow a different intrinsic relation between EW$_{Ly\alpha}$ and EW$_{LIS}$ relative to the $z \sim 2-3$ samples, characterized by higher EW$_{Ly\alpha}$ for a given EW$_{LIS}$. The increased IGM absorption at $z \sim 4$ then attenuates the EW$_{Ly\alpha}$ to the point that the $z \sim 4$ sample follows the same patterns as the lower redshift galaxies, mimicking a non-evolving EW$_{Ly\alpha}$ vs. EW$_{LIS}$ relation. For now, we favor the simpler explanation that the EW$_{LIS}$ vs. EW$_{Ly\alpha}$ relation does not evolve between $z \sim 2$ and $z \sim 4$ and that the effects of IGM absorption are not significant within our $z \sim 2-4$ samples. We also note that the lack of evolution between Lyα kinematics ($v_{Ly\alpha}$) and EW$_{Ly\alpha}$ (Section 4.5.1) are consistent with the subdominance of evolving IGM absorption in our $z \sim 2-4$ measurements. However, it will be extremely valuable to investigate the combined possible effects of IGM and ISM evolution out to $z \sim 5-6$ using existing rest-UV spectroscopic samples (e.g., Faisst et al., 2016).

4.6.2.2 The Absorbing ISM

Although $z \sim 2-4$ galaxies follow the same relations among EW$_{Ly\alpha}$, EW$_{LIS}$, and $E(B-V)$, the *average* EW$_{Ly\alpha}$ increases from $z \sim 2-4$, while the average EW$_{LIS}$ and $E(B-V)$ decrease. This evolution in average properties suggests that (at fixed UV luminosity), the covering

fraction of LIS-absorbing gas and dust decreases from $z \sim 2-4$. As demonstrated by Reddy et al. (2016), the covering fractions of various low ions is correlated with, but systematically lower than, the covering fraction of H I (f_{cov}(H I)) by a factor of 2–3. Furthermore, the ratio between the covering fractions of low ions and H I increases as f_{cov}(H I) increases. These trends, as described in Reddy et al. (2016), are consistent with a scenario in which discrete metal-enriched regions of interstellar gas are contained within the outflowing interstellar HI, whose dust-to-gas (i.e., metal-to-gas) ratio increases with increasing covering fraction of HI. Accordingly, the decrease in average EW_{LIS} from $z \sim 2$ to $z \sim 4$ corresponds to a decrease in the average covering fraction of interstellar HI.

Two factors that may contribute to the decrease in the covering fraction of interstellar H I (at fixed galaxy properties such as UV luminosity) are (1) an evolving average stellar radiation field corresponding to a harder ionizing spectrum at $z \sim 4$ than at $z \sim 2$, and (2) a decrease in the overall covering fraction of both neutral and ionized interstellar gas. We can test for the presence of both of these effects in our data.

To investigate the nature of the ionizing radiation field, we used the relative column densities of Si II and Si IV as a proxy of the ISM ionization state. As discussed in Section 4.4.1, we found that the column density of Si IV appears to increase from $z \sim 2$ to $z \sim 3-4$, At the same time, the variation in the EW ratio of Si IIλ1260 and Si IIλ1527 can be used to infer a change in the column density of Si II. In the optically thin regime, the EW of Si IIλ1260 should be ~ 5.3 times larger than that of SiIIλ1527. We observe $\mathrm{EW}_{\text{Si II}\lambda1260}/\mathrm{EW}_{\text{Si II}\lambda1527}$ ratios of 0.93 ± 0.03Å, 0.84 ± 0.07Å, and 1.30 ± 0.25Å at $z \sim 2$, 3, and 4, respectively. This progression suggests a slight decrease in Si II column density from $z \sim 2$ to $z \sim 4$. The combined increase and decrease in the respective column densities of Si IV and Si II suggest a more highly ionized ISM at $z \sim 4$ than at $z \sim 2$. We also note that, in simple, empirical terms, the ratio of the EWs of Si IV and Si II lines increases from $z \sim 2-4$, as seen in the composite spectra of Figure 4.3: compare the relative depths of Si IV and Si II features in the $z \sim 2$ (red) and the $z \sim 4$ (blue) composites.

While the balance between high and low ions in the ISM of star-forming galaxies at $z \sim 2-4$ may evolve, it also appears that the covering fraction of both neutral and ionized

phases decreases. This decrease is traced by the decreasing EW of saturated LIS lines, and by the roughly constant EW of Si IV absorption as the column density increases (Section 4.4.1). The evolution in the covering fraction of interstellar gas must reflect an evolving balance among gas accretion, star formation, and feedback. For example, star-forming galaxies at fixed UV luminosity are smaller at $z \sim 4$ than at $z \sim 2-3$, with approximately doubled SFR surface densities (Shibuya et al., 2015). Given the connection between outflow properties and SFR surface density (Heckman et al., 2000; Chen et al., 2010; Kornei et al., 2012), the higher typical SFR surface densities at $z \sim 4$ may correspond to outflows that more efficiently clear out channels through the ISM, reducing the covering fraction of gas, and allowing for the escape of Lyα photons. Alternatively, if outflows have similar properties at $z \sim 2-4$ (at fixed UV luminosity) in terms of energy and momentum input, and ability to evacuate holes in the ISM, we may be observing the accumulation of gas in the ISM and CGM as cosmic time advances. At least in our results, we do not detect significant evolution in the bulk outflow kinematics from $z \sim 2-4$ (Section 4.5.2, Section 4.6.1), so this second alternative is also plausible. A comparison with gas in galaxies modeled in cosmological zoom-in simulations (e.g., Feldmann et al., 2017), as well as observations at both lower and higher redshifts, will be crucial for understanding the evolution of the covering fraction of metals and H I in the neutral ISM of star-forming galaxies.

We now consider the connection between the covering fraction of H I and dust reddening. As shown in this work and previously (e.g., Shapley et al., 2003; Jones et al., 2012; Reddy et al., 2016), there is a strong correlation between EW_{LIS} and $E(B-V)$, such that stronger LIS absorption is associated with increased dust reddening. At the same time, there is no significant connection between the high-ionization absorption strength, EW_{HIS} and $E(B-V)$. These results suggest that dust responsible for reddening the stellar continuum in the outflowing ISM/CGM is confined to the neutral regions probed by the LIS features. We would also like to understand what fraction of the reddening and attenuation of the UV continuum takes place in the outflowing ISM/CGM as opposed to gas that is much more local to H II regions and not participating in large-scale outflows. For example, does the evolution at $z \sim 2-4$ towards lower $E(B-V)$ at fixed galaxy properties such as M_{UV}

and SFR reflect more than simply the evolution towards lower H I gas covering fraction, but also the overall lower degree of H II region chemical enrichment (and dust content) at higher redshift (at fixed galaxy properties)? Spatially resolved high-S/N measurements of EW_{LIS} and $E(B-V)$ indicating the degree of correlation between small-scale EW_{LIS} and $E(B-V)$ variations may help address this important question of where significant dust attenuation occurs.

4.6.2.3 Lyman-continuum Emission

One of the frontiers for galaxy formation studies is to quantify the contribution of star-forming galaxies to reionization (for a review see Stark et al., 2017). Measurements of the non-ionizing rest-frame UV luminosity function are extending to extremely faint magnitudes based on Hubble Frontier Fields observations (e.g., Livermore et al., 2017; Bouwens et al., 2017). However, since neither Lyman-continuum radiation nor any of the Lyman series absorption features bluewards of Lyα can be measured directly during the epoch of reionization (Vanzella et al., 2012; Shapley et al., 2016), we require another proxy for the Lyman-continuum radiation properties of $z > 6$ galaxies. Recent work at both low-redshift and $z \sim 3$ has highlighted the connection between the strength of Lyα emission, the H I covering fraction, and the escape of Lyman-continuum radiation (Shapley et al., 2003; Jones et al., 2013; Trainor et al., 2015; Reddy et al., 2016; Marchi et al., 2017; Chisholm et al., 2017, Steidel et al., in prep). Galaxies with higher ratios of Lyman-continuum to non-ionizing UV radiation tend to show stronger Lyα emission and weaker LIS absorption, and models of their UV spectra suggest lower H I covering fractions.

Here we suggest that measuring Lyα and LIS absorption properties of $z > 6$ star-forming galaxies holds great promise for estimating how Lyman-continuum escape varies with UV luminosity during the Epoch of Reionization. In particular, one promising path forward consists of using the Lyα escape fraction as a proxy for the H I covering fraction (and, accordingly the Lyman-continuum escape fraction which is $1 - f_{cov}$(H I); Jones et al., 2013; Leethochawalit et al., 2016) in bins of UV luminosity. For this method to be effective, there

are key uncertainties that will need to be addressed: (1) we will need to estimate and correct for the typical IGM absorption of the Lyα emission profile at $z \sim 6$; (2) we will require constraints on the intrinsic production rate of Lyα photons in $z \sim 6$ star-forming galaxies in order to convert the observed $\mathrm{EW}_{Ly\alpha}$ (corrected for IGM absorption) to a Lyα escape fraction. It is also tempting to use measurements of LIS absorption at $z \sim 6$ to predict f_{cov}(H I). However, given the hints of significant metallicity evolution out to $z \sim 6$ in star-forming galaxies (e.g., Stark et al., 2017), typical LIS absorption features at $z \sim 6$ may not be saturated, and therefore not offer a direct probe of the H I covering fraction. More generally, the H I gas may be optically thinner at $z \sim 6$ than at $z \sim 3$, which indicates that the absolute escape fraction of LyC photons would no longer be $1 - f_{cov}$(H I) as stated earlier. In order to understand the utility of EW_{LIS} for probing the H I covering fraction at $z \sim 6$, we should first trace the $\mathrm{EW}_{Ly\alpha}$ vs. EW_{LIS} relation out to $z \sim 6$, using high-quality $z \sim 4-6$ ground-based galaxy spectra. At even higher redshifts, rest-UV spectroscopy with the *James Webb Space Telescope* (JWST) will prove a powerful tool for constraining the Lyman-continuum emission properties of star-forming galaxies.

4.7 Summary

Rest-UV spectroscopic features provide rich insights into the key properties (structure, kinematics, covering fraction) of the ISM/CGM in star-forming galaxies. By constructing LBG samples controlled in UV absolute magnitude and stellar mass at $z \sim 2-4$, and performing systematic measurements of the spectral and galaxy properties in a uniform manner, we primarily studied the evolution in line strengths and kinematics of both emission and absorption features in the rest-UV spectra. We have found the following key results:

1. No noticeable redshift evolution is found for the relations among $\mathrm{EW}_{Ly\alpha}$, EW_{LIS}, and $E(B-V)$. In other words, Lyα, LIS lines, and dust extinction are fundamentally inter-correlated. Specifically, the redshift independence of the $\mathrm{EW}_{Ly\alpha}$ vs. EW_{LIS} relation suggests either that the covering fraction of neutral gas is the dominant factor for modulating both $\mathrm{EW}_{Ly\alpha}$ and EW_{LIS} in the same manner at all redshifts, or that the intrinsically higher

$EW_{Ly\alpha}$ due to lower metallicity and stronger radiation fields at higher redshifts at fixed galaxy property is compensated by increased absorption from the IGM. In contrast, the strength of Lyα exhibits no correlation with the HIS absorption strength, suggesting that Lyα and the HIS absorption features trace different phases of gas. The approximately constant EW_{HIS} over $z \sim 2-4$ suggests a lower covering fraction of the ionized gas at higher redshifts, given the apparent increasing Si IV column density.

2. We observe a redshift-invariant correlation between EW_{LIS} and $E(B-V)$, which is consistent with a physical picture in which dust and metal ions are embedded in the outflowing H I gas. Both the covering fraction of neutral gas, as probed by EW_{LIS}, and dust extinction seem to decrease with increasing redshift. We interpret this redshift evolution with two possible scenarios: either the $z \sim 4$ galaxies are more effective in reducing the H I covering fraction and dust content by increasing the ionization state of the ISM and driving powerful outflows, or the $z \sim 2-3$ galaxies are more efficient in accumulating gas and dust as they evolve. Individual spectra with high S/N, spectral and spatial resolution will shed light on the physical location of the dust with respect to the neutral gas.

3. The strength of Lyα emission decreases with decreasing redshift at fixed stellar mass, UV luminosity, and SFR, which likely results from a larger covering fraction of the neutral gas and higher $E(B-V)$ at lower redshifts. In the $z \sim 2$ and $z \sim 3$ samples, $EW_{Ly\alpha}$ shows little to no correlation with stellar mass, UV luminosity, and SFR. However, stronger $EW_{Ly\alpha}$ is observed at fainter galaxies with lower stellar mass and SFR at $z \sim 4$. The weakening of these trends from $z \sim 4$ to $z \sim 2$ is likely caused by a larger dynamic range of the neutral gas covering fraction at $z \sim 4$ than at $z \sim 2$ and $z \sim 3$. Although the sample incompleteness enhances the observed Lyα trends, the evolution of these relations (i.e., stronger Lyα emission at higher redshifts at fixed galaxy properties, steeper Lyα trends at $z \sim 4$ than at $z \sim 2-3$) still exists after we have accounted for differential sample incompleteness. We thus conclude that the trends are real and robust, and not simply an effect of increasing sample incompleteness to galaxies lacking Lyα emission at higher redshift and fainter magnitude.

4. Younger galaxies at $z \sim 4$ show stronger Lyα, which can be attributed to their lower

gas-phase metallicities and harder ionizing spectra. On the other hand, no visible trends are seen at $z \sim 2$ and $z \sim 3$ between $\mathrm{EW}_{Ly\alpha}$ and galaxy age. The different behavior of the $\mathrm{EW}_{Ly\alpha}$ vs. age relation can be explained by the $z \sim 2-3$ galaxies being more chemically enriched at the youngest ages than the $z \sim 4$ galaxies, which are possibly experiencing their first generation of star formation. Our results here do not support the positive correlation between Lyα and age, previously reported in some studies of $z \sim 3$ LBGs (Shapley et al., 2001; Kornei et al., 2010). In this earlier work, the authors modeled galaxy SEDs assuming 1.4 solar metallicity and the Calzetti extinction curve, and did not account for the contamination of strong nebular emission lines in the photometric bands. We found that with the most reasonable description of the stellar populations in the $z \sim 3$ galaxies in our sample (0.28 solar metallicity and the SMC extinction curve except for the highest-mass objects), the positive correlation between $\mathrm{EW}_{Ly\alpha}$ and age disappears after removing the contaminated K_s-band from SED modeling.

5. The ratio of fine-structure emission to corresponding resonant absorption does not evolve significantly with redshift at fixed dust extinction. While on average larger $\mathrm{EW}_{\mathrm{Si\ II}^*}/\mathrm{EW}_{\mathrm{Si\ II}}$ is observed at $z \sim 4$, this trend is a result of the lower dust extinction in higher-redshift galaxies, rather than an evolution with cosmic time towards larger size of the fine-structure emission region.

6. We find a flat trend between $\mathrm{EW}_{\mathrm{C\ III]}}$ and $\mathrm{EW}_{Ly\alpha}$ at $z \sim 2$ except in the quartile with the strongest Lyα emission, where the C III] emission is significantly higher than in the remaining Lyα stacks. Given that $\mathrm{EW}_{\mathrm{C\ III]}}$ depends on the physical properties of the H II regions (e.g., gas-phase metallicity, ionization parameter), this result suggests variation in the *intrinsic* Lyα production among galaxies in our samples. Galaxies with larger observed $\mathrm{EW}_{Ly\alpha}$ may not only have lower H I gas covering fractions, but also intrinsically produce more ionizing (and Lyα) photons per unit mass of stars formed.

7. We measure no strong evolution in the key rest-UV spectroscopic trends tracing interstellar kinematics. The trend that strong $\mathrm{EW}_{Ly\alpha}$ corresponds to more redshifted Lyα emission profile seems to be universal across $z \sim 2-4$, which suggests that the covering fraction of the neutral gas near $v = 0$ modifies the Lyα profile in the same manner across $z \sim$

$2-4$. On the other hand, the outflow velocities traced by the centroids of the LIS absorption features do not exhibit any evolutionary trend with redshift. We therefore speculate that the kinematics of the neutral gas are similar in LBGs in fixed UV luminosity and stellar mass ranges at $z \sim 2-4$.

Answering the key outstanding questions in the study of the evolving ISM/CGM at high redshift will require spectroscopic data with high S/N and spectral resolution, along with Integral Field Unit (IFU) spectroscopic maps. For example, rest-UV and optical spectral maps of lensed, spatially-resolved galaxies will provide key information dissecting the relative physical distribution of neutral gas and dust. Furthermore, the near-IR capabilities of the JWST will enable rest-UV and rest-optical spectroscopic studies of star-forming galaxies out to $z > 6$. With these high-quality individual, deep spectra, detailed, quantitative conclusions can be drawn on topics including: (1) the nature of the relation between dust and neutral gas; (2) the intrinsic production and escape of Lyα and Lyman-continuum photons; and (3) the detailed kinematics and spatial extent of the neutral and ionized phases of outflows. Making progress on these questions from an empirical standpoint is essential for our understanding of where the ISM/CGM absorption arises in galaxies, and a complete model of feedback in galaxy formation.

4.A Appendix

4.A.1 Individual and Composite Error Spectra

Individual error spectra are essential for creating the composite error spectra, which ideally account for both sample variance and measurement uncertainty. However, the individual error spectra were not available for all the $z \sim 2$ and $z \sim 3$ galaxies, and for the FORS2 objects in the $z \sim 4$ sample. In this subsection, we describe how we constructed the composite error spectra for the $z \sim 2-3$ and the $z \sim 4$ samples, respectively, despite the lack of some individual error spectra.

To create the composite error spectra for the $z \sim 2$ and $z \sim 3$ samples, we first recon-

structed individual error spectra for all $z \sim 2-3$ galaxies by utilizing the vast library of the individual LRIS error spectra attained in the $z \sim 1$ outflow kinematic study presented in Martin et al. (2012). In this study, a sample of 208 objects were drawn from the Deep Extragalatic Evolutionary Probe 2 (DEEP2; Newman et al., 2013) galaxy redshift survey spanning the range $0.4 \leqslant z \leqslant 1.4$ and apparent B-band magnitude $B < 24.0$, and were observed with LRIS. The 400 lines mm^{-1} and 600 lines mm^{-1} grisms were used to obtain the blue side of the spectra. 145 objects were observed with the 400-lines mm^{-1} grism and 63 objects were observed with the 600-lines mm^{-1} grism. The individual one-dimensional error spectra for the $z \sim 1$ galaxies were determined by the standard deviation at each wavelength of the corresponding science spectra of the same object from multiple exposures.

To reconstruct the individual error spectra of the $z \sim 2-3$ LRIS spectra, the main goal is to recover the shape of the error spectra, which is set by the sensitivity of the instrument in the observed frame. We first made the 400-line and 600-line error spectrum templates by stacking individual error spectra with respective spectral resolution. When being combined, these individual error spectra were scaled to a common median over $4000-5000$Å in the observed frame. We then used the IRAF *continuum* routine to fit the general shape of the two error spectrum templates with an order of 5. After obtaining the smoothed error spectrum templates, for each object in the $z \sim 2-3$ LBG sample that was observed with the 400-line (600-line) grism, we shifted the 400-line (600-line) template to the rest-frame, and scaled it such that the pixel-to-pixel noise over $1250-1400$Å in the rest-frame science spectrum matched the average flux level of the rest-frame error template across the same wavelength range.

Unfortunately, we were unable to precisely simulate the overall shape of the 300-line grating and grism error spectra, given that the $z \sim 1$ DEEP2/LRIS data were not obtained with these configurations on LRIS. For this small fraction of our sample ($\sim 7\%$ combined at $z \sim 2-3$), we adopted the shape of the 400-line grism error template for the 300-line grating and grism objects as a crude estimate. For individual 300-line galaxies, the 400-line error template was also transformed into their respective rest frames, and scaled to match the rms of corresponding science spectra over $1250-1400$Å. We note that approximating

the individual 300-line error spectra with the 400-line error template does not affect the line measurements in the composite spectra significantly. Removing the 300-line grating and grism objects from the composites (and therefore having "clean" $z \sim 2$ and $z \sim 3$ samples of only 400- and 600-line objects with well-reconstructed individual error spectra) results in a change of only $\lesssim 8\%$ or within the 1σ uncertainty for the $\mathrm{EW}_{Ly\alpha}$ measurements, and $\lesssim 5\%$ of change in the EW_{LIS}.

With estimates of the individual error spectra of the $z \sim 2$ and $z \sim 3$ galaxies in hand, we bootstrap-resampled the objects in each bin and perturbed each spectrum (in the L_λ space) in the bootstrap sample according to its own error spectrum. The perturbed spectra in the bootstrap sample were then scaled and combined (following the same procedure of constructing the science composites) to create a new composite spectrum. The process was repeated 100 times and the standard deviation of these 100 fake composites at each wavelength was adopted as the composite error spectrum for each bin.

The construction of the composite error spectra for the $z \sim 4$ sample is a bit different. While the DEIMOS objects have available individual error spectra, the FORS2 objects do not. Considering that the individual error spectra were only needed for creating the composite error spectra, we evaluated the relative contribution of bootstrap resampling and individual error spectra to the overall uncertainty for both the DEIMOS and FORS2 objects, based on their proportion in the $z \sim 4$ sample and typical S/N.[8] We first calculated the ratio of the uncertainty estimated from 'bootstrap only' to that from both bootstrap and individual error spectra for the DEIMOS data. The median value of the ratio is 0.404, which was estimated over $1250 - 1400$Å, a spectral region within which DEIMOS has a decent sensitivity. Given that the DEIMOS spectra on average have lower S/N at these wavelengths than the FORS2 spectra (median $S/N = 2.76$ and 4.07, respectively), we scaled the individual DEIMOS error spectra down by a factor of $4.07/2.76 = 1.47$ to match the S/N of the FORS2 spectra, assuming that the FORS2 error spectra have the same shape

[8]As the $z \sim 4$ sample mainly consists of DEIMOS and FORS2 objects (80 out of 91 spectra), we did not take into account the $z > 3.4$ LRIS galaxies and their reconstructed individual error spectra when estimating the overall uncertainty.

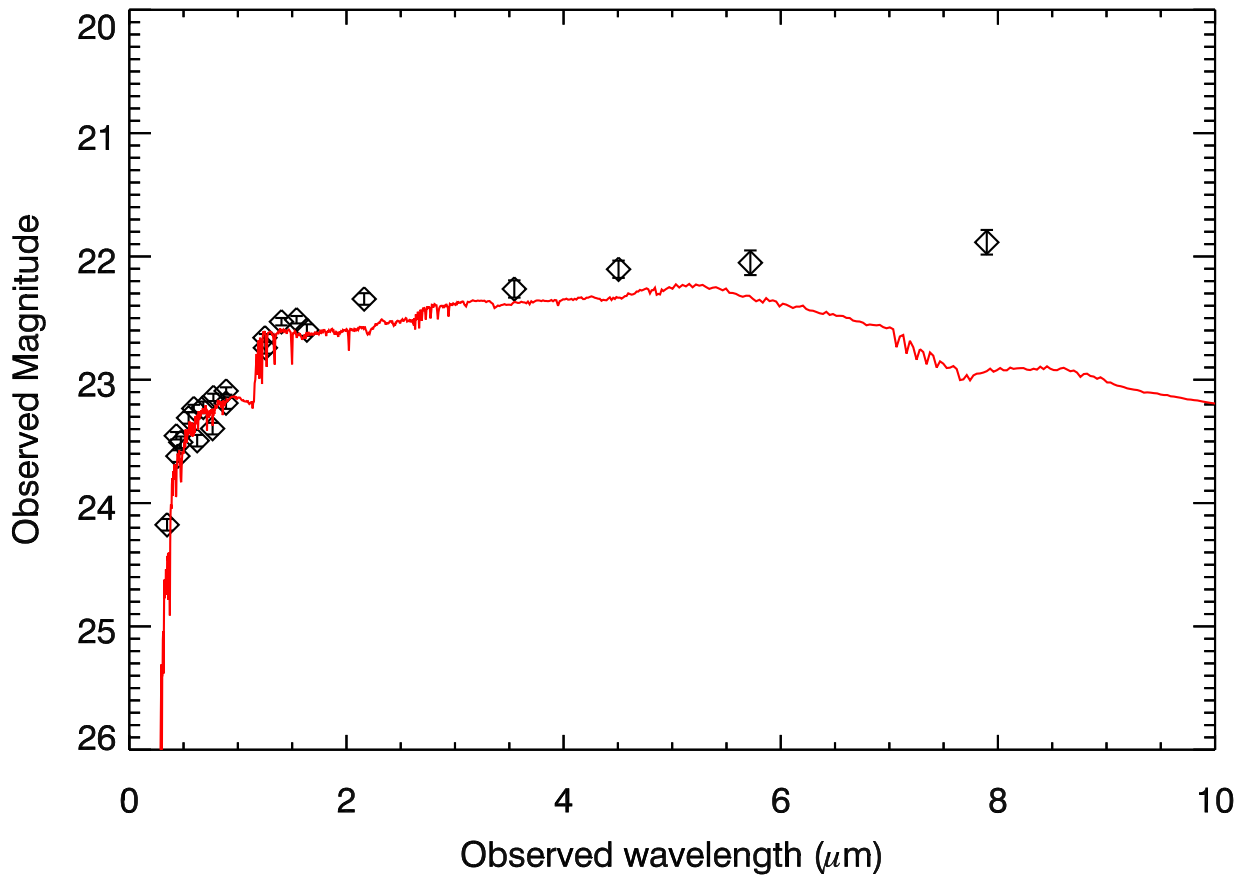

Figure 4.13: Example SED of one of the IR-excess galaxies, GOODS-BX1100 at $z = 2.08$, selected based on the $\geqslant 2\sigma$ flux excess criteria in the IRAC 3 and 4 channels, as described in Section 4.A.2. The diamonds represent the observed magnitudes in respective photometric bands used for SED modeling (Table 4.1), and the red curve shows the best-fit galaxy SED excluding photometric data from IRAC 3 and 4.

as the DEIMOS error spectra. We repeated the same process, estimating the ratio between the 'bootstrap only' and 'bootstrap + individual error spectra' for the DEIMOS spectra scaled to the S/N of the FORS2 spectra and the resulting median ratio is 0.564. These two ratios were combined with weights that correspond to the proportion of the DEIMOS and FORS spectra in the entire $z \sim 4$ sample, yielding a overall ratio of 0.460. As a result, the overall error composite spectra of the $z \sim 4$ sample was determined by dividing the error spectra evaluated from 'bootstrap only' by a factor 0.460 to account for the contribution of individual error spectra with different S/N.

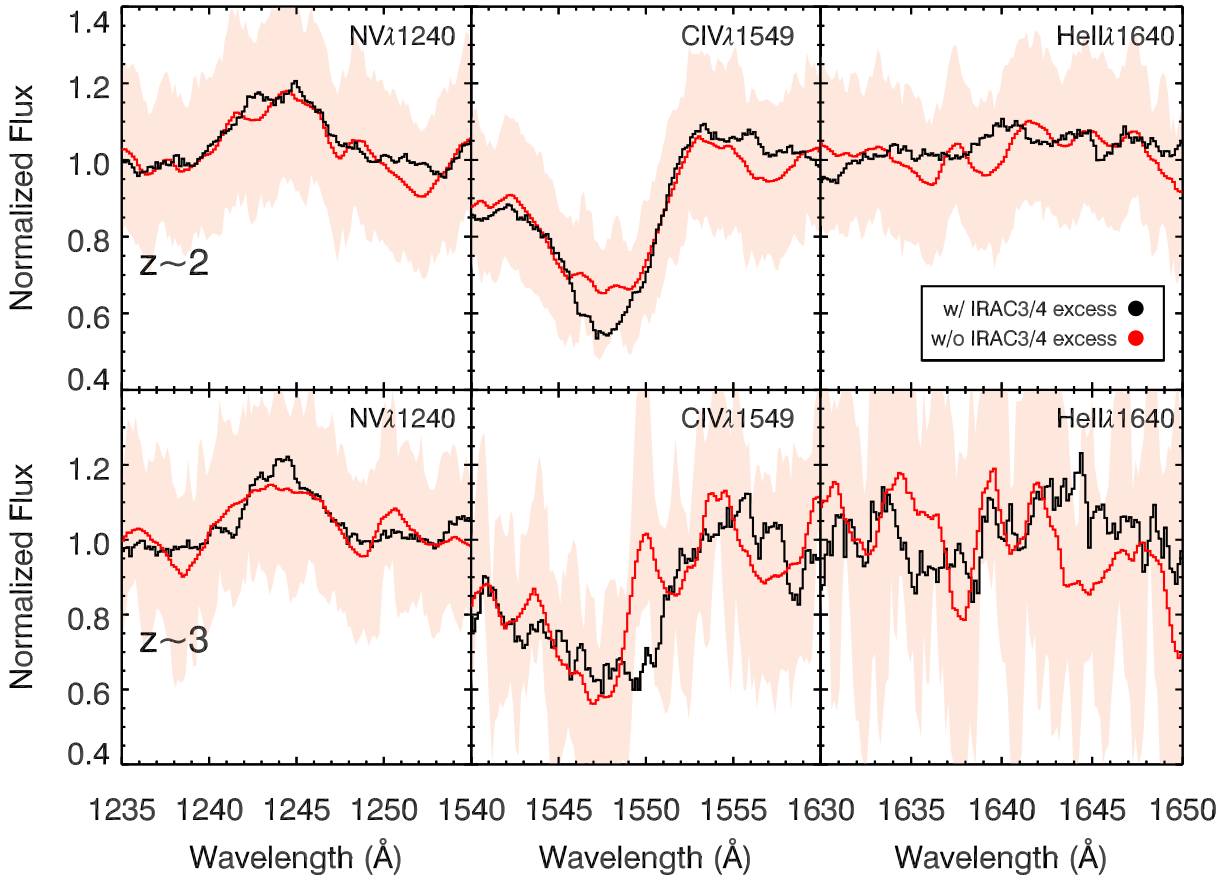

Figure 4.14: Comparison of the AGN signature profiles (N V, C IV, and He II) between the stacks of objects showing a $\geqslant 2\sigma$ excess in either IRAC channel 3 or 4 (red) and those without (black) for the $z \sim 2$ (top) and $z \sim 3$ (bottom) samples. The light red shaded area represents the 1σ uncertainty level of the "excess" composites. The $z \sim 4$ composites are not plotted because of the small number of objects meeting the flux excess threshold. Given the much smaller size of the "excess" sample compared to that of the "non-excess" sample, the "excess" composites have been smoothed to match the continuum S/N of the counterpart "non-excess" composites. This smoothing minimizes the visual difference caused by the pixel-to-pixel rms.

4.A.2 IR-excess galaxies

The process of SED modeling reveals a small fraction of objects that stand out because of their flux excess in the IRAC channels relative to the best-fit galaxy SED template. Studies have shown that monotonically rising IRAC SEDs can be an effective tool for selecting AGNs (Reddy et al., 2006; Donley et al., 2012; Hainline et al., 2012), complementary to other AGN identification methods based on X-ray properties or rest-frame optical and UV spectra. By studying a sample of 33 AGNs identified on the basis of narrow, high-ionization emission lines in the rest-frame UV, Hainline et al. (2012) found that 11 out of 16 objects with IRAC photometry show a monotonically increasing flux in the IRAC channels towards longer wavelength. These authors discovered that the "excess" in the IRAC bands could be fit by an additional power-law on top of the best-fit galaxy SED to represent the emission from hot dust associated with the AGN. Motivated by the idea that the flux excess in the IRAC bands can possibly be used as a indicator of AGN emission, we select galaxies with IR-excess in our samples, and compare their rest-UV spectra with those showing no flux excess in the mid-IR.

Fortunately, the $z \sim 2-4$ LBG spectra cover multiple high-ionization emission lines characteristic of AGN spectra, including N Vλ1240, C IVλ1549, and He IIλ1640. These emission features are clear indicators of photoionization by a non-stellar source, and are therefore typically weak and undetected individually in our redshift samples of star-forming galaxies. However, the use of composite spectra makes it possible to study these lines in greater detail and examine potential AGN activity in the LBGs in our samples.

Although objects with high-ionization UV emission features detected on an individual basis were classified as AGNs and therefore already removed from the samples presented in this work prior to the construction of composite spectra, there may exist an underlying, low-level AGN contribution in the remaining sample that can only be identified within composite spectra. In order to select objects with potential low-level AGN activity, we searched for objects in our redshift samples based on a $\geqslant 2\sigma$ flux excess threshold relative to the best-fit SED in 1) either IRAC channel 3 or channel 4 if only one band is detected, or 2) channel

3 *and* channel 4 if both are detected. In the latter case, we further required that channel 4 has a higher flux density (lower value in magnitude) than channel 3 to ensure the shape of a power-law. The flux density excess was calculated by comparing the observed magnitude in corresponding bands with the theoretical magnitude derived from the best-fit galaxy SED fit excluding IRAC channels 3 and 4. Figure 4.13 shows the SED of an IR-excess galaxy (GOODS-BX1100 in the $z \sim 2$ sample) selected based on these criteria.

A total of 55, 28, and 4 objects were selected based on the flux density excess for the $z \sim 2$, $z \sim 3$, and $z \sim 4$ samples, respectively. We did not stack the $z \sim 4$ "excess" spectra given that this sample is too small to be considered a statistical one. Figure 4.14 shows the comparison of the composite spectra with IRAC excess (red) and without (black) for the $z \sim 2$ (top) and $z \sim 3$ samples (bottom) near the wavelengths of N V, C IV, and He II. For a better visual comparison, we have smoothed the "excess" spectrum to match the pixel-to-pixel rms of its "non-excess" counterpart in order to account for the difference in continuum S/N. We found that among the 3 high-ionization emission features, N V is the strongest in all composites. The C IV emission is weak, and He II is almost not detected at all. It is worth noting that the "excess" and "non-excess" composites look fairly similar in that the former do not show specifically stronger N V, C IV, or He II emission. This result suggests that the IR-excess galaxies in our star-forming galaxy samples - which are already cleaned of IR-excess galaxies identified individually as AGNs based on strong rest-UV high-ionization lines - may not be AGNs. The flux density excess in the mid-IR may suggest evidence for hot dust due to active star formation, as observed in some local dwarf galaxies (Hainline et al., 2016). Alternatively, the minor AGN activity in these galaxies, if any, is highly obscured and does not result in distinct features in the rest-frame UV.

CHAPTER 5

Summary and Future Work

5.1 Summary

In this dissertation, I have presented three studies focusing on the characterization of both the ISM and CGM in star-forming galaxies spanning a wide redshift range, $z \sim 1-4$. This work has provided significant insights into the high-ionization kinematics of outflows and the nebular emission properties at $z \sim 1$ from the first statistical sample assembled to date, as well as the evolution of the CGM properties at $z \sim 2-4$. The main results and conclusions from each investigation are summarized below.

In Chapter 2, I compared the high- and low-ionization kinematics of the outflowing ISM/CGM, as probed by the interstellar C IV and near-UV Fe II absorption features, respectively, at $z \sim 1$. I identified 93 objects with the spectral coverage of C IV$\lambda\lambda$1548, 1550 in the DEEP2/LRIS sample, and characterized the interstellar absorption profile of this high-ionization feature by removing the P-Cygni wind profile from the observed spectra. While the centroid of interstellar C IV is more blueshifted than that of the near-UV Fe II lines at almost the 3σ level (the offset of the best-fit linear regression is $-76 \pm 26 \mathrm{km\,s^{-1}}$), the profile of interstellar C IV is very similar to that of Mg II$\lambda\lambda$2796, 2803, typically yielding comparable centroid and maximum velocities. This result suggests that the larger blueshift of C IV compared to the near-UV Fe II is most likely a result of resonant emission filling, instead of evidence of an intrinsically faster outflow motion of highly ionized gas. I further found from stacked spectra that the interstellar C IV is more blueshifted and stronger in galaxies with higher SFRs, but does show a significant correlation with other galaxy properties such as stellar mass and specific SFR, indicating that massive star formation and associated

processes drive the properties of the highly ionized gas traced by C IV.

I presented an unprecedented statistical study of the nebular C III]$\lambda\lambda$1907, 1909 emission doublet at $z \sim 1$ in Chapter 3. In the same DEEP2/LRIS sample, 184 galaxies have C III] coverage, and 40 have individual detections of C III] with a median rest-frame $\mathrm{EW_{C\ III]}} = 1.3$Å. Using stacked spectra, I found that fainter, bluer, and lower-mass galaxies tend to have stronger C III] emission. These trends are consistent with those discovered at higher redshifts ($z \gtrsim 2$), and are likely to be secondary correlations determined by the gas-phase metallicity, the hardness of ionizing spectrum, and dust content. In comparison with the results given by photoionization models, it is suggested that low metallicities and high ionization parameters enhance nebular C III] emission. The reason for the relative lack of stronger C III] emitters ($\mathrm{EW_{C\ III]}} \geq 5$Å) at $z \sim 1$ likely results from the relatively high gas-phase metallicities ($\gtrsim 0.5 Z_{\odot}$; compared to that of the $z \gtrsim 6$ C III] detections), and the lack of extremely young (age < 50Myr) stellar populations. This work has important implication for searching for C III] emitters at low redshifts, which will enable detailed modeling and characterization of their physical properties, helping us gain a better understanding of the sources that contribute to reionization within the first billion years of cosmic time.

In Chapter 4, I presented the first comprehensive evolutionary analysis of the rest-UV spectroscopic properties in LBGs at $z \sim 2-4$. Samples in each of three redshift bins were constructed to span the same dynamic range in stellar mass and UV luminosity, and systematic, uniform measurements were performed on spectral lines and SED modeling. By studying the stacked spectra, I found that the intercorrelation among the strengths of Lyα emission, low-ionization interstellar absorption lines, and dust content (as probed by $E(B-V)$) is redshift-independent. This key result indicates that the radiative transfer of Lyα photons through ISM and CGM is very similar in all star-forming galaxies at $z \sim 2-4$, and that dust is coupled with neutral gas in general. Furthermore, it is shown that the covering fraction of the neutral gas, as traced by Lyα emission, is smaller at higher redshift at fixed galaxy properties (e.g., UV luminosity, stellar mass, SFR, and age). At $z \sim 4$, Lyα is found to be more prominent in fainter, younger, bluer galaxies with lower stellar masses and SFRs, while the trends between Lyα and galaxy properties are almost flat at $z \sim 2-3$.

This difference is most likely caused by the larger dynamic range in covering fraction of the neutral gas at $z \sim 4$ than at $z \sim 2-3$, enabling us to probe the young galaxies with very little dust. In terms of the ionized gas, the decoupling between Lyα and the high-ionization line strengths suggests that they trace difference phases of gas. The ionized gas appears to have a lower covering fraction at higher redshift as suggested by the doublet ratio of Si IV. Differences in the intrinsic Lyα photon production in the H II regions are also suggested by the data, specifically in the $z \sim 4$ composite made of galaxies in the quartile with the strongest Lyα emission, which is expected to have the strongest nebular C III] emission among all stacked spectra binned according to Lyα EW. Drawing quantitative conclusion on topics such as the production and escape of Lyα photons, and the connection between dust and neutral gas is an important step forward in galaxy formation and evolution. Spectroscopic data with high S/N and spectral resolution will be of great help for a full understanding of the evolving ISM/CGM.

5.2 Ongoing and future work

The investigations presented in this dissertation represent an effort to improve our understanding of the neutral and ionized phases of ISM and CGM in distant star-forming galaxies from various aspects. Future studies with high-quality data from new observational facilities are required to further address the remaining questions in the kinematics and structure of multi-phase outflows, the nature of strong nebular line emitters and their H II region properties, and the connection between neutral ISM/CGM and dust. In the following sections, I describe ongoing investigations that will expand upon the work presented herein and discuss the future outlook on these topics with the upcoming generation of telescopes.

5.2.1 Detailed modeling of high-ionization absorption profiles

Characterizing the structure and kinematics of multi-phase galactic outflows remains a key goal in the study of the ISM/CGM of star-forming galaxies. In Chapter 2, I demonstrated that the small but significant blueshift interstellar C IV shows relative to the near-UV Fe II

is more likely to be caused by emission filling than the faster motion of the highly ionized gas. While our explanation is supported by the similarity in the C IV and Mg II profiles, the possibly of the latter scenario cannot be fully ruled out given the low resolution of our spectra. Spectroscopic data with higher S/N and spectral resolution will enable the resolution of the C IV doublet. Based on such data, we will further be able to decompose both the C IV doublet and low-ionization features into systemic and outflow components. By modeling the observed profiles with a systemic component (fixed at $v = 0$) and an outflow component ($v < 0$), one can break the degeneracy of the two proposed explanations (i.e., emission filling and faster motion of the C IV-absorbing gas) by directly comparing the outflow velocity between the low- and high-ionization features, and inferring the level of emission filling from the profile of the systemic component. Such investigations will greatly enrich our current knowledge of the multi-phase outflow structure, the connection between feedback and the CGM, and provide more detailed observational inputs for galaxy formation simulations.

5.2.2 Lower-redshift EELGs

As we discussed in Chapter 3, large C III] EWs ($\geqslant 5$Å) are fairly common at $z > 2$. Several studies measured $\gtrsim 10$Å C III] EW in galaxies formed prior to and during the epoch of reionization ($z > 6$; Zitrin et al., 2015; Stark et al., 2015, 2017). Although these extreme C III] emitters at $z > 6$ are not representative of the majority of "main sequence" star-forming galaxies at lower redshift, they are important for our understanding of the physical conditions in galaxies at early times. However, due to the low S/N, conducting metal-line studies of such galaxies is exceptionally challenging. An alternative way to learn about these $z > 6$ galaxies is by using lower-redshift analogs. With lower-redshift observations, we can potentially obtain detailed, higher S/N information, on the physical properties (e.g., metallicity, ionization parameter, dust extinction) from rest-UV and optical spectroscopy, and infer the stellar populations from SED fits using multi-wavelength photometry.

One of our current ongoing investigations focuses on a sample of galaxies at $z = 1.2 - 2.3$ that were selected to be the analogs of $z > 6$ C III] emitters. Our new sample is

likely to significantly increase the number of known C III] emitters at this redshift range. These galaxies are typically classified as "extreme emission-line galaxies" (EELGs), and were selected based on the presence of extraordinarily strong [O III]$\lambda\lambda$4959, 5007 (rest-frame EW $\gtrsim$ 780Å) and/or blue ($\lesssim$ 0.4 mag) rest-frame $U-B$ color. Based on the tight correlation between C III] and [O III] strengths (e.g., Stark et al., 2014), and the dependence of C III] EW on $U-B$ color discussed in Chapter 3, the majority of these galaxies are expected to fall into the "C III] emitter" category.

Our sample was drawn from the COSMOS and AEGIS fields covered by the 3D-HST Survey (Momcheva et al., 2016). The data were collected during two observing runs in March, 2017 with Keck I/LRIS, and the sky was mostly clear for both nights. The galaxy spectra were obtained with multi-object slitmasks using 1.2″ slits. Fifty five galaxies were targeted (28 in the COSMOS field, and 27 in the AEGIS field). Our sample was observed with the 400 lines mm^{-1} grism blazed at 3400Å on the blue side, and the 600 lines mm^{-1} red grating blazed at 5000Å on the red side. The integration time for the masks is 9 hours for the COSMOS field and 8.3 hours for the AEGIS field. The blue side of the spectra covers C III] for galaxies at $z < 1.62$ (9 objects in the COSMOS field, and 12 objects in the AEGIS field), along with Lyα and multiple rest-far-UV interstellar absorption lines. C III] falls in the red side for galaxies with $z > 1.62$ (19 and 15 objects for the COSMOS and AEGIS fields, respectively).

The blue side of the spectra has been fully reduced. In brief, the 2D spectra were first flat fielded, cleaned of cosmic rays and background-subtracted. Individual 2D exposures were then combined, and extracted into one dimension (1D), and wavelength and flux calibrated. Figure 5.1 to 5.4 show a few examples of the detections of C III], Lyα, and absorption lines in the observed-frame spectra. The redshifts of the galaxies are provided in the 3D-HST catalog, and will be further verified based on the C III] feature and other nebular features if detected, and/or Lyα and LIS lines with assumed velocity offsets.

The reduction of the red-side spectra is ongoing, and is expected to be finished at the beginning of summer 2018. Comprehensive measurements and analyses of the spectral features will follow immediately.

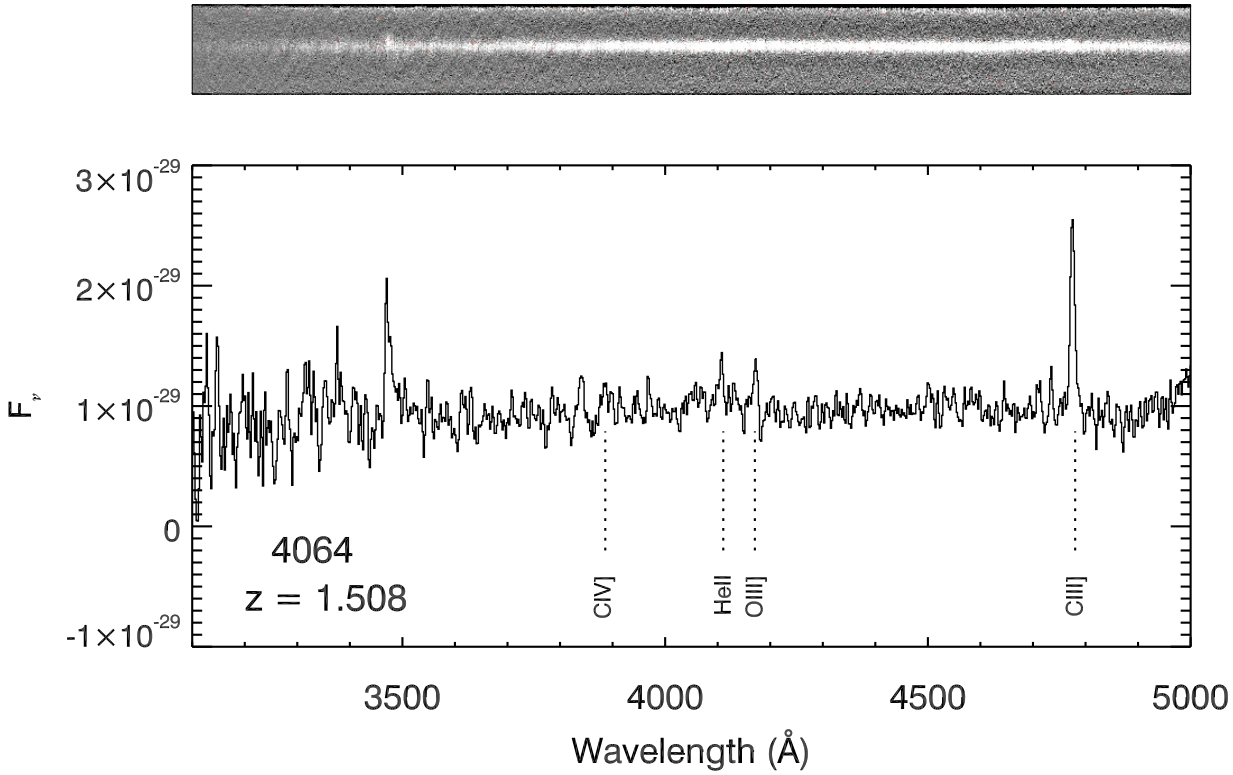

Figure 5.1: Blue-side spectrum of object 4064 in the COSMOS field. As one of the EELGs, 4064 has multiple nebular emission lines detected, including C IV, He II, O III], and C III].

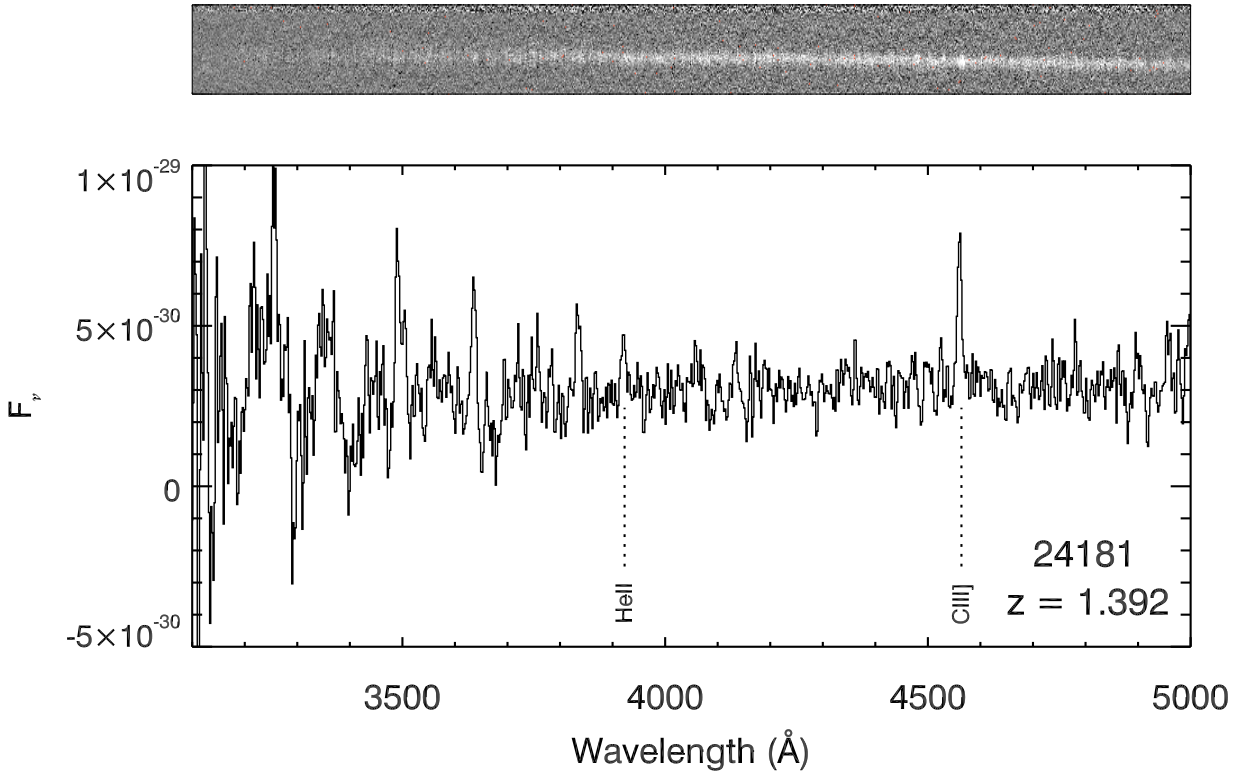

Figure 5.2: Blue-side spectrum of object 24181 in the AEGIS field, showing the detections of C III] and He II.

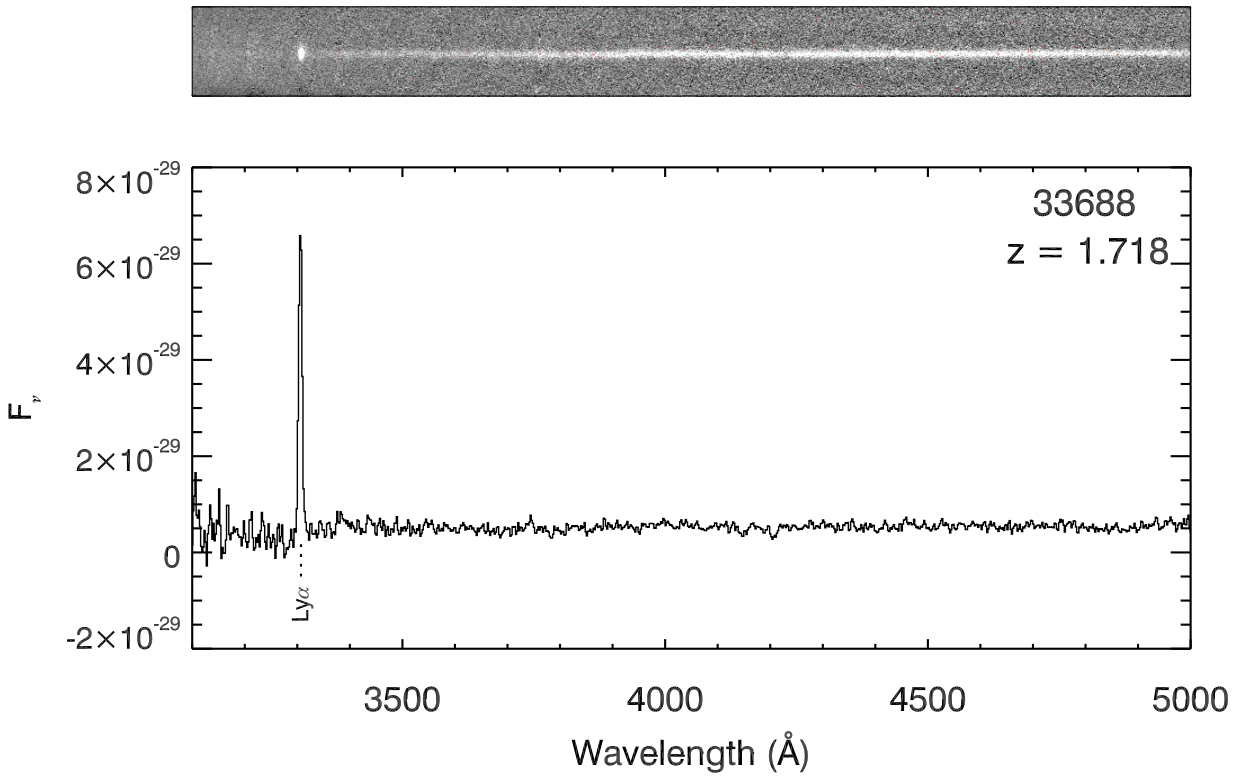

Figure 5.3: Blue-side spectrum of object 33688 in the AEGIS field, showing strong Lyα emission.

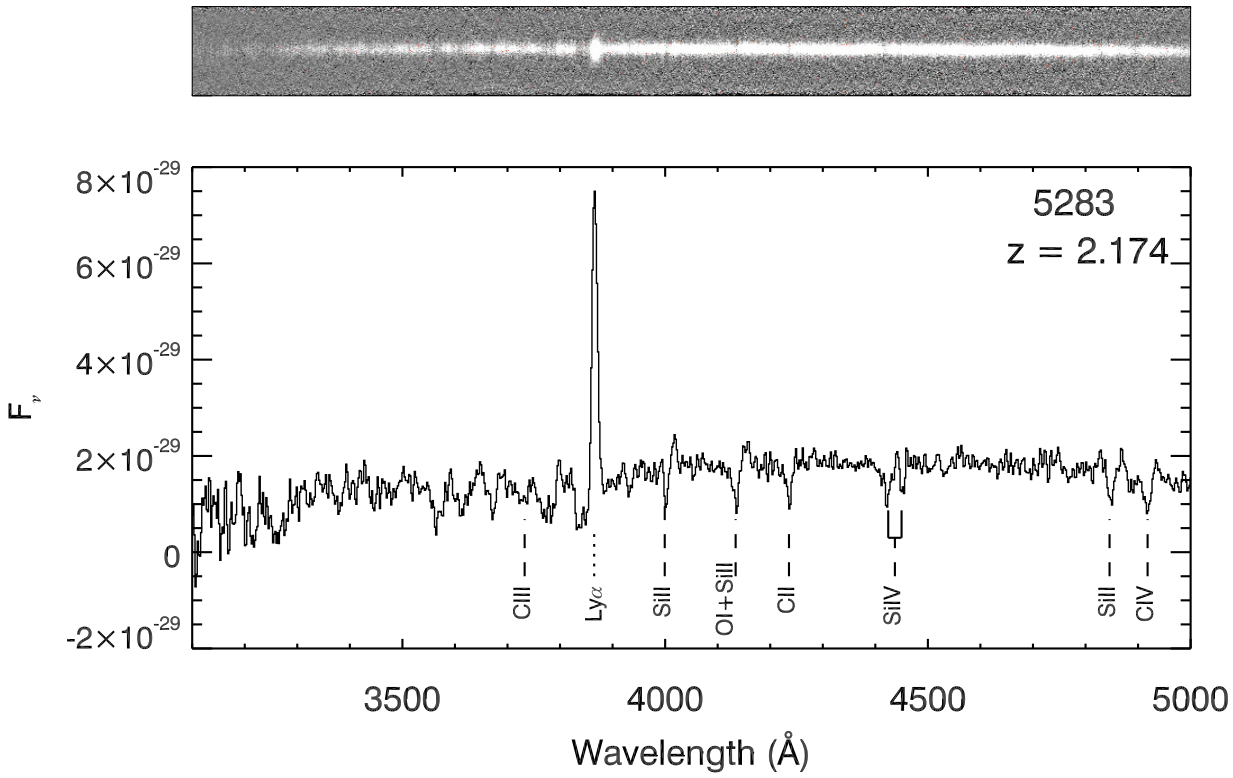

Figure 5.4: Blue-side spectrum of object 5283 in the COSMOS field, showing both Lyα emission and multiple interstellar absorption lines over $3500 - 5000$Å. Emission (dotted lines) and absorption (dashed lines) lines are identified.

Given that our sample is a subset of the 3D-HST targets, multi-band imaging, optical and IR photometry, and grism data are available for the galaxies. The targeted C III] detection (> 5Å), along with that of other weaker emission features (e.g., C IV], He II, O III] and Si III]), will provide rich information on the physical parameters such as the ionization parameter and the C/O abundance ratio. The coverage of [O II], Hβ and [O III] for objects at $z = 1.95 - 2.3$ with the WFC3/G141 grism will further enable the measurement of the gas-phase metallicity. Finally, stellar population parameters can be obtained from the publicly available 3D-HST photometry catalogs, providing additional galaxy properties and stacking parameters. These multi-dimensional data will allow detailed characterization of the physical properties of close analogs of the $z > 6$ EELGs, constructing comprehensive profiles, through analogy, of the galaxies likely responsible for cosmic reionization.

5.2.3 Lyα, low-ionization interstellar absorption, and dust

One important goal for galaxy studies is to understand the formation and distribution of dust in the ISM of actively star-forming galaxies. I presented a preliminary analysis in Chapter 4 on the fundamental nature of the correlations among Lyα emission, LIS absorption, and $E(B-V)$. This analysis was limited in that the measurements from stacked spectra were not entirely independent, and that the adoption of the median $E(B-V)$ of each stack could introduce non-negligible uncertainties. One way to improve the investigation is by acquiring a sample of deep, individual galaxy spectra with high S/N. Different galaxies will provide different lines of sight, allowing a more detailed examination of the variation in the neutral gas and dust covering fractions. Furthermore, higher-quality photometric data of those individual galaxies will enable a more accurate description of the stellar populations through SED modeling, reducing the systematics associated with $E(B-V)$.

Selecting deep galaxy spectra from the VANDELS survey (Pentericci et al., 2018) is a step forward in this direction. VANDELS is a spectroscopic survey designed to obtain ultra-deep, medium resolution, optical spectra of primarily $z > 2.5$ star-forming galaxies, the majority of which will be selected from the Chandra Deep Field South (CDFS) and UKIDSS Ultra

Deep Survey (UDS) fields covered by HST multi-band imaging. The survey was carried out with the VIsible Multi-Object Spectrograph (VIMOS) on the Very Large Telescope, and the typical exposure time ranges from 20 to 80 hours per source. The current data release is based on the observations from August 2015 until January 2016, and include 879 sources that had their observing time completed or reached 50%.

We therefore conduct an investigation to study the connection among Lyα, LIS lines, and dust extinction using the VANDEL galaxies. The galaxy sample of this investigation will be drawn primarily from two categories of the VANDELS survey: the bright ($H_{AB} < 24$ mag) star-forming galaxies and the fainter ($H_{AB} < 27$ mag) LBGs. Additional constraints ($i \leqslant 26$ mag, $2.95 \leqslant z_{phot} \leqslant 4.5$) will be applied to match the sample with the $z \sim 3 - 4$ samples described in Chapter 4 in brightness. Moreover, to utilize the unparalleled multi-wavelength photometry and stellar population parameters in the 3D-HST catalogs, the galaxies will further be required to be in the HST F606W footprint and have an unambiguous match in coordinates. We have applied the criteria above to the VANDELS dataset and assembled a sample of several tens of star-forming galaxies at $z \sim 3 - 4$. The exceptionally high S/N of the VANDELS spectra will enable accurate measurements of Lyα, LIS and HIS absorption lines, nebular and fine-structure emission features, and dust extinction. The detailed determination of the spectral properties on an individual galaxy basis will provide new insights into the nature of the relation between dust and neutral gas, as well as the kinematics and spatial extent of the neutral and ionized phases of outflows.

Future observational facilities will significantly enhance our capability of studying higher redshift galaxies in greater detail, answering some of the key remaining questions in galaxy formation and evolution. For example, the soon-to-be-launched James Webb Space Telescope (JWST) will extend the rest-UV and rest-optical spectroscopic studies of star-forming galaxies out to $z > 10$, providing a comprehensive picture of the evolution of ISM/CGM from the reionization epoch to the peak epoch of the cosmic star formation. The spectroscopic sensitivity of JWST will also greatly increase the current sample size of high-redshift EELGs, enabling detailed statistical studies of this galaxy population and significantly contributing to the physical picture of cosmic reionization.

Bibliography

Akerman, C. J., Carigi, L., Nissen, P. E., Pettini, M., & Asplund, M. 2004, A&A, 414, 931

Bayliss, M. B., Rigby, J. R., Sharon, K., Wuyts, E., Florian, M., Gladders, M. D., Johnson, T., & Oguri, M. 2014, ApJ, 790, 144

Berg, D. A., Skillman, E. D., Henry, R. B. C., Erb, D. K., & Carigi, L. 2016, ApJ, 827, 126

Berry, M., Gawiser, E., Guaita, L., Padilla, N., Treister, E., Blanc, G. A., Ciardullo, R., Francke, H., & Gronwall, C. 2012, ApJ, 749, 4

Bordoloi, R., Lilly, S. J., Knobel, C., Bolzonella, M., Kampczyk, P., Carollo, C. M., Iovino, A., Zucca, E., Contini, T., Kneib, J.-P., Le Fevre, O., Mainieri, V., Renzini, A., Scodeggio, M., Zamorani, G., Balestra, I., Bardelli, S., Bongiorno, A., Caputi, K., Cucciati, O., de la Torre, S., de Ravel, L., Garilli, B., Kovač, K., Lamareille, F., Le Borgne, J.-F., Le Brun, V., Maier, C., Mignoli, M., Pello, R., Peng, Y., Perez Montero, E., Presotto, V., Scarlata, C., Silverman, J., Tanaka, M., Tasca, L., Tresse, L., Vergani, D., Barnes, L., Cappi, A., Cimatti, A., Coppa, G., Diener, C., Franzetti, P., Koekemoer, A., López-Sanjuan, C., McCracken, H. J., Moresco, M., Nair, P., Oesch, P., Pozzetti, L., & Welikala, N. 2011, ApJ, 743, 10

Bordoloi, R., Lilly, S. J., Hardmeier, E., Contini, T., Kneib, J.-P., Le Fevre, O., Mainieri, V., Renzini, A., Scodeggio, M., Zamorani, G., Bardelli, S., Bolzonella, M., Bongiorno, A., Caputi, K., Carollo, C. M., Cucciati, O., de la Torre, S., de Ravel, L., Garilli, B., Iovino, A., Kampczyk, P., Kovač, K., Knobel, C., Lamareille, F., Le Borgne, J.-F., Le Brun, V., Maier, C., Mignoli, M., Oesch, P., Pello, R., Peng, Y., Perez Montero, E., Presotto, V., Silverman, J., Tanaka, M., Tasca, L., Tresse, L., Vergani, D., Zucca, E., Cappi, A., Cimatti, A., Coppa, G., Franzetti, P., Koekemoer, A., Moresco, M., Nair, P., & Pozzetti, L. 2014, ApJ, 794, 130

Borthakur, S., Heckman, T., Strickland, D., Wild, V., & Schiminovich, D. 2013, ApJ, 768, 18

Bouwens, R. J., van Dokkum, P. G., Illingworth, G. D., Oesch, P. A., Maseda, M., Ribeiro, B., Stefanon, M., & Lam, D. 2017, ArXiv e-prints, arXiv:1711.02090

Bouwens, R. J., Aravena, M., Decarli, R., Walter, F., da Cunha, E., Labbé, I., Bauer, F. E., Bertoldi, F., Carilli, C., Chapman, S., Daddi, E., Hodge, J., Ivison, R. J., Karim, A., Le Fevre, O., Magnelli, B., Ota, K., Riechers, D., Smail, I. R., van der Werf, P., Weiss, A., Cox, P., Elbaz, D., Gonzalez-Lopez, J., Infante, L., Oesch, P., Wagg, J., & Wilkins, S. 2016, ApJ, 833, 72

Brammer, G. B., van Dokkum, P. G., Franx, M., Fumagalli, M., Patel, S., Rix, H.-W., Skelton, R. E., Kriek, M., Nelson, E., Schmidt, K. B., Bezanson, R., da Cunha, E., Erb, D. K., Fan, X., Förster Schreiber, N., Illingworth, G. D., Labbé, I., Leja, J., Lundgren, B., Magee, D., Marchesini, D., McCarthy, P., Momcheva, I., Muzzin, A., Quadri, R., Steidel, C. C., Tal, T., Wake, D., Whitaker, K. E., & Williams, A. 2012, ApJS, 200, 13

Bruzual, G., & Charlot, S. 2003a, MNRAS, 344, 1000

—. 2003b, MNRAS, 344, 1000

Bundy, K., Ellis, R. S., Conselice, C. J., Taylor, J. E., Cooper, M. C., Willmer, C. N. A., Weiner, B. J., Coil, A. L., Noeske, K. G., & Eisenhardt, P. R. M. 2006, ApJ, 651, 120

Calzetti, D., Armus, L., Bohlin, R. C., Kinney, A. L., Koornneef, J., & Storchi-Bergmann, T. 2000, ApJ, 533, 682

Caruana, J., Bunker, A. J., Wilkins, S. M., Stanway, E. R., Lorenzoni, S., Jarvis, M. J., & Ebert, H. 2014, MNRAS, 443, 2831

Chabrier, G. 2003, PASP, 115, 763

Chen, Y.-M., Tremonti, C. A., Heckman, T. M., Kauffmann, G., Weiner, B. J., Brinchmann, J., & Wang, J. 2010, AJ, 140, 445

Chisholm, J., Orlitová, I., Schaerer, D., Verhamme, A., Worseck, G., Izotov, Y. I., Thuan, T. X., & Guseva, N. G. 2017, A&A, 605, A67

Chisholm, J., Tremonti, C. A., Leitherer, C., Chen, Y., & Wofford, A. 2016, MNRAS, 457, 3133

Coil, A. L., Weiner, B. J., Holz, D. E., Cooper, M. C., Yan, R., & Aird, J. 2011, ApJ, 743, 46

de Barros, S., Vanzella, E., Amorín, R., Castellano, M., Siana, B., Grazian, A., Suh, H., Balestra, I., Vignali, C., Verhamme, A., Zamorani, G., Mignoli, M., Hasinger, G., Comastri, A., Pentericci, L., Pérez-Montero, E., Fontana, A., Giavalisco, M., & Gilli, R. 2016, A&A, 585, A51

Dean, C. A., & Bruhweiler, F. C. 1985, ApJS, 57, 133

Donley, J. L., Koekemoer, A. M., Brusa, M., Capak, P., Cardamone, C. N., Civano, F., Ilbert, O., Impey, C. D., Kartaltepe, J. S., Miyaji, T., Salvato, M., Sanders, D. B., Trump, J. R., & Zamorani, G. 2012, ApJ, 748, 142

Du, X., Shapley, A. E., Martin, C. L., & Coil, A. L. 2016, ApJ, 829, 64

—. 2017, ApJ, 838, 63

Elbaz, D., Daddi, E., Le Borgne, D., Dickinson, M., Alexander, D. M., Chary, R.-R., Starck, J.-L., Brandt, W. N., Kitzbichler, M., MacDonald, E., Nonino, M., Popesso, P., Stern, D., & Vanzella, E. 2007, A&A, 468, 33

Erb, D. K., Pettini, M., Shapley, A. E., Steidel, C. C., Law, D. R., & Reddy, N. A. 2010, ApJ, 719, 1168

Erb, D. K., Pettini, M., Steidel, C. C., Strom, A. L., Rudie, G. C., Trainor, R. F., Shapley, A. E., & Reddy, N. A. 2016, ApJ, 830, 52

Erb, D. K., Quider, A. M., Henry, A. L., & Martin, C. L. 2012, ApJ, 759, 26

Erb, D. K., Shapley, A. E., Pettini, M., Steidel, C. C., Reddy, N. A., & Adelberger, K. L. 2006a, ApJ, 644, 813

Erb, D. K., Steidel, C. C., Shapley, A. E., Pettini, M., Reddy, N. A., & Adelberger, K. L. 2006b, ApJ, 647, 128

—. 2006c, ApJ, 646, 107

Erb, D. K., Steidel, C. C., Trainor, R. F., Bogosavljević, M., Shapley, A. E., Nestor, D. B., Kulas, K. R., Law, D. R., Strom, A. L., Rudie, G. C., Reddy, N. A., Pettini, M., Konidaris, N. P., Mace, G., Matthews, K., & McLean, I. S. 2014, ApJ, 795, 33

Faber, S. M., Phillips, A. C., Kibrick, R. I., Alcott, B., Allen, S. L., Burrous, J., Cantrall, T., Clarke, D., Coil, A. L., Cowley, D. J., Davis, M., Deich, W. T. S., Dietsch, K., Gilmore, D. K., Harper, C. A., Hilyard, D. F., Lewis, J. P., McVeigh, M., Newman, J., Osborne, J., Schiavon, R., Stover, R. J., Tucker, D., Wallace, V., Wei, M., Wirth, G., & Wright, C. A. 2003, in Proc. SPIE, Vol. 4841, Instrument Design and Performance for Optical/Infrared Ground-based Telescopes, ed. M. Iye & A. F. M. Moorwood, 1657–1669

Faber, S. M., Willmer, C. N. A., Wolf, C., Koo, D. C., Weiner, B. J., Newman, J. A., Im, M., Coil, A. L., Conroy, C., Cooper, M. C., Davis, M., Finkbeiner, D. P., Gerke, B. F., Gebhardt, K., Groth, E. J., Guhathakurta, P., Harker, J., Kaiser, N., Kassin, S., Kleinheinrich, M., Konidaris, N. P., Kron, R. G., Lin, L., Luppino, G., Madgwick, D. S., Meisenheimer, K., Noeske, K. G., Phillips, A. C., Sarajedini, V. L., Schiavon, R. P., Simard, L., Szalay, A. S., Vogt, N. P., & Yan, R. 2007, ApJ, 665, 265

Faisst, A. L., Capak, P. L., Davidzon, I., Salvato, M., Laigle, C., Ilbert, O., Onodera, M., Hasinger, G., Kakazu, Y., Masters, D., McCracken, H. J., Mobasher, B., Sanders, D., Silverman, J. D., Yan, L., & Scoville, N. Z. 2016, ApJ, 822, 29

Feldmann, R., Quataert, E., Hopkins, P. F., Faucher-Giguère, C.-A., & Kereš, D. 2017, MNRAS, 470, 1050

Ferland, G. J., Korista, K. T., Verner, D. A., Ferguson, J. W., Kingdon, J. B., & Verner, E. M. 1998, PASP, 110, 761

Finley, H., Bouché, N., Contini, T., Epinat, B., Bacon, R., Brinchmann, J., Cantalupo, S., Erroz-Ferrer, S., Marino, R. A., Maseda, M., Richard, J., Schroetter, I., Verhamme, A., Weilbacher, P. M., Wendt, M., & Wisotzki, L. 2017, A&A, 605, A118

Garnett, D. R., Skillman, E. D., Dufour, R. J., Peimbert, M., Torres-Peimbert, S., Terlevich, R., Terlevich, E., & Shields, G. A. 1995, ApJ, 443, 64

Giavalisco, M., Koratkar, A., & Calzetti, D. 1996, ApJ, 466, 831

Giavalisco, M., Ferguson, H. C., Koekemoer, A. M., Dickinson, M., Alexander, D. M., Bauer, F. E., Bergeron, J., Biagetti, C., Brandt, W. N., Casertano, S., Cesarsky, C., Chatzichristou, E., Conselice, C., Cristiani, S., Da Costa, L., Dahlen, T., de Mello, D., Eisenhardt, P., Erben, T., Fall, S. M., Fassnacht, C., Fosbury, R., Fruchter, A., Gardner, J. P., Grogin, N., Hook, R. N., Hornschemeier, A. E., Idzi, R., Jogee, S., Kretchmer, C., Laidler, V., Lee, K. S., Livio, M., Lucas, R., Madau, P., Mobasher, B., Moustakas, L. A., Nonino, M., Padovani, P., Papovich, C., Park, Y., Ravindranath, S., Renzini, A., Richardson, M., Riess, A., Rosati, P., Schirmer, M., Schreier, E., Somerville, R. S., Spinrad, H., Stern, D., Stiavelli, M., Strolger, L., Urry, C. M., Vandame, B., Williams, R., & Wolf, C. 2004, ApJ, 600, L93

Grimes, J. P., Heckman, T., Aloisi, A., Calzetti, D., Leitherer, C., Martin, C. L., Meurer, G., Sembach, K., & Strickland, D. 2009, ApJS, 181, 272

Guaita, L., Talia, M., Pentericci, L., Verhamme, A., Cassata, P., Lemaux, B. C., Orlitova, I., Ribeiro, B., Schaerer, D., Zamorani, G., Garilli, B., Le Brun, V., Le Fèvre, O., Maccagni, D., Tasca, L. A. M., Thomas, R., Vanzella, E., Zucca, E., Amorin, R., Bardelli, S., Castellano, M., Grazian, A., Hathi, N. P., Koekemoer, A., & Marchi, F. 2017, A&A, 606, A19

Gutkin, J., Charlot, S., & Bruzual, G. 2016, MNRAS, 462, 1757

Hainline, K. N., Reines, A. E., Greene, J. E., & Stern, D. 2016, ApJ, 832, 119

Hainline, K. N., Shapley, A. E., Greene, J. E., Steidel, C. C., Reddy, N. A., & Erb, D. K. 2012, ApJ, 760, 74

Hathi, N. P., Le Fèvre, O., Ilbert, O., Cassata, P., Tasca, L. A. M., Lemaux, B. C., Garilli, B., Le Brun, V., Maccagni, D., Pentericci, L., Thomas, R., Vanzella, E., Zamorani, G., Zucca, E., Amorín, R., Bardelli, S., Cassarà, L. P., Castellano, M., Cimatti, A., Cucciati, O., Durkalec, A., Fontana, A., Giavalisco, M., Grazian, A., Guaita, L., Koekemoer, A., Paltani, S., Pforr, J., Ribeiro, B., Schaerer, D., Scodeggio, M., Sommariva, V., Talia, M., Tresse, L., Vergani, D., Capak, P., Charlot, S., Contini, T., Cuby, J. G., de la Torre, S., Dunlop, J., Fotopoulou, S., López-Sanjuan, C., Mellier, Y., Salvato, M., Scoville, N., Taniguchi, Y., & Wang, P. W. 2016, A&A, 588, A26

Heckman, T. M., Armus, L., & Miley, G. K. 1990, ApJS, 74, 833

Heckman, T. M., Lehnert, M. D., Strickland, D. K., & Armus, L. 2000, ApJS, 129, 493

Heckman, T. M., Sembach, K. R., Meurer, G. R., Strickland, D. K., Martin, C. L., Calzetti, D., & Leitherer, C. 2001, ApJ, 554, 1021

Henry, A., Scarlata, C., Martin, C. L., & Erb, D. 2015, ApJ, 809, 19

Henry, R. B. C., Edmunds, M. G., & Köppen, J. 2000, ApJ, 541, 660

Jaskot, A. E., & Ravindranath, S. 2016, ApJ, 833, 136

Jones, T., Martin, C., & Cooper, M. C. 2015, ApJ, 813, 126

Jones, T., Stark, D. P., & Ellis, R. S. 2012, ApJ, 751, 51

Jones, T. A., Ellis, R. S., Schenker, M. A., & Stark, D. P. 2013, ApJ, 779, 52

Kashino, D., Silverman, J. D., Rodighiero, G., Renzini, A., Arimoto, N., Daddi, E., Lilly, S. J., Sanders, D. B., Kartaltepe, J., Zahid, H. J., Nagao, T., Sugiyama, N., Capak, P., Carollo, C. M., Chu, J., Hasinger, G., Ilbert, O., Kajisawa, M., Kewley, L. J., Koekemoer, A. M., Kovač, K., Le Fèvre, O., Masters, D., McCracken, H. J., Onodera, M., Scoville, N., Strazzullo, V., Symeonidis, M., & Taniguchi, Y. 2013, ApJ, 777, L8

Konno, A., Ouchi, M., Ono, Y., Shimasaku, K., Shibuya, T., Furusawa, H., Nakajima, K., Naito, Y., Momose, R., Yuma, S., & Iye, M. 2014, ApJ, 797, 16

Konno, A., Ouchi, M., Shibuya, T., Ono, Y., Shimasaku, K., Taniguchi, Y., Nagao, T., Kobayashi, M. A. R., Kajisawa, M., Kashikawa, N., Inoue, A. K., Oguri, M., Furusawa, H., Goto, T., Harikane, Y., Higuchi, R., Komiyama, Y., Kusakabe, H., Miyazaki, S., Nakajima, K., & Wang, S.-Y. 2018, PASJ, 70, S16

Kornei, K. A., Shapley, A. E., Erb, D. K., Steidel, C. C., Reddy, N. A., Pettini, M., & Bogosavljević, M. 2010, ApJ, 711, 693

Kornei, K. A., Shapley, A. E., Martin, C. L., Coil, A. L., Lotz, J. M., Schiminovich, D., Bundy, K., & Noeske, K. G. 2012, ApJ, 758, 135

Kornei, K. A., Shapley, A. E., Martin, C. L., Coil, A. L., Lotz, J. M., & Weiner, B. J. 2013, ApJ, 774, 50

Kulas, K. R., Shapley, A. E., Kollmeier, J. A., Zheng, Z., Steidel, C. C., & Hainline, K. N. 2012, ApJ, 745, 33

Laursen, P., Sommer-Larsen, J., & Razoumov, A. O. 2011, ApJ, 728, 52

Leethochawalit, N., Jones, T. A., Ellis, R. S., Stark, D. P., & Zitrin, A. 2016, ApJ, 831, 152

Lehner, N., Zech, W. F., Howk, J. C., & Savage, B. D. 2011, ApJ, 727, 46

Leitherer, C., Ortiz Otálvaro, P. A., Bresolin, F., Kudritzki, R.-P., Lo Faro, B., Pauldrach, A. W. A., Pettini, M., & Rix, S. A. 2010, ApJS, 189, 309

Leitherer, C., Tremonti, C. A., Heckman, T. M., & Calzetti, D. 2011, AJ, 141, 37

Liang, C. J., & Chen, H.-W. 2014, MNRAS, 445, 2061

Liang, C. J., Kravtsov, A. V., & Agertz, O. 2016, MNRAS, 458, 1164

Livermore, R. C., Finkelstein, S. L., & Lotz, J. M. 2017, ApJ, 835, 113

Madau, P., & Dickinson, M. 2014, ARA&A, 52, 415

Maiolino, R., Nagao, T., Grazian, A., Cocchia, F., Marconi, A., Mannucci, F., Cimatti, A., Pipino, A., Ballero, S., Calura, F., Chiappini, C., Fontana, A., Granato, G. L., Matteucci, F., Pastorini, G., Pentericci, L., Risaliti, G., Salvati, M., & Silva, L. 2008, A&A, 488, 463

Mannucci, F., Cresci, G., Maiolino, R., Marconi, A., & Gnerucci, A. 2010, MNRAS, 408, 2115

Marchi, F., Pentericci, L., Guaita, L., Ribeiro, B., Castellano, M., Schaerer, D., Hathi, N. P., Lemaux, B. C., Grazian, A., Le Fèvre, O., Garilli, B., Maccagni, D., Amorin, R., Bardelli, S., Cassata, P., Fontana, A., Koekemoer, A. M., Le Brun, V., Tasca, L. A. M., Thomas, R., Vanzella, E., Zamorani, G., & Zucca, E. 2017, A&A, 601, A73

Markwardt, C. B. 2009, in Astronomical Society of the Pacific Conference Series, Vol. 411, Astronomical Data Analysis Software and Systems XVIII, ed. D. A. Bohlender, D. Durand, & P. Dowler, 251

Martin, C. L. 1999, ApJ, 513, 156

—. 2005, ApJ, 621, 227

Martin, C. L., & Bouché, N. 2009, ApJ, 703, 1394

Martin, C. L., Shapley, A. E., Coil, A. L., Kornei, K. A., Bundy, K., Weiner, B. J., Noeske, K. G., & Schiminovich, D. 2012, ApJ, 760, 127

Martin, C. L., Shapley, A. E., Coil, A. L., Kornei, K. A., Murray, N., & Pancoast, A. 2013, ApJ, 770, 41

Maseda, M. V., Brinchmann, J., Franx, M., Bacon, R., Bouwens, R. J., Schmidt, K. B., Boogaard, L. A., Contini, T., Feltre, A., Inami, H., Kollatschny, W., Marino, R. A., Richard, J., Verhamme, A., & Wisotzki, L. 2017, A&A, 608, A4

Momcheva, I. G., Brammer, G. B., van Dokkum, P. G., Skelton, R. E., Whitaker, K. E., Nelson, E. J., Fumagalli, M., Maseda, M. V., Leja, J., Franx, M., Rix, H.-W., Bezanson,

R., Da Cunha, E., Dickey, C., Förster Schreiber, N. M., Illingworth, G., Kriek, M., Labbé, I., Ulf Lange, J., Lundgren, B. F., Magee, D., Marchesini, D., Oesch, P., Pacifici, C., Patel, S. G., Price, S., Tal, T., Wake, D. A., van der Wel, A., & Wuyts, S. 2016, ApJS, 225, 27

Murray, N., Quataert, E., & Thompson, T. A. 2005, ApJ, 618, 569

Newman, J. A., Cooper, M. C., Davis, M., Faber, S. M., Coil, A. L., Guhathakurta, P., Koo, D. C., Phillips, A. C., Conroy, C., Dutton, A. A., Finkbeiner, D. P., Gerke, B. F., Rosario, D. J., Weiner, B. J., Willmer, C. N. A., Yan, R., Harker, J. J., Kassin, S. A., Konidaris, N. P., Lai, K., Madgwick, D. S., Noeske, K. G., Wirth, G. D., Connolly, A. J., Kaiser, N., Kirby, E. N., Lemaux, B. C., Lin, L., Lotz, J. M., Luppino, G. A., Marinoni, C., Matthews, D. J., Metevier, A., & Schiavon, R. P. 2013, ApJS, 208, 5

Noeske, K. G., Weiner, B. J., Faber, S. M., Papovich, C., Koo, D. C., Somerville, R. S., Bundy, K., Conselice, C. J., Newman, J. A., Schiminovich, D., Le Floc'h, E., Coil, A. L., Rieke, G. H., Lotz, J. M., Primack, J. R., Barmby, P., Cooper, M. C., Davis, M., Ellis, R. S., Fazio, G. G., Guhathakurta, P., Huang, J., Kassin, S. A., Martin, D. C., Phillips, A. C., Rich, R. M., Small, T. A., Willmer, C. N. A., & Wilson, G. 2007, ApJ, 660, L43

Oesch, P. A., Labbé, I., Bouwens, R. J., Illingworth, G. D., Gonzalez, V., Franx, M., Trenti, M., Holden, B. P., van Dokkum, P. G., & Magee, D. 2013, ApJ, 772, 136

Oke, J. B., Cohen, J. G., Carr, M., Cromer, J., Dingizian, A., Harris, F. H., Labrecque, S., Lucinio, R., Schaal, W., Epps, H., & Miller, J. 1995, PASP, 107, 375

Onodera, M., Carollo, C. M., Lilly, S., Renzini, A., Arimoto, N., Capak, P., Daddi, E., Scoville, N., Tacchella, S., Tatehora, S., & Zamorani, G. 2016, ApJ, 822, 42

Osterbrock, D. E., & Ferland, G. J. 2006, Astrophysics of gaseous nebulae and active galactic nuclei

Papovich, C., Dickinson, M., & Ferguson, H. C. 2001, ApJ, 559, 620

Pauldrach, A. W. A., Hoffmann, T. L., & Lennon, M. 2001, A&A, 375, 161

Pentericci, L., Grazian, A., Fontana, A., Castellano, M., Giallongo, E., Salimbeni, S., & Santini, P. 2009, A&A, 494, 553

Pentericci, L., Grazian, A., Fontana, A., Salimbeni, S., Santini, P., de Santis, C., Gallozzi, S., & Giallongo, E. 2007, A&A, 471, 433

Pentericci, L., Grazian, A., Scarlata, C., Fontana, A., Castellano, M., Giallongo, E., & Vanzella, E. 2010, A&A, 514, A64

Pentericci, L., Vanzella, E., Fontana, A., Castellano, M., Treu, T., Mesinger, A., Dijkstra, M., Grazian, A., Bradač, M., Conselice, C., Cristiani, S., Dunlop, J., Galametz, A., Giavalisco, M., Giallongo, E., Koekemoer, A., McLure, R., Maiolino, R., Paris, D., & Santini, P. 2014, ApJ, 793, 113

Pentericci, L., Garilli, R. J. M. B., Cucciati, O., Franzetti, P., Iovino, A., Amorin, R., Bolzonella, M., Bongiorno, A., Carnall, A. C., Castellano, M., Cimatti, A., Cirasuolo, M., Cullen, F., DeBarros, S., Dunlop, J. S., Elbaz, D., Finkelstein, S., Fontana, A., Fontanot, F., Fumana, M., Gargiulo, A., Guaita, L., Hartley, W., Jarvis, M., Juneau, S., Karman, W., Maccagni, D., Marchi, F., Marmol-Queralto, E., Nandra, K., Pompei, E., Pozzetti, L., Scodeggio, M., Sommariva, V., Talia, M., Almaini, O., Balestra, I., Bardelli, S., Bell, E. F., Bourne, N., Bowler, R. A. A., Brusa, M., Buitrago, F., Caputi, C., Cassata, P., Charlot, S., Citro, A., Cresci, G., Cristiani, S., Curtis-Lake, E., Dickinson, M., Faber, S. M., Fazio, G., Ferguson, H. C., Fiore, F., Franco, M., Fynbo, J. P. U., Galametz, A., Georgakakis, A., Giavalisco, M., Grazian, A., Hathi, N. P., Jung, I., Kim, S., Koekemoer, A. M., Khusanova, Y., Le Fèvre, O., Lotz, J., Mannucci, F., Maltby, D., Matsuoka, K., McLeod, D., Mendez-Hernandez, H., Mendez-Abreu, J., Mignoli, M., Moresco, M., Mortlock, A., Nonino, M., Pannella, M., Papovich, C., Popesso, P., Rosario, D. J., Rosati, P., Salvato, M., Santini, P., Schaerer, D., Schreiber, C., Stark, D., Tasca, L. A. M., Thomas, R., Treu, T., Vanzella, E., Wild, V., Williams, C., Zamorani, G., & Zucca, E. 2018, ArXiv e-prints, arXiv:1803.07373

Pettini, M., Rix, S. A., Steidel, C. C., Adelberger, K. L., Hunt, M. P., & Shapley, A. E. 2002, ApJ, 569, 742

Pettini, M., Shapley, A. E., Steidel, C. C., Cuby, J.-G., Dickinson, M., Moorwood, A. F. M., Adelberger, K. L., & Giavalisco, M. 2001, ApJ, 554, 981

Prochaska, J. X., Kasen, D., & Rubin, K. 2011, ApJ, 734, 24

Quider, A. M., Pettini, M., Shapley, A. E., & Steidel, C. C. 2009, MNRAS, 398, 1263

Reddy, N. A., Pettini, M., Steidel, C. C., Shapley, A. E., Erb, D. K., & Law, D. R. 2012, ApJ, 754, 25

Reddy, N. A., Steidel, C. C., Erb, D. K., Shapley, A. E., & Pettini, M. 2006, ApJ, 653, 1004

Reddy, N. A., Steidel, C. C., Pettini, M., Adelberger, K. L., Shapley, A. E., Erb, D. K., & Dickinson, M. 2008, ApJS, 175, 48

Reddy, N. A., Steidel, C. C., Pettini, M., Bogosavljević, M., & Shapley, A. E. 2016, ApJ, 828, 108

Reddy, N. A., Oesch, P. A., Bouwens, R. J., Montes, M., Illingworth, G. D., Steidel, C. C., van Dokkum, P. G., Atek, H., Carollo, M. C., Cibinel, A., Holden, B., Labbé, I., Magee, D., Morselli, L., Nelson, E. J., & Wilkins, S. 2018, ApJ, 853, 56

Rigby, J. R., Bayliss, M. B., Gladders, M. D., Sharon, K., Wuyts, E., Dahle, H., Johnson, T., & Peña-Guerrero, M. 2015, ApJ, 814, L6

Rix, S. A., Pettini, M., Leitherer, C., Bresolin, F., Kudritzki, R.-P., & Steidel, C. C. 2004, ApJ, 615, 98

Rubin, K. H. R., Prochaska, J. X., Koo, D. C., Phillips, A. C., Martin, C. L., & Winstrom, L. O. 2014, ApJ, 794, 156

Rubin, K. H. R., Prochaska, J. X., Ménard, B., Murray, N., Kasen, D., Koo, D. C., & Phillips, A. C. 2011, ApJ, 728, 55

Rudie, G. C., Steidel, C. C., Trainor, R. F., Rakic, O., Bogosavljević, M., Pettini, M., Reddy, N., Shapley, A. E., Erb, D. K., & Law, D. R. 2012, ApJ, 750, 67

Rupke, D. S., Veilleux, S., & Sanders, D. B. 2005, ApJS, 160, 115

Salim, S., Rich, R. M., Charlot, S., Brinchmann, J., Johnson, B. D., Schiminovich, D., Seibert, M., Mallery, R., Heckman, T. M., Forster, K., Friedman, P. G., Martin, D. C., Morrissey, P., Neff, S. G., Small, T., Wyder, T. K., Bianchi, L., Donas, J., Lee, Y.-W., Madore, B. F., Milliard, B., Szalay, A. S., Welsh, B. Y., & Yi, S. K. 2007, ApJS, 173, 267

Salpeter, E. E. 1955, ApJ, 121, 161

Sanders, R. L., Shapley, A. E., Kriek, M., Reddy, N. A., Freeman, W. R., Coil, A. L., Siana, B., Mobasher, B., Shivaei, I., Price, S. H., & de Groot, L. 2015, ApJ, 799, 138

Schenker, M. A., Ellis, R. S., Konidaris, N. P., & Stark, D. P. 2014, ApJ, 795, 20

Schwartz, C. M., & Martin, C. L. 2004, ApJ, 610, 201

Schwartz, C. M., Martin, C. L., Chandar, R., Leitherer, C., Heckman, T. M., & Oey, M. S. 2006, ApJ, 646, 858

Seibert, M., Martin, D. C., Heckman, T. M., Buat, V., Hoopes, C., Barlow, T., Bianchi, L., Byun, Y.-I., Donas, J., Forster, K., Friedman, P. G., Jelinsky, P., Lee, Y.-W., Madore, B. F., Malina, R., Milliard, B., Morrissey, P., Neff, S., Rich, R. M., Schiminovich, D., Siegmund, O., Small, T., Szalay, A. S., Welsh, B., & Wyder, T. K. 2005, ApJ, 619, L55

Senchyna, P., Stark, D. P., Vidal-García, A., Chevallard, J., Charlot, S., Mainali, R., Jones, T., Wofford, A., Feltre, A., & Gutkin, J. 2017, MNRAS, 472, 2608

Shapley, A. E., Steidel, C. C., Adelberger, K. L., Dickinson, M., Giavalisco, M., & Pettini, M. 2001, ApJ, 562, 95

Shapley, A. E., Steidel, C. C., Pettini, M., & Adelberger, K. L. 2003, ApJ, 588, 65

Shapley, A. E., Steidel, C. C., Strom, A. L., Bogosavljević, M., Reddy, N. A., Siana, B., Mostardi, R. E., & Rudie, G. C. 2016, ApJ, 826, L24

Shen, S., Madau, P., Guedes, J., Mayer, L., Prochaska, J. X., & Wadsley, J. 2013, ApJ, 765, 89

Shibuya, T., Ouchi, M., & Harikane, Y. 2015, ApJS, 219, 15

Skelton, R. E., Whitaker, K. E., Momcheva, I. G., Brammer, G. B., van Dokkum, P. G., Labbé, I., Franx, M., van der Wel, A., Bezanson, R., Da Cunha, E., Fumagalli, M., Förster Schreiber, N., Kriek, M., Leja, J., Lundgren, B. F., Magee, D., Marchesini, D., Maseda, M. V., Nelson, E. J., Oesch, P., Pacifici, C., Patel, S. G., Price, S., Rix, H.-W., Tal, T., Wake, D. A., & Wuyts, S. 2014, ApJS, 214, 24

Stanway, E. R., Eldridge, J. J., & Becker, G. D. 2016, MNRAS, 456, 485

Stark, D. P., Ellis, R. S., Bunker, A., Bundy, K., Targett, T., Benson, A., & Lacy, M. 2009, ApJ, 697, 1493

Stark, D. P., Ellis, R. S., Chiu, K., Ouchi, M., & Bunker, A. 2010, MNRAS, 408, 1628

Stark, D. P., Richard, J., Siana, B., Charlot, S., Freeman, W. R., Gutkin, J., Wofford, A., Robertson, B., Amanullah, R., Watson, D., & Milvang-Jensen, B. 2014, MNRAS, 445, 3200

Stark, D. P., Richard, J., Charlot, S., Clément, B., Ellis, R., Siana, B., Robertson, B., Schenker, M., Gutkin, J., & Wofford, A. 2015, MNRAS, 450, 1846

Stark, D. P., Ellis, R. S., Charlot, S., Chevallard, J., Tang, M., Belli, S., Zitrin, A., Mainali, R., Gutkin, J., Vidal-García, A., Bouwens, R., & Oesch, P. 2017, MNRAS, 464, 469

Steidel, C. C., Adelberger, K. L., Shapley, A. E., Pettini, M., Dickinson, M., & Giavalisco, M. 2003, ApJ, 592, 728

Steidel, C. C., Erb, D. K., Shapley, A. E., Pettini, M., Reddy, N., Bogosavljević, M., Rudie, G. C., & Rakic, O. 2010, ApJ, 717, 289

Steidel, C. C., Shapley, A. E., Pettini, M., Adelberger, K. L., Erb, D. K., Reddy, N. A., & Hunt, M. P. 2004, ApJ, 604, 534

Steidel, C. C., Strom, A. L., Pettini, M., Rudie, G. C., Reddy, N. A., & Trainor, R. F. 2016, ApJ, 826, 159

Steidel, C. C., Rudie, G. C., Strom, A. L., Pettini, M., Reddy, N. A., Shapley, A. E., Trainor, R. F., Erb, D. K., Turner, M. L., Konidaris, N. P., Kulas, K. R., Mace, G., Matthews, K., & McLean, I. S. 2014, ApJ, 795, 165

Strom, A. L., Steidel, C. C., Rudie, G. C., Trainor, R. F., Pettini, M., & Reddy, N. A. 2017, ApJ, 836, 164

Sugahara, Y., Ouchi, M., Lin, L., Martin, C. L., Ono, Y., Harikane, Y., Shibuya, T., & Yan, R. 2017, ApJ, 850, 51

Tilvi, V., Papovich, C., Finkelstein, S. L., Long, J., Song, M., Dickinson, M., Ferguson, H. C., Koekemoer, A. M., Giavalisco, M., & Mobasher, B. 2014, ApJ, 794, 5

Trainor, R. F., Steidel, C. C., Strom, A. L., & Rudie, G. C. 2015, ApJ, 809, 89

Trainor, R. F., Strom, A. L., Steidel, C. C., & Rudie, G. C. 2016, ApJ, 832, 171

Tremonti, C. A., Heckman, T. M., Kauffmann, G., Brinchmann, J., Charlot, S., White, S. D. M., Seibert, M., Peng, E. W., Schlegel, D. J., Uomoto, A., Fukugita, M., & Brinkmann, J. 2004, ApJ, 613, 898

Treu, T., Schmidt, K. B., Trenti, M., Bradley, L. D., & Stiavelli, M. 2013, ApJ, 775, L29

Treu, T., Trenti, M., Stiavelli, M., Auger, M. W., & Bradley, L. D. 2012, ApJ, 747, 27

Tumlinson, J., Peeples, M. S., & Werk, J. K. 2017, ARA&A, 55, 389

Vanzella, E., Cristiani, S., Dickinson, M., Kuntschner, H., Moustakas, L. A., Nonino, M., Rosati, P., Stern, D., Cesarsky, C., Ettori, S., Ferguson, H. C., Fosbury, R. A. E., Giavalisco, M., Haase, J., Renzini, A., Rettura, A., Serra, P., & GOODS Team. 2005, A&A, 434, 53

Vanzella, E., Cristiani, S., Dickinson, M., Kuntschner, H., Nonino, M., Rettura, A., Rosati, P., Vernet, J., Cesarsky, C., Ferguson, H. C., Fosbury, R. A. E., Giavalisco, M., Grazian, A., Haase, J., Moustakas, L. A., Popesso, P., Renzini, A., Stern, D., & GOODS Team. 2006, A&A, 454, 423

Vanzella, E., Cristiani, S., Dickinson, M., Giavalisco, M., Kuntschner, H., Haase, J., Nonino, M., Rosati, P., Cesarsky, C., Ferguson, H. C., Fosbury, R. A. E., Grazian, A., Moustakas, L. A., Rettura, A., Popesso, P., Renzini, A., Stern, D., & GOODS Team. 2008, A&A, 478, 83

Vanzella, E., Giavalisco, M., Dickinson, M., Cristiani, S., Nonino, M., Kuntschner, H., Popesso, P., Rosati, P., Renzini, A., Stern, D., Cesarsky, C., Ferguson, H. C., & Fosbury, R. A. E. 2009, ApJ, 695, 1163

Vanzella, E., Pentericci, L., Fontana, A., Grazian, A., Castellano, M., Boutsia, K., Cristiani, S., Dickinson, M., Gallozzi, S., Giallongo, E., Giavalisco, M., Maiolino, R., Moorwood, A., Paris, D., & Santini, P. 2011, ApJ, 730, L35

Vanzella, E., Guo, Y., Giavalisco, M., Grazian, A., Castellano, M., Cristiani, S., Dickinson, M., Fontana, A., Nonino, M., Giallongo, E., Pentericci, L., Galametz, A., Faber, S. M., Ferguson, H. C., Grogin, N. A., Koekemoer, A. M., Newman, J., & Siana, B. D. 2012, ApJ, 751, 70

Vanzella, E., De Barros, S., Cupani, G., Karman, W., Gronke, M., Balestra, I., Coe, D., Mignoli, M., Brusa, M., Calura, F., Caminha, G.-B., Caputi, K., Castellano, M., Christensen, L., Comastri, A., Cristiani, S., Dijkstra, M., Fontana, A., Giallongo, E., Giavalisco, M., Gilli, R., Grazian, A., Grillo, C., Koekemoer, A., Meneghetti, M., Nonino, M., Pentericci, L., Rosati, P., Schaerer, D., Verhamme, A., Vignali, C., & Zamorani, G. 2016, ApJ, 821, L27

Verhamme, A., Schaerer, D., Atek, H., & Tapken, C. 2008, A&A, 491, 89

Verhamme, A., Schaerer, D., & Maselli, A. 2006, A&A, 460, 397

Weiner, B. J., Coil, A. L., Prochaska, J. X., Newman, J. A., Cooper, M. C., Bundy, K., Conselice, C. J., Dutton, A. A., Faber, S. M., Koo, D. C., Lotz, J. M., Rieke, G. H., & Rubin, K. H. R. 2009, ApJ, 692, 187

Whitaker, K. E., Franx, M., Leja, J., van Dokkum, P. G., Henry, A., Skelton, R. E., Fumagalli, M., Momcheva, I. G., Brammer, G. B., Labbé, I., Nelson, E. J., & Rigby, J. R. 2014, ApJ, 795, 104

Willmer, C. N. A., Faber, S. M., Koo, D. C., Weiner, B. J., Newman, J. A., Coil, A. L., Connolly, A. J., Conroy, C., Cooper, M. C., Davis, M., Finkbeiner, D. P., Gerke, B. F., Guhathakurta, P., Harker, J., Kaiser, N., Kassin, S., Konidaris, N. P., Lin, L., Luppino, G., Madgwick, D. S., Noeske, K. G., Phillips, A. C., & Yan, R. 2006, ApJ, 647, 853

Wolfe, A. M., & Prochaska, J. X. 2000, ApJ, 545, 591

York, D. G., Adelman, J., Anderson, Jr., J. E., Anderson, S. F., Annis, J., Bahcall, N. A., Bakken, J. A., Barkhouser, R., Bastian, S., Berman, E., Boroski, W. N., Bracker, S., Briegel, C., Briggs, J. W., Brinkmann, J., Brunner, R., Burles, S., Carey, L., Carr, M. A., Castander, F. J., Chen, B., Colestock, P. L., Connolly, A. J., Crocker, J. H., Csabai, I., Czarapata, P. C., Davis, J. E., Doi, M., Dombeck, T., Eisenstein, D., Ellman, N., Elms, B. R., Evans, M. L., Fan, X., Federwitz, G. R., Fiscelli, L., Friedman, S., Frieman, J. A., Fukugita, M., Gillespie, B., Gunn, J. E., Gurbani, V. K., de Haas, E., Haldeman, M., Harris, F. H., Hayes, J., Heckman, T. M., Hennessy, G. S., Hindsley, R. B., Holm, S., Holmgren, D. J., Huang, C.-h., Hull, C., Husby, D., Ichikawa, S.-I., Ichikawa, T., Ivezić, Ž., Kent, S., Kim, R. S. J., Kinney, E., Klaene, M., Kleinman, A. N., Kleinman, S., Knapp, G. R., Korienek, J., Kron, R. G., Kunszt, P. Z., Lamb, D. Q., Lee, B., Leger, R. F., Limmongkol, S., Lindenmeyer, C., Long, D. C., Loomis, C., Loveday, J., Lucinio, R., Lupton, R. H., MacKinnon, B., Mannery, E. J., Mantsch, P. M., Margon, B., McGehee, P., McKay, T. A., Meiksin, A., Merelli, A., Monet, D. G., Munn, J. A., Narayanan, V. K., Nash, T., Neilsen, E., Neswold, R., Newberg, H. J., Nichol, R. C., Nicinski, T., Nonino, M., Okada, N., Okamura, S., Ostriker, J. P., Owen, R., Pauls, A. G., Peoples, J., Peterson, R. L., Petravick, D., Pier, J. R., Pope, A., Pordes, R., Prosapio, A., Rechenmacher,

R., Quinn, T. R., Richards, G. T., Richmond, M. W., Rivetta, C. H., Rockosi, C. M., Ruthmansdorfer, K., Sandford, D., Schlegel, D. J., Schneider, D. P., Sekiguchi, M., Sergey, G., Shimasaku, K., Siegmund, W. A., Smee, S., Smith, J. A., Snedden, S., Stone, R., Stoughton, C., Strauss, M. A., Stubbs, C., SubbaRao, M., Szalay, A. S., Szapudi, I., Szokoly, G. P., Thakar, A. R., Tremonti, C., Tucker, D. L., Uomoto, A., Vanden Berk, D., Vogeley, M. S., Waddell, P., Wang, S.-i., Watanabe, M., Weinberg, D. H., Yanny, B., Yasuda, N., & SDSS Collaboration. 2000, AJ, 120, 1579

Zahid, H. J., Geller, M. J., Kewley, L. J., Hwang, H. S., Fabricant, D. G., & Kurtz, M. J. 2013, ApJ, 771, L19

Zakamska, N. L., Strauss, M. A., Krolik, J. H., Collinge, M. J., Hall, P. B., Hao, L., Heckman, T. M., Ivezić, Ž., Richards, G. T., Schlegel, D. J., Schneider, D. P., Strateva, I., Vanden Berk, D. E., Anderson, S. F., & Brinkmann, J. 2003, AJ, 126, 2125

Zitrin, A., Ellis, R. S., Belli, S., & Stark, D. P. 2015, ApJ, 805, L7